Exploring the Features and Challenges of Proteolysis Targeting Chimera (PROTAC) Development

Citation

Permanent link

Terms of Use

Share Your Story

HARVARD UNIVERSITY
Graduate School of Arts and Sciences

DISSERTATION ACCEPTANCE CERTIFICATE

The undersigned, appointed by the

Department of

have examined a dissertation entitled

presented by

candidate for the degree of Doctor of Philosophy and hereby
certify that it is worthy of acceptance.

Signature _____
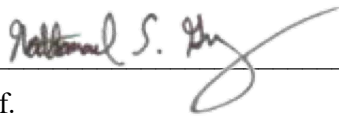
Typed name: Prof.

Signature _____

Typed name: Prof.

Signature _____

Typed name: Prof.

Signature _____

Typed name: Prof.

Signature _____

Typed name: Prof.

Date:

Exploring the Features and Challenges of Proteolysis Targeting Chimera (PROTAC)

Development

A dissertation presented

by

Inchul You

to

The Committee on Higher Degrees in Chemical Biology

in partial fulfillment of the requirements

for the degree of

Doctor of Philosophy

in the subject of

Chemical Biology

Harvard University

Cambridge, Massachusetts

October 2022

Dissertation Advisor: Dr. Nathanael S. Gray   Inchul You

Exploring the Features and Challenges of Proteolysis Targeting Chimera (PROTAC)

Development

Abstract

Small molecule inhibitors offer a powerful approach to modulate biological systems, having been successfully used as probes to interrogate protein functions and as drug therapies. However, many proteins of therapeutic interest are difficult to target with traditional small molecules due to either a lack of conventional drug-binding pockets or because they possess scaffolding activities that are not addressable by enzymatic inhibition. In contrast, targeted protein degradation (TPD), a pharmacological approach in which an E3 ligase is recruited into close proximity to a target of interest to induce its ubiquitination and subsequent proteasomal degradation, has emerged as a therapeutic modality with the potential to pursue targets previously deemed 'undruggable'. Here, we explore different features of TPD, ranging from assessing the degradability of different targets, redirecting the neo-substrate specificity of immunomodulatory imide drugs (IMiDs) and expanding the E3 ligase toolbox for proteolysis targeting chimera (PROTAC) development.

Chapter 2 describes the development of INY-03-041, the first reported small molecule AKT degrader. While AKT is an attractive therapeutic target with several ATP-competitive and allosteric inhibitors, these inhibitors have displayed a lack of efficacy or tolerability in clinical trials. As an alternative approach to inhibiting AKT activity, we conjugated the AKT inhibitor GDC-0068 to lenalidomide, a cereblon (CRBN)-recruiting ligand, to generate INY-03-041 as a

potent and highly selective AKT degrader. The relatively slow kinetics of INY-03-041-induced AKT degradation also prompted us to generate INY-05-040, an AKT degrader with improved degradation kinetics, through conjugating GDC-0068 with a Von Hippel-Lindau (VHL) ligand. Both INY-03-041 and INY-05-040 not only displayed enhanced anti-proliferative effects, but also induced more potent and durable inhibition of downstream signaling relative to AKT inhibitors, demonstrating the potential advantages of AKT-targeted degradation.

In Chapter 3, we employ small molecule degraders to interrogate the discrepancies observed between ERK5 kinase inhibition and genetic ERK5 ablation. As selective ATP-competitive ERK5 inhibitors were unable to recapitulate the anti-proliferative or anti-inflammatory effects observed from genetic ERK5 knockdown, it has been proposed that kinase-independent functions of ERK5 may play key roles in ERK5 signaling. Thus, we developed INY-06-061, a heterobifunctional degrader of ERK5, to investigate the therapeutic potential of inhibiting ERK5 signaling. While our studies suggest that acute pharmacological degradation of ERK5 does not inhibit cellular proliferation or immune response, INY-06-061 offers a valuable chemical probe to further explore the biological functions of ERK5.

In Chapter 4, we rationally redirect the neo-substrate specificity of IMiD-conjugated PROTACs to target the transcription factor Helios (IKZF2) as a proof-of-concept study. Through conjugation of the CDK4/6 inhibitor palbociclib to the IMiD-based Helios degrader DKY709, we generate ALV-07-082-03, a triple degrader of CDK4/CDK6/Helios. ALV-07-082-03 exhibited heightened immunostimulatory effects relative to palbociclib or DKY709 alone, highlighting the potential to synergistically target and degrade multiple proteins with one compound.

Chapter 5 employs covalent ligand discovery to identify ZNL-06-031 as a covalent DCAF11 binder. Through the incorporation of ZNL-06-031 as an E3 ligase recruiter for

PROTACs, we explore the degradable target space of DCAF11-based PROTACs. In addition, we also develop DCAF11 degraders as potential chemical probes to study DCAF11 function.

In sum, this work not only highlights the opportunities that come with PROTAC development, but also the challenges to overcome in the rapidly developing field.

Table of Contents

List of Figures and Tables

Figures

Tables

Acknowledgements

First, I would like to thank my advisor, Nathanael Gray. Your guidance and support have been instrumental throughout my development in graduate school, and I can't imagine myself finishing my degree in any other lab. Thank you for instilling in me the value of carrying out good science and always showing appreciation for the work that's been carried out regardless of the results.

Thank you to the entire Gray lab throughout the years for creating such a great environment to work in. If it weren't for the many chemists that were willing to teach me, I don't think I would have stuck with chemistry in graduate school. In particular, I would like to thank Baishan Jiang and Guangyan Du, who have given me continuous advice, whether it was about science or my career, even after leaving the lab. I would also like to thank Sean Toenjes for being such a great collaborator in my last year of graduate school.

Specifically, I would like to thank Eric Wang for mentoring me in graduate school. I don't think I would have ever thought of making a transition into biology if you weren't in lab, so thank you for teaching me everything I know. I think everyone in labs knows that I was able to do what I can due to your mentorship. I will be forever grateful for your support, encouragement, and scientific advice, even though it was never a part of the job description.

Thank you to my dissertation advice committee members -Sara Buhrlage, Alex Toker and David Weinstock- for your feedback and guidance throughout my PhD. I would also like to thank the Chemical Biology program at Harvard for creating a stress-free environment for graduate students.

Finally, I would like to thank my family for their constant support and encouragement. Thank you for always believing in me and creating an environment for me so that I could pursue a career in science.

Chapter 1: Introduction

Ubiquitin Proteasome System

The ubiquitin proteasome system (UPS) is a highly regulated pathway that degrades misfolded, damaged, or unwanted proteins. In this pathway, proteins are targeted for degradation by the 26S proteasome through the transfer of ubiquitin molecules by the ubiquitin-activating enzymes (E1), ubiquitin-conjugating enzymes (E2), and ubiquitin-protein enzymes (E3) (Ciechanover et al., 2000). The initial step of tagging proteins with ubiquitin involves covalent bond formation of ubiquitin with an active cysteine of an E1 through the use of ATP (Haas and Rose, 1982). The ubiquitin is then transferred to another cysteine of the next member of the cascade, the E2 (Jentsch, 1992). Finally, the E3 ubiquitin ligase recruits the protein substrate into close proximity with the E2-bound ubiquitin, promoting the transfer of ubiquitin to a lysine of the target protein (**Figure 1-1**) (Kleiger and Mayor, 2014). With the identification of over 600 E3 ligases, but only two E1 and approximately 40 E2 family members, the E3 ligases drive specificity in the ubiquitin protease pathway (Deshaies and Joazeiro, 2009).
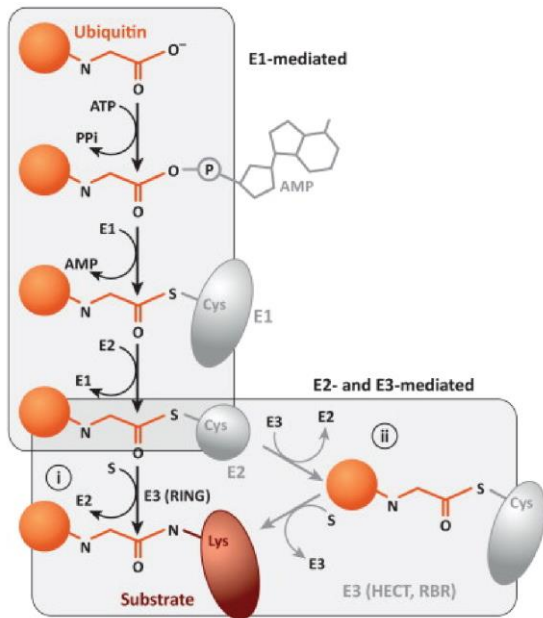
Figure 1-1. Schematic representation of the UPS pathway (adapted from Kleiger and Mayor, 2014).

Due to the importance of the UPS for maintaining cellular homeostasis, proteasome inhibitors have been developed as cancer therapies. Bortezomib (marketed as Velcade), a covalent inhibitor of the 26S proteasome, has demonstrated clinical efficacy through inhibition of nuclear factor kappa B (NF-κB) activation and is currently FDA-approved for the treatment of multiple myeloma and mantle cell lymphoma (Adams, 2001; Thibaudeau and Smith, 2019). A second generation proteasome inhibitor carfilzomib (Kyprolis) has also been FDA-approved for the treatment of relapsed/refractory multiple myeloma (Engelhardt et al., 2018). Despite the clinical success of proteasome inhibitors in the clinic, they are associated with high rates of resistance and dose-limiting toxicities (Goldberg, 2012). Thus, new strategies are necessary to further uncover the therapeutic potential of targeting the UPS.

Targeted Protein Degradation

Rather than inhibiting the ubiquitin proteasome pathway, harnessing the degradation machinery for targeted protein degradation (TPD) has emerged as an alternative therapeutic approach. While inducing cellular protein knockdown or knockout through genetic means, including RNA interference (RNAi) and CRISPR/Cas9, have been widely applied to probe protein function, limited delivery and off-target effects have significantly hindered their progress as therapeutics (Conde and Artzi, 2015; Modell et al., 2022). Therefore, developing small molecule degraders has garnered significant interest from both academic labs and industry.

Proteolysis targeting chimeras (PROTACs) are heterobifunctional molecules which consist of a small molecule binder of a protein of interest (POI) chemically conjugated to an E3 ligase ligand. Recruitment of the E3 ligase into close proximity of the POI induces ubiquitination of the POI and subsequent proteasomal dependent degradation (**Figure 1-2**). The first PROTAC, dubbed

Protac-1, was reported in 2001, in which F-box protein β-TRCP was recruited to methionine aminopeptidase-2 (MetAP-2) to induce MetAP-2 degradation in extracts from unfertilized Xenopus laevis eggs (Sakamoto et al., 2001). While subsequent studies demonstrated that the E3 ligases mouse double minute 2 homolog (MDM2) and von Hippel-Lindau (VHL) could be recruited to induce degradation of androgen receptor (AR) and 12-kDa FK506 binding protein (FKBP12), respectively, these compounds suffered from low degradation potency and poor cell permeability issues, stalling further advances in the field (Schneekloth et al., 2008; Schneekloth et al., 2004).
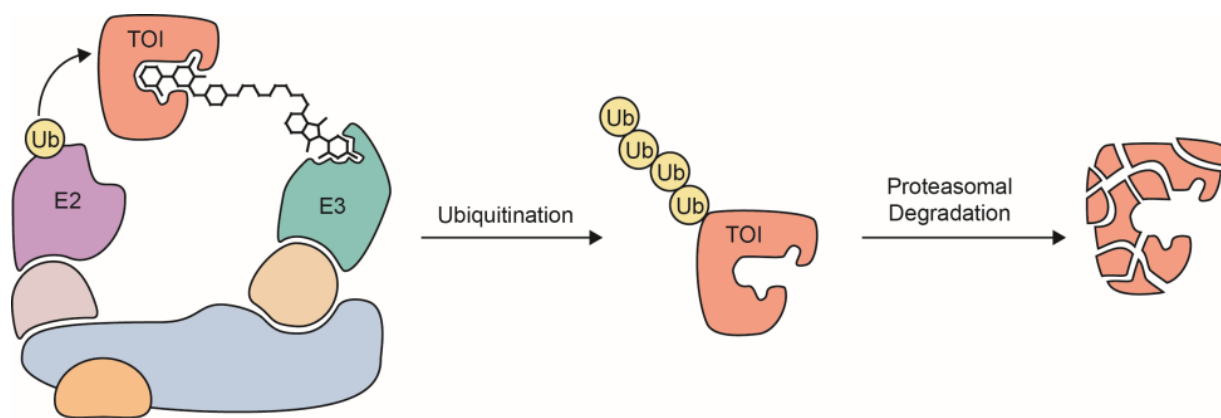
Figure 1-2. General depiction of a PROTAC's mechanism of action. One end of the molecule engages with the target of interest (TOI), while the other end engages with an E3 ubiquitin ligase. With the formation of a ternary complex, the TOI undergoes ubiquitination and subsequent proteasomal degradation.

Two major breakthroughs that uncovered the therapeutic viability of small molecule degraders were made in the 2010s. First, the E3 ligase cereblon (CRBN) was discovered to be the target of thalidomide and its analogues, lenalidomide and pomalidomide (Ito et al., 2010; Kronke et al., 2014). In addition, significant medicinal chemistry efforts led to the development of a potent and cell-permeable ligand for the E3 ligase VHL (Buckley et al., 2012a; Buckley et al., 2012b).

Identification of these E3 ligase ligands with improved drug-like properties led to the generation of CRBN- and VHL-based PROTACs that not only displayed improved degradation potencies and cellular permeability relative to previous PROTACs, but also demonstrated the ability to induce protein degradation *in vivo* (Bondeson et al., 2015; Winter et al., 2015). These breakthroughs spurred the PROTAC gold rush, with over 1000 PROTACS having been reported to date (Weng et al., 2021).

PROTACs offer several potential advantages over traditional small molecules. As PROTACs are thought to act in a 'pseudo-catalytic' manner, sub-stoichiometric amounts of drug may be required to elicit the desired pharmacology (Sun et al., 2019). Consistently, extended pharmacodynamic effects of PROTACs have been observed *in vivo*, even after the drug was cleared from systemic circulation, suggesting that PROTACs may provide wider therapeutic windows (Bai et al., 2019; Mares et al., 2020). Other advantages of PROTACs include the ability to enhance selectivity of multi-targeted inhibitors (Jiang et al., 2019; Olson et al., 2018), abrogate scaffolding functions that are otherwise unamendable to enzymatic inhibition (Adhikari et al., 2020; Cromm et al., 2018) and overcome resistance mutations (Dobrovolsky et al., 2018). Furthermore, the target-binding moiety of PROTACs needs to bind, but not necessarily inhibit the POI, thereby expanding the landscape of druggable targets (Békés et al., 2022).

Beyond PROTACs, other pharmacological strategies for TPD include 'molecular glues' (Dong et al., 2021), lysosome-targeting chimeras (LYTACs) (Banik et al., 2020), photoswitchable PROTACs (photoPROTACs) (Pfaff et al., 2019) and autophagy-targeting chimeras (AUTACs) (Takahashi et al., 2019). However, this thesis will focus on highlighting the different features of PROTAC technology. In Chapter 2 and 3, we expand the degradable target space of CRBN- and VH-based PROTACs through the development and characterization of AKT and ERK5 degraders,

respectively. In Chapter 4, we redirect the neo-substrate specificity of PROTACs through the use of alternative CRBN modulators as the E3 ligase ligand and report the development of a triple CDK4, CDK6 and Helios degrader. Finally, Chapter 5 presents the discovery of a novel covalent DCAF11 binder. Through generation of DCAF11-recuriting PROTACs, we further investigate the potential of DCAF11 to be utilized as a general E3 ligase for PROTAC development.

AKT and its role in oncology

AKT is a family of serine/threonine (Ser/Thr) kinases that is involved in multiple biological processes, such cell growth, angiogenesis and metabolism (Risso et al., 2015). In humans, the AKT kinase family consists of three isoforms (AKT1, AKT2 and AKT3) that are derived from distinct genes (Toker, 2012). The three isoforms share a high degree of sequence homology, with conserved pleckstrin homology (PH) and catalytic domains (Hanada et al., 2004). While there is growing evidence for AKT isoform-specific substrate phosphorylation, the majority of AKT substrates have been reported to be regulated by all three isoforms (Manning and Toker, 2017; Wang et al., 2017).

All AKT isoforms are activated by essentially identical mechanisms: stimulation of receptor tyrosine kinases (RTKs) or G-protein-coupled receptors (GPCRs) leads to the recruitment and activation of phosphoinositide 3-kinase (PI3K), which phosphorylates phosphatidylinositol-4,5-biphophate (PIP$_2$) to produce phosphatidylinositol-3,4,5-triphosphate (PIP$_3$) (Vanhaesebroeck et al., 2010). AKT then engages PIP$_3$ via its PH domain, resulting in its localization to the plasma membrane and induction of a conformational change that enables phosphorylation at two critical residues: Thr308 and Ser473 in AKT1, Thr309 and Ser474 in AKT2, and Thr305 and Ser472 in AKT3 (Calleja et al., 2007; Sarbassov et al., 2005). Phosphorylation of Thr308, located in the activation loop of the kinase domain, is regulated by phosphoinositide-dependent kinase 1 (PDK1)

(Alessi et al., 1997), while phosphorylation of Ser473 is mediated by the mechanistic target of rapamycin complex 2 (mTORC2), which stabilizes AKT in its active state and promotes maximal activity (Alessi et al., 1996; Sarbassov *et al.*, 2005). While phosphorylation of Thr308 is required for kinase activity of AKT1, phosphorylation of Ser473 is not, as AKT1 has been reported to be active, albeit weakly, in the absence of phosphorylation at this site (Yang et al., 2002).

Upon full activation, AKT phosphorylates a wide variety of substrates, including metabolic enzymes and transcription factors, that have a consensus recognition motif of R-X-R-X-X-S/T-ϕ (where X is any amino acid and ϕ is a preference for hydrophobic residues) (Manning and Toker, 2017). While there are over 100 reported substrates for AKT, the activation of AKT primarily promotes cell growth/proliferation and changes in metabolism (Manning and Cantley, 2007).

As AKT is a central component of the PI3K/AKT signaling pathway, AKT dysregulation has been associated with various diseases, especially cancer (Altomare and Testa, 2005). Hyperactivation of AKT is one of the most common molecular perturbations in cancer, which occurs through an assortment of different mechanisms, including overexpression or amplification of AKT (Cheng et al., 1992), activating mutations of upstream RTKs or PI3K (Shayesteh et al., 1999), or inactivating mutations of tumor suppressor gene phosphatase and tensin homolog 10 (PTEN) (Cantley and Neel, 1999). Thus, the pro-survival and pro-growth effects of PI3K/AKT pathway activation make AKT an attractive therapeutic target in oncology.

Figure 1-3. Chemical structures of selected AKT inhibitors. Top row represents ATP-competitive inhibitors, while bottom row represents allosteric inhibitors.
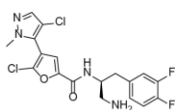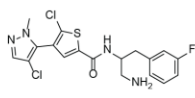
Several ATP-competitive and allosteric AKT inhibitors are currently being investigated in the clinic, either as monotherapies or combination strategies (**Figure 1-3**). While multiple ATP-competitive AKT inhibitors, including uprosertib (GSK2141795), afuresertib (GSK2110183), GSK690693, ipatasertib (GDC-0068) and capivasertib (AZD5363), have undergone testing in phase I trials, limited efficacy was observed as monotherapies in molecularly unselected patient populations (Aghajanian et al., 2018; Saura et al., 2017). Of the ATP-competitive inhibitors, capivasertib (AZD5363) has progressed furthest in clinical trials and is currently under phase III clinical investigation in combination with fulvestrant for treating HR+/HER2- breast cancers (NCT04305496).
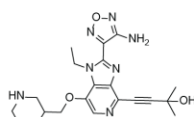
Allosteric AKT inhibitors under clinical investigation include MK-2206, miransertib (ARQ-092), ARQ-751 and BAY1125976. As these inhibitors target an allosteric pocket within the PH-domain/kinase-domain interface that stabilizes the inactive conformation of AKT (Wu et al., 2010), allosteric inhibitors have the potential to offer better selectivity profiles than ATP-competitive inhibitors. However, the most extensively investigated inhibitor MK-2206 has

8

displayed limited efficacy as a monotherapy in phase II trials across a range of tumor types, as well as dose-limiting toxicities (Ahn et al., 2015; Yap et al., 2011). ARQ-092, on the other hand, demonstrated acceptable tolerability, although limited efficacy was observed in both solid and hematological cancers (Coleman et al., 2021; Yu et al., 2015). Finally, a covalent allosteric AKT inhibitor, borussertib, has been reported to demonstrate preclinical efficacy in *KRAS*-mutant pancreatic and colorectal cancers, but has yet to advance to clinical trials (Uhlenbrock et al., 2019).

Several factors may hinder the efficacy of AKT inhibitors in the clinic. Due to the high sequence homology among the kinase domains of AGC kinases, ATP-competitive inhibitors may suffer from a lack of selectivity, leading to dose-limiting toxicities (Huck and Mochalkin, 2017). In addition, kinase-independent functions of AKT that promote cancer cell survival have been reported (Vivanco et al., 2014). To address these issues, Chapter 2 of this thesis will describe the development of the first reported small molecule degrader of AKT as a different pharmacological approach to targeting AKT.

Biological Functions of ERK5

Mitogen-activated protein kinases (MAPKs) are highly conserved enzymes that are ubiquitously expressed throughout all eukaryotic cells. As one of the central signaling pathways that mediate intracellular communication between membranal receptors and their target proteins, the MAPK cascade regulates a wide variety of cellular processes, including cell proliferation, apoptosis, differentiation and stress response (Coulthard et al., 2009; Mebratu and Tesfaigzi, 2009; Sun et al., 2015).

The MAPK signaling cascade is activated by either a small GTP-binding protein (Ras) or an adaptor protein, which transmits its signal to the MAPK kinase kinase (MAP3K) proteins of the cascade. Upon activation, the MAP3K proteins phosphorylate the MAPK kinases (MAPKKs),

which further induce phosphorylation and subsequent activation of the MAPKs. Unlike the MAP3Ks and MAPKKs, which are used mainly for signal transmission, the MAPKs, as well as the subsequently activated MAPK-activated protein kinases (MAPKAPKs) can phosphorylate a wide variety of substrates that regulate various cellular processes (Wortzel and Seger, 2011).
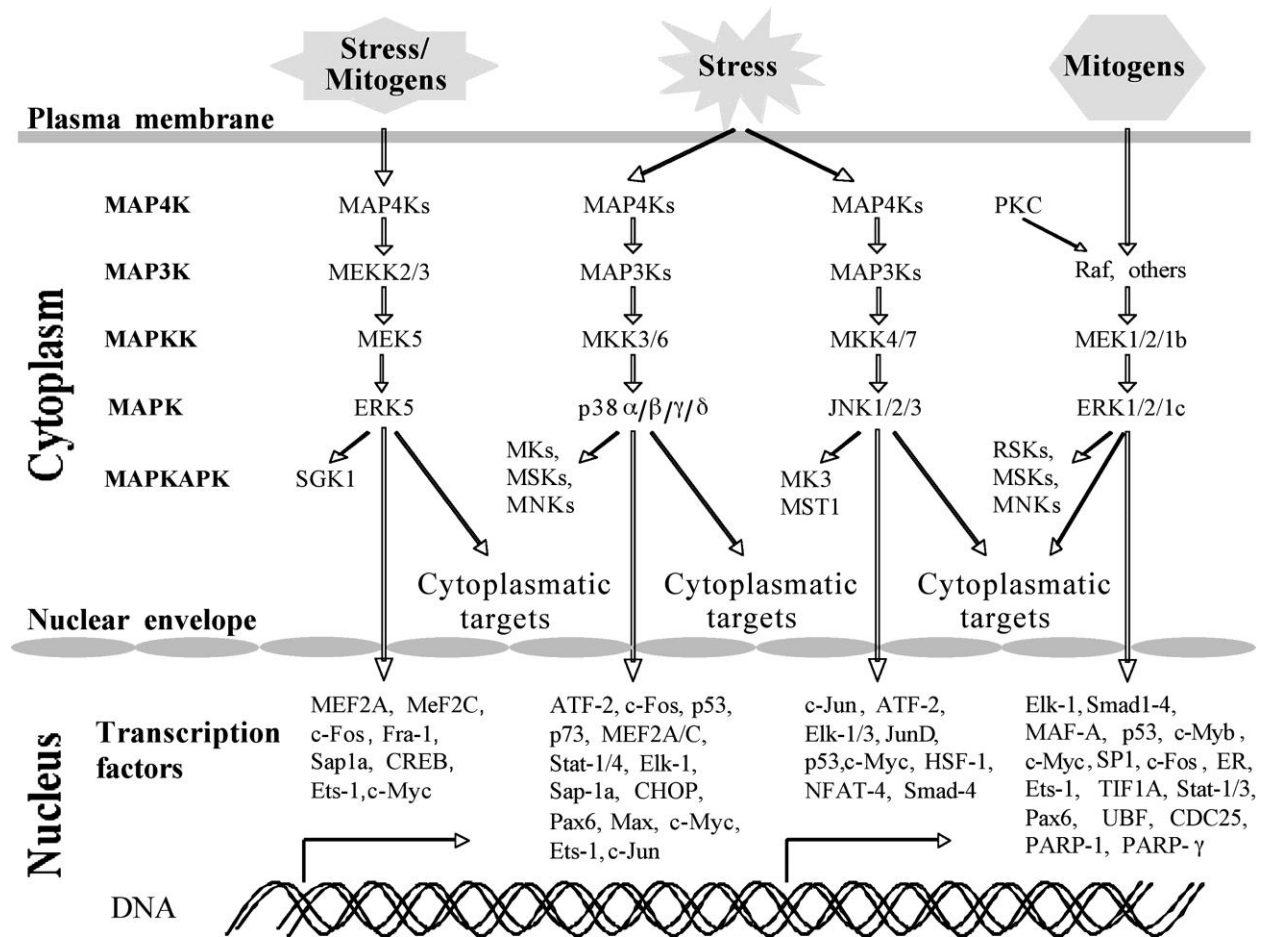
Figure 1-4. General schematic representation of the MAPK cascades (Plotnikov et al., 2011)

There are four distinct MAPK cascades identified in mammalian cells: the extracellular signal regulated kinase 1/2 (ERK1/2), c-Jun N-terminal kinase (JNK), p38 and ERK5 signaling cascades (Plotnikov *et al.*, 2011) (**Figure 1-4**). The ERK1/2 cascade has been reported to mainly transmit mitogenic signals (Yoon and Seger, 2006), while JNK and p38 signaling cascades seem to mainly be activated by stress-related stimuli (Davis, 1994; Kyriakis and Avruch, 2001). Due to

the therapeutic implications of targeting ERK1/2, JNK, and p38 in cancer and inflammation, these signaling cascades have been extensively studied.

In contrast, ERK5 is the least studied member of the MAPK family. Unlike the other MAPK signaling cascades, ERK5 may play equal roles in both mitogenic and stress signaling (Nishimoto and Nishida, 2006) and has been associated with a diverse range of cellular functions, including cellular proliferation, migration and angiogenesis (Hoang et al., 2017; Roberts et al., 2009). Despite mediating mitogenic signals similarly to ERK1/2, ERK5 signaling cannot be compensated by other MAPK pathways (Nishimoto and Nishida, 2006). Accordingly, Erk5 null mice display defects in vascular and cardiac development, highlighting the unique role of ERK5 mediating angiogenesis, at least in the embryonic stages of mice (Regan et al., 2002). With a unique C-terminal domain that contains a myocyte enhancer factor 2 (MEF2)-interacting domain (Yan et al., 2001) and transcriptional activation domain (TAD) (Kasler et al., 2000), MEF2D is one of the few validated substrates specific to ERK5 (Yang et al., 1998). Other putative substrates of ERK5 include the transcription factors Sap-1a, c-Fos and c-MYC (English et al., 1998; Kamakura et al., 1999). However, these interactions remain poorly elucidated and further studies are required to validate their roles in the ERK5 signaling cascade.

Despite the lack of mechanistic studies regarding the ERK5 pathway, genetic knockdown or ablation studies have implicated ERK5 to play critical roles in various diseases, most notably in cancer and inflammation. For example, genetic knockdown of ERK5 has been reported to suppress proliferation in prostate cancers (Mehta et al., 2003; Ramsay et al., 2011), while ERK5 activation has been observed as resistance mechanisms to Raf-MEK1/2-ERK1/2 targeted therapies in RAS- and BRAF-driven cancers (Song et al., 2017; Vaseva et al., 2018). In addition, ERK5 has

been implicated as a meditator of inflammation-driven cancers (Finegan et al., 2015; Giurisato et al., 2018).

As phenotypes observed from genetic knockdown or deletion of ERK5 suggested that targeting ERK5 could have therapeutic potential in various disease settings, several selective ATP-competitive ERK5 inhibitors, including AX15836 and BAY-885, were developed (Lin et al., 2016; Nguyen et al., 2019). However, these inhibitors were unable to recapitulate the anti-proliferative or anti-inflammatory phenotypes in cancer and endothelial cells, respectively, that were previously reported through genetic knockdown of ERK5. One explanation for the discrepancies observed between ERK5 kinase inhibition and genetic ERK5 ablation is that ERK5 has key kinase-independent functions. In addition, a recent study suggests that inhibition of the ERK5 kinase domain leads to activation of its transcriptional activation domain, paradoxically driving ERK5-dependent transcription (Lochhead et al., 2020). Thus, development of chemical probes to interrogate the discrepancies observed between genetic modulation and kinase inhibition of ERK5 will be beneficial in further elucidating ERK5 functions, as well as determining its therapeutic potential. Chapter 3 of this thesis presents the development and characterization of the first reported ERK5 degrader to validate phenotypes reported to be associated with genetic ERK5 ablation.

Immunomodulatory imide drugs and neo-substrate specificity

Thalidomide is an infamous drug known for its teratogenic effects following its use as an anti-emetic for pregnant woman, leading to widespread birth defects and miscarriages in the late 1950s and early 1960s (Miller and Strömland, 1999). Further studies have shown that thalidomide, along with its analogues lenalidomide and pomalidomide (**Figure 1-5**), have immunomodulatory and anti-inflammatory properties (Haslett et al., 1998; Sampaio et al., 1991), leading to their

designation as immunomodulatory imide drugs (IMiDs). Despite the lack of understanding of the mechanism of action of IMiDs, IMiDs have been FDA-approved for the treatment of various diseases, including multiple myeloma (Palumbo et al., 2012), mantle cell lymphoma (Habermann et al., 2009) and myelodysplastic syndrome (MDS) with del(5q) (List et al., 2006).
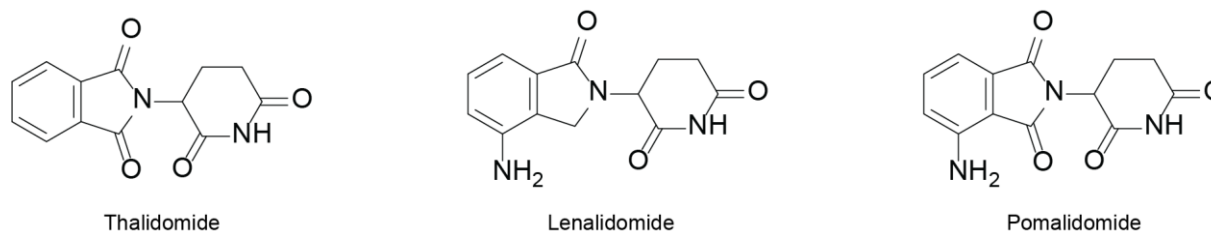
Figure 1-5. Chemical structures of select IMiDs

In 2010, a major breakthrough was made in elucidating the mechanism of action of thalidomide, as cereblon (CRBN) was identified to bind to thalidomide (Ito *et al.*, 2010). CRBN is a substrate adaptor protein of the CRL4^{CRBN} E3 ubiquitin ligase, which comprises of cullin 4 (CUL4), DNA damage binding protein 1 (DDB1) and Ring-box 1 (RBX1). Building on this observation, proteomics analysis revealed that the IMiDs promoted CRBN-dependent degradation of transcription factors Ikaros (IKZF1) and Aiolos (IKZF3) (Kronke *et al.*, 2014; Lu et al., 2014), suggesting that IMiDs acted as 'molecular glues' to recruit its substrates (known as neo-substrates) to CRBN. Additional studies identified ZFP91 (An et al., 2017), casein kinase 1α (Kronke et al., 2015), GSPT1 (Matyskiela et al., 2016), SALL4 (Donovan et al., 2018) and IKZF2 (Helios) (Wang et al., 2021b) to be neo-substrates of various CRBN modulators. While there is no obvious sequence homology among the reported neo-substrates, they all share a characteristic β-hairpin loop and a key glycine residue that interacts with the phthalimide moiety of IMiDs (An *et al.*, 2017; Matyskiela *et al.*, 2016; Petzold et al., 2016).

With the discovery that IMiDs imparted gain-of-function properties to the cullin RING E3 ubiquitin ligase CRL4^{CRBN}, IMiDs were next used as E3 ligase recruiters for the development of

heterobifunctional degraders, also known as proteolysis targeting chimeras (PROTACs). The first reported PROTAC that hijacked the CRL4^{CRBN} complex was dBET1, which induced potent bromodomain and extra-terminal (BET) protein degradation (Winter *et al.*, 2015). To date, over 1000 PROTACs have been reported (Weng *et al.*, 2021). While ligands for multiple E3 ligases, such as VHL, MDM2, DCAF15, DCAF16 and RNF114, have been identified, IMiDs remain one of the most utilized E3 ligase ligands for PROTAC development (Wang et al., 2021a), especially in the clinic (Mullard, 2021).

As the CRBN ligands of PROTACs can retain their ability to act as molecular glues, PROTACs have the potential to degrade the IMiDs' neo-substrates as well (Remillard et al., 2017). While the canonical neo-substrates (i.e., Ikaros and Aiolos) are often considered to be unwanted off-targets of PROTACs, maintaining the degradation of these neo-substrates also provides the opportunity to synergistically degrade multiple proteins with a single compound. For example, inducing triple degradation of BTK, Ikaros and Aiolos using thalidomide-based PROTACs demonstrated enhanced anti-proliferative effects in mantle cell lymphoma cells relative to selective BTK degraders (Dobrovolsky *et al.*, 2018). In addition, co-degradation of BTK and GSPT1 also displayed enhanced anti-proliferative effects in diffuse large B cell lymphoma and acute myeloid leukemia cells (Yang et al., 2021). In Chapter 4 of the thesis, we exploit the activities of the E3 ligase-binding moiety to develop PROTACs that induce simultaneous degradation of CDK4, CDK6 and Helios and demonstrate the possibility of re-directing the neo-substrate specificity of PROTACs by utilizing alternative CRBN modulators.

Expanding the E3 ligase toolbox for PROTAC development

Although the human genome encodes for more than 600 E3 ubiquitin ligases (Kleiger and Mayor, 2014), only a handful of E3 ligases have successfully been utilized for PROTAC

development (Burslem and Crews, 2020). In fact, most of the reported PROTACs recruit either the Cullin Ring E3 ubiquitin ligase substrate adaptor CRBN or von-Hippel-Landau tumor suppressor protein (VHL) (Ishida and Ciulli, 2021). While CRBN- and VHL-based PROTACs have been shown to degrade a wide variety of proteins (Weng *et al.*, 2021), solely relying on these two E3 ubiquitin ligases likely limits the degradable target space. For example, KRAS^{G12C} and tubulin have been reported to resist degradation by CRBN-recruiting PROTACs (Gasic et al., 2020; Zeng et al., 2020). In addition, kinase-directed CRBN- and VHL-based PROTACs have been shown to degrade different targets, suggesting that incorporation of additional E3 ligases may expand the degradable target space (Donovan et al., 2020).

Resistance mechanisms to CRBN- and VHL-based PROTACs have also been reported. Consistent with the mechanism of resistance to IMiDs in multiple myeloma (Zhu et al., 2011), resistance to CRBN-based BET PROTACs was caused by genetic deletion of the *CRBN* gene in OVCAR8 cells (Zhang et al., 2019a). In contrast, resistance to VHL-based BET PROTACs was caused not by deletion of the *VHL* gene, but through abolishment of CUL2 function (Zhang *et al.*, 2019a). While no PROTACs have currently reached clinics for drug resistance to emerge, this study indicates that PROTAC resistance could emerge from mutations in the degradation machinery. This may, however, be prevented if essential E3 ligases can be recruited for PROTAC development.
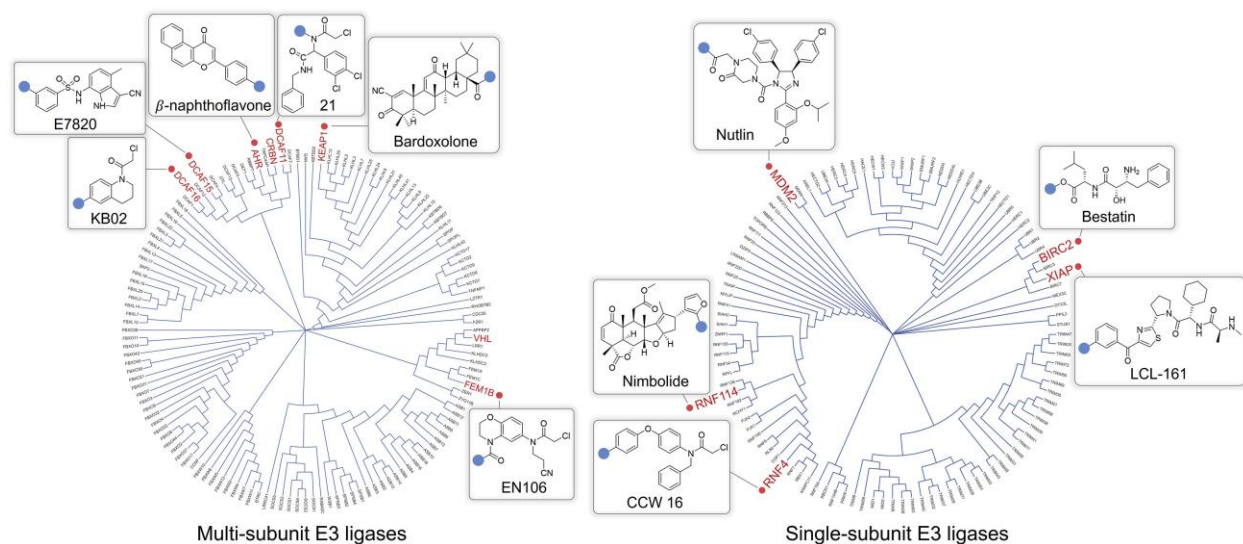
Figure 1-6. List of E3 ligases and corresponding ligands that have been incorporated as PROTACs (Kramer and Zhang, 2022).

Substantial efforts have been carried out in order to expand the E3 ligase toolbox for PROTAC development, resulting in the incorporation of multiple E3 ligase ligands for TPD (**Figure 1-6**). Beyond CRBN and VHL, PROTACs have been generated by previously reported E3 ligase ligands of MDM2 (Hines et al., 2019), cIAP (Itoh et al., 2010), AhR (Ohoka et al., 2019), KEAP1 (Du et al., 2022; Wei et al., 2021) and DCAF15 (Li et al., 2020). However, few advantages have been observed over CRBN- or VHL-based PROTAC, stalling implementation of these E3 ligase ligands for general PROTAC development.

Identification of new E3 ligase ligands have heavily relied on chemoproteomics approaches, resulting in the discovery of several covalent E3 ligase ligands. Specifically, activity-based protein profiling (ABPP) (Backus et al., 2016) has been utilized to identify E3 ligands for RNF4 (Ward et al., 2019) , RNF114 (Spradlin et al., 2019) and FEM1B (Henning et al., 2022), which were further incorporated for PROTAC development. Additionally, phenotypical degradation assays carried out in combination with affinity purification mass spectrometry strategies have demonstrated that

DCAF16 (Zhang et al., 2019b) and DCAF11 (Zhang et al., 2021) can be recruited for targeted protein degradation.

There are several potential advantages of electrophilic PROTACs. For example, as they covalently label the E3 ligase, electrophilic PROTACs are thought to induce pseudo-binary complexes, which could improve kinetic stability of the protein-protein interactions to enhance degradation efficiency (Kramer and Zhang, 2022). In addition, DCAF16 and DCAF11-recruiting PROTACs induced degradation of target proteins with low fractional occupancies of their respective E3 ligases, which may minimize perturbing the endogenous degradation machinery (Zhang *et al.*, 2019b; Zhang *et al.*, 2021). However, electrophilic PROTACs also carry the disadvantages of traditional covalent ligands, which include metabolic liabilities and toxicity concerns (Singh et al., 2011). Furthermore, the degradable target space explored with newly identified E3 ligase ligands has been limiting, as most have been incorporated as BRD4 or FKBP12 degraders. In Chapter 5 of this thesis, we describe the discovery of a novel covalent DCAF11 ligand and further investigate the degradable target space of DCAF11-recruiting PROTACs.

Chapter 2: Discovery and Characterization of AKT Degraders

Attributions

The work is this chapter is adapted from a manuscript published in *Cell Chemical Biology* entitled "Discovery of an AKT Degrader with Prolonged Inhibition of Downstream Signaling" by You and Erickson *et al*, as well as a manuscript in preparation entitled "Multi-omic profiling of breast cancer cells uncovers stress MAPK-associated sensitivity to AKT degradation" by Erickson and You *et al*.

Contributions

Alex Toker and Nathanael Gray conceived the concept of AKT degraders and supervised the project. Ralitsa Madsen analyzed omics datasets, performed COSMOS, and supervised the project. Inchul You designed and synthesized the compounds, and conducted experiments required for their initial chemical and biological characterization. Emily C. Erickson designed and performed all other cell culture-based experiments. Aurelien Dugourd assisted with the COSMOS installation and subsequent result interpretation. Katherine A. Donovan performed proteomics experiments. Emily C. Erickson, Ralitsa R. Madsen and Alex Toker wrote the manuscript and prepared figures for publication. All authors reviewed the final manuscript.

Introduction

The serine/threonine kinase AKT is a central component of the phosphoinositide 3-kinase (PI3K) signaling cascade and is a key regulator of critical cellular processes, including proliferation, survival and metabolism (Manning and Toker, 2017). The AKT protein kinase family is comprised of three highly homologous isoforms, AKT1, AKT2 and AKT3, that possess both redundant functions and isoform-specific activities (Toker, 2012). Hyperactivation of AKT, due to gain-of-function mutations or amplification of oncogenes (receptor tyrosine kinases, PI3K) or inactivation of tumor suppressor genes (PTEN, INPP4B, PHLPP), is one of the most common molecular perturbations in cancer and promotes malignant phenotypes associated with tumor initiation and progression (Cantley and Neel, 1999; Fruman et al., 2017; Shayesteh *et al.*, 1999). Thus, AKT is an attractive therapeutic target and significant efforts have been made to develop AKT targeted therapies (Brown and Banerji, 2017).

Current strategies to target AKT have focused on ATP-competitive, allosteric and covalent inhibitors. Several ATP-competitive inhibitors, such as ipatasertib (GDC-0068) and capivasertib (AZD5363), are currently under clinical investigation in phase II and III studies (Oliveira et al., 2019; Turner et al., 2019). However, these inhibitors suffer from a lack of selectivity among the AGC kinase family, which may limit their clinical efficacy or tolerability (Huck and Mochalkin, 2017). By contrast, allosteric inhibitors which target the pleckstrin homology (PH) domain, such as MK-2206 and miransertib (ARQ-092), exhibit a high degree of specificity towards AKT, but either lack significant efficacy in the clinic or require further clinical evaluation (Do et al., 2015; Keppler-Noreuil et al., 2019). Covalent allosteric inhibitors which target AKT at Cys296 and Cys310 have been reported, but have not advanced to clinical trials (Uhlenbrock *et al.*, 2019).

An alternative pharmacological approach to inhibiting AKT activity is to directly reduce cellular AKT protein levels via targeted protein degradation. Heterobifunctional degraders, also known as PROTACs (proteolysis targeting chimeras), consist of a moiety that binds to an E3 ubiquitin ligase chemically linked to a second moiety that engages a target protein, thereby recruiting the E3 ligase into close proximity to the target protein to induce its ubiquitination and subsequent proteasomal degradation (Winter *et al.*, 2015). Several advantages of degraders over inhibitors have been reported, which include enhancing the selectivity of multi-targeted inhibitors (CDK9) (Olson *et al.*, 2018), abrogating non-kinase dependent functions (FAK) (Cromm *et al.*, 2018), and overcoming resistance mutations (BTK) (Dobrovolsky *et al.*, 2018). Because the pharmacological effects of degraders depend on the re-synthesis rate of the target protein rather than sustained target occupancy, small molecule degraders may also have significantly prolonged effects in comparison to reversible inhibitors. However, while the potential for degraders to achieve an extended pharmacological duration of action has been noted, there have been no reported degraders to date that highlight such a feature (Churcher, 2018). Given the long half-life of AKT (Basso et al., 2002) and its importance in cancer etiology and progression, AKT is an attractive protein to target for degradation.

Here, we report the development of INY-03-041 and INY-05-040, pan-AKT degraders that induce potent degradation of all three AKT isoforms for an extended period of time. Through cell-based assays, we demonstrate that the AKT degraders exhibit more potent and prolonged effects on downstream signaling than GDC-0068, which may explain their enhanced anti-proliferative effects across a panel of 288 cancer lines in comparison to the parent catalytic inhibitor. Using a multi-omics approach, combined with computational network modeling and experimental validation, we uncovered several degrader-selective cellular phenotypes in breast cancer cells,

including potent activation of the stress mitogen activated protein kinases (MAPKs) c-Jun N-terminal kinase 1 (JNK1) and p38α. Additional breast cancer cell line analyses revealed that a signature of baseline JNK1 activation predicts lower sensitivity to AKT degradation, suggesting a novel biomarker for future therapeutic stratification.

Design and development of a pan-AKT degrader INY-03-041

To develop an AKT-targeting heterobifunctional degrader, we designed compounds based on GDC-0068, the most advanced AKT inhibitor in clinical trials (Oliveira *et al.*, 2019). The co-crystal structure of GDC-0068 bound to AKT1 (PDB ID: 4EKL) revealed that the isopropylamine is solvent-exposed, suggesting that the amine could serve as a suitable attachment site for linkers without adversely affecting affinity to AKT (**Figure 2-1A**). A ten hydrocarbon linker was used to conjugate GDC-0068 with lenalidomide to generate INY-03-041 (**Figure 2-1B**).

To verify that conjugation of the linker and lenalidomide did not affect the ability of INY-03-041 to bind to AKT, INY-03-041 was tested in a commercially-available fluorescence resonance energy transfer (FRET)-based assay (Invitrogen, Z'-Lyte) for AKT1, AKT2, and AKT3 inhibition (**Table 2-1**). INY-03-041 had similar inhibitory activity against AKT1 ($IC_{50} = 2.0$ nM), AKT2 ($IC_{50} = 6.8$ nM), and AKT3 ($IC_{50} = 3.5$ nM) as GDC-0068 (IC_{50}s for AKT1, 2, and 3 = 5, 18, and 8 nM, respectively) (Blake et al., 2012), demonstrating that INY-03-041 retained comparable biochemical affinity to all three AKT isoforms as its parent inhibitor. In addition, we evaluated the biochemical selectivity of INY-03-041 against a panel of 468 kinases at 1 μM (KINOMEscan) and observed that INY-03-041 had a similar selectivity profile as GDC-0068 (**Figure 2-1C**). Although INY-03-041 scored as a strong binder of RET (V804M) in the KINOMEscan assay, this was confirmed to be a false positive, as its biochemical IC_{50} was determined to be >10000 nM (Invitrogen, LanthaScreen) (**Table 2-1**).
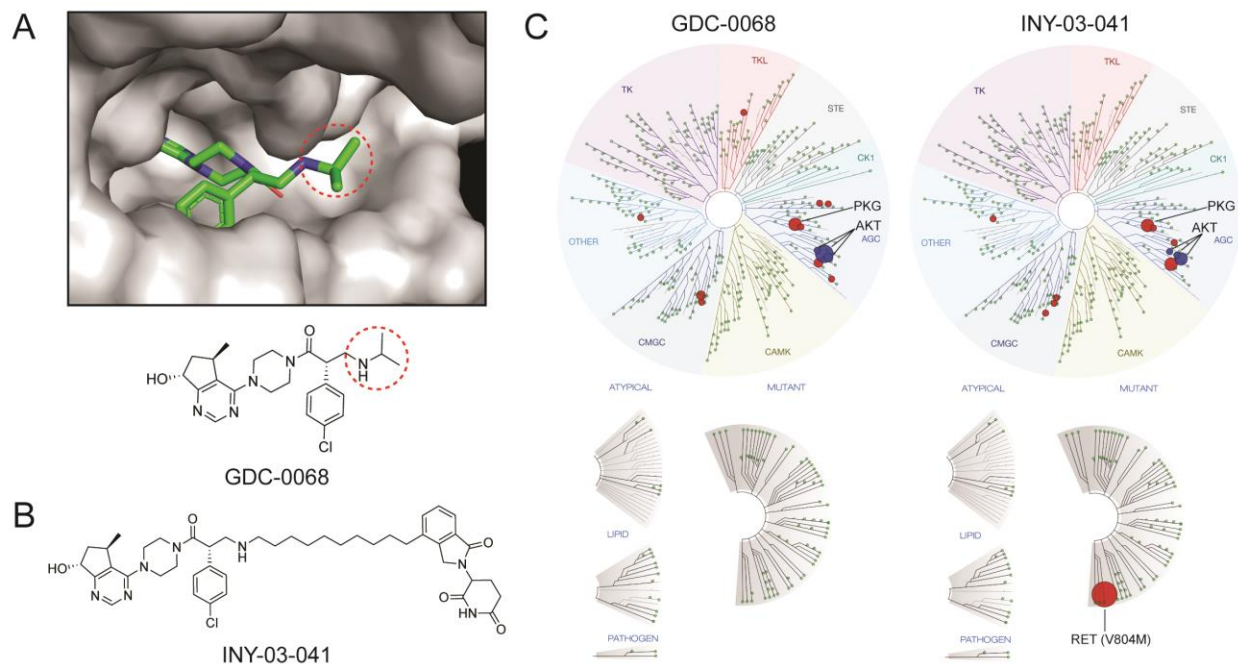
Figure 2-1. Design and development of INY-03-041. (A) Co-crystal structure of GDC-0068 (green) bound to AKT1 (gray, PDB: 4EKL) revealing solvent-exposed isopropylamine (circled) where linker was attached. (B) Chemical structure of INY-03-041. (C) TREEspot visualization of the biochemical kinome selectivity profile of GDC-0068 and INY-03-041 (1 μM). AKT isoforms are highlighted in blue, while all other inhibited kinases are highlighted in red.

Table 2-1. Z'lyte kinase assays (Invitrogen) were conducted to assess IC50 values for all kinases listed in the table with the exception of RET (V804M) which was assayed using LanthaScreen assays (Invitrogen). N/A stands for not available.

	Compound	
Kinase	INY-03-041	INY-03-112
	IC$_{50}$ (nM)	IC$_{50}$ (nM)
AKT1	2.0	1.5
AKT2	6.8	13.7
AKT3	3.5	4.5
PKG1	33.2	N/A
S6K1	37.3	N/A
PKN1	51.7	N/A
ßMSK2	3.3	N/A
Haspin	4020	N/A
RET (V804M)	>10000	N/A

INY-03-041 is a potent and highly selective pan-AKT degrader

After verifying that INY-03-041 engaged AKT biochemically, we sought to characterize its degradation activity in cells. We first chose to evaluate the AKT degrader in the triple negative breast cancer cell line MDA-MB-468 due to their high expression of all three AKT isoforms. We found that INY-03-041 induced potent degradation of all three AKT isoforms in a dose-dependent manner after a 12-hour treatment, with maximal degradation observed between 100 to 250 nM (**Figure 2-2A**). At concentrations of 500 nM and greater, we observed diminished AKT degradation, consistent with the hook effect, in which independent engagement of AKT and CRBN by INY-03-041 prevents formation of a productive ternary complex (An and Fu, 2018). Treatment of MDA-MB-468 cells with 250 nM of INY-03-041 over time revealed partial degradation of all AKT isoforms within 4 hours and progressive loss of AKT abundance out to 24 hours (**Figure 2-2B**).

To ensure that INY-03-041-induced AKT degradation was dependent on CRBN, we synthesized INY-03-112, a negative control compound with an N-methylated glutarimide that substantially weakens CRBN binding (**Figure 2-3A**) (Brand et al., 2018). INY-03-112 did not induce potent degradation of any AKT isoform (**Figure 2-3B**), demonstrating that INY-03-041-induced AKT degradation was CRBN-dependent. Furthermore, co-treatment of INY-03-041 with bortezomib, a proteasome inhibitor, or MLN-4924, a NEDD8-activating enzyme inhibitor that prevents neddylation required for the function of cullin RING ligases such as CRL4^{CRBN} (Soucy et al., 2009), prevented AKT destabilization, indicating that degradation was dependent on the ubiquitin-proteasome system (**Figure 2-2C**). Finally, we co-treated INY-03-041 with excess quantities of either GDC-0068 or lenalidomide to compete for binding to AKT or CRBN,

respectively, both of which prevented AKT degradation, demonstrating that engagement to both AKT and CRBN are required for INY-03-041-induced AKT degradation (**Figure 2-2C**).

To broadly assess degrader selectivity, MOLT4 cells, a cell line that is amenable to proteomics and expresses all three AKT isoforms, were treated with 250 nM of INY-03-041 for 4 hours and an unbiased, multiplexed mass spectrometry (MS)-based proteomic analysis was performed (Donovan *et al.*, 2018). This analysis identified significant downregulation of all three AKT isoforms, as well as RNF166, a ring-finger protein known to be downregulated by lenalidomide treatment (**Figure 2-2D**) (Kronke *et al.*, 2015). Although INY-03-041 exhibited potent *in vitro* inhibition of S6K1 ($IC_{50} = 37.3$ nM) and PKG1 ($IC_{50} = 33.2$ nM), both of which are known off-targets of GDC-0068, no downregulation of either kinases was observed in the proteomics (**Figure 2-2D**). Further immunoblot analysis confirmed that INY-03-041 did not induce S6K1 degradation (**Figure 2-3C**). While the time course (**Figure 2-2B)** indicates that stronger AKT degradation would be observed at longer time points, it is likely that the results would be confounded by subsequent transcriptional changes caused by AKT degradation.

As CRBN-targeting degraders often destabilize zinc finger proteins, and because we observed IMiD-induced downregulation of RNF166, we examined whether INY-03-041 affected protein abundance levels of Ikaros (IKZF1) and Aiolos (IKZF3), well-established targets of lenalidomide (Kronke *et al.*, 2014). Immunoblot analysis revealed weak IKZF1 and IKZF3 degradation after 24 hours of drug treatment, albeit at relatively high concentrations of 500 nM or greater, indicating that INY-03-041 is primarily a selective degrader for AKT (**Figure 2-3C**).
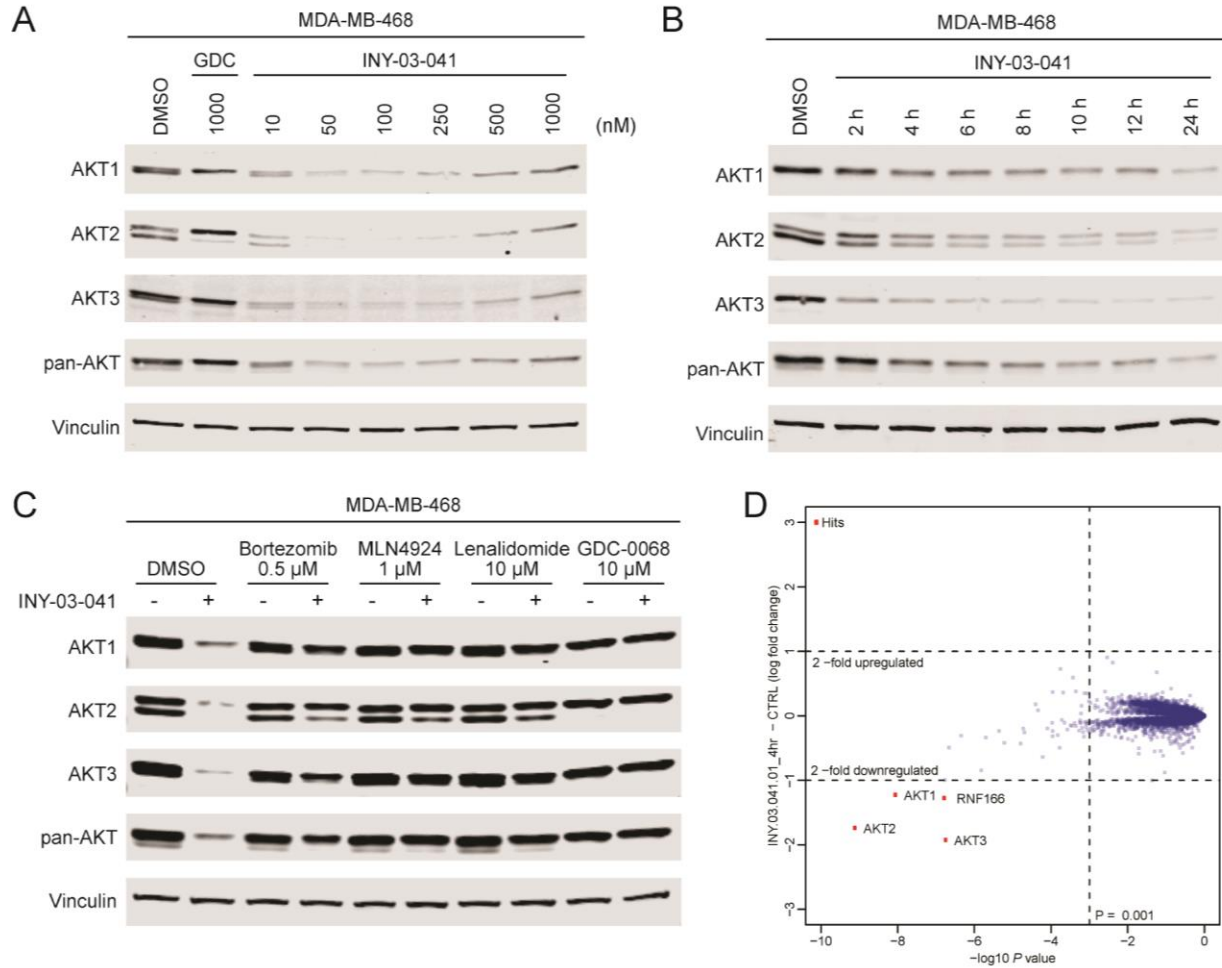
Figure 2-2. INY-03-041 induces potent degradation of AKT isoforms dependent on CRBN, neddylation, and the proteasome. (A) Immunoblots for AKT1, AKT2, AKT3, pan-AKT and Vinculin in MDA-MB-468 cells after 12-hour treatment with DMSO, GDC-0068 (GDC), or INY-03-041 at the concentrations indicated (n=4). (B) Immunoblots for AKT1, AKT2, AKT3, pan-AKT and Vinculin in MDA-MB-468 cells after treatment with INY-03-041 (250 nM) at indicated times or DMSO (24 h) (n=4). (C) Immunoblots for AKT1, AKT2, AKT3, pan-AKT and Vinculin after 12-hour co-treatment of MDA-MB-468 cells with DMSO, bortezomib (0.5 μM), MLN-4924 (1 μM), lenalidomide (Len, 10 μM), or GDC-0068 (GDC, 10 μM) and either INY-03-041 (250 nM) or DMSO (n=4). (D) Scatterplot depicts the change in relative protein abundance of INY-03-041 (250 nM, 4 hour) treated MOLT4 cells compared to DMSO vehicle control treated cells. Protein abundance measurements were made using TMT quantitative mass spectrometry and significant changes were assessed by moderated t-test as implemented in the limma package (Ritchie et al., 2015). The $\log_2$ fold change ($\log_2$ FC) is shown on the y-axis and negative $\log_{10}$ p value (-$\log_{10}$ p value) on the x-axis for three independent biological replicates of each treatment.
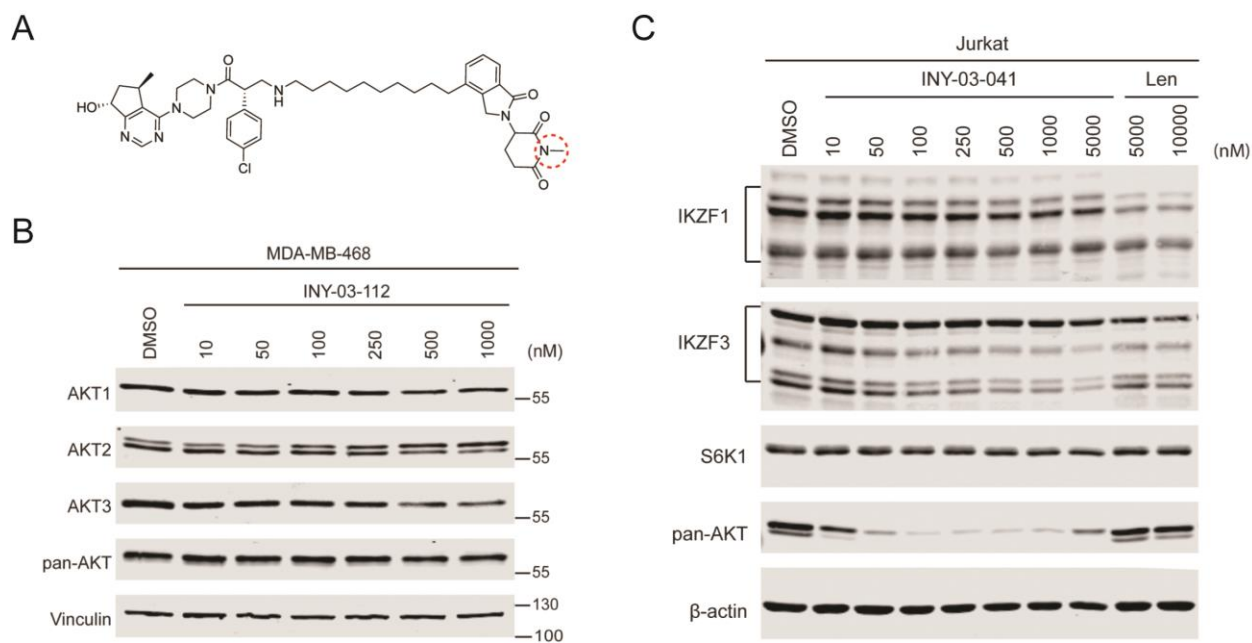
Figure 2-3 INY-03-041 requires CRBN binding to induce highly selective AKT degradation. (A) Chemical structure of negative control compound INY-03-112, with N-methylated glutarimide circled. (B) Immunoblots for AKT1, AKT2, AKT3, pan-AKT and Vinculin in MDA-MB-468 cells after 12-hour treatment with DMSO or INY-03-112 at the concentrations indicated (n=2). (C) Immunoblots for IKZF1, IKZF3, S6K1, panAKT and β-actin in Jurkat cells after 24-hour treatment with DMSO, INY-03-041, or lenalidomide (Len) at the concentrations indicated (n=3).

INY-03-041 exhibits enhanced anti-proliferative effects compared to GDC-0068

As AKT has well-characterized functions in regulating cell proliferation, we next compared the anti-proliferative effects of AKT degradation and inhibition using growth rate inhibition (GR) to account for variation in division rates among cells, as this can confound other drug response metrics, such as IC_{50} values (Hafner et al., 2017). In a panel of cell lines with PI3K pathway mutations that have been reported to be sensitive (ZR-75-1, T47D, LNCaP, and MCF-7) and insensitive (MDA-MB-468 and HCC1937) to AKT inhibition (**Table 2-2**) (Lin et al., 2013), we found that INY-03-041 was most potent in ZR-75-1 cells (GR_{50} = 16 nM), with a 14-fold increased potency compared to GDC-0068 (GR_{50} = 229 nM). The anti-proliferative effect of INY-03-041 was degradation-dependent, as INY-03-112 was significantly less potent (GR_{50} = 413 nM)

than INY-03-041 and had a comparable GR_{50} value to GDC-0068 (**Figure 2-4A; Table 2-3**). Similar trends were seen in the other cell lines sensitive to AKT inhibition, with 8- to 14- fold lower GR_{50} values for INY-03-041 in comparison to GDC-0068 (**Figures 2-4A-D**; **Table 2-3**). In addition, lenalidomide, used as a control for RNF166, IKZF1, and IKZF3 degradation, did not have strong anti-proliferative effects, suggesting that the enhanced anti-proliferative effects were due to AKT degradation (**Figures 2-4A-D**).

While INY-03-041 displayed enhanced anti-proliferative effects compared to GDC-0068 in MDA-MB-468 and HCC1937 cells, there were no apparent differences in GR_{50} values between INY-03-041 and INY-03-112, its non-CRBN binding control (**Figures 2-4E and F**; **Table 2-3**). Thus, the anti-proliferative effects of INY-03-041 in these cell lines were likely due to off-target effects unrelated to AKT degradation that manifest at elevated concentrations of INY-03-041 and INY-03-112. This is consistent with previous studies reporting resistance of MDA-MB-468 and HCC1937 to AKT inhibition (Lin *et al.*, 2013), and indicates that AKT degradation has similar phenotypic effects as AKT inhibition in these cell lines. Overall, the data show that INY-03-041 suppresses proliferation more potently than GDC-0068, and highlight the potential therapeutic value of targeted AKT degradation.
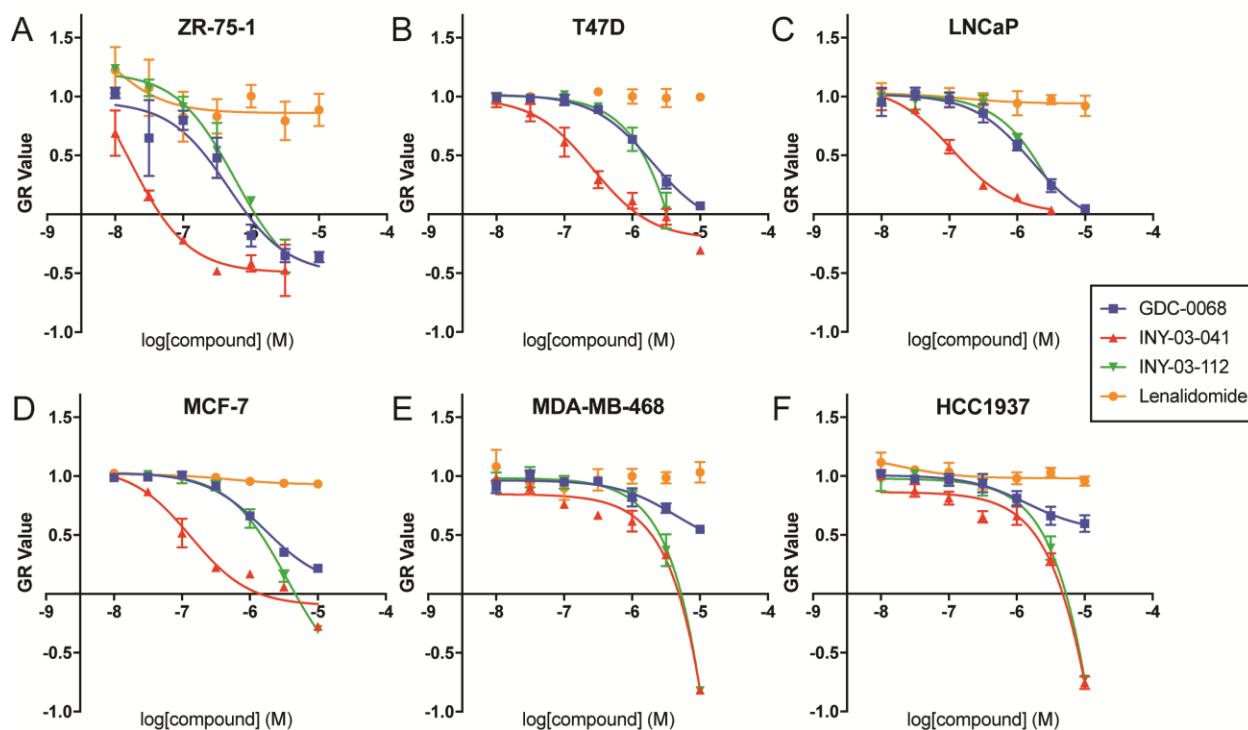
Figure 2-4. INY-03-041 induces enhanced anti-proliferative effects compared to GDC-0068. GR values across concentrations in (A) ZR-75-1, (B) T47D, (C) LNCaP, (D) MCF-7, (E) MDA-MB-468, and (F) HCC1937 cells after 72-hour treatment with GDC-0068 (blue), INY-03-041 (red), INY-03-112 (green), and lenalidomide (orange). Error bars represent standard deviation of three technical replicates.

Table 2-2. Hormone receptor and mutational status of PIK3CA and PTEN in cancer cell line panel. The tissue, cancer subtype and status of each gene as wild-type (wt), mutated (mut) or deleted (del) is indicated. Triple negative breast cancer (TNBC).

Cell Line	Tissue	Cancer Subtype	PIK3CA	PTEN
ZR-75-1	Breast	Luminal A	wt	mut (L108R)
T47D	Breast	Luminal A	mut (H1047R)	wt
LNCaP	Prostate	Androgen-dependent	wt	del/mut
MCF-7	Breast	Luminal A	mut (E545K)	wt
MDA-MB-468	Breast	TNBC – Basal A	wt	del
HCC1937	Breast	TNBC – Basal A	wt	del

Table 2-3. GR values indicate anti-proliferative advantage of INY-03-041. GR values were calculated after 72-hour treatment with the compounds indicated over a range of concentrations. GR_{50} values represent compound potency, GR_{max} values measure the efficacy of the drug at high concentrations. GR_{AOC} captures changes in potency and efficacy and is calculated by integrating GR curve over a range of concentrations.

GR_{50} (µM)

Cell Line	INY-03-041	INY-03-112	GDC-0068	Lenalidomide
ZR-75-1	0.016	0.413	0.229	inf
T47D	0.178	1.34	1.53	inf
LNCaP	0.130	1.38	1.32	inf
MCF-7	0.148	1.49	1.72	inf
MDA-MB-468	1.69	2.70	12.9	inf
HCC1937	1.65	2.42	inf	inf

GR_{max}

Cell Line	INY-03-041	INY-03-112	GDC-0068	Lenalidomide
ZR-75-1	-0.688	-0.517	-0.384	0.744
T47D	-0.321	-0.163	0.054	0.999
LNCaP	0.011	0.212	0.017	0.829
MCF-7	-0.305	-0.332	0.218	0.910
MDA-MB-468	-0.819	-0.832	0.518	0.940
HCC1937	-0.813	-0.726	0.538	0.905

GR_{AOC}

Cell Line	INY-03-041	INY-03-112	GDC-0068	Lenalidomide
ZR-75-1	1.17	0.329	0.705	0.085
T47D	0.630	0.198	0.285	-0.010
LNCaP	0.549	0.186	0.330	0.042
MCF-7	0.627	0.320	0.243	0.021
MDA-MB-468	0.430	0.319	0.140	0.033
HCC1937	0.415	0.313	0.156	-0.008

INY-03-041 suppresses downstream signaling more potently than GDC-0068

Given the enhanced anti-proliferative effects of INY-03-041 compared to GDC-0068, we sought to compare their effects on downstream AKT signaling. In T47D cells, which were highly sensitive to INY-03-041 in terms of anti-proliferation, we confirmed that INY-03-041 induced potent AKT degradation, with no detectable levels of all three AKT isoforms observed after a 24-hour treatment with 250 nM of INY-03-041 (**Figure 2-5**).
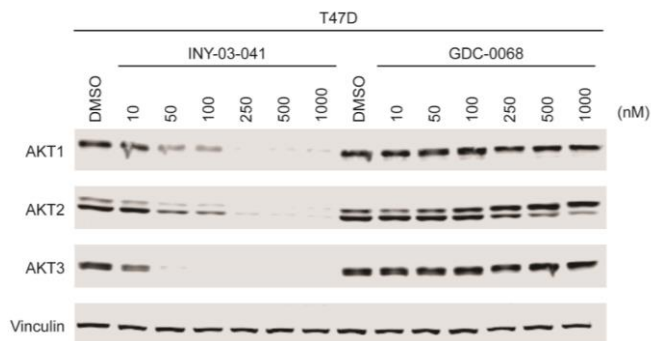
Figure 2-5. INY-03-041 induces degradation of AKT isoforms in T47D cells. Immunoblots of AKT1, AKT2, AKT3, and Vinculin after treating T47D cells for 24 hours with DMSO, INY-03-041, or GDC-0068 at the concentrations indicated (n=3).

INY-03-041 treatment resulted in robust and dose-dependent inhibition of phosphorylated PRAS40 (pPRAS40) and GSK3β (pGSK3β), well-established direct substrates of AKT (Cross et al., 1995; Wang et al., 2012), as well as S6 (pS6), a downstream marker of AKT activity (Lin *et al.*, 2013) (**Figure 2-6A**). While 250 nM INY-03-041 significantly reduced pPRAS40, pGSK3β, and pS6 levels, doses up to 1 µM of GDC-0068 were required to observe comparable effects (**Figure 2-6A**). To test whether these effects were generalizable across distinct cell lines, we also compared the effects of INY-03-041 and GDC-0068 in MDA-MB-468, MOLT4, IGROV1 and PC3 cells (**Figure 2-6A** and **Figures 2-7A-C**). Similar to that observed in T47D cells, INY-03-041 significantly reduced phosphorylation of PRAS40, GSK3β and S6 at 250 nM, while weaker responses were seen with equivalent doses of GDC-0068 (**Figure 2-6A** and **Figures 2-7A-C**). Although INY-03-041 suppresses downstream AKT signaling more potently than GDC-0068 in a variety of cancer cell lines, longer time points were required for INY-03-041 to display maximal pharmacodynamic effects relative to GDC-0068 (**Figures 2-8A-C**), consistent with the rate of AKT degradation observed.

Notably, we also found that INY-03-041 promoted sustained destabilization of all three AKT isoforms for at least 96 hours after treatment with 250 nM of INY-03-041 in both T47D and

MDA-MB-468 cells (**Figure 2-6B**). This durable AKT degradation resulted in sustained inhibition of downstream signaling, as pPRAS40 levels were also significantly reduced for up to 96 hours (**Figure 2-6B**). By contrast, treatment with an equivalent dose of GDC-0068 not only resulted in less pronounced inhibition of pPRAS40, but the duration of this effect was also shorter (**Figure 2-6B**).

To further characterize the mechanism underlying the extended duration of AKT degradation induced by INY-03-041, we performed compound washout experiments after 12 hours of treatment with either 250 nM of INY-03-041 or GDC-0068. We observed no detectable rebound of AKT levels for up to 96 hours after washout in INY-03-041 treated cells (**Figure 2-6C**), suggesting that the re-synthesis rate of AKT is slow. Consistently, INY-03-041 potently suppressed levels of pPRAS40 for up to 96 hours after washout, while washout in GDC-0068 treated cells resulted in rebound of pPRAS40, as would be expected of a reversible inhibitor (**Figure 2-6C**). Taken together, our data suggest that INY-03-041-mediated AKT degradation resulted in more potent and durable pharmacological effects than AKT inhibition.
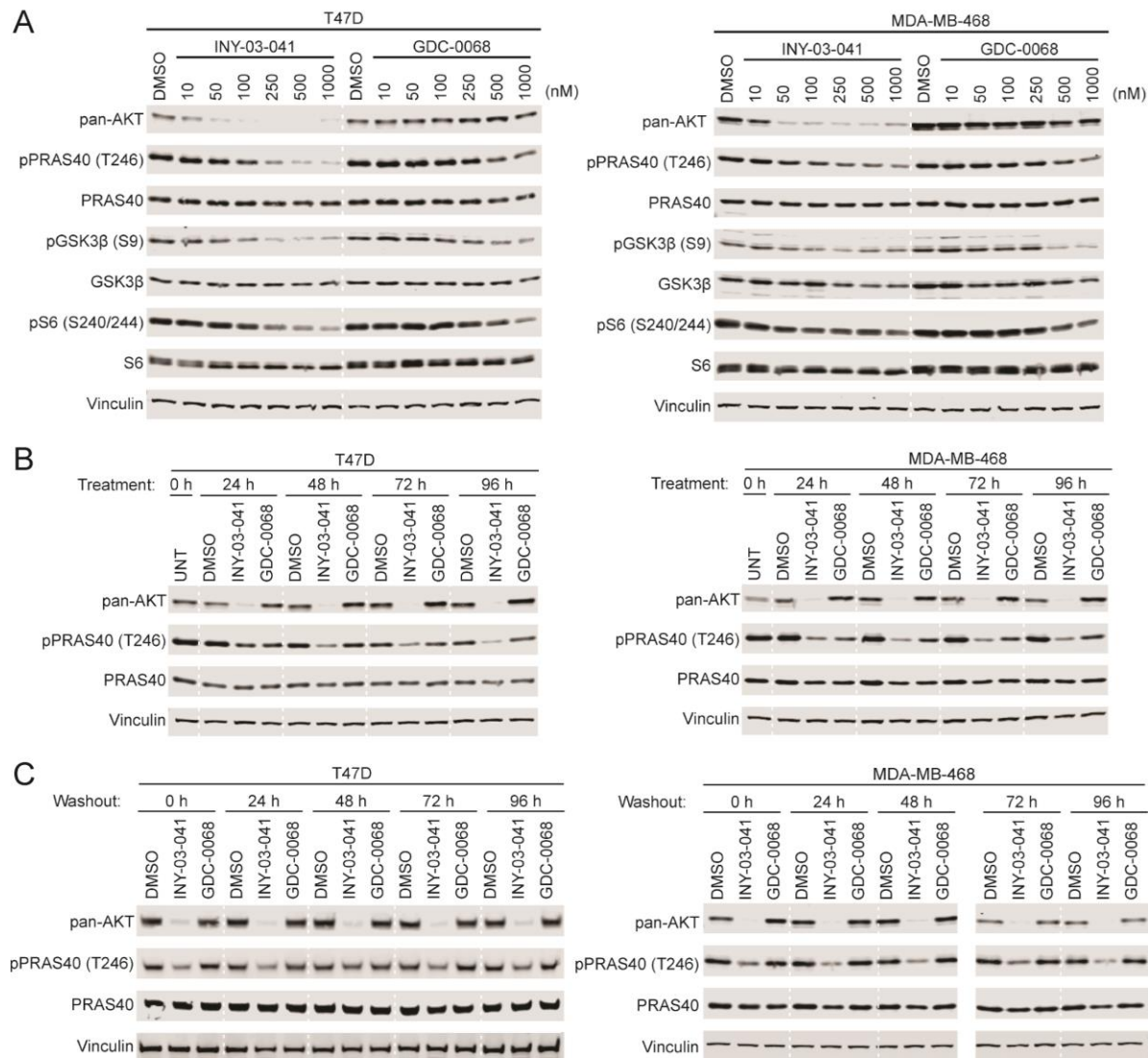
Figure 2-6. INY-03-041 exhibits more potent and durable downstream signaling effects than GDC-0068. (A) Immunoblots of pan-AKT, phospho-PRAS40 (T246), total PRAS40, phospho-GSK3β (S9), total GSK3β, phospho-S6 (S240/244), total S6 and Vinculin after treating T47D or MDA-MB-468 cells for 24 hours with DMSO, INY-03-041, or GDC-0068 at the concentrations indicated (n=3). (B) Immunoblots of pan-AKT, phospho-PRAS40 (T246), total PRAS40 and Vinculin after treatment of T47D or MDA-MB-468 cells with 250 nM of INY-03-041 or GDC-0068 at time points indicated (n=3). (C) Immunoblots of pan-AKT, phospho-PRAS40 (T246), total PRAS40 and Vinculin in T47D or MDA-MB-468 cells treated for 12 hours with INY-03-041 or GDC-0068 (250 nM), followed by washout for indicated times (n=4). Solid vertical white line indicates samples run on separate gels.
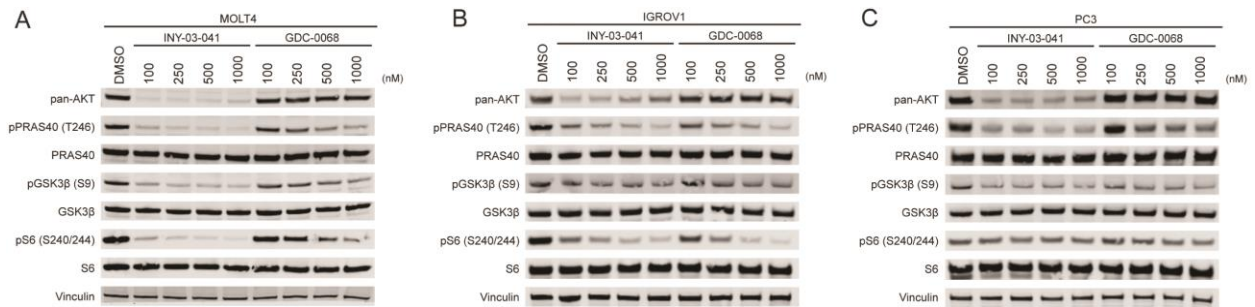
Figure 2-7. INY-03-041 induces potent downregulation of AKT signaling in MOLT4, IGROV1 and PC3 cells. Immunoblots of pan-AKT, phospho-PRAS40 (T246), total PRAS40, phospho-GSK3β (S9), total GSK3β, phospho-S6 (S240/244), total S6 and Vinculin in (A) MOLT4, (B) IGROV1 and (C) PC3 cells after treatment with DMSO, INY-03-041, or GDC-0068 for 24 hours at concentrations indicated (n=2)
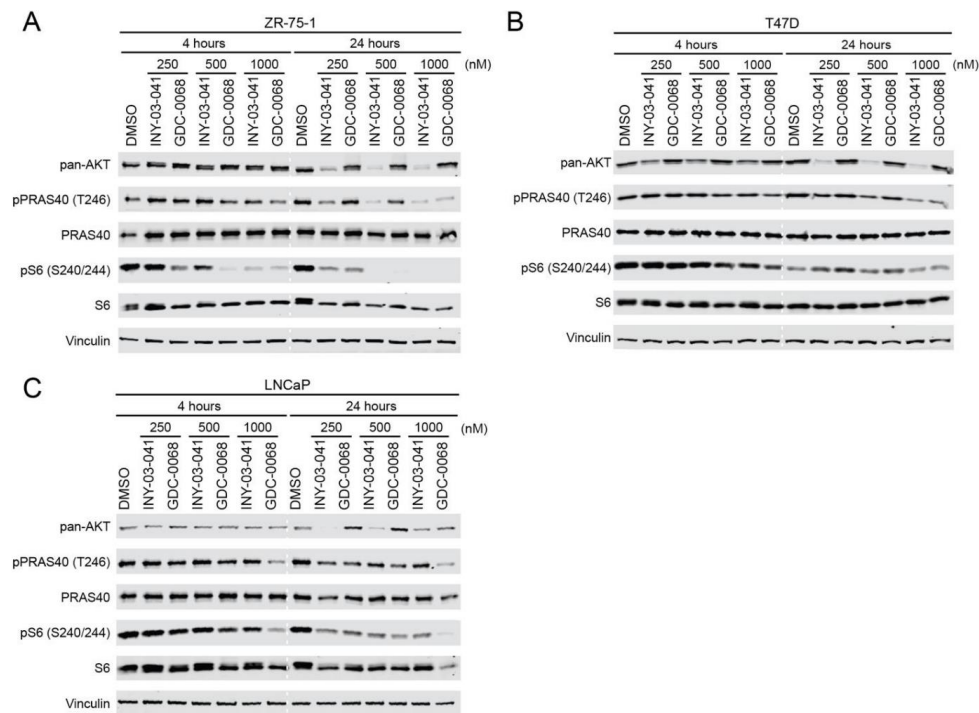
Figure 2-8. INY-03-041 requires longer time points than GDC-0068 to display inhibition of downstream AKT signaling. Immunoblots of pan-AKT, phospho-PRAS40 (T246), total PRAS40, phospho-S6 (S240/244), total S6 and Vinculin in (A) ZR-75-1, (B) T47D and (C) LNCaP cells after treatment with DMSO, INY-03-041, and GDC-0068 for 4 or 24 hours at indicated concentrations (n=2).

Development of INY-05-040, an improved, second-generation AKT degrader

Despite the potency and selectivity of INY-03-041, the degrader revealed relatively slow (12 hours) cellular degradation kinetics of all three AKT isoforms. We therefore developed an improved, second-generation AKT degrader, INY-05-040, consisting of GDC-0068 conjugated to a von Hippel-Lindau (VHL) ligand via a ten-hydrocarbon linker (**Figure 2-9A**). To generate the matched negative control compound, INY-05-040-Neg (**Figure 2-9A**), we incorporated a diastereoisomer of the VHL ligand that substantially loses activity towards VHL (Raina et al., 2016). The biochemical selectivity of INY-05-040 was comparable to GDC-0068 across a panel of 468 kinases (**Figure 2-10A**). Proteomics analysis in MOLT4 cells confirmed pan-AKT downregulation following 4-hour treatment with 250 nM INY-05-040 (**Figure 2-10B**).

All subsequent evaluation of INY-05-040 was performed in human breast cancer cell lines due to the high prevalence of PI3K/AKT pathway activation. Exposure of the estrogen receptor-positive (ER+) and *PIK3CA^{H1047R}*-mutant T47D cell line to increasing doses of INY-050-040 for 5 h (**Figure 2-9B**), or over a time course using a dose of 100 nM (**Figure 2-9C**) revealed a substantially improved dose- and time-dependent reduction in total AKT levels compared to the first-generation degrader, INY-03-041. This was mirrored by potent suppression of downstream PRAS40 (T246) and S6 (S240/S244) phosphorylation (**Figures 2-9B and C**). INY-05-040 also outperformed GDC-0068 in T47D cells treated for 24 h, with >500 nM of GDC-0068 required to achieve a comparable suppression of signaling relative to 50 to 100 nM of INY-05-040 (**Figure 2-9D**). As GDC-0068 is also a component of the negative control compound, INY-05-040-Neg, the latter also suppressed signaling at higher concentrations (**Figure 2-10C**). Importantly, unlike non-covalent, catalytic inhibition of AKT with GDC-0068, INY-05-040 treatment of T47D cells resulted in sustained AKT reduction and suppression of downstream signaling for at least 72 hours

following compound washout (**Figure 2-9E**). Consistent with proteasomal-dependent degradation, pharmacological abrogation of the proteasome function or neddylation prevented AKT degradation by INY-05-040 (**Figure 2-10F**). We also replicated these experiments in *PTEN-*deficient triple-negative breast cancer (TNBC) cell line MDA-MB-468 (**Figures 2-10D, E, F, and G**). Notably, cells exposed to INY-05-040 also exhibited reduced levels of total ribosomal S6 protein (**Figures 2-9C, D, and E**).

Consistent with long-term suppression of AKT signaling, both INY-03-041 and INY-05-040 displayed potent anti-proliferative effects across four different breast cancer cell lines well below the concentrations required for an equivalent response with either catalytic or allosteric AKT inhibitors (**Figures 2-10H and I**).

Finally, we tested the pharmacodynamic properties of the AKT degraders *in vivo*, using a BT-474C breast cancer xenograft model. Following 4 day treatment, both INY-03-041 and INY-05-040 led to potent downregulation of pan-Akt levels, accompanied by downregulation of pPRAS40 (T246) and pS6 (S240/244) in the tumor model (**Figure 2-9F**). This suppression of downstream signaling *in vivo* was equivalent to that observed with GDC-0068, which may be the consequence of poor pharmacokinetic properties of the degraders relative to GDC-0068.
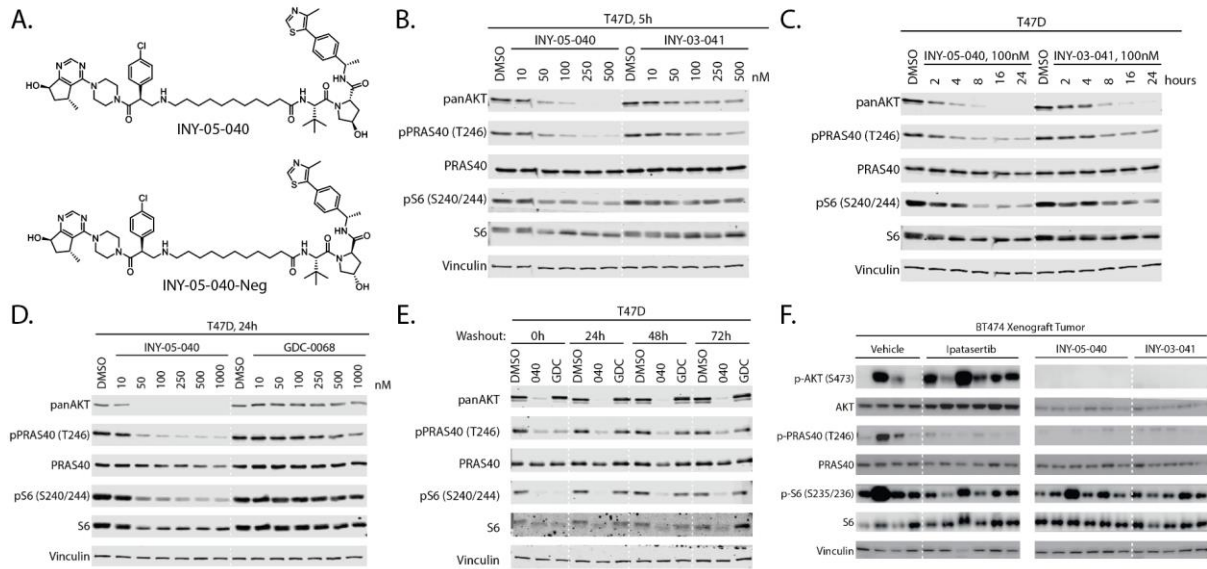
Figure 2-9. Design and characterization of INY-05-040. (A) Chemical structures of INY-05-040 and negative control INY-05-040-Neg. (B) Immunoblots for panAKT, phospho-PRAS40 (T246), total PRAS40, phospho-S6 (S240/244), total S6, and Vinculin after treatment of T47D cells treated for 5 h with INY-05-040 or INY-03-041 at the indicated concentrations. (C) Immunoblots for panAKT, phospho-PRAS40 (T246), total PRAS40, phospho-S6 (S240/244), total S6, and Vinculin after treatment of T47D cells treated with INY-05-040 (100 nM) or INY-03-041 (100 nM) for the indicated times. (D) Immunoblots for panAKT, phospho-PRAS40 (T246), total PRAS40, phospho-S6 (S240/244), total S6, and Vinculin after 24-h treatment of T47D cells with INY-05-040 or GDC-0068 at the indicated concentrations. (E) Immunoblots for panAKT, phospho-PRAS40 (T246), total PRAS40, phospho-S6 (S240/244), total S6, and Vinculin in T47D cells treated with INY-05-040 (100 nM) or GDC-0068 (100 nM) for 5 h followed by washout for the indicated times. (F) Immunoblots for panAKT, phospho-PRAS40 (T246), total PRAS40, phospho-S6 (S235/236), total S6, and Vinculin in BT-474 mouse xenograft tumors treated with vehicle (10% DMSO, 25% Kleptose), Ipatasertib (12.5 mg/kg), INY-05-040 (25 mg/kg), or INY-03-041 (25 mg/kg) for 3 days, with a terminal treatment 4 h prior to protein harvest.
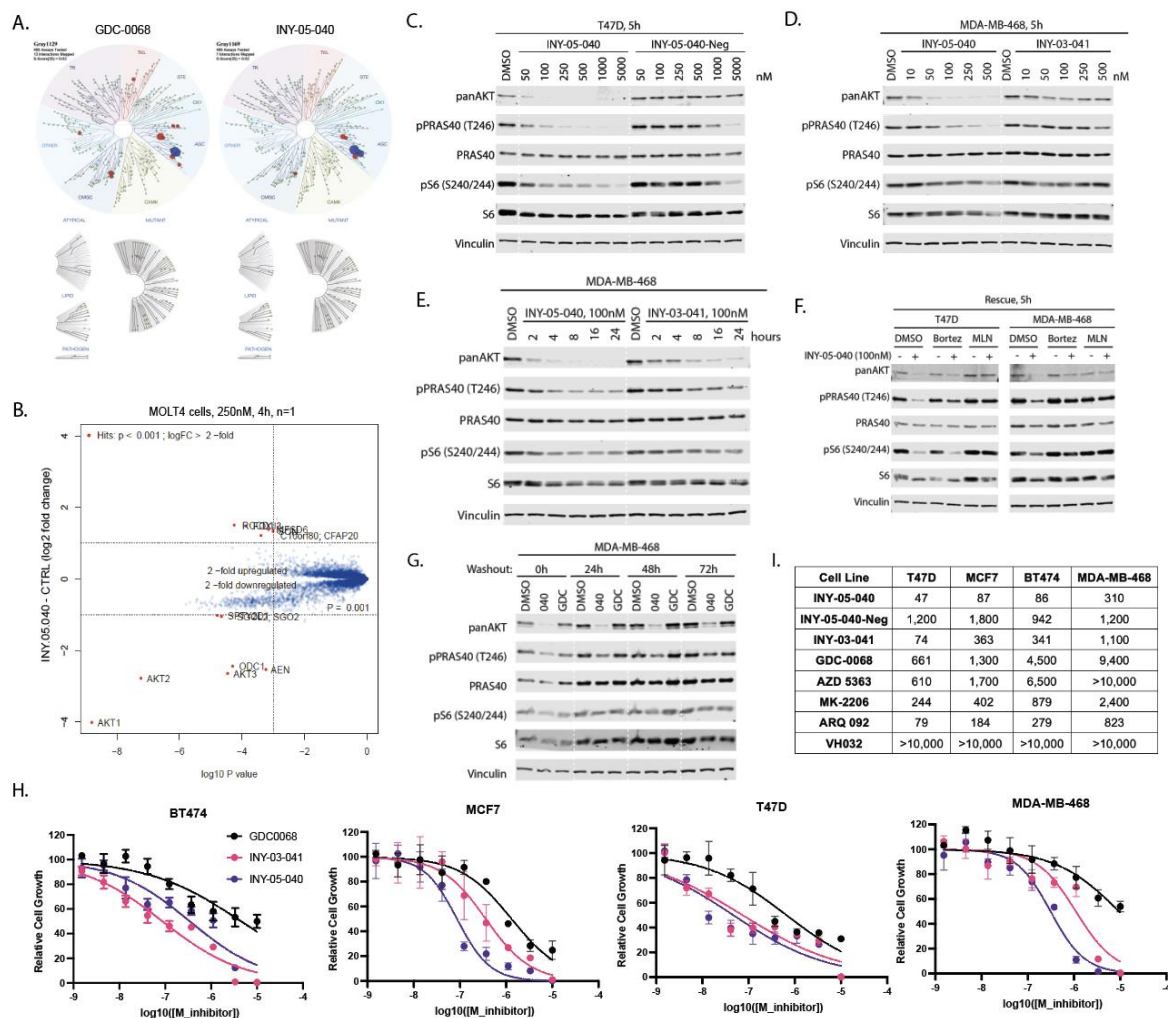
Figure 2-10. INY-05-040 biochemical selectivity and proteomics. (A) TREEspot visualization of the biochemical selectivity profile of GDC-0068 and INY-05-040 (1 µM). AKT isoforms are highlighted in blue, all other inhibited kinases are highlighted in red. (B) Volcano plot of relative protein abundance changes following 4-h treatment of MOLT4 cells with INY-05-040 (250 nM) versus DMSO (vehicle), assayed using tandem mass tag quantitative mass spectrometry. The log2 fold change (FC) is shown on the y axis and -log10(p-value) on the x axis for one independent biological replicate for each treatment; FDR < 0.05. (C) Immunoblots for panAKT, phospho-PRAS40 (T246), total PRAS40, phospho-S6 (S240/244), total S6, and Vinculin after 5-h treatment of T47D cells with DMSO, INY-05-040 (040) or INY-05-040-Neg at the indicated doses. (D) Immunoblots for the same components as in (C), representing MDA-MB-468 cells treated for 5 h with DMSO, INY-05-040 or GDC-0068 at the indicated concentrations. (E) Immunoblots for the same components as in (C), representing MDA-MB-468 cells treated with DMSO, INY-05-040 (100 nM) or INY-03-041 (100 nM) for the indicated times. (F) Immunoblots for the same components as in (C), representing 5 h co-treatment of T47D and MDA-MB-468 cells with DMSO, bortezomib (0.5 µM), MLN-4924 (1 µM), and either INY-05-040 (100 nM) or DMSO.

Figure 2-10 (continued)

(G) Immunoblots for the same components as in (C), representing MDA-MB-468 cells treated with DMSO, INY-05-040 (100 nM) or GDC-0068 (100 nM) for 5 h, followed by washout for the indicated times. (H) CellTiter Glo assay evaluating percent inhibition in cell growth relative to DMSO treatment in T47D, MCF7, BT-474, or MDA-MB-468 cells, treated for 72 h with INY-03-041, INY-05-040 or GDC-0068. (I) Table representing cell line-specific EC_{50} values (nM) calculated from the respective CellTiter Glo assays in (H).

Multi-omics profiling reveals AKT degrader-selective responses

To identify mechanisms unique to AKT degradation relative to catalytic inhibition, we performed mRNA sequencing (RNAseq) in T47D breast cancer cells. To limit confounding effects of differential potencies, we determined that 100 nM of INY-05-040 and 500 nM of GDC-0068 would result in comparable suppression of downstream signaling (**Figure 2-11**). All studies were performed using nutrient- and grown factor-replete cell culture media.
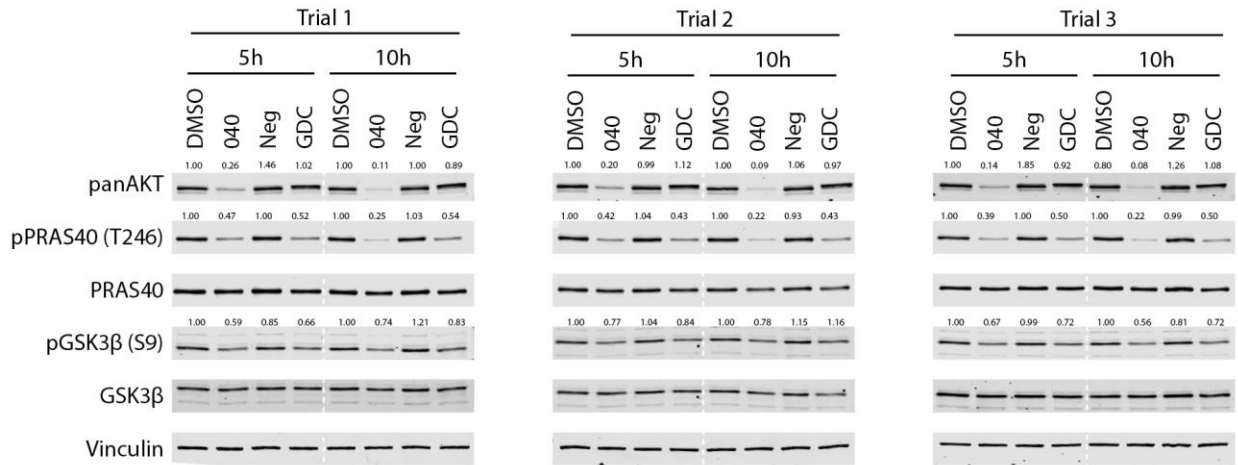
Figure 2-11. Signaling immunoblots related to RNAseq. Immunoblots for panAKT, phospho-PRAS40 (T246), total PRAS40, phospho-GSK3β (S9), total GSK3β, phospho-S6 (S240/244), total S6, and Vinculin after treatment of T47D cells for 5 h or 10 h with DMSO, 100 nM INY-05-040 (040), 100 nM INY-05-040-Neg (Neg), or 500 nM GDC-0068 (GDC), collected in parallel with the corresponding RNAseq samples. Quantification of AKT represents protein abundance over Vinculin, relative to the corresponding DMSO condition for each time point. Quantification of remaining phosphorylated proteins represent normalization to the corresponding total protein, relative to the DMSO signal for each time point.

Consistent with shared targets, the transcriptomes of GDC-0068- and INY-05-040-treated cells clustered closely together, separate from the DMSO- and INY-05-040-Neg-treated cells, according to an unsupervised principal component analysis (PCA) (**Figure 2-12A**). In agreement with the slower onset of AKT degradation, 5-hour treatment with INY-05-040 resulted in differential expression of only 194 transcripts (100 downregulated, 94 upregulated; absolute fold-change $\geq$ 1.3; FDR $\leq$ 0.05), compared to 511 transcripts (249 upregulated, 262 downregulated) with GDC-0068 during the same time period (**Figure 2-12B**). By contrast, 10-hour treatment with INY-05-040 led to differential expression of 1394 transcripts (626 downregulated, 768 upregulated; absolute fold-change $\geq$ 1.3; FDR $\leq$ 0.05), whereas the extent of GDC-0068-induced transcriptional changes remained stable at 543 transcripts (243 downregulated, 300 upregulated) (**Figure 2-12B**). Across all differentially expressed transcripts, more than 700 were unique to 10-hour treatment with INY-05-040, compared to less than 100 unique changes observed with GDC-0068 (**Figures 2-13A and B**). No differential expression was observed in response to treatment with the control compound INY-05-040-Neg (**Figure 2-12B**).

We next conducted gene set enrichment analysis (GSEA) using the HALLMARK gene signature collection provided by the Broad Institute Molecular Signature Database (MSigDB) (Liberzon et al., 2015). At 10 hours, both INY-05-040 and GDC-0068 triggered a transcriptional footprint consistent with suppression of cycle cell, glycolysis, oxidative phosphorylation, mTORC1 and the unfolded protein response (**Figures 2-12C and D**). Although 5-hour treatment with GDC-0068 resulted in a larger number of distinct gene signatures with positive enrichment scores, most of these no longer reached statistical significance after 10 hours (**Figure 2-12D**), suggesting emerging adaptation to catalytic AKT inhibition. After 10-hour treatment, positively enriched gene signatures were largely shared between degrader and catalytic inhibitor, although

the underlying gene expression shifts often appeared more robust with the degrader, evidenced by the higher statistical significance (**Figures 2-12C and D**).

We next used DoRothEA, a transcriptional footprint-based method featuring a curated gene regulator network (Garcia-Alonso et al., 2018), to predict differences in transcription factor (TF) regulation between INY-05-040 and GDC-0068 at 10 hours. Overall, TF activity predictions were highly concordant between the two compounds (Spearman's *Rho* = 0.91; p < 0.001), with two notable exceptions. The lipid and sterol metabolism-regulating transcription factors SREBP1 and SREBP2 were predicted as strongly inhibited with GDC-0068, but not INY-05-040 (**Figure 2-12E**). A correlation analysis across the previously generated HALLMARK gene signature enrichments revealed a similar discordance with respect to cholesterol homeostasis and androgen response signatures (**Figure 2-12F**). Of note, these two signatures share four transcripts related to lipid and cholesterol synthesis: *SCD, IDI1, HMGCR, HMGCS1*. Both *HMGCR* and *HMGCS1* belong to the list of SREBP1 and 2 targets, in which expression was significantly upregulated upon 10 hour treatment with INY-05-040, but not GDC-0068 (**Figure 2-13C**).

These findings were further supported by results from precision nuclear run-on sequencing (PRO-seq), which allows mapping of RNA polymerase active sites with base-pair resolution (Mahat et al., 2016). In addition, unlike RNAseq, which captures steady-state mRNA levels, changes in the expression of a transcript in PRO-seq reflect immediate differences in active transcription. Similar to the bulk transcriptomes, PRO-seq datasets from degrader-and GDC-0068-treated samples clustered together and away from DMSO-treated controls (**Figure 2-13D**). A substantially higher number of genes were differentially transcribed in response to AKT degradation (**Figures 2-13E and F**), with further functional enrichment analyses supporting transcriptional regulation of SREBP1/2 and cholesterol homeostasis as defining differences

between GDC-0068 and INY-05-040 (**Figures 2-12G and H**). Such activation of SREBP1 and 2, despite potent AKT/mTORC1 inhibition, would be most consistent with a phenotype of cholesterol depletion (Shimano and Sato, 2017).

Given evidence for altered metabolic homeostasis, we next assessed the metabolic profile of T47D cells treated with INY-05-040 and GDC-0068. For comparison, we also included an allosteric (MK-2206) and second catalytic (AZD5363) inhibitor. Treatments were performed for 24 hours to allow capture of robust and persistent changes, while minimizing the signaling rebound observed with continuous GDC-0068 treatment (**Figure 2-14**). LC-MS-based metabolomics showed that AKT degradation led to the largest number of differentially abundant metabolites (FDR $\leq$ 0.05; **Figure 2-12I**). Many metabolite changes were shared across all AKT-targeting compounds. Several nucleosides and their phosphorylated derivatives were elevated, including inosine, guanosine, IMP, GMP, AMP and CMP. Metabolite changes unique to INY-05-040 included intermediates of the hexosamine biosynthesis pathway, the pentose phosphate pathway, glycolysis, the tricarboxylic acid cycle, glutathione and cholesterol metabolism (**Figure 2-12I**). Notably, only AKT degradation caused upregulation of methylmalonic acid (MMA), which is known to act as a potent inhibitor of the rate-limiting cholesterol biosynthesis enzyme, HMGCR (Goedeke et al., 2021). Taken together, the multi-omics approach supports a widespread perturbation of cellular homeostasis in T47D cells in response to INY-05-040, with unique responses to AKT degradation pertaining to cholesterol homeostasis.
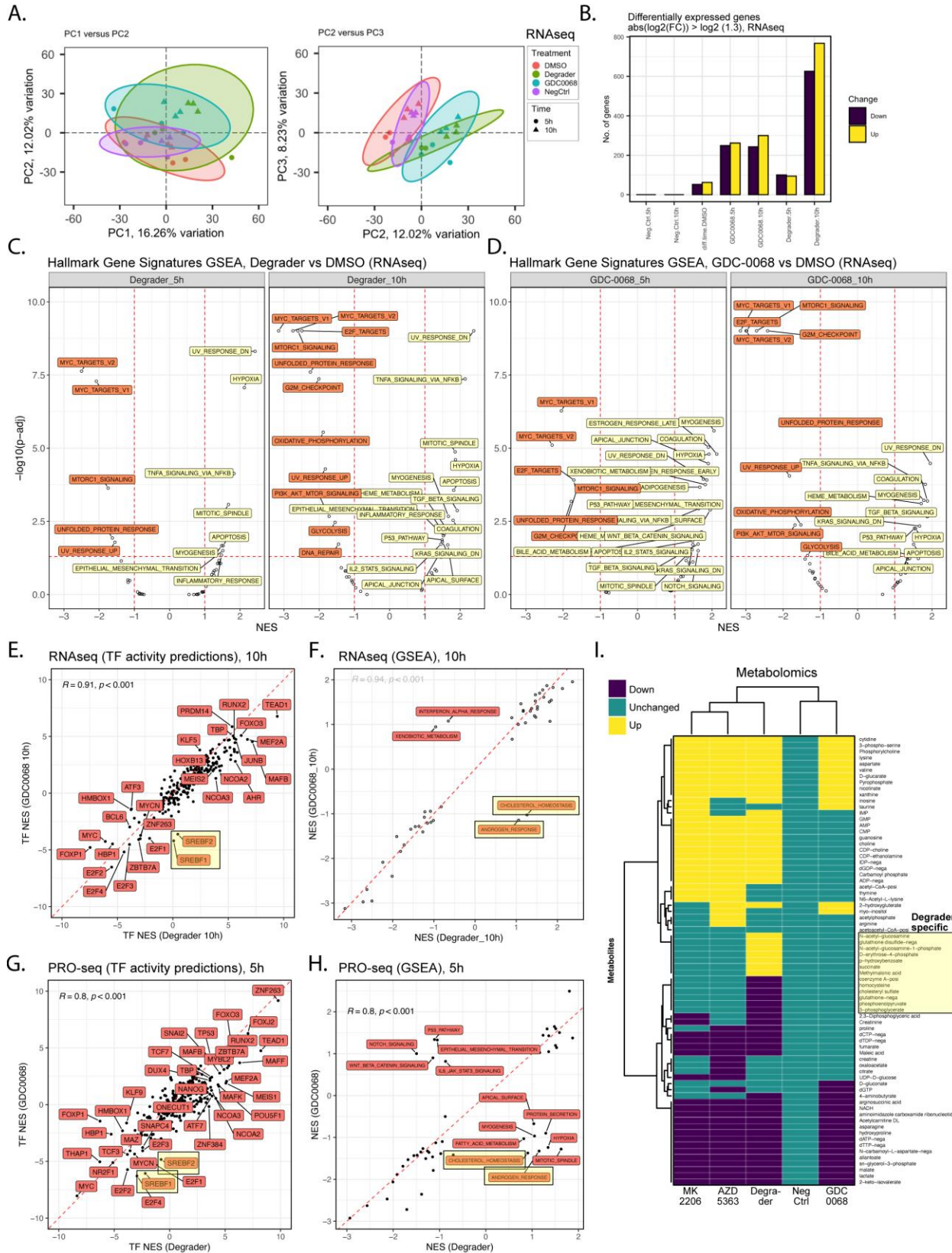
Figure 2-12 (continued). Multi-omic profiling of INY-05-040 and GDC-0068 in T47D cells. (A) Principal component analysis (PCA) projection of the transcriptomic dataset, comprising n=3 independent experiments per treatment (DMSO; Degrader: 100 nM INY-05-040; 500 nM GDC-0068; NegCtrl: 100 nM INY-05-040-Neg) and time point (5 h and 10 h). Ellipses are drawn around each group at 95 % confidence level. The first three independent axes (PCs) of highest variation are shown. (B) Number of differentially up- and downregulated transcripts (absolute fold-change $\geq$ 1.3) following differential gene expression analysis (FDR $\leq$ 0.05) across the indicated comparisons. Comparisons are relative to the corresponding DMSO-treated control; for example, Neg.Ctrl.5h refers to the effect of 10 h treatment with INY-05-040-Neg vs 10 h treatment with DMSO. The exception is "diff.time.DMSO" which evaluates differential expression as a function of time in culture (treatment with DMSO for 10 h versus treatment with DMSO for 5 h). (C) and (D) Gene set enrichment analysis (GSEA) on the mSigDb HALLMARK collection, based on the ranked *t* values from all genes for the indicated treatments relative to the corresponding DMSO-treated controls. Gene sets are labelled if the absolute normalized enrichment score (NES) exceeds 1 and the adjusted p-value falls below 0.05 (FDR). (E) Spearman's correlation analysis of transcription factor (TF) activity predictions following 10 h treatment with either Degrader or GDC-0068. TF footprint analyses were performed with DoRothEA. SREBF1 (protein name: SREPB1) and SREBF2 (protein name: SREBP2) activity predictions are highlighted due to their divergence between Degrader and GDC-0068, with lower activity predictions observed only in GDC-0068-treated cells. (F) Spearman's correlation analysis of GSEA-derived NES for individual HALLMARK gene sets following 10 h treatment with either Degrader or GDC-0068. "CHOLESTEROL HOMEOSTASIS" and "ANDROGEN RESPONSE" hallmark gene sets are highlighted as having positive and negative NES in Degrader- and GDC-0068-treated cells, respectively. (G) As for (E) but based with PRO-seq data corresponding to Degrader and GDC-0068 treatments of T47D cells for 5 h, relative to DMSO-treated control; TF activity predictions were calculated from *t* values from all genes following differential gene expression analysis (FDR $\leq$ 0.05; n = 2 independent experiments). (H) As for (F) but with the PRO-seq data used in (G). (I) Hierarchical clustering (Euclidean distance) of differential metabolite abundance (FDR $\leq$ 0.05) following 24-h treatments of T47D with either AZD 5383 (Capivasertib; catalytic pan-AKT inhibitor; 2 µM), Degrader (INY-05-040; 100 nM), GDC-0068 (catalytic AKT inhibitor; 500-750 nM), MK2205 (allosteric pan-AKT inhibitor; 1 µM) or NegCtrl (INY-05-040-Neg; 100 nM). Differential abundance analysis was performed relative to DMSO-treated controls (n = 9 samples per treatment, from 3 independent experiment with 3 replicates per experiment). More than 85% of the observed differences in metabolite abundance for a given treatment corresponded to at least a 20% change relative to DMSO-treated cells. Metabolites that were uniquely regulated upon treatment with Degrader are highlighted.
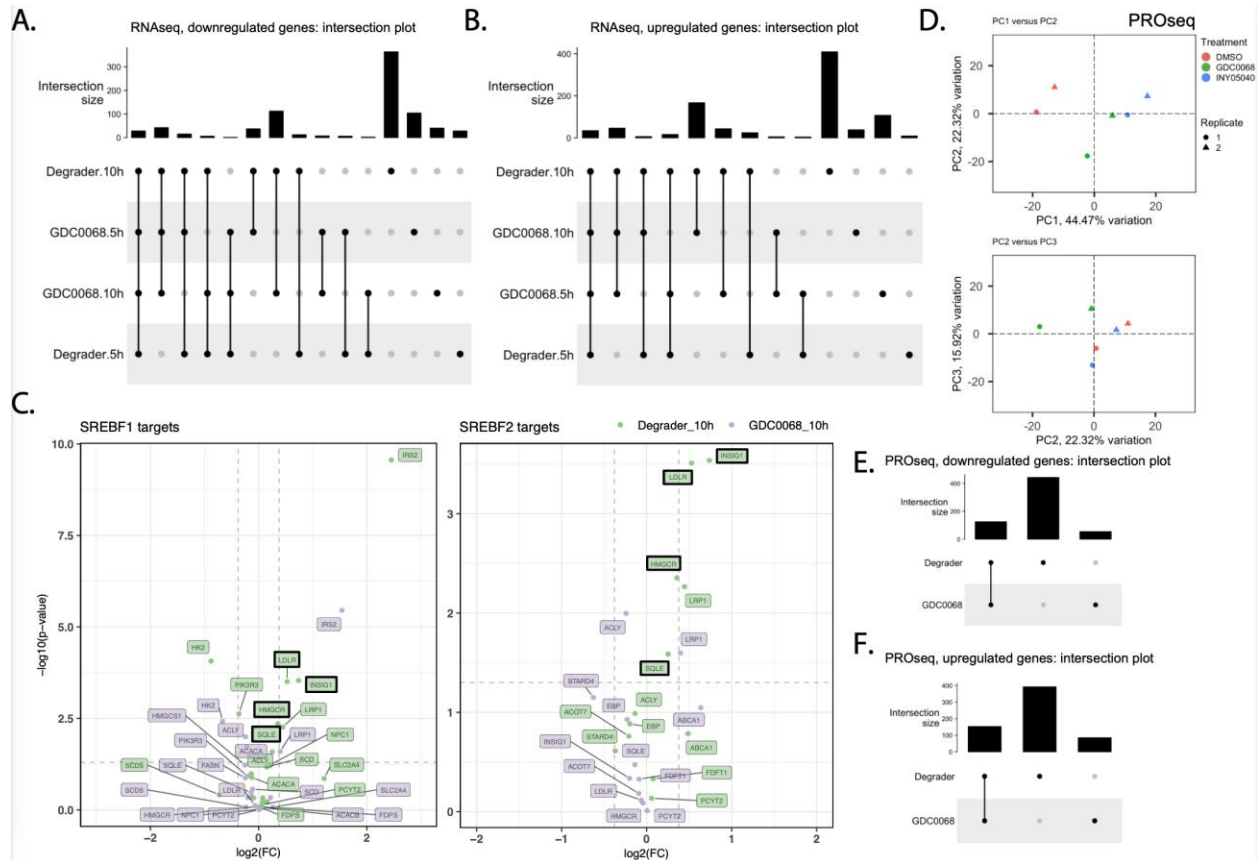
Figure 2-13. Supporting multi-omic data analyses (T47D breast cancer cells). UpSet intersection plots for up- (A) and downregulated (B) transcripts, respectively, for the indicated treatments relative to DMSO. Fold-change cut-off for differential expression was 1.3; FDR < 0.05. Only genes with HGNC (HUGO Gene Nomenclature Committee) annotation were included in the final count. (C) Volcano plot of SREBF1 and SREBF2 target gene expression in Degrader- and GDC0068-treated T47D cells. The horizontal dotted line indicates the adjusted p-value cut-off for statistical significance (FDR < 0.05); the vertical dotted lines specify the cut-off corresponding to a fold-change of log2(1.3) for up- or downregulation. The target genes correspond to those used for transcription factor footprint estimates with DoRothEA. Black rectangles are used to highlight cholesterol synthesis genes that are selectively upregulated in Degrader- but not GDC-0068-treated cells after 10 hours. (D) Principal component analysis (PCA) of the PROseq dataset, comprising n = 2 independent experiments per treatment (all performed for 5 h). The first three independent axes (principal components; PCs) of highest variation are shown. (E) and (F) As for (A) and (B), respectively, but using differentially expressed genes from the PROseq dataset.
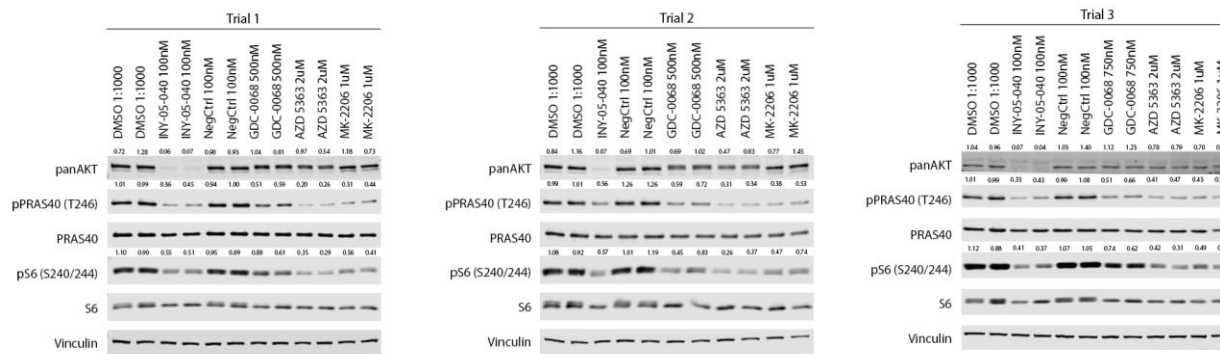
Figure 2-14. Signaling immunoblots related to metabolomics. Immunoblots for panAKT, phospho-PRAS40 (T246), total PRAS40, phospho-S6 (S240/244), total S6, and Vinculin after treatment of T47D cells for 24 h with DMSO, INY-05-040, INY-05-040-Neg, GDC-0068, AZD 5363, or MK-2206 as indicated; samples were collected in parallel with the corresponding metabolomics samples. Note that the dose of GDC-0068 was increased to 750 nM in Trial 3 to retain consistent levels of signaling suppression relative to the previous experiments. Quantification of AKT represents protein abundance over Vinculin, relative to the average of the replicate DMSO samples. Quantification of remaining phosphorylated proteins represent normalization to the corresponding total protein, relative to the average of the replicate DMSO samples.

Casual Oriented Search of Multi-Omic Space (COSMOS) identifies altered stress MAPK signaling downstream of AKT degradation

We next reasoned that an integrated, trans-omic integration of the previous datasets may enable us to generate testable mechanistic hypotheses regarding previously unknown signaling changes downstream of AKT degradation. We applied a network analysis approach, COSMOS, to integrate transcriptomic and metabolomic datasets (Dugourd et al., 2021) following treatment with INY-05-040 and GDC-0068 for 10 and 24 hours, respectively (**Figure 2-15A**). Briefly, COSMOS relies on an extensive prior knowledge network (PKN) of signaling pathways, transcriptional regulation and metabolic reactions, in combination with an Integer Linear Programming (ILP) optimization strategy to identify the smallest coherent subnetwork casually connecting as many deregulated TFs and metabolites in the input data as possible (Liu et al., 2019). Input data to COSMOS consisted of the background transcriptome of T47D cells, in addition to treatment-specific DoRothEA-derived TF activity predictions and differentially abundant metabolites. The resulting networks enable identification of top degree signaling network nodes (hubs), which are essential for holding a network together due to their high number of connections (Barabási et al., 2011). Replicate COSMOS runs identified MAPK1 (ERK2) and MAPK3 (ERK1) as top degree nodes in both INY-05-040 and GDC-0068 networks (**Figures 2-15B and C**), consistent with known compensatory RAS/MAPK signaling activation following potent PI3K/AKT pathway inhibition (Carracedo et al., 2008). Focusing on unique differences, we noted that the stress MAPKs, MAPK8 (JNK1) and MAPK14 (p38α), were among the top degree notes in INY-05-040-specific networks (**Figure 2-15B**).

To corroborate these findings, we next retrieved the MSigDb curated gene sets (C2 collection) featuring transcriptional changes downstream of JNK/p38 perturbation and performed

GSEA using the RNA seq dataset. Three gene signatures related to TNFα signaling were positively enriched in INY-05-040-treated cells after 10 hours, with two of the signatures representing transcriptional changes (**Figure 2-15D**) that are either completely or partially dependent on p38 (Phong et al., 2010). While one of these two p38-dependent signatures was also observed in response to GDC-0068, the significance and the magnitude of enrichment were not as strong as that observed in INY-05-040 treated cells (**Figure 2-15D**). This is also consistent with the weaker enrichment of the hallmark gene signature "TNFα signaling via NFκB" in response to GDC-0068 relative to INY-05-040 (**Figures 2-12C and D**). Taken together, these integrated analyses point toward potent AKT degradation-induced activation of stress MAPK signaling and inflammatory gene signatures.
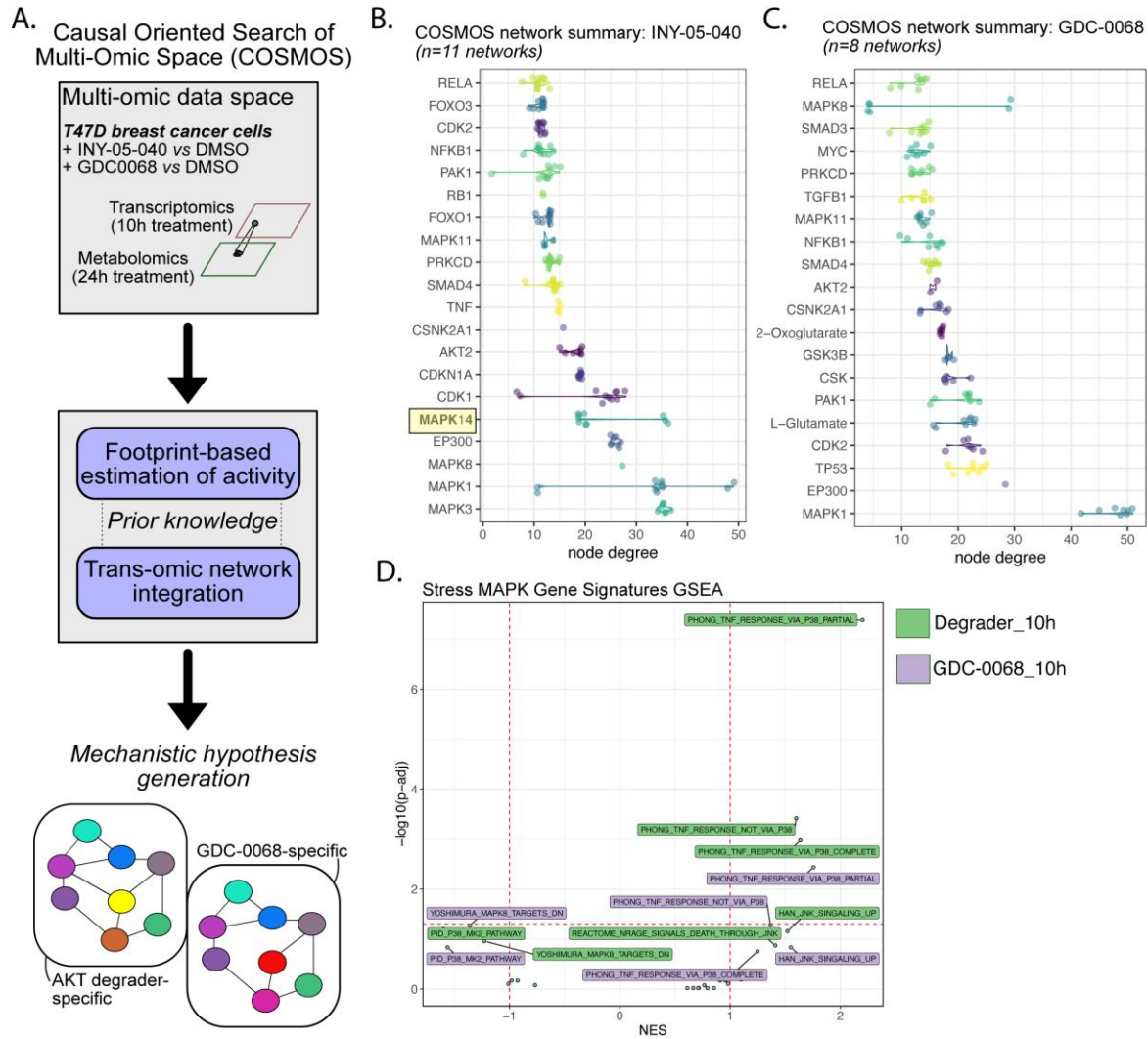
Figure 2-15. Causal Oriented Search of Multi-Omics Space (COSMOS)-based integration of transcriptomic and metabolomic datasets to identify treatment-specific networks. (A) Schematic illustrating the principle of COSMOS and the datasets used for multi-omic integration and predictions of treatment-specific signaling networks. (B) and (C) Top degree nodes from Degrader- and GDC-0068-specific networks plotted in increasing order. MAPK14 (protein: p38α) is highlighted as a Degrader network-specific top degree node. The raw COSMOS networks are included in Fig. S5 (n = 11 independent runs using Degrader data; n = 8 independent runs for GDC-0068 data). (D) Complementary GSEA analyses using stress MAPK-related gene sets (mSigDb C2 collection), based on the ranked t values from all genes for the indicated treatments relative to the corresponding DMSO treatment. Gene sets are labelled if the absolute normalized enrichment score (NES) exceeds 1.

Activation of stress MAPK signaling in response to AKT degradation

To validate the COSMOS predictions, we first determined the kinetics of p38/JNK signaling over a time course in a panel of breast cancer cells (**Figures 2-16A and B, 2-17A and B**). We observed portent AKT degrader-specific induction of p38α phosphorylation (T180/Y182) and the JNK target p-cJun(S73), as well as the expected increase in c-Jun protein levels (**Figure 2-16A**). Consistent with the COSMOS-based predictions, AKT degradation resulted in more robust stress MAPK signaling induction.

Among the different breast cancer cell lines examined, we found that the ER-positive BT474 cells exhibited a near-binary difference in stress MAPK activation in response to AKT degradation relative to catalytic inhibition. Following 48-hour treatment with INY-05-040, BT-474 cells exhibited strong induction of p-cJun (S73) and cJun, which was sustained for at least 72 hours (**Figure 2-16A**). We hypothesized that induction of stress MAPK signaling contributes to AKT degrader-associated cytotoxicity. To test this, BT-474 and T47D cells were pre-treated with low does (50 nM) of the covalent pan-JNK inhibitor JNK-IN-8 for 24 hours, followed by addition of either INY-05-040 or GDC00068 for 120 hours. The two cell lines were chosen as models for potent (BT-474) and low (T47D) cytotoxic responses to AKT degradation. Consistently, INY-05-040-induced cytotoxic response in T47D cells were fully neutralized by JNK inhibition (**Figure 2-16C**). In BT474 cells, however, combined AKT degradation and JNK inhibition only led to a small, partial rescue of cytotoxicity (**Figure 2-16C**); The increased levels of cleaved-PARP, a marker of apoptosis, were also no reduced by co-treatment with JNK-IN-8 in INY-05-040-treated BT-474 cells (**Figure 2-18**). We therefore conclude that acute and sustained stress MAPK activation is a marker of potent suppression of AKT signaling downstream of INY-05-040, but that this mechanism is not sufficient to explain the cytotoxic effects of AKT degradation.
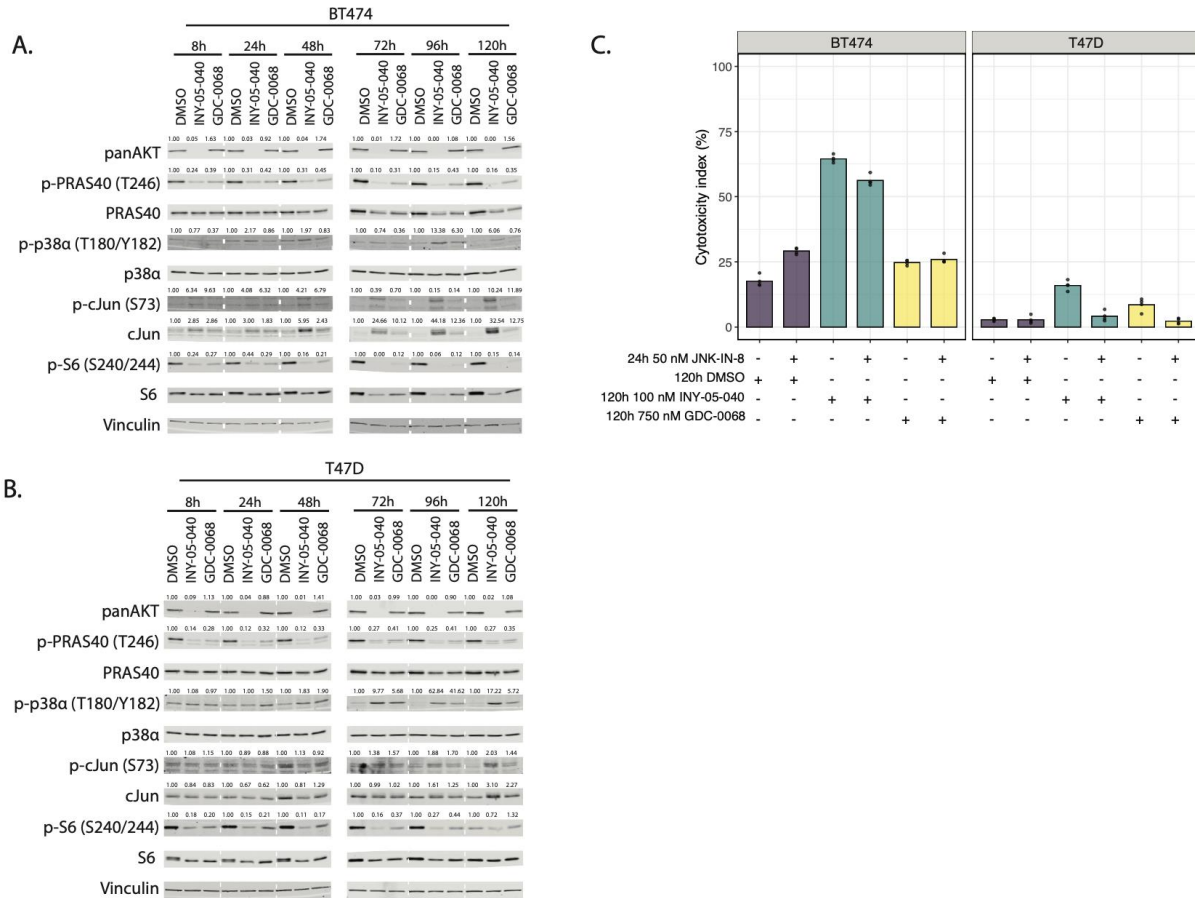
Figure 2-16. Validation of COSMOS-predicted MAPK Stress Kinase Signaling. Immunoblots for panAKT, phospho-PRAS40 (T246), total PRAS40, phospho-p38α (T180/Y182), total p38α, phospho-cJun (S73), total cJun, phospho-S6 (S240/244), total S6, and Vinculin after treatment of (A) BT-474 or (B) T47D cells for the indicated times with DMSO, 100 nM INY-05-040, or 750 nM GDC-0068. Quantification of AKT and cJun represents protein abundance over Vinculin, relative to the corresponding DMSO condition for each time point. Quantification of remaining phosphorylated proteins represent normalization to the corresponding total protein, relative to the DMSO signal for each time point. (C) Cytotoxicity index assayed using CellTox Green, in BT-474 or T47D cells treated for 24 h with either DMSO or 50 nM JNK-IN-8, followed by 120-h co-treatment with either DMSO, INY-05-040 (100 nM) or GDC-0068 (750 nM). The cytotoxicity index represents cytotoxicity values corrected for background fluorescence and normalized to total signal following chemical permeabilization (used as proxy measure for total cell number). For conditions of interest, the following statistics were generated using bootstrap-coupled estimation: unpaired mean percentage-point difference of JNK-IN-8 versus DMSO = 11.5 [95CI 8.89; 13.2]; unpaired mean percentage-point difference of INY-05-040 + JNK-IN-8 versus INY-05-040 = -8.31 [95CI -10.1; -5.75].
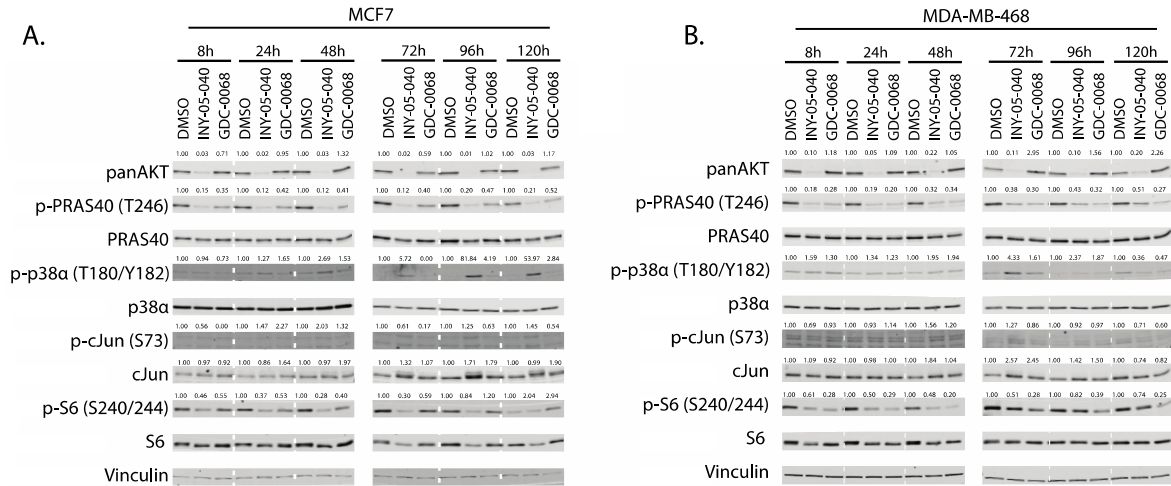
Figure 2-17. Stress MAPK signaling activation in MCF7 and MDA-MB-468 cells. Immunoblots for panAKT, phospho-PRAS40 (T246), total PRAS40, phospho-p38α (T180/Y182), total p38α, phospho-c-Jun (S73), total cJun, phospho-S6 (S240/244), total S6, and Vinculin after DMSO, INY-05-040 (100 nM) or GDC-0068 (750 nM) treatment of (A) MCF7 or (B) MDA-MB-468 cells for the indicated times. Quantification of AKT and cJun represents protein abundance over Vinculin, relative to the corresponding DMSO condition for each time point. Quantification of remaining phosphorylated proteins represent normalization to the corresponding total protein, relative to the DMSO signal for each time point.

BT-474 Plate 1 BT-474 Plate 2

24h 50 nM JNK-IN-8	-	+	-	+	-	-		-	+	-	+	-	-
120h DMSO	+	+	-	-	-	-		+	+	-	-	-	-
120h 100 nM INY-05-040	-	-	+	+	-	-		-	-	+	+	-	-
10 µM Bortezomib (h)	-	-	-	-	24	48		-	-	-	-	24	48

panAKT

p-p38α (T180/Y182)

p38α

p-cJun (S73)

cJun

p-S6 (S240/244)

S6

PARP FL

CL

| CL-PARP/beta-actin norm DMSO | 1.00 | 1.32 | 2.59 | 2.39 | 2.53 | 4.21 | | 1.00 | 1.20 | 3.19 | 3.63 | 3.37 | 5.28 |

Vinculin
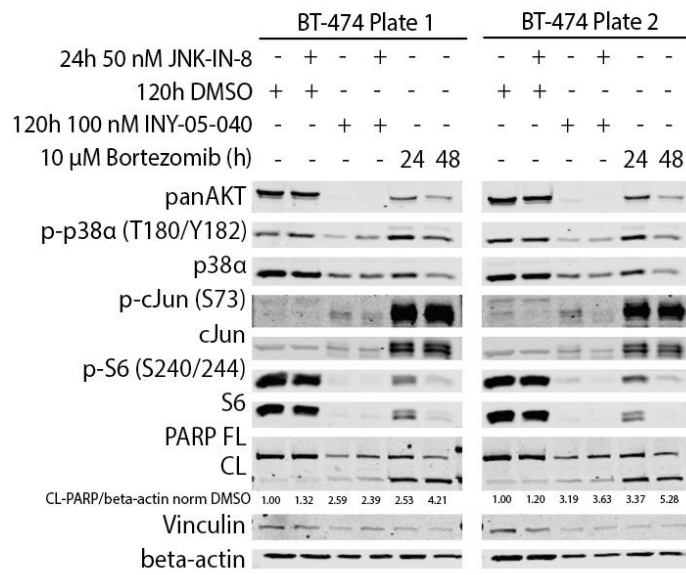
beta-actin

Figure 2-18. Co-treatment of BT-474 cells with INY-05-040 and JNK-IN-8. Immunoblots for panAKT, phospho-p38α (T180/Y182), total p38α, phospho-c-Jun (S73), total cJun, phospho-S6 (S240/244), total S6, PARP (FL: full lengths; CL: cleaved), Vinculin, and beta-actin after 24 h pre-treatment of BT474 cells with either DMSO or 50 nM JNK-IN-8, followed by 120-h co-treatment with either DMSO, INY-05-040 (100 nM) or GDC-0068 (750 nM). Treatment with Bortezomib (10 µM) for 24 h and 48 h was used as positive control. Two technical replicates (indicated with Plate 1 and Plate 2) were processed in parallel. brightfield Quantification for cleaved (CL) PARP was performed by measuring the intensity of the indicated lower band, normalized to beta-actin, relative to DMSO.

Global cell line screening identifies stress MAPK-associated resistance biomarkers

Given the improved cellular potency of INY-05-040, including robust downstream transcriptional and metabolic changes, we next undertook global cancer cell line profiling to determine whether these properties translate into more potent grown suppression relative to GDC-0068. Briefly, cell lines across multiple linages were challenged with a range of doses of compounds and cell number relative to day 0 were assessed to measure suppression of cell growth. Across 288 cancer cell lines, spanning 18 different cancer lineages, INY-05-040 exhibited superior growth-inhibitory activity (**Figure 2-19A**). This was based on calculation of the drug concentration required to reduce overall growth by 50% (GI50adj, **Figure 2-20A**), including adjustments for cell line-specific differences in growth rate. Strikingly, while GI50adj calculation was possible for all cell lines treated with INY-05-040, this was not possible for 161 cell lines treated with GDC-0068 due to the lack of sufficient growth suppression (**Figure 2-19A**). Consequently, the median GI50adj value for GDC-0068 in the screen was higher than 10 µM, compared to 1.1 µM for INY-05-040 and 3.1 µM for INY-03-041.

To identify functional biomarkers predictive of sensitivity to INY-05-040 in the 21 breast cancer cell lines profiled, we took advantage of the measured GI50adj values and the corresponding baseline transcriptomic, proteomic and reverse phase protein array (RPPA) data (**Figure 2-20A**) publicly available through the Cancer Dependency Map project (Tsherniak et al., 2017). We classified breast cancer cells into sensitive, intermediate and resistant if the measured GI50adj was less than 0.5 µM, between 0.5 and 1 µM, and higher than 1 µM, respectively (**Figure 2-19B**). Subsequent unsupervised PCA using either transcriptomic or proteomic datasets revealed a notable separation of INY-05-040 sensitive vs. resistant breast cancer cell lines, which was not simply driven by ER expression as assessed by PAM50 status (**Figure 2-20B**). This was also

55

observed for 4 out of 5 breast cancer cell lines that belong to the basal A subtype. By contrast, only 1 out of 6 basal B breast cancer cell lines were sensitive to INY-05-040, with 4 out of the 6 cell lines exhibiting resistance (**Figure 2-19B**).

We next took the cell specific PC1 loadings from the transcriptomic and proteomic data and correlated these with the actual GI50adj values. This revealed strong and statistically significant correlations for either comparison (Spearman's *Rho* > 0.8, p < 0.001), with higher PC1 loadings associated with the higher GI50adj values and thus resistance to INY-05-040 (**Figures 2-20C and D**). To identify the molecular features driving the observed separation in the two datasets, we performed GSEA on the two PC1 loadings (transcriptomic and proteomic data). Gene sets that were positively enriched for alongside either PC1 were highly concordant and characterized by strong enrichment for epithelial mesenchymal transition and inflammatory signaling (**Figure 2-20E**). Strikingly, most of these positive enrichments overlapped with those observed upon acute 10-hour treatment of T47D breast cancer cells with INY-05-040 (**Figure 2-20F**). Based on our mechanistic data on acute JNK activation and sensitivity to INY-05-040, we reasoned that the correlation between inflammatory gene signatures and INY-05-040 resistance in the breast cancer panel may reflect an already high baseline JNK activation and thus adaptation to stress MAPK signaling. Accordingly, we found that both *JNK1* mRNA levels (**Figure 2-20G**), JNK1 phosphorylation (**Figure 2-20H**) and cJun phosphorylation (**Figure 2-20I**) exhibited a positive and statistically significant correlation with INY-05-040 GI50adj values. Importantly, BT-474 cells had the lowest GI50adj and the lowest values for the aforementioned markers of JNK1 activation. Taken together, our data demonstrate superior potency of INY-05-040-induced AKT degradation over catalytic inhibition across cancer cell lines, with low baseline levels of stress MAPK signaling correlating with heightened AKT degrader sensitivity in breast cancer cells.
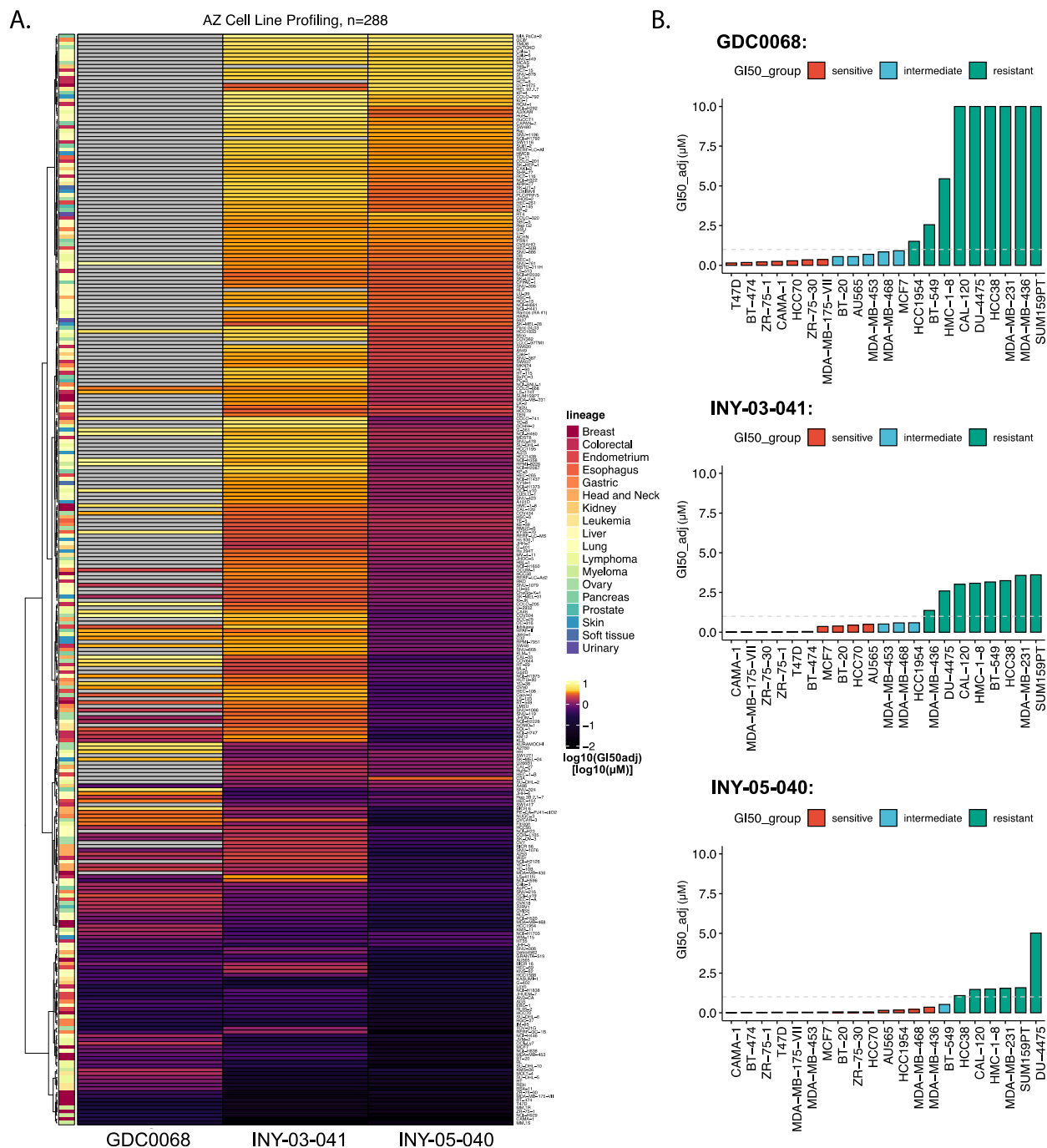
Figure 2-19. Cancer cell line screen of GDC-0068, INY-03-041, and INY-05-040. (A) Heatmap of cell line-specific GI50adj values for each compound, with Euclidean distance-based clustering of the cell lines (rows). (B) Barplots indicating the GI50adj values for each compound in breast cancer cell lines only, colored according to sensitivity to the respective compound (sensitive: GI50adj < 0.5 μM; intermediate: 0.5 μM < GI50adj < 1 μM; resistant: GI50adj > 1 μM). The dotted horizontal line indicates GI50adj = 1 μM.
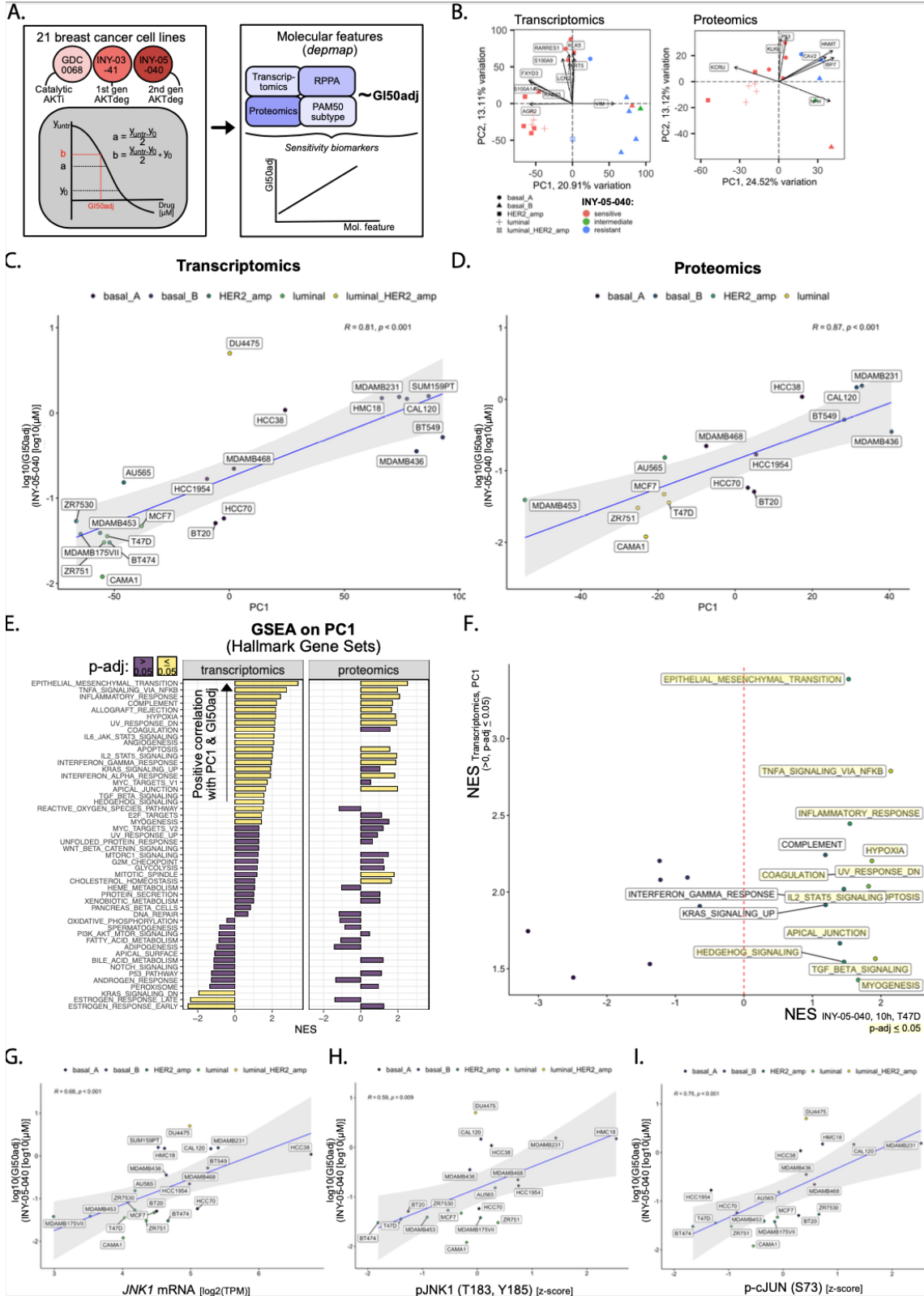
Figure 2-20 (continued). Integration of cell line screen data with publicly available omics datasets to identify sensitivity biomarkers for INY-05-040. (A) Analytical workflow for cell line screen processing and subsequent integration of the growth response metric (GI50adj) with publicly available cell line omics data from the DepMap project. A total of 288 cancer cell lines were profiled with GDC-0068, INY-03-41 and INY-05-040. Subsequent integrative analyses focused on breast cancer cell lines only. Note that the applied growth response metric (GI50adj) takes into account cell line growth which is a known confounder in drug sensitivity measurements. The final output corresponds to the concentration of drug that results in 50 % cell growth inhibition. (B) PCA on breast cancer-specific transcriptomics and proteomics data, with coloring according to sensitivity to INY-05-040 (sensitive: GI50adj < 0.5 µM; intermediate: 0.5 µM ≤ GI50adj ≤ 1 µM; resistant: GI50adj > 1 µM). The PAM50 subtype of each cell line is specified by shape. Transcripts and proteins contributing the most to the observed data structure alongside PC1 and PC2 are labelled. (C) and (D) Spearman's correlation analysis of PC1 values for each cell line and the corresponding GI50adj value for INY-05-040. A linear regression line with 95% confidence intervals (shaded area) is included in each analysis, demonstrating that cell line-specific PC1 scores can be used as proxy measures for INY-04-050 sensitivity (i.e., the higher the PC1 score, the more resistant the cell line). (E) GSEA (mSigDb HALLMARK gene sets) using transcript and protein loading values alongside the respective PC1, a proxy measure for sensitivity to INY-04-050; FDR ≤ 0.05. NES: normalized enrichment score. (F) A plot of all gene sets that were significantly and positively enriched for across PC1 loadings from the depmap transcriptomic data, and the corresponding NES from the T47D dataset following 10 h treatment with INY-05-040. Highlighted gene signatures were also statistically significant (FDR ≤ 0.05) in the T47D dataset. (G), (H) and (I) Spearman's correlation analysis of *JNK1* mRNA expression (G), pJNK1 (T183/Y187) (H) and p-cJun (S73) with the cell line-specific GI50adj value for INY-05-040. A linear regression line with 95% confidence intervals (shaded area) is included in each analysis. Reverse phase protein phosphorylation (RPPA) data were obtained from the depmap project and subset for the signals of interest.

Discussion and conclusion

Targeted protein degradation (TPD) has emerged as both a novel therapeutic approach and powerful experimental tool to evaluate the effects of acute protein depletion on cellular networks. Here, we report the development of both INY-03-041 and INY-05-040, potent and highly selective degraders of AKT. Using a multi-omics approach in breast cancer cells, we found that AKT degradation led to unique transcriptomic and metabolomic changes, concomitant with potent activation of stress MAPK signaling. Furthermore, low baseline levels of JNK activation were associated with increased sensitivity to AKT degradation across a panel of breast cancer cell lines.

The on-going search for targeted agents to treat patients with PI3K pathway hyperactivation has focused on identification of more selective compounds or effective combinations to limit toxicity and improve patient selection (Jansen et al., 2016). Recent efforts have led to the development of PI3Kα selective inhibitor alpelisib, approved for the treatment of advanced hormone receptor-positive, HER2-negative breast cancer, in combination with ER antagonist fulvestrant (André et al., 2019). Alpelisib was also approved for the treatment of developmental overgrowth disorders collectively known as *PIK3CA*-related overgrowth spectrum (PROS) (Madsen and Semple, 2022). Despite this progress, both cancers and diseases of PI3K pathway activation urgently need expansion of available treatment options to address issues of resistance and/or poor tolerability. Independent lines of evidence, including this current study, indicate that TPD of PI3K pathway components may represent a novel therapeutic strategy, with the added benefit of sustained inhibition of downstream signaling (Song et al., 2022). This property may partially be explained by the inability of various negative feedback mechanisms within the PI3K/AKT pathway to overcome inhibition when a critical downstream transducer in absent. Prolonged cellular stress can also suppress AKT/mTORC1 activity, alongside a more complete

shutdown of protein translation, which may contribute to the self-sustained loop of continued suppression of AKT signaling. This hypothesis is supported by the washout experiments in which pathway reactivation was not observed and remained low for at least 72 hours after degrader removal, in stark contrast with the ATP-competitive inhibitor GDC-0068.

The successful development of improved therapies against cancers with activated PI3K/AKT signaling rests upon identifying new mechanistic insights into the underlying protein network, particularly in response to inhibitory modalities. Using a network biology framework, COSMOS, we demonstrate how systematic integration of a prior knowledge with context-specific transcriptomic and metabolomic data can be used to identify and subsequently test mechanistic hypotheses on AKT degradation-selective signaling outcomes. This approach identified the stress MAPKs, p38α (*MAPK14*) and JNK1 (*MAPK8*), as differentially activated in breast cancer cells treated with INY-05-040. The observed quantitative differences would have challenging to resolve with conventional approaches, emphasizing the power of computational integration of multi-omics data and temporal analyses.

We posit that both the duration and potency of AKT pathway inhibition is critical for eliciting the stress MAPK stress response observed with INY-05-040. At present, the precise mechanistic link between AKT degradation and stress MAPK activation remains undescribed. We speculate that ribosomal stress may contribute to the induction of stress MAPKs, since AKT and mTORC1 promote ribosome biogenesis through transcriptional and translational mechanisms. Conversely, disruption of any given step in the ribosome biogenesis has been shown to cause ribosomal stress (Zhou et al., 2015). Accordingly, AKT degradation, but not catalytic inhibition, led to a potent and sustained reduction of total ribosomal S6 protein levels, which would be

consistent with the low stability of ribosomal proteins in the absence of functional ribosome production (Warner, 1977).

The involvement of the stress MAPK and inflammatory signaling in the cellular response to AKT degradation is further supported by integration of growth inhibition measurements with publicly available omics data. The observation that the same transcriptional and signaling signatures induced upon degrader treatment of T47D cells are already elevated at baseline in breast cancer cells with lower sensitivity to INY-05-040 suggest that the low baseline stress MAPK and inflammatory signaling activity may be a pre-requisite for potent cell growth suppression upon AKT degradation.

In summary, we demonstrate vastly improved suppression of cancer cell growth with INY-05-040 and illustrate how TPD, in combination with integrated systems-level analyses, can be used to uncover novel biology that is inaccessible with conventional kinase inhibitors.

Materials and methods

Cell lines. MOLT4, Jurkat, ZR-75-1, LNCaP, T47D, MCF-7, MDA-MB-468, BT-474 and HCC1937 cells were cultured in RPMI media (Wisent Bioproducts) supplemented with 10% heat inactivated fetal bovine serum (Thermo Fisher Scientific) and 100U/mL Penicillin-Streptomycin (Gibco) at 37 °C in the presence of 5% CO_2. IGROV1 and PC3 cells were cultured in DMEM media (Gibco) supplemented with 10% heat inactivated fetal bovine serum (Thermo Fisher Scientific) and 100U/mL Penicillin-Streptomycin (Gibco) at 37 °C in the presence of 5% CO_2

Immunoblotting. Cells were washed once in 1x PBS then lysed in RIPA buffer (150 mM Tris-HCl, 150 mM NaCl, 0.5% (w/v) sodium deoxycholate, 1% (v/v) NP-40, pH 7.5) containing 0.1% (w/v) sodium dodecyl sulfate, 1 mM sodium pyrophosphate, 20 mM sodium fluoride, 50 nM calyculin, and 0.5% (v/v) protease inhibitor cocktail (Sigma-Aldrich) for 15 min. Cell extracts were precleared by centrifugation at 18,800 x g for 10 min at 4 °C. The Bio-Rad DC protein assay was used to assess protein concentration as per the manufacturer's instructions, and sample concentration was normalized using 2x SDS sample buffer. Next, 20 mg of protein lysates and PageRuler Plus (Fisher) prestained protein ladder were resolved on 10% acrylamide gels by SDS-polyacrylamide gel electrophoresis and electrophoretically transferred to nitrocellulose membrane (BioRad) at 100 volts for 90 min. Membranes were blocked in 5% (w/v) nonfat dry milk (Fisher) or 5% (w/v) bovine serum albumin (Boston Bioproducts) in Tris-buffered saline (TBS) for 1 h, then incubated with specific primary antibodies diluted 1:1000 in 5% (w/v) bovine serum albumin in TBS-T (TBS with 0.05% Tween-20) at 4 °C overnight, shaking. The primary antibodies used are pan-AKT (Cell Signaling Technology, #4691 and #9275), pAKT (S473, Cell Signaling Technology, #4060), pAKT(T246, Cell Signaling Technology, #2997), PRAS40 (Cell Signaling

63

Technology, #2691), pPRAS40 (T246, Cell Signaling Technology, #13175), GSK3β (Cell Signaling Technology, #9315), pGSK3β (Cell Signaling Technology, #9336), TSC2 (Cell Signaling Technology, #3990), pTSC2 (T1462, Cell Signaling Technology, #3617), Vinculin (Cell Signaling Technology, #13901), ERK1/2 (Cell Signaling Technology, #4695), pERK1/2 (Cell Signaling Technology, #9101), 4EBP (Cell Signaling Technology, #9452), S6 (Cell Signaling Technology, #2217), pS6 (S240/244, Cell Signaling Technology, #5364), pS6 (S235/236, Cell Signaling Technology, #4858), p38 (Cell Signaling Technology, #8690) phospho-p38 (Cell Signaling Technology, #4511), cJun (Cell Signaling Technology, #9165), and phospho-cJun (Cell Signaling Technology, #3270). The next day, membranes were washed 3 times for 5 min each with TBS-T then incubated for 1 h at room temperature with fluorophore-conjugated secondary antibodies (LI-COR Biosciences) in 5% (w/v) nonfat dry milk, protected from light. The membrane was washed again 3 times for 5 min each with TBS-T, followed by a final 5-min wash in TBS, then imaged with a LI-COR Odyssey CLx Imaging System (LI-COR Biosciences).

Quantification was performed in ImageStudioLite Software (Licor Biosciences) by drawing rectangles around bands to capture band signal intensities: total pixel intensity minus background pixel intensity. Relative phospho-protein signal was performed for each lane by dividing phospho-protein signal intensity by corresponding total protein signal intensity, while relative AKT signal was calculated by dividing AKT signal intensity by Vinculin signal intensity. Normalization to DMSO samples was performed by dividing relative signal intensity for each condition by the corresponding DMSO signal intensity values.

In Vitro Kinase Assays. Z'-LYTE assays were conducted for AKT1, AKT2, AKT3, PKG1, S6K1, PKN1, ßMSK2, and Haspin at Life Technologies in a 10-point dose response using K_m ATP concentrations. LanthaScreen assays were conducted for RET (V804M) in a 10-point dose response at Life Technologies.

Proliferation assays. T47D, MDA-MB-468, MCF-7 or BT-474 cells were plated in 384 well plates at 250 cells per well. After 24 h, cells were treated with GDC-0068, AZD5363, MK-2206, ARQ-092, INY-03-041, INY-05-040, INY-05-040-Neg, or VH032 compounds at concentrations indicated for 72 h. The anti-proliferative effects of these compounds were assessed using the Cell Titer Glo assay kit (Promega Cat) following manufacturer protocol. EC_{50} values were determined using GraphPad Prism using nonlinear regression curve fitting.

CellTox Green Cell Death Assay. Cell viability was assayed with a CellTox Green cell death assay. Cells in 96-well plates (ThermoFisher) were treated with a 1:1000 dilution (in assay buffer) of CellTox Green dye for 30 min at room temperature, protected from light. Fluorescence intensity, corresponding to binding of CellTox Green dye to double-stranded DNA from dead cells, was measured on a SpectraMax iD3 Microplate Reader (485 nm excitation / 520 nm emission) from the bottom, with an integration time of 400 ms and 9 multi-point readings per well. To estimate the total number of cells for subsequent normalization, all wells were subsequently permeabilized with 0.1% Triton X-100 (Fisher Scientific Cat), and enough CellTox Green reagent to maintain "1X" final concentration. After incubating for 30 min at room temperature, protected from light, the final fluorescence intensity was measured as above. Readings from each well were averaged and corrected by subtracting the average background signal from wells with medium and CellTox

Green and no cells. The cytotoxicity index was calculated for treatments of interest by dividing background-corrected non-permeabilized readings by the corresponding permeabilized readings to assess the percentage cell death. Each assay run was quality checked by inclusion of a standard curve of increasing cell number, followed by permeabilization and measurement of the CellTox Green signal. All raw data and annotated analysis scripts are available on the associated OSF project website (https://osf.io/fasqp/).

In parallel, cell health and CellTox Green uptake were also assessed by light microscopy, with image capture on a Keyence BZ-X800 (brightfield and 488 nm) and an ECHO Scope (brightfield only; 10X). These images were used as internal QC and are not incorporated in the final manuscript but have been deposited on the OSF project website (https://osf.io/fasqp/) as further supporting evidence.

Growth Rate Assay and Analysis. Cell lines were plated at densities ranging from 500 to 2000 cells per well in a 384-well plate using a Matrix WellMate Reagent Dispenser (ThermoFisher) and allowed 24 hours to adhere to plate prior to treatment. A D300 Digital Dispenser (Hewlett-Packard) was used to treat cells with dilution series of compounds as indicated. At the time of treatment and after 72 hours of treatment, cells were stained and fixed for subsequent analysis. Cells were stained with LIVE/DEAD Far Red Dead Cell Stain (LDR) (ThermoFisher) at 1:2000 for 1 hour at 37 °C. Cells were fixed for 30 minutes at room temperature in 4% formaldehyde (Sigma Aldrich) then permeabilized with 0.5% Triton X-100 in PBS. Cells were blocked for 1 hour using Odyssey Blocking Buffer (LI-COR Biosciences) and stained overnight at 4°C with 2 µg/ml Hoechst 33342 (Sigma Aldrich). An Operetta microscope was used to image fixed cells, and data was stored and analyzed using Columbus software (PerkinElmer). Nuclei were segmented by Hoechst signal

using the Columbus system (PerkinElmer). The average LDR and Hoechst intensities were determined within the nuclear area. Dead cells were classified by LDR signal. Experiments were performed in technical triplicate.

RNA sequencing

Sample Preparation. Snap-frozen cells were thawed on ice and RNA extracted with Takara's Nucleospin RNA Plus kit (Takara) according to the manufacturer's instructions. RNA integrity was assessed for quantity and purity by Nanodrop 1000. Samples were submitted to Novogene for integrity assessment (Agilent 2100 analysis), mRNA library preparation (unstranded), and paired-end (150 bp) sequencing on a NovaSeq S4 flow cell.

Raw read mapping, counting and differential expression. Raw read processing was performed with the Nextflow (version 20.07.1) nf-core RNAseq pipeline (version 1.4.2), with Spliced Transcripts Aligment to a Reference (STAR) for read alignment to the human genome (Homo_sapiens.GRCh38.96.gtf) and featureCounts for counting of mapped reads (multimapped reads were discarded).

All subsequent data processing was performed in R, with differential gene expression analysis following the limma-voom method. Filtering of low gene expression counts was performed with the *TCGAbiolinks* package with quantile value 0.75 (chosen empirically based on the observed count distribution). Next, read count normalization was performed with the trimmed mean of M (TMM) method. PCA was done using the *PCAtools* package. The mean-variance relationship was modelled with voom(), followed by linear modelling and computation of moderated t-statistics

using the lmFit() and eBayes() functions in the *limma* package. Experimental replicate was included as a batch effect term in the model. The associated p-values for assessment of differential gene expression were adjusted for multiple comparisons with the Benjamini-Hochberg method at false-discovery rate (FDR) = 0.05. Adjustments were performed separately for each contrast of interest. Subsequent gene annotations were performed with *BioMart* within R using the associated ENSEMBL Gene IDs as key values. Intersection plots and heatmaps were generated using the *ComplexHeatmap* package. Clustering was performed using the Ward.D2 method. Columns were clustered according to Euclidean distance, while rows (genes) were clustered according to Spearman's correlation, i.e. patterns of change as opposed to maximum values.

Gene set enrichment analysis. The *msigdbr* package was used to retrieve the indicated gene signatures. GSEA was performed with the *fgsea* package, using the list of all genes ranked according to their *t* statistic for a comparison of interest. The choice to use *the t* statistic ensures that the gene ranking considers signal magnitude (fold-change) as well as uncertainty of estimation. Normalized enrichment values and associated p-values were calculated with the fgseaMultilevel() function, using default settings. The normalized enrichment score computed by the algorithm corresponds to the enrichment score normalized to mean enrichment of random samples, using the same gene set size.

Transcription factor footprint analysis. The voom-normalized counts were used to predict transcription factor activities with DoRothEA, choosing regulons within confidence groups "A", "B" and "C" (low-confidence regulons in groups "D" and "E" were therefore not considered). As per the developer's recommendations, the "minsize" argument in the options was set to "5", and

"eset.filter" was set to "FALSE". Exact details can be retrieved from the deposited code. Annotated scripts for all analysis steps post-read processing are provided on the OSF project webpage (https://osf.io/3f2m5/).

Precision nuclear run-on sequencing (PRO-seq)

Sample Preparation. To harvest cell pellets for PRO-seq, cells were washed once with 8 mL room temperature 1X PBS then trypsinized for 5 min. Trypsin was quenched with ice cold DMEM + 10% FBS and cells were collected in a 50 mL conical tube and placed onto ice immediately. Cells were spun at 300 x g for 4 min at 4 °C, supernatant was removed, and cells were resuspended in 250 mL Buffer W (10 mM Tris-Cl, pH 8.0; 10 mM KCl; 250 mM Sucrose; 5 mM MgCl2; 1 mM EGTA; 0.5 mM DTT; 10 % (v/v) Glycerol; Protease inhibitor tablet (EDTA-free), 0.02% SUPERase-IN RNAse inhibitor) to obtain a single-cell suspension by pipetting. 10 mL of Buffer P (10 mM Tris-Cl, pH 8.0; 10 mM KCl; 250 mM Sucrose; 5 mM MgCl$_2$; 1 mM EGTA; 0.1 % (v/v) Igepal CA-630; 0.5 mM DTT; 0.05 % (v/v) Tween-20; 10 % (v/v) Glycerol; Protease inhibitor tablet (EDTA-free), 0.02% SUPERase-IN RNAse inhibitor) was added and cells were incubated on ice for 5 min, then spun at 400 x g for 4 min at 4 °C. Supernatant was removed and Buffer W was added and pipetted gently 2-3 times to resuspend cell suspension. An additional 9 mL of Buffer W was added to each tube, and cells were spun at 400 x g for 4 min at 4 °C. An additional wash with Buffer W was completed as above and supernatant was carefully decanted so cell pellets were not disturbed. Pellets were resuspended in Buffer F (50 mM Tris-Cl, pH 8.0; 40 % (v/v) glycerol; 5 mM MgCl$_2$; 1.1 mM EDTA; 0.5 mM DTT, and SUPERase-IN RNAse inhibitor) and transferred to a 1.5 mL tube. The 50 mL tube was rinsed once more with 250 µL of

Buffer F and added to the corresponding 1.5 mL tube for a final volume of 500 µL per sample. 10 µL was reserved for counting after dilution 1:10 and 1:20 in PBS, both with and without trypan blue to calculate the fraction of permeabilized cells. Cells were diluted to 1 x 10^6 permeabilized cells per 100 µL and a total of 5 x 10^6 cells were aliquoted in 500 µL of Buffer F and snap frozen in liquid nitrogen and stored at -80 °C until further processing. RNAse-free water was used to make all reagents and solutions, and solutions were filter sterilized with 0.2 mM filters into RNAse-free plastic bottles. Two independent biological replicates were collected, alongside the corresponding protein samples to confirm drug action at the signaling level.

PRO-seq library construction. Aliquots of frozen (-80 °C) permeabilized cells were thawed on ice and pipetted gently to fully resuspend. Aliquots were removed and permeabilized cells were counted using a Luna II, Logos Biosystems instrument. For each sample, 1 million permeabilized cells were used for nuclear run-on, with 50,000 permeabilized *Drosophila* S2 cells added to each sample for normalization. Nuclear run-on assays and library preparation were performed essentially as described in Reimer et al. with the following modifications: 2X nuclear run-on buffer consisted of (10 mM Tris (pH 8), 10 mM $MgCl_2$, 1 mM DTT, 300 mM KCl, 40 µM/ea biotin-11-NTPs (Perkin Elmer), 0.8 U/µL SuperaseIN (Thermo), 1% sarkosyl). Run-on reactions were performed at 37 °C. Adenylated 3' adapter was prepared using the 5' DNA adenylation kit (NEB) and ligated using T4 RNA ligas' 2, truncated KQ (NEB, per manufacturer's instructions with 15% PEG-8000 final) and incubated at 16 °C overnight. 180 µL of betaine blocking buffer (1.42 g of betaine brought to 10 mL with binding buffer supplemented to 0.6 uM blocking oligo (TCCGACGATCCCACGTTCCCGTGG/3InvdT/)) was mixed with ligations and incubated 5 min at 65 °C and 2 min on ice prior to addition of streptavidin beads. After T4 polynucleotide kinase

(NEB) treatment, beads were washed once each with high salt, low salt, and blocking oligo wash (0.25X T4 RNA ligase buffer (NEB), 0.3 µM blocking oligo) solutions and resuspended in 5' adapter mix (10 pmol 5' adapter, 30 pmol blocking oligo, water). The 5' adapter ligation was per Reimer et al. but with 15% PEG-8000 final. Eluted cDNA was amplified 5-cycles (NEBNext Ultra II Q5 master mix (NEB) with Illumina TruSeq PCR primers RP-1 and RPI-X) following the manufacturer's suggested cycling protocol for library construction. The product (preCR) was serially diluted and used for test amplification to determine the optimal PCR conditions for the final libraries. The pooled libraries were paired-end sequenced using the Illumina NovaSeq platform.

PRO-seq raw read processing. All custom scripts described herein are available on the AdelmanLab Github (https://github.com/AdelmanLab/NIH_scripts). Using a custom script (trim_and_filter_PE.pl), FASTQ read pairs were trimmed to 41 bp per mate, and read pairs with a minimum average base quality score of 20 retained. Read pairs were further trimmed using cutadapt 1.14 to remove adapter sequences and low-quality 3' bases (--match-read-wildcards -m 20 -q 10). R1 reads, corresponding to RNA 3' ends, were then aligned to the spiked in Drosophila genome index (dm3) using Bowtie 1.2.2 (-v 2 -p 6 –best –un), with those reads not mapping to the spike genome serving as input to the primary genome alignment step (using Bowtie 1.2.2 options -v 2 –best). Reads mapping to the hg38 reference genome were then sorted, via samtools 1.3.1 (-n), and subsequently converted to bedGraph format using a custom script (bowtie2stdBedGraph.pl) that counts each read once at the exact 3' end of the nascent RNA. Because R1 in PRO-seq reveals the position of the RNA 3' end, the "+" and "-" strands were swapped to generate bedGraphs representing 3' end positions at single nucleotide resolution. Annotated transcription start sites

were obtained from human (GRCh38.99) GTFs from Ensembl. After removing transcripts with (immunoglobulin, Mt_tRNA, Mt_rRNA) biotypes, PRO-seq signal in each sample was calculated in the window from the annotated TSS to +150 nt downstream, using a custom script, make_heatmap.pl. Given good agreement between replicates and similar return of spike-in reads, bedGraphs were merged within conditions, and depth-normalized, to generate 27igwig files binned at 10 bp.

Refinement of gene annotation (GGA) using PRO-seq and RNAseq. The corresponding paired-end RNA-seq reads were mapped to the hg38 reference genome via HISAT2 v2.2.1 (--known-splicesite-infile). To select gene-level features for differential expression analysis, and for pairing with PRO-seq data, we assigned a single, dominant TSS and transcription end site (TES) to each active gene. This was accomplished using a custom script, get_gene_annotations.sh (available at https://github.com/AdelmanLab/GeneAnnotationScripts), which uses RNAseq read abundance and PRO-seq R2 reads (RNA 5' ends) to identify dominant TSSs, and RNAseq profiles to define most commonly used TESs. RNAseq and PRO-seq data from all conditions were used for this analysis, to comprehensively capture gene activity in these samples. Reads were summed within the TSS to TES window for each active gene using the make_heatmap script (https://github.com/AdelmanLab/NIH_scripts), which counts each read once, at the exact 3' end location of the nascent RNA.

Differential expression analysis. All subsequent processing of the PRO-seq count data were as described above for the RNAseq count data. Filtering of low counts was performed with the

TCGAbiolinks package with quantile value 0.1. Annotated scripts for the associated analysis steps are provided on the OSF project webpage (https://osf.io/3f2m5/).

Metabolomics

Sample Preparation. For metabolite extraction, media was aspirated, and cells were washed once with ice-cold PBS on wet ice. Ice-cold 80% (v/v) mass spec-grade methanol was added, the plate was transferred to dry ice and scraped, and the resulting solution was collected. Protein samples were collected in duplicate for normalization to protein content and signaling validation as described above. Insoluble material was pelleted by centrifugation at 20,000 x g for 5 min, and the resulting supernatant was evaporated under nitrogen gas. Samples were resuspended in 20 µL HPLC-grade water for LC/MS analysis.

Data Acquisition. For polar metabolite profiling, 5 µL from each sample were injected and analyzed using a 5500 QTRAP hybrid triple quadrupole mass spectrometer (AB/SCIEX) coupled to a Prominence UFLC HPLC system (Shimadzu) with HILIC chromatography (Waters Amide XBridge), via selected reaction monitoring (SRM) with polarity switching. A total of 295 endogenous water-soluble metabolites were targeted for steady-state analyses. Electrospray source voltage was +4950 V in positive ion mode and −4500 V in negative ion mode. The dwell time was 3 ms per SRM transition 32. Peak areas from the total ion current for each metabolite were integrated using MultiQuant v2.1.1 software (AB/SCIEX).

Data Analysis. Prior to differential abundance analysis, the raw metabolomics data were preprocessed as follows. Untrusted metabolites were removed from the datasets; these included: SBP, shikimate, shikimate-3-phosphate, spermidine, spermine, succinyl-CoA-methylmalonyl-CoA-nega, trehalose-6-phosphate, trehalose-sucrose, malonyl-CoA-nega, N-acetyl spermidine, N-acetyl spermine, Acetylputrescine, NAD+_nega, NADH-nega, NADP+_nega, NADPH-nega, O8P-O1P, OBP, propionyl-CoA-neg, putrescine, acetoacetyl-CoA_neg, acetyl-CoA_neg, Cellobiose, coenzyme A_nega, glutathione, glutathione disulfide-posi. Next, metabolites with low peak intensities (<10,000) across at least 50% of the samples were removed. Finally, all metabolites with 0 intensity in more than 3 samples were also removed; any metabolites with 0 intensity in < 3 samples were removed in the final differential abundance analysis steps. Metabolomics data normalized to matched protein samples from three independent experiments, each including three separate cell cultures per treatment, were combined into one dataset. Metabolites with missing ("NA") or negative values in at least one trial were removed, resulting in 169 metabolites included in the final analyses. These were processed for differential abundance testing using the limma-voom method, with quantile normalization due to significant heteroscedascity. Subsequent linear modelling and computation of moderated *t*-statistics was performed with *lmFit()* and *eBayes()* as for the RNAseq data, including experimental replicate as blocking factor due to a noticeable batch effect. Heatmap generation and clustering of differentially abundant metabolites was performed as described for the RNAseq data. Annotated scripts for the associated analysis steps are provided on the OSF project webpage (https://osf.io/3f2m5/)

Causal Oriented Search of Multi-Omic Space (COSMOS). The RNAseq input data for COSMOS consisted of transcription factor *t* values from DoRothEA and the *limma-voom*-based *t* statistic for all genes, irrespective of significance, for a given contrast of interest (GDC-0068 *versus* DMSO; INY-05-040 *vs* DMSO). The latter served as additional constraints on the solver. Metabolite data for COSMOS consisted of the *limma-voom*-based *t* statistic for metabolites with unadjusted p-value $\leq$ 0.05, resulting in 58 metabolites for GDC-0068 and 77 metabolites for INY-05-040. The decision to use unadjusted p-values for filtering was made *a priori* due to well-known fact of high correlation across groups of metabolites, thus making the resulting corrections for multiple comparisons overly restrictive. Metabolite names had to be mapped to their corresponding PubChem ID, which was facilitated by the R packages *KEGGREST* and *webchem*. Exact code for generation of both RNAseq and metabolite values in the correct format for COSMOS, as well as extensive details on all required installations and subsequent code for running COSMOS on a high-performance computer cluster, are provided on the accompanying OSF project page (https://osf.io/tdvur/). Briefly, the algorithm relies on CARNIVAL's Integer Linear Programming (ILP) optimization, which was rerun multiple times for each dataset to determine the most consistent network predictions. Settings for each run, including the resulting network gap values, are provided in an accompanying table on the OSF project page. Differences included explicit indication of AKT1/2 inhibition (AKT3 was not expressed in T47D cells) as well as shuffling of individual *t* values for the background transcriptome, thus artificially forcing the solver to initiate the optimization from different starting points. A "forward" optimization run to connect deregulated transcription factors ("signaling" input) as starting points to metabolites was performed first, followed by a "backward" optimization run connecting metabolites to signaling components. These optimization runs were used as the basis for the actual forward and final runs

defining the output of the algorithm. Time limits for solving were set empirically, ensuring that the gap values of the resulting networks were $\leq$ 5% (indicative of a good fit). This was achieved for all runs except for one backward run (gap = 9.68%) using GDC-0068 input data. For each network run, we have provided the COSMOS script and its output as separate text files, including all run-specific settings and final gap values (https://osf.io/tdvur/). Subsequent network analysis and visualization was performed in R, using the rCy3 package to interface with Cytoscape. For the final visualization, a filter was applied such that text was only displayed for nodes with betweenness values of $\geq$ 0.05, the size of the text is indicative of the degree, and the color of the node indicative of its COSMOS-derived activation value. Betweenness is a measure of the number of shortest paths going through a node, i.e. how much a node acts as point of connection or information transmission.

Cancer Cell Line Growth Inhibition Screen. The high throughput line screen was outsourced to Horizon by Astra Zeneca. A detailed description of the protocol, alongside cell-line specific culture conditions and GI50 curve fits, are included on the OSF project webpage (https://osf.io/us45v/). Briefly, the 288 cell lines were thawed and expanded until they reached their expected doubling times, at which point the screening beings. Cells were seeded in 25 µL of growth media in black 384-well tissue culture and equilibrated at 37 °C and 5% CO_2 for 24 h before treatment. At the time of treatment, a set of assay plates were collected for initial (V_0) measurements of ATP (used as proxy for viability) using the luminescence-based CellTiter Glo 2.0 (Promega) assay and an Envision plate reader (Perkin Elmer). Compounds were transferred to the remaining treatment plates using and Echo acoustic liquid handling system; 25 nL of each compound was added at the appropriate concentration for all combination dose points. Plates were incubated with compound

for either 3 or 6 days, followed by ATP measurements with CellTiter Glo. All data points were collected via automated processes and subjected to quality control, followed by analysis using Horizon's proprietary software.

Horizon utilizes Growth Inhibition (GI) as a measure of cell growth. The GI percentages are calculated by applying the following test and equation:

$$If \ T<V\_0 : 100*(1-(T-V\_0)/V\_0)$$

$$If \ T\geq V\_0 : 100*(1-(T-V\_0)/(V-V\_0))$$

where T is the signal measure for a test drug, V is the untreated/vehicle-treated control measure, and V_0 is the untreated/vehicle control measure at time zero (see above). This formula is derived from the Growth Inhibition calculation used in the National Cancer Institute's NCI-60 high throughput screen.

The GI50adj value is defined as the drug concentration that reduces total cell growth by 50%; this value was set to the maximum concentration of drug used in the assay (10 µM) if 50 % total cell growth inhibition was not attained in the tested concentration range.

Computational Integration with DepMap Datasets. Publicly available transcriptomic, proteomic and RPPA data, alongside the relevant metadata, for breast cancer cells of interest were retrieved from DepMap using the *depmap* R package. PCA, GSEA, hierarchical clustering and heatmap generation as part of subsequent integration with experimental GI50adj data were performed as described for RNA sequencing. RNAseq data were obtained as *transcrips per million* (TPM) and were subject to quantile-based filtering (quantile threshold = 0.25), using the *TCGAbiolinks* package, to remove lowly-expressed genes. We used non-parametric Spearman's correlation to measure the strength of association between variables of interest. GI50adj values were log-

transformed (base10) for visualization. For RPPA data, all antibodies labeled with "Caution" were excluded from analysis; the remaining antibody measurements were converted to z-scores prior to visualization. Annotated scripts for the associated analysis steps are provided on the OSF project webpage (https://osf.io/us45v/).

Pharmacodynamic Analyses in BT474C Xenografts. BT474C pharmacodynamic animal studies were conducted according to AstraZeneca's Global Bioethics Policy in accordance with the PREPARE and ARRIVE guidelines. Female Nude mice were surgically implanted with a 0.36mg/60d 17β-estradiol pellet (Innovative Research of America) into the left subcutaneous flank. The following day BT474c cells were implanted at 5×10^6 cells per mouse (suspended in 50% DMEM:50% Matrigel) into the right subcutaneous flank. Mouse weights were monitored twice weekly up until dosing, after which mouse weights were monitored daily. Tumors were measured twice weekly by caliper, with tumor volumes calculated using the formula:

Volume = (π x Maximum measure(Length or Width) x Minimum measure(Length or Width) x

Minimum measure (Length or Width))/6000

Mice were randomized by tumor volume into either control or treatment groups when average tumor volume reached 0.5 cm^3. GDC-00068 was dosed perorally twice a day for 4 days at 12.5mg/kg (5ml/kg)(0.5% HPMC, 0.1% Tween 80). INY-05-040 and INY-03-041 were dosed for 4 days as a once daily intraperitoneal injection at 25mg/kg (5ml/kg) (10% DMSO/20% Captisol, pH 5.0 with gluconic acid). On the final day of dosing, 4 h post dosing AM dose, mice were humanely killed, and tumor tissue was collected and immediately snap frozen in liquid nitrogen before storage at -80 °C. Protein was extracted from snap-frozen tumor fragments by adding 900 µL of extraction buffer (20 mM Tris at pH 7.5, 137 mM NaCl, 10% Glycerol, 50

78

mM NaF, 1 mM Na$_3$VO$_4$, 1% SDS, 1% NP40 substitute) with complete protease inhibitor cocktail (Roche; 1 tablet per 50 mL). Samples were homogenized twice for 30 seconds at 6.5m/s in a fast-prep machine with an incubation at 4 °C for 5 min between runs. Lysates were then sonicated in a chilled Diagenode Bioruptor for two cycles (setting: HIGH) of 30 s ON/30s OFF. Lysates were cleared twice by centrifugation, followed by protein concentration estimation with the Pierce BCA Protein Assay Kit (Thermo Fisher Scientific). Approximately 40 µg of protein was run on a NuPAGE 4–12% Bis-Tris gel (Thermo Fisher Scientific) using standard methods. Following protein separation, protein was transferred onto nitrocellulose membranes using dry transfer with iBlot2 (Thermo Fisher Scientific). Primary antibodies were diluted in Tris-buffered saline (TBS)/0.05% Tween (TBS/T) supplemented with 5% Marvel, and incubated overnight at 4 °C. The membranes were washed three times for 15 min each in 20 m of TBS/T. A secondary horseradish peroxidase (HRP)-linked antibody was diluted 1:2000 in TBS/T supplemented with 5 % Marvel and incubated for 1 h at room temperature. The membranes were washed three times for 15 min each in 20 mL of TBS/T, and the signal detected using chemiluminesent SuperSignal West Dura Extended Duration Substrate (Thermo Fisher Scientific).

TMT LC-MS3 mass spectrometry. MOLT4 cells were treated with DMSO (biological triplicate) INY-03-041 (250 nM, 4 hours) or INY-05-040 (250 nM, 4 hours), and cells were harvested by centrifugation. Cell lysis and Tandem Mass Tagged (TMT) tryptic peptides were prepared for LC-MS analysis following procedures published (Donovan *et al.*, 2018).

Data were collected using an Orbitrap Fusion Lumos mass spectrometer (Thermo Fisher Scientific, San Jose, CA, USA) coupled with a Proxeon EASY-nLC 1200 LC pump (Thermo Fisher Scientific). Peptides were separated on a 50 cm 75 µm inner diameter EasySpray ES903

microcapillary column (Thermo Fisher Scientific). Peptides were separated using a 190 min gradient of 6 - 27% acetonitrile in 1.0% formic acid with a flow rate of 300 nL/min.

Each analysis used a MS3-based TMT method as described previously (McAlister et al., 2014). The data were acquired using a mass range of m/z 340 – 1350, resolution 120,000, AGC target 5 $\times$ 105, maximum injection time 100 ms, dynamic exclusion of 120 s for the peptide measurements in the Orbitrap. Data dependent MS2 spectra were acquired in the ion trap with a normalized collision energy (NCE) set at 35%, AGC target set to 1.8×104 and a maximum injection time of 120 ms. MS3 scans were acquired in the Orbitrap with HCD collision energy set to 55%, AGC target set to 2×105, maximum injection time of 150 ms, resolution at 50,000 and with a maximum synchronous precursor selection (SPS) precursor set to 10.

Proteome Discoverer 2.4 (Thermo Fisher Scientific) was used for .RAW file processing and controlling peptide and protein level false discovery rates, assembling proteins from peptides, and protein quantification from peptides. MS/MS spectra were searched against a Swissprot human database (February 2020) with both the forward and reverse sequences as well as known contaminants such as human keratins. Database search criteria were as follows: tryptic with two missed cleavages, a precursor mass tolerance of 20 ppm, fragment ion mass tolerance of 0.6 Da, static alkylation of cysteine (57.0215 Da), static TMT labeling of lysine residues and N-termini of peptides (304.2071 Da), and variable oxidation of methionine (15.9949 Da). TMT reporter ion intensities were measured using a 0.003 Da window around the theoretical m/z for each reporter ion in the MS3 scan. The peptide spectral matches with poor quality MS3 spectra were excluded from quantitation (summed signal-to-noise across channels < 100 and precursor isolation specificity < 0.5), and the resulting data was filtered to only include proteins with a minimum of 2 unique peptides quantified. Reporter ion intensities were normalized and scaled using in-house

scripts in the R framework (Team, 2014).Statistical analysis was carried out using the limma

package within the R framework (Ritchie *et al.*, 2015).

General chemistry methods. Reagents and solvents were purchased from commercial suppliers and were used without further purification unless otherwise noted. Reactions were monitored using a Waters Acquity UPLC/MS system (Waters PDA eλ Detector, QDa Detector, Sample manager - FL, Binary Solvent Manager) using Acquity UPLC® BEH C18 column (2.1 x 50 mm, 1.7 μm particle size): solvent gradient = 85% A at 0 min, 1% A at 1.7 min; solvent A = 0.1% formic acid in Water; solvent B = 0.1% formic acid in Acetonitrile; flow rate: 0.6 mL/min. Products were purified by flash column chromatography using CombiFlash®Rf with Teledyne Isco RediSep® normal-phase silica flash columns (4 g, 12 g, 24 g, 40 g or 80 g) and preparative HPLC using Waters SunFireTM Prep C18 column (19 x 100 mm, 5 μm particle size) using a gradient of 15-75% methanol in water containing 0.05% trifluoroacetic acid (TFA) over 48 min (60 min run time) at a flow of 40 mL/min. ^{1}H NMR spectra were recorded on 500 MHz Bruker Avance III spectrometer, and chemical shifts are reported in million (ppm, δ) downfield from tetramethylsilane (TMS). Coupling constants (J) are reported in Hz. Spin multiplicities are described as s (singlet), br (broad singlet), d (doublet), t (triplet), q (quartet) and m (multiplet). Purities of assayed compounds were in all cases greater than 95%, as determined by reverse-phase HPLC analysis.

Abbreviations Used

DCM, Dichloromethane; DIEA, N,N-Diisopropylethylamine; DMF, Dimethylformamide; TEA, Triethylamine; DMP, Dess–Martin periodinane; STAB, Sodium triacetoxyborohydride; DCE, 1,2-Dichloroethane;MeOH, Methanol

Chemistry Synthetic Schemes for INY-03-041

Scheme 1
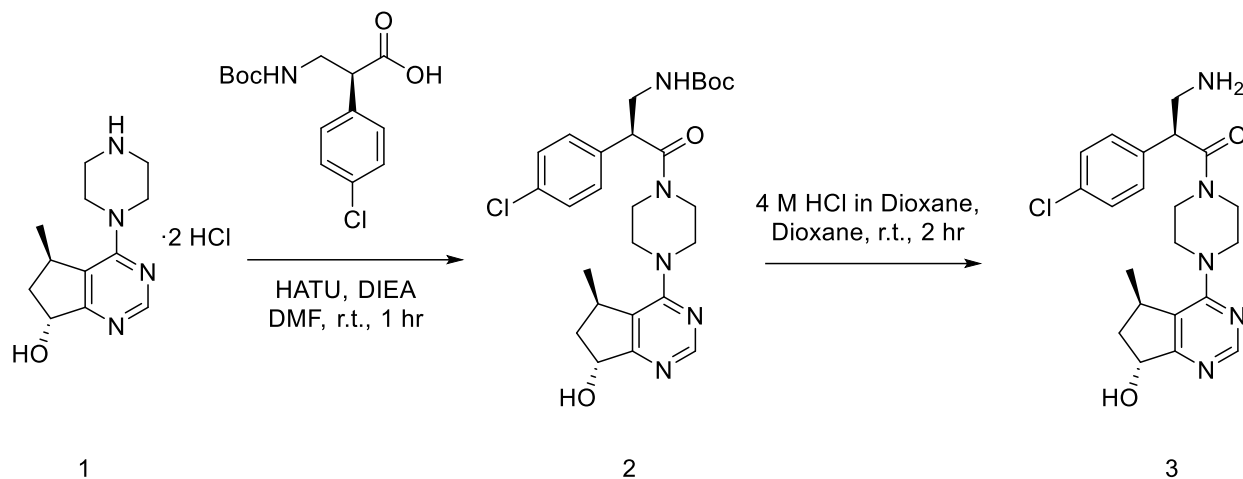
Scheme 2
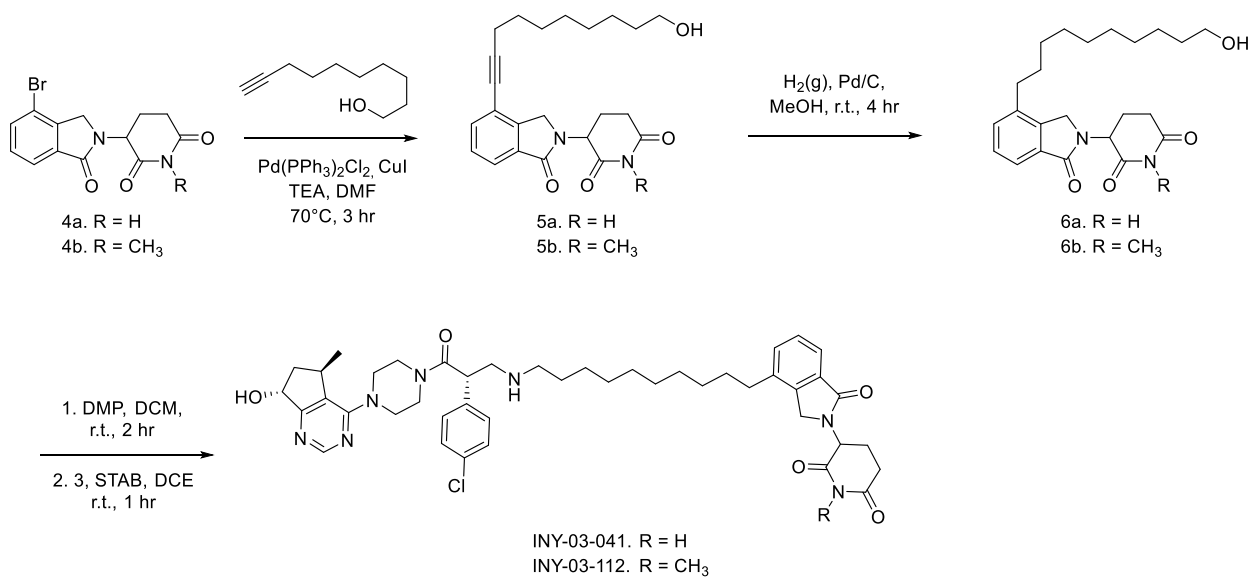
Chemical Synthesis of 3

Tert-butyl((S)-2-(4-chlorophenyl)-3-(4-((5R,7R)-7-hydroxy-5-methyl-6,7-dihydro-5H-cyclopenta[d]pyrimidin-4-yl)piperazin-1-yl)-3-oxopropyl)carbamate (2):

To a solution of known intermediate **1** (Blake et al., 2012) (727 mg, 2.37 mmol), (S)-3-((tert-butoxycarbonyl)amino)-2-(4-chlorophenyl)propanoic acid (711 mg, 2.37 mmol) and HATU (902 mg, 2.37 mmol) in DMF (12 mL) was added DIEA (2.1 mL) and stirred for 1 hour at r.t. The reaction mixture was diluted ethyl acetate (30 mL) and washed with water (2 x 15 mL) and brine (2 x 15 mL). The organic layer was dried over anhydrous sodium sulfate, filtered, and concentrated in vacuo to afford **2** as a yellow oil (1.22 g, 100% yield). The crude was used directly for the next reaction. LC-MS: m/z 516.27 [M+1].

(S)-3-amino-2-(4-chlorophenyl)-1-(4-((5R,7R)-7-hydroxy-5-methyl-6,7-dihydro-5H-cyclopenta[d]pyrimidin-4-yl)piperazin-1-yl)propan-1-one (3):

To a solution of intermediate **2** (1.22 g, 2.37 mmol) in dioxane (7 mL) was added 4 M HCl in dioxane (5 mL). The reaction was stirred at r.t. for 4 hours. The reaction mixture was concentrated in vacuo and purified by reverse-phase HPLC (95-35% water in methanol) to obtain **3** as a TFA salt. The resultant TFA salt was dissolved in a mixture of 4:1 chloroform: isopropanol (50 mL) and washed with sat. aq sodium bicarbonate (50 mL) to give **3** as a white foam (868 mg, 88% yield). LC-MS: m/z 416.25 [M+1]. ^{1}H NMR (500 MHz, DMSO-d6) δ 8.43 (s, 1H), 7.43 – 7.38 (m, 2H), 7.35 – 7.28 (m, 2H), 4.84 (t, J = 7.3, 6.2 Hz, 1H), 4.07 (dd, J = 8.3, 5.3 Hz, 1H), 3.73 – 3.66 (m, 1H), 3.64 – 3.56 (m, 3H), 3.52 – 3.35 (m, 4H), 3.22 – 3.16 (m, 1H), 3.09 (dd, J = 12.6, 8.3 Hz, 1H), 2.72 – 2.67 (m, 1H), 2.01 – 1.87 (m, 2H), 1.04 (dd, J = 6.5, 3.9 Hz, 3H).

Synthesis of INY-03-041 and INY-03-112

3-(4-(10-hydroxydec-1-yn-1-yl)-1-oxoisoindolin-2-yl)piperidine-2,6-dione (5a)

Known intermediate **4a** (Zhou et al., 2018) (500 mg, 1.55 mmol), dec-9-yn-1-ol (478 mg, 3.10 mmol), Pd(PPh$_3$)$_2$Cl$_2$ (113 mg, 0.16 mmol) and CuI (61 mg, 0.32 mmol) were dissolved in TEA (4 mL) and DMF (8 mL). The reaction mixture was flushed with nitrogen (x3) and stirred at 70 °C for 3 hours. The reaction mixture was cooled to r.t., diluted with ethyl acetate (50 mL) and filtered through celite. The organic layer was washed with brine (3 x 20 mL), dried over anhydrous sodium sulfate, filtered and concentrated in vacuo. The crude material was purified by column chromatography on silica gel (9:1 DCM:MeOH) to afford **5a** as a pale yellow solid (503 mg, 82% yield). LC-MS: m/z 397.24 [M+1]. ^{1}H NMR (500 MHz, DMSO-d6) δ 11.00 (s, 1H), 7.71 (dd, J = 7.6, 1.0 Hz, 1H), 7.64 (dd, J = 7.7, 1.0 Hz, 1H), 7.52 (t, J = 7.6 Hz, 1H), 5.76 (s, 2H), 5.15 (dd, J = 13.3, 5.2 Hz, 1H), 4.45 (d, J = 17.6 Hz, 1H), 4.31 (d, J = 17.6 Hz, 1H), 3.37 (t, J = 6.5 Hz, 2H), 2.92 (ddd, J = 17.3, 13.6, 5.5 Hz, 1H), 2.64 – 2.57 (m, 1H), 2.50 – 2.40 (m, 2H), 2.06 – 1.99 (m, 1H), 1.62 – 1.54 (m, 2H), 1.47 – 1.37 (m, 3H), 1.36 – 1.23 (m, 5H), 1.18 (t, J = 7.3 Hz, 1H).

3-(4-(10-hydroxydecyl)-1-oxoisoindolin-2-yl)piperidine-2,6-dione (6a)

To a solution of intermediate **5a** (100 mg, 0.25 mmol) in MeOH (10 mL) was added Pd/C (10 mg). H$_2$ (g) was introduced to the reaction mixture, and the reaction was stirred at r.t. for 4 hours. The reaction mixture was filtered over celite and concentrated in vacuo to afford **6a** as a white solid (91 mg, 91% yield). LC-MS: m/z 401.30 [M+1]. ^{1}H NMR (500 MHz, DMSO-d6) δ 10.98 (s, 1H), 7.60 – 7.54 (m, 1H), 7.50 – 7.41 (m, 2H), 5.13 (dd, J = 13.3, 5.1 Hz, 1H), 4.45 (d, J = 17.2 Hz, 1H), 4.34 – 4.28 (m, 2H), 3.36 (td, J = 6.5, 4.9 Hz, 2H), 2.92 (ddd, J = 17.3, 13.7, 5.4 Hz, 1H),

2.66 – 2.58 (m, 3H), 2.43 (qd, J = 13.3, 4.5 Hz, 1H), 2.01 (dtd, J = 12.7, 5.2, 2.2 Hz, 1H), 1.66 – 1.54 (m, 2H), 1.43 – 1.35 (m, 2H), 1.33 – 1.21 (m, 12H).

3-(4-(10-(((S)-2-(4-chlorophenyl)-3-(4-((5R,7R)-7-hydroxy-5-methyl-6,7-dihydro-5H-cyclopenta[d]pyrimidin-4-yl)piperazin-1-yl)-3-oxopropyl)amino)decyl)-1-oxoisoindolin-2-yl)piperidine-2,6-dione (INY-03-41)

To a solution of intermediate **6a** (83 mg, 0.21 mmol) in DCM (4 mL) was added DMP (132 mg, 0.31 mmol). The reaction was stirred at r.t. for 2 hours. The reaction mixture was filtered and concentrated in vacuo to obtain 10-(2-(2,6-dioxopiperidin-3-yl)-1-oxoisoindolin-4-yl)decanal (84 mg, quantitative yield). LC-MS: m/z 399.27 [M+1]. The crude material was then dissolved in DCE (2 mL), followed by addition of intermediate **3** (131 mg, 0.31 mmol). The reaction was stirred at r.t. for 30 minutes, after which STAB (89 mg, 0.42 mmol) was added. The reaction mixture was stirred for an additional 1 hour. The reaction was quenched by sat. aq sodium bicarbonate (10 mL) and extracted with DCM (3 x 20 mL). The organic layers were combined, dried over anhydrous sodium sulfate, filtered and concentrated in vacuo. The crude residue was purified by reverse-phase HPLC (75-15% water in methanol) to obtain **INY-03-041** (TFA salt). The resultant TFA salt was dissolved in 4:1 chloroform:isopropanol (10 mL) and washed with sat. aq sodium bicarbonate. The organic layer was dried over anhydrous sodium sulfate, filtered and concentrated in vacuo to afford title compound as an off-white solid (42 mg, 25% yield). LC-MS: m/z 798.42 [M+1]. ^{1}H NMR (500 MHz, DMSO-d6) δ 8.43 (s, 1H), 7.56 (dd, J = 5.4, 3.2 Hz, 1H), 7.45 – 7.43 (m, 2H), 7.41 (d, J = 8.2 Hz, 2H), 7.34 (d, J = 8.2 Hz, 2H), 5.38 (d, 1H), 5.13 (dd, J = 13.3, 5.1 Hz, 1H), 4.87 – 4.80 (m, 1H), 4.45 (d, J = 17.1 Hz, 1H), 4.29 (dd, J = 15.4, 7.6 Hz, 2H), 3.70 – 3.56 (m, 5H), 3.51 – 3.42 (m, 3H), 3.41 – 3.36 (m, 1H), 3.24 – 3.16 (m, 2H), 2.92 (ddd, J = 17.9, 13.8,

5.4 Hz, 1H), 2.77 – 2.71 (m, 1H), 2.63 (t, J = 7.5 Hz, 3H), 2.60 – 2.55 (m, 2H), 2.42 (tt, J = 13.3, 6.6 Hz, 1H), 2.04 – 1.93 (m, 2H), 1.93 – 1.87 (m, 1H), 1.62 – 1.55 (m, 2H), 1.41 – 1.35 (m, 2H), 1.32 – 1.26 (m, 4H), 1.22 (s, 8H), 1.03 (d, J = 6.8 Hz, 3H).

3-(4-(10-hydroxydec-1-yn-1-yl)-1-oxoisoindolin-2-yl)-1-methylpiperidine-2,6-dione (5b)

5b was synthesized with similar procedures as **5a** using intermediate **4b** (90 mg, 0.27 mmol) as the starting material. **5b** was obtained as a light orange solid (49 mg, 44% yield). LC-MS: m/z 411.51 [M+1]. ^{1}H NMR (500 MHz, DMSO-d6) δ 7.71 (dd, J = 7.6, 1.0 Hz, 1H), 7.63 (dd, J = 6.8, 1.2 Hz, 1H), 7.52 (t, J = 7.6 Hz, 1H), 5.21 (dd, J = 13.5, 5.1 Hz, 1H), 4.44 (d, J = 17.6 Hz, 1H), 4.30 (d, J = 17.6 Hz, 1H), 3.36 (t, J = 6.5 Hz, 2H), 3.04 – 2.95 (m, 4H), 2.79 – 2.72 (m, 1H), 2.47 (t, J = 7.1 Hz, 2H), 2.45 – 2.39 (m, 1H), 2.03 (dtd, J = 12.7, 5.2, 2.2 Hz, 1H), 1.61 – 1.52 (m, 2H), 1.47 – 1.34 (m, 4H), 1.34 – 1.24 (m, 6H).

3-(4-(10-hydroxydecyl)-1-oxoisoindolin-2-yl)-1-methylpiperidine-2,6-dione (6b)

6b was synthesized with similar procedures as **6a** using intermediate **5b** (42 mg, 0.1 mmol) as the starting material. **6b** was obtained as an off-white solid (33 mg, 79% yield). LC-MS: m/z 415.57 [M+1]. ^{1}H NMR (500 MHz, DMSO-d6) δ 7.60 – 7.53 (m, 1H), 7.49 – 7.43 (m, 2H), 5.20 (dd, J = 13.4, 5.1 Hz, 1H), 4.45 (d, J = 17.1 Hz, 1H), 4.32 – 4.27 (m, 2H), 3.36 (td, J = 6.6, 5.1 Hz, 2H), 3.01 (s, 3H), 3.00 – 2.95 (m, 1H), 2.79 – 2.74 (m, 1H), 2.66 – 2.61 (m, 2H), 2.48 – 2.39 (m, 1H), 2.08 – 1.98 (m, 1H), 1.63 – 1.56 (m, 2H), 1.43 – 1.34 (m, 2H), 1.32 – 1.22 (m, 12H).

3-(4-(10-((((S)-2-(4-chlorophenyl)-3-(4-((5R,7R)-7-hydroxy-5-methyl-6,7-dihydro-5H-cyclopenta[d]pyrimidin-4-yl)piperazin-1-yl)-3-oxopropyl)amino)decyl)-1-oxoisoindolin-2-yl)-1-methylpiperidine-2,6-dione (INY-03-112)

INY-03-112 was synthesized with similar procedures as **INY-03-041** using intermediate **6b** (27 mg, 0.07 mmol) as the starting material. **INY-03-112** was obtained as an off-white solid (9 mg, 16% yield). LC-MS: m/z 812.47 [M+1]. ^{1}H NMR (500 MHz, DMSO-d6) δ 8.43 (s, 1H), 7.57 (dd, J = 5.8, 2.8 Hz, 1H), 7.49 – 7.43 (m, 4H), 7.37 – 7.32 (m, 2H), 5.40 (d, J = 5.5 Hz, 1H), 5.21 (dd, J = 13.4, 5.1 Hz, 1H), 4.83 (q, J = 6.3 Hz, 1H), 4.45 (d, J = 17.1 Hz, 1H), 4.38 (dd, J = 8.9, 5.1 Hz, 1H), 4.29 (d, J = 17.1 Hz, 1H), 3.76 – 3.41 (m, 8H), 3.41 – 3.34 (m, 3H), 3.10 (t, J = 10.0 Hz, 1H), 3.01 (s, 3H), 2.99 – 2.95 (m, 1H), 2.83 – 2.73 (m, 3H), 2.63 (t, J = 7.7 Hz, 2H), 2.43 (qd, J = 13.2, 4.5 Hz, 1H), 2.05 – 1.87 (m, 3H), 1.59 (t, J = 7.5 Hz, 2H), 1.50 (s, 2H), 1.33 – 1.27 (m, 4H), 1.23 (s, 8H), 1.02 (d, J = 6.9 Hz, 3H).

Chemistry synthetic scheme of INY-05-040
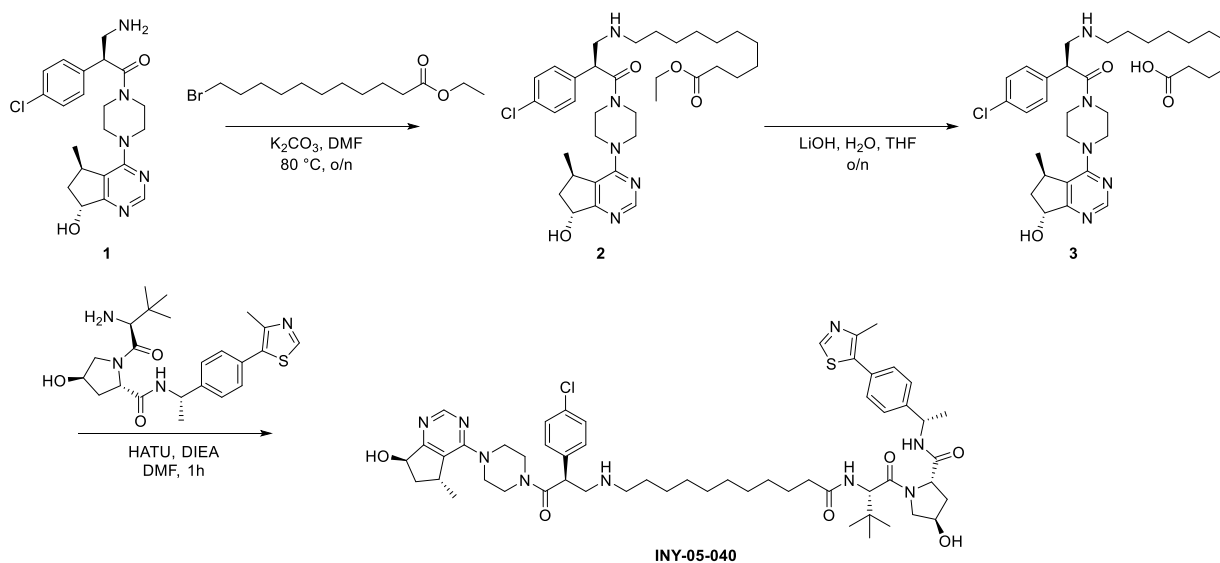
Synthesis of INY-05-040 and INY-05-040-Neg

Ethyl 11-(((S)-2-(4-chlorophenyl)-3-(4-((5R,7R)-7-hydroxy-5-methyl-6,7-dihydro-5H-cyclopenta[d]pyrimidin-4-yl)piperazin-1-yl)-3-oxopropyl)amino)undecanoate (2)

(S)-3-amino-2-(4-chlorophenyl)-1-(4-((5R,7R)-7-hydroxy-5-methyl-6,7-dihydro-5H-cyclopenta[d]pyrimidin-4-yl)piperazin-1-yl)propan-1-one (150 mg, 0.36 mmol) was dissolved in DMF (2 mL). Potassium carbonate (150 mg, 1.08 mmol) was added to the reaction mixture, followed by dropwise addition of ethyl 11-bromoundecanoate (96 mg, 0.32 mmol). The reaction was stirred at 80 °C overnight. The next day, the reaction mixture was filtered and purified by reverse phase high-performance liquid chromatography (HPLC; 75% to 15% water in methanol) to obtain title compound as a yellow oil (133 mg, 56% yield). LC-MS: m/z 628.4 [M+1].

11-(((S)-2-(4-chlorophenyl)-3-(4-((5R,7R)-7-hydroxy-5-methyl-6,7-dihydro-5H-cyclopenta[d]pyrimidin-4-yl)piperazin-1-yl)-3-oxopropyl)amino)undecanoic acid (3)

6 N LiOH (1 mL) and THF (tetrahydrofuran; 1 mL) were added to ethyl 11-(((S)-2-(4-chlorophenyl)-3-(4-((5R,7R)-7-hydroxy-5-methyl-6,7-dihydro-5H-cyclopenta[d]pyrimidin-4-yl)piperazin-1-yl)-3-oxopropyl)amino)undecanoate (133 mg, 0.18 mmol).The reaction mixture was stirred overnight. The next day, 1 N HCl was added to pH ~3, and the solid was filtered and

collected to obtain the title compound (128 mg, 99% yield) as a crude, which was used without further purification. LC-MS: m/z 600.42 [M+1].

(2S,4R)-1-((S)-2-(11-(((S)-2-(4-chlorophenyl)-3-(4-((5R,7R)-7-hydroxy-5-methyl-6,7-dihydro-5H-cyclopenta[d]pyrimidin-4-yl)piperazin-1-yl)-3-oxopropyl)amino)undecanamido)-3,3-dimethylbutanoyl)-4-hydroxy-N-((S)-1-(4-(4-methylthiazol-5-yl)phenyl)ethyl)pyrrolidine-2-carboxamide (INY-05-040)

(2S,4R)-1-((S)-2-amino-3,3-dimethylbutanoyl)-4-hydroxy-N-((S)-1-(4-(4-methylthiazol-5-yl)phenyl)ethyl)pyrrolidine-2-carboxamide (81 mg, 0.17 mmol), HATU (hexafluorophosphate azabenzotriazole tetramethyl uronium; 64 mg, 0.17 mmol), DIEA (N,N-diisopropylethylamine; 200 µL, 1.18 mmol), and DMF (dimethylformamide; 1 mL) were added to 11-(((S)-2-(4-chlorophenyl)-3-(4-((5R,7R)-7-hydroxy-5-methyl-6,7-dihydro-5H-cyclopenta[d]pyrimidin-4-yl)piperazin-1-yl)-3-oxopropyl)amino)undecanoic acid (120 mg, 0.17 mmol). The reaction was stirred for 1 h, after which the reaction was purified by reverse-phase HPLC (80% to 20% water in methanol) to obtain INY-05-040 (40 mg, 22% yield). ^{1}H NMR (500 MHz, DMSO) δ 9.27 (s, 1H), 9.06 (s, 1H), 8.88 (s, 1H), 8.77 (s, 1H), 8.40 (d, J = 7.8 Hz, 1H), 7.78 (d, J = 9.3 Hz, 1H), 7.49 – 7.43 (m, 3H), 7.41 – 7.38 (m, 3H), 5.30 (t, J = 7.9 Hz, 1H), 4.92 (p, J = 7.2 Hz, 1H), 4.75 (dd, J = 8.8, 4.8 Hz, 1H), 4.52 (d, J = 9.3 Hz, 1H), 4.43 (t, J = 8.0 Hz, 1H), 4.31 – 4.25 (m, 1H), 4.03 (d, J = 42.1 Hz, 2H), 3.91 – 3.78 (m, 3H), 3.72 – 3.50 (m, 6H), 3.45 – 3.33 (m, 1H), 3.08 – 3.02 (m, 1H), 2.90 – 2.82 (m, 2H), 2.47 (s, 3H), 2.29 – 2.20 (m, 1H), 2.19 – 1.99 (m, 4H), 1.83 – 1.76 (m, 1H), 1.67 – 1.59 (m, 2H), 1.55 – 1.40 (m, 3H), 1.38 (d, J = 7.0 Hz, 2H), 1.24 (s, 12H), 1.11 (dd, J = 14.1, 6.9 Hz, 3H), 0.94 (s, 9H). LC-MS: m/z 1026.6 [M+1].

(2R,4S)-1-((S)-2-(11-(((S)-2-(4-chlorophenyl)-3-(4-((5R,7R)-7-hydroxy-5-methyl-6,7-dihydro-5H-cyclopenta[d]pyrimidin-4-yl)piperazin-1-yl)-3-oxopropyl)amino)undecanamido)-3,3-dimethylbutanoyl)-4-hydroxy-N-((S)-1-(4-(4-methylthiazol-5-yl)phenyl)ethyl)pyrrolidine-2-carboxamide (INY-05-040-Neg)

INY-05-040-Neg was synthesized using similar procedures as INY-05-040 using (2R,4S)-1-((S)-2-(11-(((S)-2-(4-chlorophenyl)-3-(4-((5R,7R)-7-hydroxy-5-methyl-6,7-dihydro-5H-cyclopenta[d]pyrimidin-4-yl)piperazin-1-yl)-3-oxopropyl)amino)undecanamido)-3,3-dimethylbutanoyl)-4-hydroxy-N-((S)-1-(4-(4-methylthiazol-5-yl)phenyl)ethyl)pyrrolidine-2-

carboxamide as the starting material. ^{1}H NMR (500 MHz, DMSO) δ 8.99 (s, 1H), 8.70 (s, 1H), 8.54 (s, 1H), 8.40 (s, 1H), 8.06 (d, J = 8.0 Hz, 1H), 7.89 (d, J = 7.8 Hz, 1H), 7.49 (d, 2H), 7.45 – 7.44 (m, 3H), 7.38 – 7.35 (m, 2H), 5.20 (t, J = 7.6 Hz, 1H), 4.91 (p, 1H), 4.48 (dd, J = 8.7, 5.0 Hz, 1H), 4.42 – 4.37 (m, 2H), 4.33 – 4.28 (m, 1H), 3.98 (s, 1H), 3.80 (dd, J = 10.4, 5.4 Hz, 2H), 3.77 – 3.58 (m, 6H), 3.56 – 3.45 (m, 3H), 3.14 – 3.07 (m, 1H), 2.94 – 2.86 (m, 2H), 2.47 (s, 3H), 2.29 – 2.21 (m, 1H), 2.14 – 1.93 (m, 6H), 1.62 – 1.52 (m, 2H), 1.52 – 1.38 (m, 3H), 1.32 (d, J = 7.0 Hz, 3H), 1.26 – 1.17 (m, 13H), 1.08 (d, J = 6.9 Hz, 3H), 0.97 (s, 9H). LC-MS: m/z 1026.57 [M+1].

Chapter 3: Exploring the Pharmacological Consequences of ERK5 Degradation

Attributions

The work is this chapter is adapted from a manuscript accepted in *Cell Chemical Biology* entitled "Acute pharmacological degradation of ERK5 does not inhibit cellular immune response or proliferation" by You *et al*.

Contributions

N.S.G. conceived the study. I.Y. designed and synthesized the compounds. I.Y. and E.S.W. designed and conducted the biological profiling of compounds. K.A.D. and N.M.K. performed the proteomics. A.S.B., M.G.R., M.M.R. and J.A.R carried out the PRISM screen. I.Y. and E.S.W. wrote the manuscript, with guidance from E.S.F. and N.S.G.

Funding Acknowledgments

Introduction

Extracellular signal-regulated kinase 5 (ERK5) is a relatively understudied member of the mitogen-activated protein kinase (MAPK) family that has been associated with a wide range of cellular functions, including proliferation and inflammation (Finegan *et al.*, 2015; Zhou et al., 1995). Unlike the conventional MAPKs, ERK5 contains a unique, 400 amino acid C-terminal domain that consists of a nuclear localization signal (NLS) and transcriptional activation domain (TAD) (Kasler *et al.*, 2000). Upon cellular stimulation by mitogens, agonists of Toll-like receptor-2 (TLR2) and cellular stresses, mitogen-activated protein kinase kinase 5 (MEK5) phosphorylates the TEY motif in the activation loop of ERK5, leading to ERK5 activation (Abe et al., 1996; Kato et al., 1997; Mody et al., 2003; Wilhelmsen et al., 2012). Consequently, the activated kinase domain of ERK5 auto-phosphorylates its C-terminal domain at multiple sites, promoting its own nuclear translocation (Kondoh et al., 2006; Morimoto et al., 2007). While ERK5 can directly phosphorylate various transcription factors, such as myocyte enhancer factor 2 (MEF2), the non-catalytic C-terminal tail has also been shown to interact with transcription factors and mediate gene expression (Kato *et al.*, 1997; Sohn et al., 2005).

As a key integrator of cellular signaling, ERK5 may play important roles in various diseases, including cancer and inflammation (Wang and Tournier, 2006). For example, overexpression or constitutive activation of MEK5 or ERK5 has been observed in various malignancies, such as prostate cancer and hepatocellular carcinoma, and genetic knockdown of ERK5 resulted in suppressed proliferation of various tumor models (Hoang *et al.*, 2017; Mehta *et al.*, 2003; Zen et al., 2009). In addition, knockdown of ERK5 indicated that it mediates inflammation by promoting the expression of inflammatory cytokines in primary human endothelial cells and monocytes (Wilhelmsen et al., 2015).

As studies involving genetic deletion or knockdown of ERK5 suggested that ERK5 may be a promising therapeutic target, multiple ATP-competitive ERK5 inhibitors were developed. The first reported ERK5 inhibitor, XMD8-92, demonstrated promising *in vitro* and *in vivo* anti-tumor efficacy, as well as anti-inflammatory activity (Wilhelmsen *et al.*, 2015; Yang et al., 2010). However, further investigation revealed that the biological effects of XMD8-92 and its analogue, XMD17-109, stem from off-target activities against the bromodomain and extra-terminal (BET) family of proteins, as the subsequently developed selective ERK5 inhibitors AX15836 and BAY-885 had no anti-proliferative or anti-inflammatory effects (Lin *et al.*, 2016; Nguyen *et al.*, 2019). This was in contrast to phenotypes observed from genetic ERK5 knockdown, suggesting that kinase-independent activities of ERK5 may play crucial roles in ERK5 signaling (Simões et al., 2016). Furthermore, some ERK5 inhibitors, such as XMD17-109 and AX15836, have been reported to drive nuclear translocation of ERK5, leading to paradoxical activation of ERK5 transcriptional activity (Lochhead *et al.*, 2020). Thus, new chemical strategies are necessary to explore the biological functions of ERK5.

Heterobifunctional degraders, also known as PROTACs (proteolysis targeting chimeras), are molecules in which a small molecule that binds to select target proteins is chemically conjugated to a ligand of an E3 ubiquitin ligase. These bivalent molecules are able to recruit the E3 ligase into close proximity to the target protein and thereby induce its ubiquitination and subsequent proteasomal degradation (Nalawansha and Crews, 2020; Winter *et al.*, 2015). Unlike traditional small molecule inhibitors, degraders enable acute pharmacological depletion of target proteins. Therefore, development of ERK5 degraders would allow direct chemical knockdown of ERK5 that more closely represents genetic knockdown or deletion studies, as well as investigation

of the non-enzymatic functions of ERK5 that are not possible to assess with ATP-competitive inhibitors.

Here, we characterize INY-06-061, a highly selective and potent ERK5 degrader. In contrast to genetic depletion of ERK5, acute pharmacological degradation of ERK5 via treatment with INY-06-061 did not result in anti-proliferative effects in a panel of cancer cell lines. Moreover, INY-06-061-induced ERK5 degradation did not suppress inflammatory cytokine responses in primary endothelial cells. While INY-06-061 treatment did not phenocopy genetic ERK5 loss in the biological contexts explored in this study, INY-06-061 is a useful chemical probe to interrogate the discrepancies observed between ERK5 kinase inhibition and genetic ERK5 ablation.

Discovery and characterization of initial degraders INY-05-091 and INY-05-128

To develop degraders of ERK5, we initially designed heterobifunctional compounds that incorporated the benzodiazepine analogues XMD17-109 and JWG-071 as ERK5 binding moieties (**Figure 3-1**). Both XMD17-109 and JWG-071 have high binding affinities for ERK5, with reported IC_{50} values of 162 and 88 nM, respectively. Although XMD17-109 also binds to and inhibits BRD4 and other members of the BET family proteins, JWG-071 is an optimized analogue with significantly reduced affinity for the off-target BET family proteins (Wang et al., 2018). Conjugation of a von Hippel-Landau (VHL) binding moiety (Raina *et al.*, 2016) to XMD17-109 and JWG-071 with a six-hydrocarbon linker resulted in the bivalent compounds INY-05-091 and INY-05-128, respectively (**Figure 3-1**).

Linker attachment at the terminal piperazine did not compromise ERK5 binding, as both INY-05-091 and INY-05-128 retained high binding affinities for ERK5 (**Table 3-1**). Moreover, INY-05-091 and INY-05-128 induced ERK5 degradation after 5-hour treatment in MOLT4 cells (**Figure 3-2A**), with DC_{50} values of 167 and 281 nM, respectively (**Figure 3-2B**). Consistent with

the selectivity profiles of the parental inhibitors XMD17-109 and JWG-071, INY-05-091 induced

potent BRD4 degradation, while treatment with INY-05-128 had no effect on BRD4 protein levels

(**Figure 3-2A**).
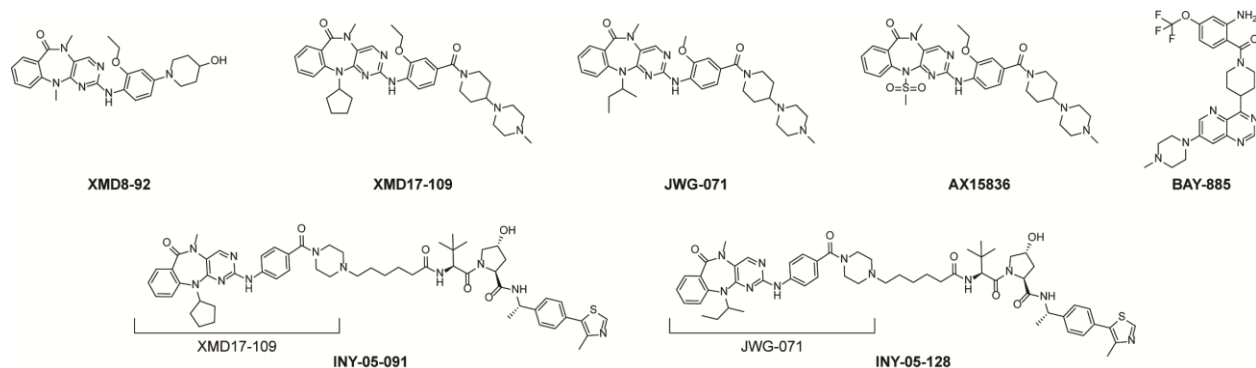
Figure 3-1. Chemical structures of reported ERK5 inhibitors and initial ERK5 degraders INY-05-091 and INY-05-128.

Table 3-1. Biochemical K_d values (nM) of ERK5 binding compounds.

Compound	Kinase	Kd (nM)
XMD8-92	ERK5	38
XMD17-109	ERK5	4.4
JWG-071	ERK5	11
INY-05-091	ERK5	15
INY-05-128	ERK5	40
BAY-885	ERK5	0.87
INY-06-061	ERK5	12
INY-06-086	ERK5	1.7
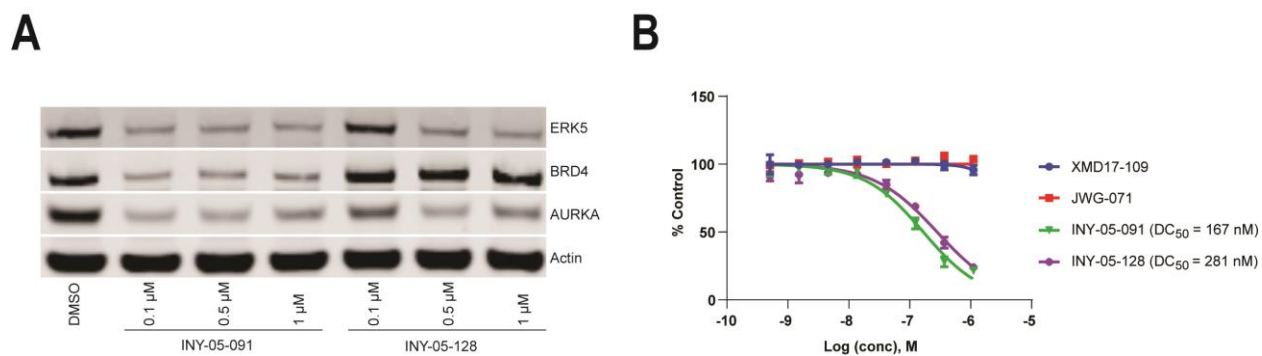
Figure 3-2. INY-05-091 and INY-05-128 induce ERK5 degradation in MOLT4 cells. (A) Immunoblots for ERK5, BRD4, AURKA, and Actin from MOLT4 cells treated with INY-05-091 or INY-05-128 at indicated concentrations for 5 hours. Representative of 3 biological replicates. (B) DC_{50} values of INY-05-091 and INY-05-128. Normalized luminescence intensity of MOLT4 ERK5-HiBiT cells treated with the indicated compounds and concentrations for 5 hours. Error bars represent standard deviation of three biological replicates. DC_{50} values were determined using Graphpad Prism nonlinear regression curve fit.

We next examined the anti-proliferative effects of the two heterobifunctional degraders in MOLT4 cells. As expected of compounds that target BRD4, both INY-05-091 and its parental inhibitor XMD17-109 displayed potent anti-proliferative activities (**Figure 3-3A**). Notably, we observed that JWG-071 and INY-05-128 also exhibited anti-proliferative activities, with EC_{50} values of 2.4 and 1.1 µM, respectively, even though they did not target BET family proteins. In contrast, AX15836 and BAY-885, both of which are reported to be ERK5 selective inhibitors, did not have strong anti-proliferative effects, with EC_{50}s over 10 µM (**Figure 3-3A**).

Based on previous reports (Lin *et al.*, 2016; Ramsay *et al.*, 2011), we had hypothesized that depletion of ERK5 would have different pharmacology than inhibition of its kinase domain. To rule out the possibility that the observed anti-proliferative activity was due to off-targets, we performed a global assessment of the selectivity profiles of INY-05-091 and INY-05-128 through global, quantitative multiplexed mass spectrometry (MS)-based proteomics analysis. As expected, this analysis revealed potent downregulation of ERK5 (MAPK7) protein levels by both INY-05-091 and INY-05-128, with BRD3 and BRD4 as additional downregulated targets for INY-05-091.

Surprisingly, both compounds also induced downregulation of the cell cycle regulator Aurora Kinase A (AURKA) (**Figures 3-3A and 3-3B**), which was validated through immunoblot analysis (**Figure 3-2A**). As such, we attributed the potent anti-proliferative activity of INY-05-128 to the loss of AURKA signaling rather than depletion of ERK5. Therefore, while INY-05-091 and INY-05-128 demonstrate that ERK5 can be successfully targeted for degradation via VHL-based heterobifunctional degraders, the multi-targeted selectivity profiles of both compounds make them inappropriate tools for studying ERK5 biology.
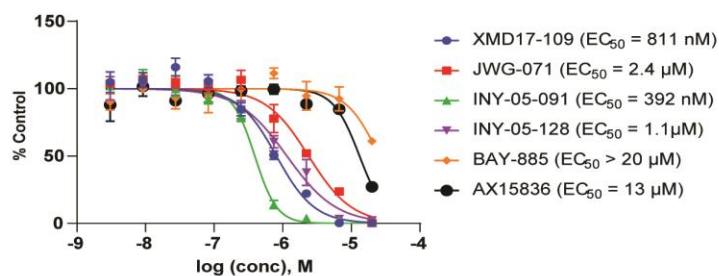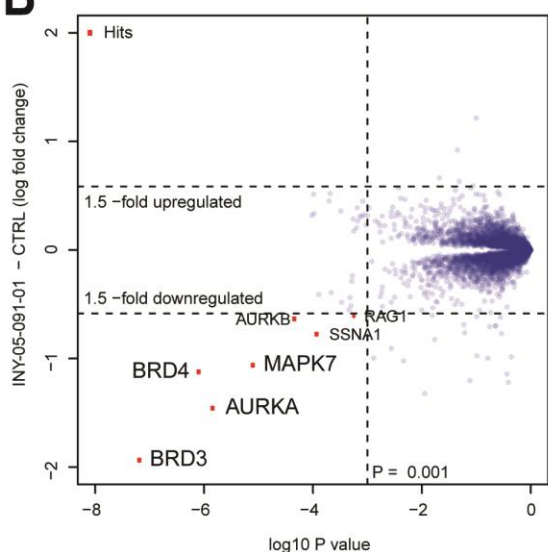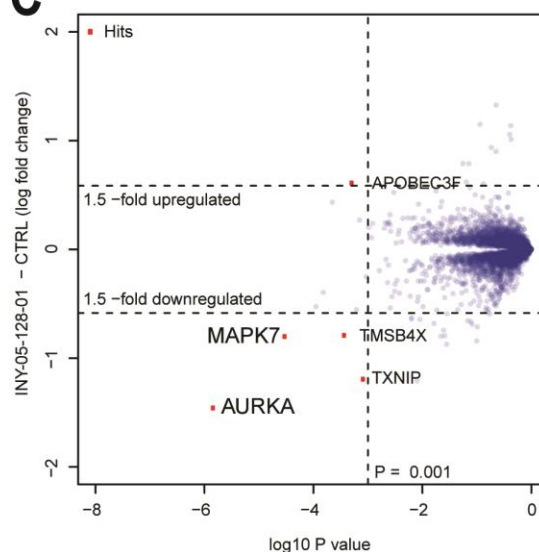
Figure 3-3. Characterization of INY-05-091 and INY-05-128. (A) MOLT4 cells were treated with the indicated compounds and concentrations for 3 days. Anti-proliferative effects of compounds were assessed using CellTiter-Glo. Error bars represent standard deviation of three biological replicates. (B) Quantitative proteomics showing relative abundance of proteins from MOLT4 cells treated for 5 hours with 250 nM of INY-05-091. (C) Quantitative proteomics showing relative abundance of proteins from MOLT4 cells treated for 5 hours with 250 nM of INY-05-128.

Identification of INY-06-061, a potent and highly selective ERK5 degrader

To generate selective ERK5-targeting degraders, we sought to develop compounds based off of the selective ERK5 inhibitor BAY-885 (Nguyen *et al.*, 2019). However, synthesis of BAY-885 with the pyrido[3,2-d]pyrimidine core resulted in poor yields, leading to difficulties carrying out structural-activity relationships (SAR) studies for PROTAC development. Analysis of published SAR for BAY-885 revealed that removal of the N5 nitrogen to convert the pyrido[3,2-

d]pyrimidine core into a quinazoline did not significantly compromise ERK5 binding, leading to the development of INY-06-086 (**Figure 3-4A**). Not only did INY-06-086 retain high binding affinity towards ERK5 (**Table 3-1**), but its biochemical selectivity profile across the kinome was similarly selective for ERK5 as BAY-885 (**Figure 3-4B**) (Nguyen *et al.*, 2019).
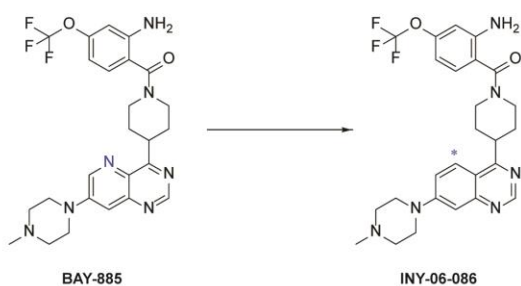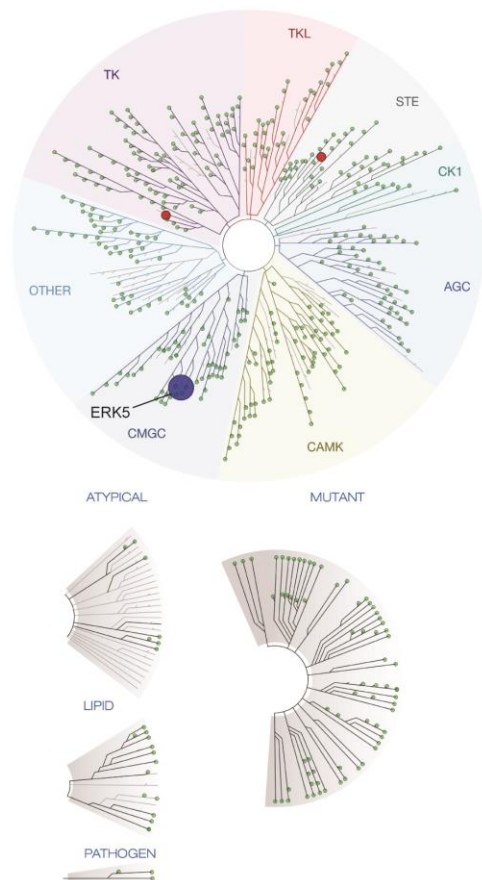
Figure 3-4. Structure and biochemical selectivity profile of INY-06-086. (A) Chemical structures of BAY-885 and INY-06-086. Differences are highlighted by blue asterisks or letters. (B) Tree*spot* visualization of the biochemical kinase profile of INY-06-086 at 1 µM. ERK5 is highlighted in blue, while other inhibited kinases are highlighted in red.

We next synthesized an ERK5 degrader with a six-hydrocarbon linker conjugating INY-06-086 to a VHL ligand to obtain INY-06-061 (**Figure 3-5A**). INY-06-061 retained comparable binding affinity for ERK5 (K_d = 12 nM) as BAY-885 (K_d = 1 nM), demonstrating that linker attachment at the terminal piperazine did not impede the ability of INY-06-061 to bind to ERK5 (**Table 3-1**). In addition, INY-06-061 displayed a similar selectivity profile to both the parental inhibitor INY-06-086 and the original ERK5 inhibitor BAY-885 (Nguyen *et al.*, 2019) across a panel of 468 kinases at 1 µM, with high selectivity for ERK5 (**Figure 3-5B**).
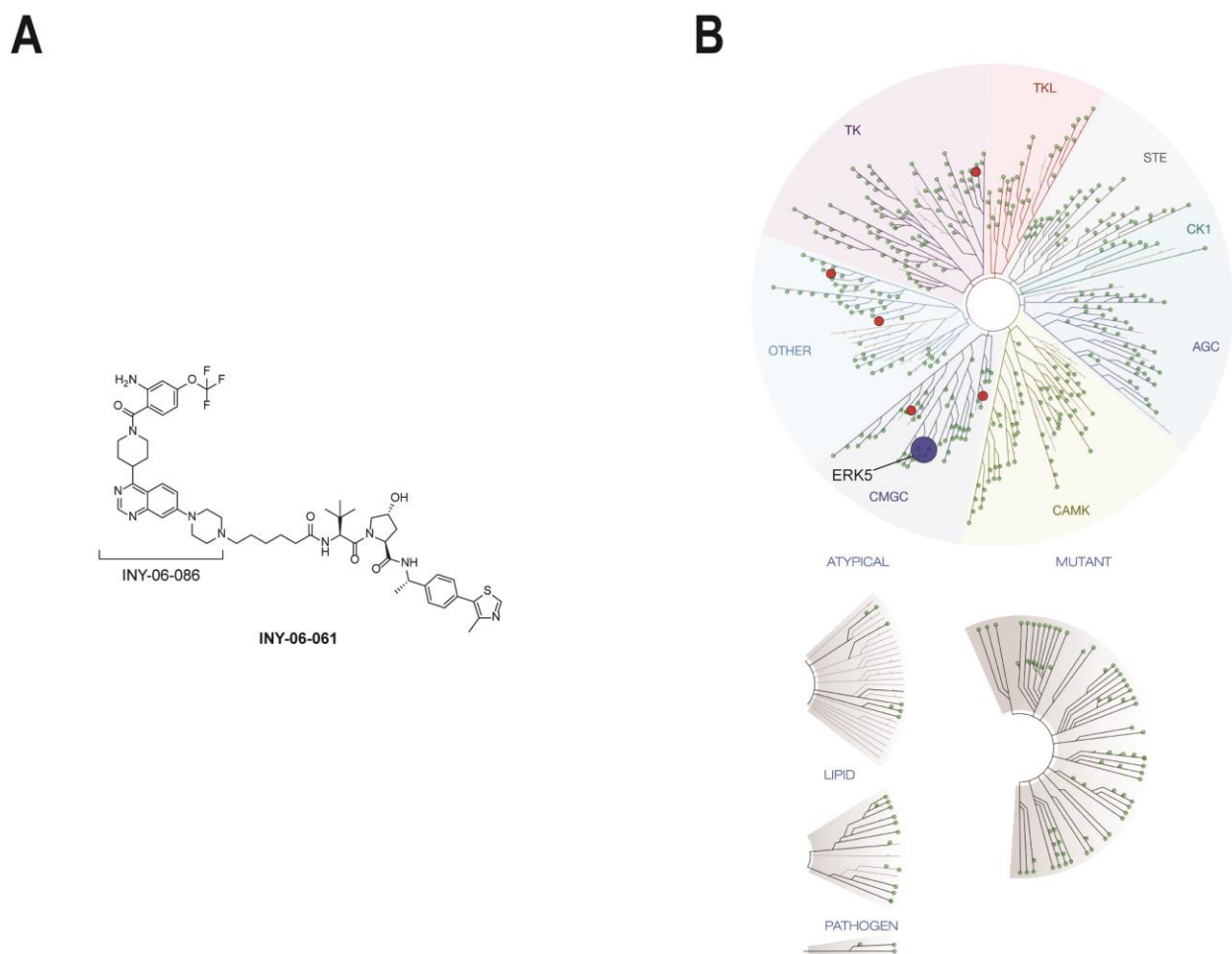
Figure 3-5. Structure and biochemical selectivity profile of INY-06-061. (A) Chemical structures of INY-06-061. (B) Tree*spot* visualization of the biochemical kinase profile of INY-06-061 at 1 µM. ERK5 is highlighted in blue, while other inhibited kinases are highlighted in red.

After verifying that INY-06-061 engaged ERK5 biochemically, we assessed the ability of the compound to destabilize ERK5 in MOLT4 cells. We found that INY-06-061 induced potent ERK5 degradation in a dose-dependent manner after 5-hour treatment in MOLT4 cells, with a DC_{50} value of 21 nM (**Figures 3-6A and 3-6B**). At concentrations of 5 µM or greater, we observed diminished ERK5 degradation consistent with the hook effect, in which independent engagement of INY-06-061 to ERK5 and VHL prevents ternary complex formation (**Figure 3-6A**). In contrast to INY-05-091 and INY-05-128, INY-06-061 did not destabilize BRD4 or AURKA (**Figure 3-6A**), which was further verified through MS-based global proteomics profiling analysis. Of the ~7,700 proteins quantified, ERK5 (MAPK7) was the only protein whose abundance was significantly downregulated in MOLT4 cells treated with 100 nM of INY-06-061 for 5 hours (**Figure 3-6C**), indicating that INY-06-061 is a potent and highly selective ERK5 degrader.
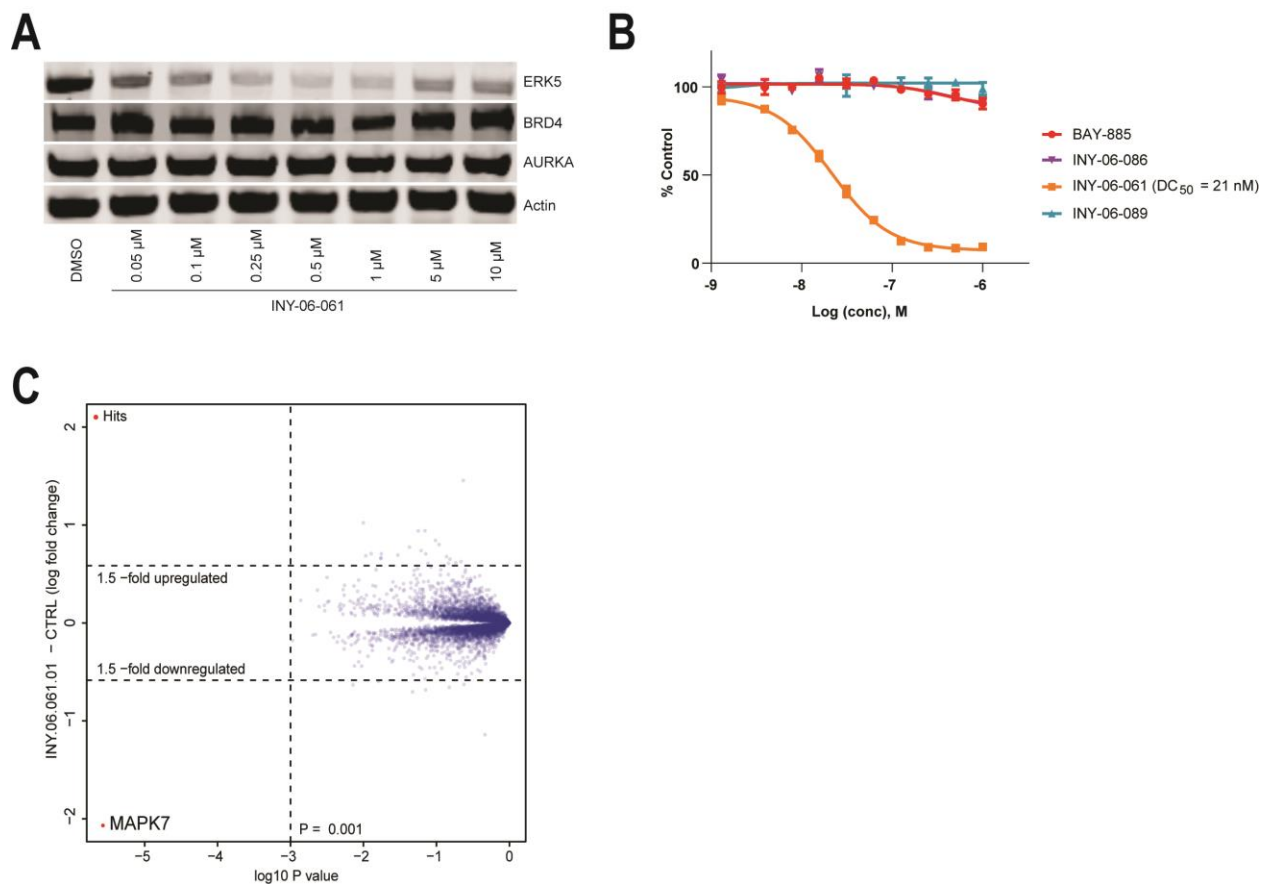
Figure 3-6. Characterization of INY-06-061. (A) Immunoblots of ERK5, BRD4, AURKA, and Actin in MOLT4 cells treated with INY-06-061 at indicated concentrations for 5 hours. Representative of 2 biological replicates. (B) DC_{50} values of INY-06-061. Normalized luminescence intensity of MOLT4 ERK5-HiBiT cells treated with indicated compounds and concentrations for 5 hours. Error bars represent standard deviation of three biological replicates. DC_{50} values were determined using Graphpad Prism nonlinear regression curve fit. (C) Quantitative proteomics showing relative abundance of proteins in MOLT4 cells treated for 5 hours with 100 nM of INY-06-061.

To verify the mechanism of action of INY-06-061, we pre-treated cells with either the proteasome inhibitor bortezomib or the NEDD8-activating enzyme E1 (NAE1) inhibitor MLN4924, which prevents activation of cullin-RING ligases such as $CRL2^{VHL}$. We found that this prevented ERK5 destabilization, demonstrating that INY-06-061-induced ERK5 degradation was dependent on the ubiquitin-proteasome system (**Figure 3-7A**). In addition, pre-treatment with excess quantities of BAY-885 to compete for ERK5 binding prevented INY-06-061-induced ERK5 degradation, demonstrating that engagement to ERK5 was required (**Figure 3-7A**). Finally,

we synthesized INY-06-089, a negative control analogue of INY-06-061 that incorporates a diastereoisomer of the VHL ligand with significantly compromised binding affinity for VHL (**Figure 3-7B**) (Raina *et al.*, 2016). INY-06-089 was unable to induce ERK5 downregulation at concentrations up to 5 µM, indicating that INY-06-061 acts in a proteasome- and VHL- dependent manner (**Figure 3-6B** and **3-7C**).
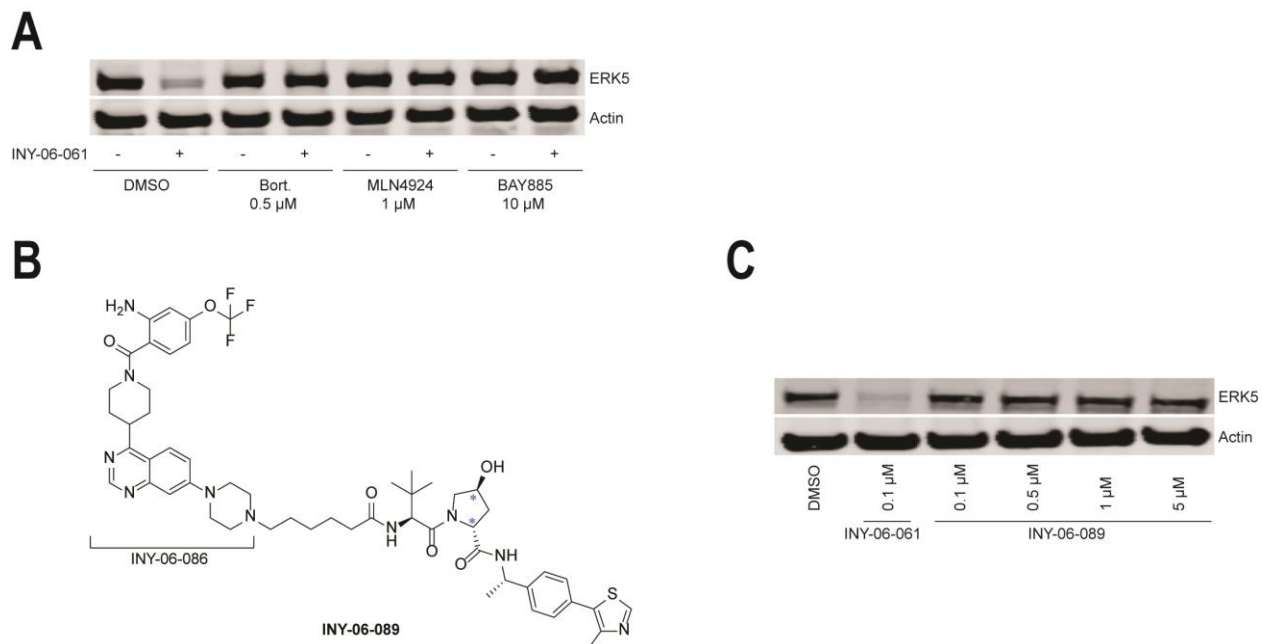
Figure 3-7. Mechanism of action of INY-06-061. (A) Immunoblots of ERK5 and Actin in MOLT4 cells pre-treated with bortezomib (0.5 µM), MLN-4924 (1 µM), and BAY-885 (10 µM) for 0.5 hours, followed by treatment with INY-06-061 (100 nM) for 5 hours. Representative of 2 biological replicates. (B) Structure of INY-06-089. Differences with INY-06-061 are highlighted by blue asterisks. (C) Immunoblots of ERK5 and Actin in MOLT4 cells treated with INY-06-061 or INY-06-089 at indicated concentrations for 5 hours. Representative of 2 biological replicates.

Pharmacological downregulation of ERK5 does not display anti-proliferative effects in various cancer models

Next, using the chemical tools developed here, as well as previously published ERK5 inhibitors, we explored the pharmacological consequences of ERK5 inhibition and degradation on cell proliferation in various cellular cancer models. In cell lines reported to have constitutively active ERK5 signaling (BT-474) (Esparís-Ogando et al., 2002) or genomic amplification of ERK5 (SNU-449) (Zen *et al.*, 2009), INY-06-061 did not induce degradation-dependent anti-proliferative effects (**Figures 3-8A** and **3-8B**). Specifically, in both BT-474 and SNU-449 cells, the EC_{50} values of INY-06-061 and the negative control analogue INY-06-089 were over 20 µM, similar to that of the parental ligand INY-06-086 and the reported ERK5 inhibitors AX15836 and BAY-885 (**Figures 3-8A** and **3-8B**). As expected from its BRD4 inhibitory activity, XMD17-109 was the only compound to display anti-proliferative effects in both cell lines.
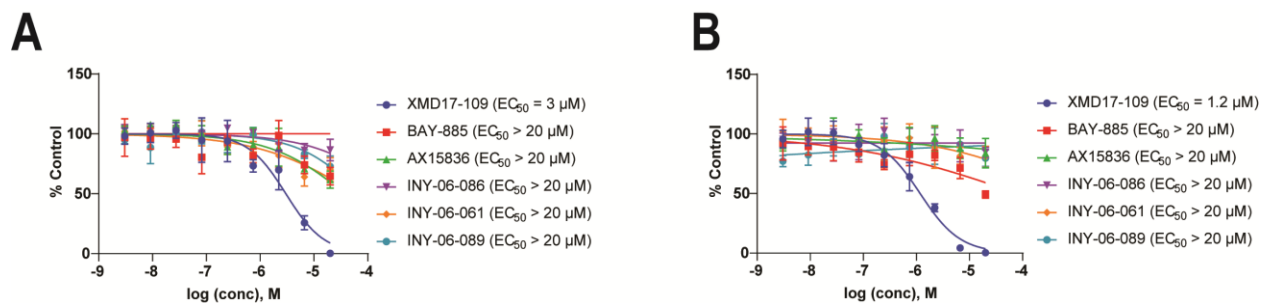
Figure 3-8. Anti-proliferative effects of ERK5 inhibition or degradation in various cancer models. Anti-proliferative effects in (A) BT-474 and (B) SNU-449 after 3d treatment with indicated compounds and concentrations. Error bars represent standard deviation of three biological replicates.

To broadly profile the anti-proliferative activity of INY-06-061, we submitted INY-06-061 to the PRISM platform (Broad Institute) to evaluate its anti-proliferative activity in a panel of 750 cell lines. Consistent with Dependency Map (DepMap) data (Meyers et al., 2017) which indicates a lack of dependency on ERK5 expression for cell growth, there were no cell lines identified to be sensitive to INY-06-061 treatment, with all IC_{50} values observed to be above 1 µM.

As the PRISM screen was carried out in cells at basal conditions, we next investigated the effects of ERK5 degradation on cell proliferation of stimulated cells. Previous studies have reported that IL-6 activates ERK5 in multiple myeloma MM.1S cells and that overexpressing a dominant negative form of ERK5 inhibits IL-6 induced cell proliferation (Carvajal-Vergara et al., 2005). Therefore, we compared the proliferation of IL-6 stimulated MM.1S cells in the presence of various ERK5 modulators at 500 nM and 1 µM. At basal conditions, INY-06-061 did not induce potent anti-proliferative effects, with an EC_{50} of 6 µM (**Figure 3-9A**). Treatment of MM.1S cells with IL-6 promoted proliferation as expected, but treatment with INY-06-061 or the selective ERK5 inhibitors AX15836 and BAY-885 had no effect on IL-6-induced proliferation at both 500 nM and 1 µM. In contrast, the dual BRD4/ERK5 inhibitor XMD17-109 showed significant inhibition of IL-6-induced MM.1S cell proliferation (**Figures 3-9B** and **3-9C**). Thus, our study demonstrates that acute pharmacological degradation of ERK5 has no anti-proliferative effects in multiple cancer cell lines previously reported to be regulated by ERK5.
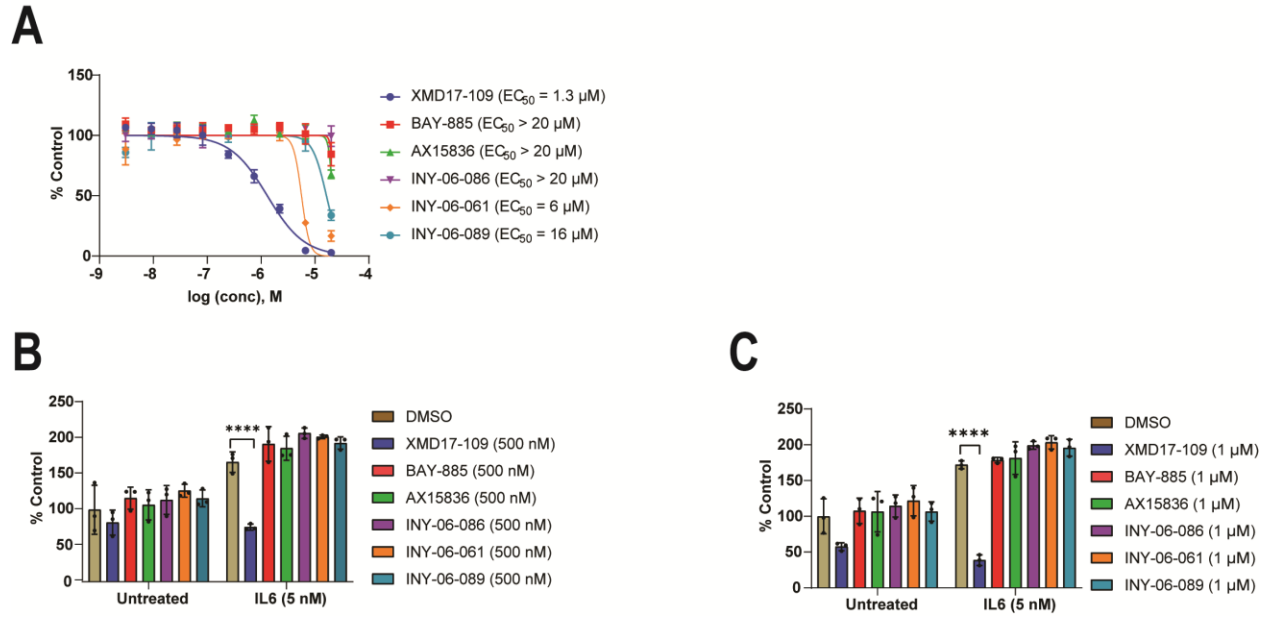
Figure 3-9. Anti-proliferative effects of ERK5 inhibition or degradation in MM.1S cells. (A)Anti-proliferative effects in MM.1S cells after 3d treatment with indicated compounds and concentrations. Error bars represent standard deviation of three biological replicates. MM.1S cells were pre-treated with (B) 500 nM or (C) 1 µM of indicated compounds, followed by addition of 5 nM recombinant human IL-6. Anti-proliferative effects were assessed after 3d treatment. Error bars represent standard deviation of three biological replicates. Significance was assessed by two-way ANOVA with Bonferroni's correction for multiple comparisons (**** indicates $p \leq 0.0001$).

INY-06-061-induced ERK5 degradation does not reduce pro-inflammatory cytokine secretion in human endothelial cells

Previous studies have reported that ERK5 mediates pro-inflammatory responses in endothelial cells (ECs) upon inflammatory stimulation (Wilhelmsen *et al.*, 2015). While selective ERK5 inhibitors failed to suppress IL-6 and IL-8 secretion in human umbilical vein endothelial cells (HUVECs) upon inflammatory stimulation, siRNA-mediated knockdown of ERK5 was reported to significantly reduce the secretion of IL-6 and IL-8 (Lin *et al.*, 2016). This contrasting phenotype between small molecule-mediated inhibition of ERK5 kinase activity and siRNA-mediated knockdown of ERK5 suggested that non-catalytic functions of ERK5 may regulate inflammatory responses in ECs.

To determine whether ERK5 degradation could recapitulate the reported effects of ERK5 knockdown on EC inflammation, we first assessed the ability of INY-06-061 to degrade ERK5 in HUVECs. 5-hour treatment with 1 µM of INY-06-061 revealed potent downregulation of ERK5, suggesting that 5-hour pre-treatment before inflammatory stimulation would be sufficient to significantly reduce ERK5 protein levels (**Figure 3-10A**). We next pre-treated HUVECs with reported ERK5 inhibitors (XMD8-92, XMD17-109, BAY-885) and the bivalent degrader INY-06-061 for 5 hours. In addition to the negative control analogue INY-06-089, we also pre-treated with a combination of BAY-885 and JQ1 to mimic the pharmacology of XMD8-92 and XMD17-109. After 5-hour pre-treatment, the cells were stimulated with lipopolysaccharide (LPS), a Toll-like receptor 4 (TLR4) agonist, after which the culture supernatants were subjected to immunoassays to measure secreted IL-6 and IL-8 levels. As expected, pre-treatment with the non-selective ERK5 inhibitors XMD8-92 and XMD17-109 (Wilhelmsen *et al.*, 2015), as well as the combination of BAY-885 and JQ1 led to reduced IL-6 and IL-8 secretion upon LPS stimulation, while BAY-885

and the negative control analogue INY-06-089 had no effect (**Figures 3-10B** and **3-10C**). Notably, pre-treatment with INY-06-061 also did not significantly suppress IL-6 and IL-8 secretion upon LPS stimulation (**Figures 3-10B** and **3-10C**), in contrast to the reported genetic knockdown studies (Lin *et al.*, 2016; Wilhelmsen *et al.*, 2015).

To determine whether extended ERK5 degradation could better recapitulate previously reported phenotypes, we also pre-treated HUVECs with the same set of compounds for 24 hours before stimulating with LPS. While INY-06-061-induced ERK5 degradation was maintained for 24 hours (**Figure 3-10D**), the longer pre-treatment did not affect IL-6 and IL-8 secretion levels. Consistent with the 5-hour pre-treatment, only XMD8-92, XMD17-109 and the combination of BAY-885 and JQ1 significantly reduced IL-6 and IL-8 secretion, while BAY-885 and INY-06-061 had no effect (**Figures 3-10E** and **3-10F**). Therefore, our study indicates that INY-06-061-induced ERK5 destabilization does not suppress IL-6 and IL-8 secretion upon inflammatory stimulation.
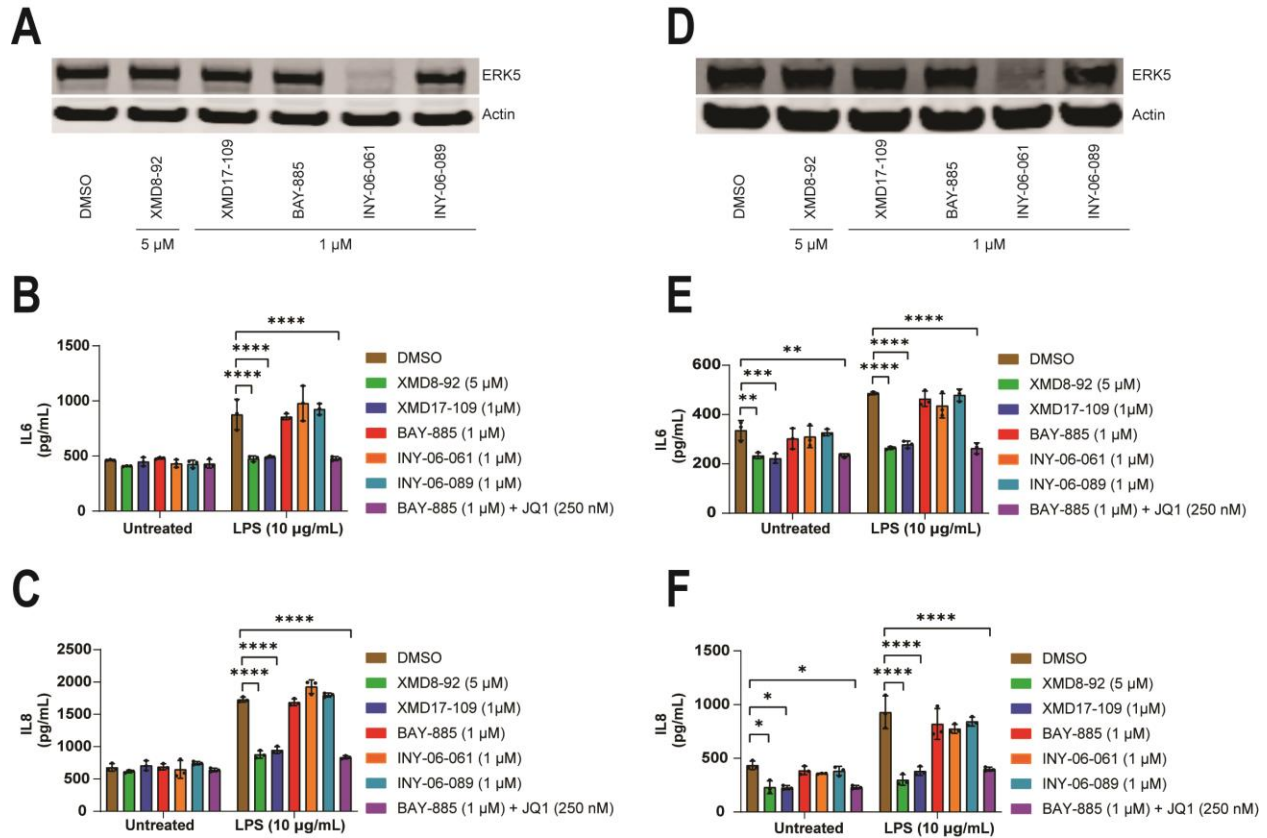
Figure 3-10. INY-06-061-induced ERK5 degradation does not reduce pro-inflammatory cytokine secretion in human endothelial cells. (A) Immunoblots of ERK5 and Actin from HUVECs treated with indicated compounds and concentrations for 5 hours. Representative of 2 biological replicates (B) IL-6 and (C) IL-8 secretion levels were quantified in HUVECs pre-treated with indicated compounds and concentrations for 5 hours, followed by LPS stimulation (10 µg/mL) for 6 hours. Significance was assessed by two-way ANOVA with Bonferroni's correction for multiple comparisons (**** indicates p < 0.0001). (D) Immunoblots of ERK5 and Actin from HUVECs treated with the indicated compounds and concentrations for 24 hours. Representative of 2 biological replicates. (E) IL-6 and (F) IL-8 secretion levels were quantified in HUVECs pre-treated with indicated compounds and concentrations for 24 hours, followed by LPS stimulation (10 µg/mL) for 6 hours. Significance was assessed by two-way ANOVA with Bonferroni's correction for multiple comparisons (* indicates $p \leq 0.05$; ** indicates $p \leq 0.01$; *** indicates $p \leq 0.001$; **** indicates $p \leq 0.0001$).

Discussion

Recent identification of ERK5 as a potential therapeutic target in cancer and inflammation prompted medicinal chemistry campaigns that resulted in the development of selective ERK5 inhibitors such as AX15836 and BAY-885 (Lin *et al.*, 2016; Nguyen *et al.*, 2019). However, these inhibitors were not able to recapitulate phenotypes observed through genetic modulation of ERK5 abundance or activity, such as siRNA knockdown or overexpression of a kinase dead ERK5 mutant (Lin *et al.*, 2016). While explanations such as potential kinase-independent functions of ERK5 or paradoxical activation of ERK5-regulated transcription by ERK5 inhibitors (Lochhead *et al.*, 2020) have been proposed, no chemical probes have been available to interrogate the discrepancies observed between ERK5 inhibition and genetic depletion or inactivation.

To develop chemical tools for acute, pharmacological destabilization of ERK5, we initially characterized the non-selective ERK5 degraders INY-05-091 and INY-05-128, which incorporated XMD17-109 and JWG-071 as parental ligands, respectively (Wang *et al.*, 2018). Consistent with previous reports, we re-confirmed engagement of the BET family of proteins by XMD17-109, as INY-05-091 induced potent off-target degradation of BRD4. On the other hand, INY-05-128, based on the more selective inhibitor JWG-071, did not affect protein levels of the BET family of proteins. However, further characterization of JWG-071 and INY-05-128 not only revealed different anti-proliferative effects compared to selective ERK5 inhibitors, but global proteomics analysis also revealed potent AURKA downregulation by INY-05-128. Thus, phenotypes observed by JWG-071 and INY-05-128 may be caused by off-target inhibition of AURKA signaling, which highlights the importance of identifying off-target activities of small molecules.

Further medicinal chemistry efforts led to the characterization of INY-06-061, which induced potent and highly selective destabilization of ERK5 protein levels. As treatment with INY-06-061 leads to rapid pharmacological depletion of ERK5 protein, any potential scaffolding and transcriptional functions of ERK5 should be eliminated. However, INY-06-061-induced ERK5 degradation did not recapitulate the anti-proliferative or anti-inflammatory phenotypes reported through genetic ablation of ERK5. As many of the reported studies above investigated the role of ERK5 through genetic knockdown methods with RNA interference (RNAi), the phenotypes observed may have resulted from non-specific or off-target effects of RNAi (Birmingham et al., 2006; Jackson et al., 2006). In addition, as INY-06-061 is unlikely to induce 100% degradation of the available ERK5 protein pool, residual levels of ERK5 may still be sufficient to mediate ERK5 signaling. Thus, our study suggests that non-catalytic functions of ERK5 and paradoxical activation of ERK5 transcription through ERK5 inhibition may not account for the phenotypic differences observed between ERK5 inhibition and genetic ablation, at least in the *in vitro* and *ex vivo* settings studied here. However, further investigation is required to more fully understand the biological roles of ERK5.

In addition to its effects on cellular proliferation and inflammation, genetic approaches have identified roles of ERK5 in additional biological processes, including lipid metabolism (Cristea et al., 2020) and senescence of melanoma cells (Tubita et al., 2022). Therefore, INY-06-061 will be a useful chemical probe to further validate reported phenotypes of ERK5 identified through genetic means. Furthermore, ERK5 has been reported to be a crucial regulator of the activity of myeloid cells within the tumor microenvironment (Giurisato *et al.*, 2018), metastasis (Hoang et al., 2021) and angiogenesis (Pi et al., 2005), suggesting that further investigations,

especially *in vivo*, will be required to fully understand the pharmacological consequences of ERK5 degradation.

Conclusion

ERK5 function has been investigated through a wide variety of methods, including inhibition by small molecules, depletion via RNA interference and genetic knockout. As discrepancies between genetic knockdown and inhibition of ERK5 have been reported, small molecule approaches to interrogate the differences between loss of ERK5 protein and inhibition of its kinase activity are necessary. Here, we develop and characterize INY-06-061, a potent and highly selective small molecule degrader of ERK5. While our studies indicate that INY-06-061-induced ERK5 destabilization does not have potent anti-proliferative or anti-inflammatory effects in multiple cancer cell lines or HUVECs, respectively, further studies are necessary to understand the biological roles ERK5. Thus, INY-06-061 will be a valuable chemical probe to not only study the pharmacological effects of ERK5 degradation, but also to investigate the differences in phenotypes induced by ERK5 inhibition and genetic depletion.

Materials and methods

Cell lines. MOLT4 (Male, CVCL_0013), BT-474 (Female, CVCL_A4CL), SNU-449 (Male, CVCL_0454) and MM.1S (Female, CVCL_8792) cells were cultured in RPMI (Gibco) supplemented with 10% heat inactivated fetal bovine serum and 100 U/mL Penicillin-Streptomycin (Gibco) at 37 °C in the presence of 5% CO_2.

Primary Cells. Primary Umbilical Vein Endothelial Cells; Normal, Human, Pooled (HUVECs from ATCC) were grown in vascular cell basal medium (ATCC) supplemented with endothelial cell growth kit-VEGF (ATCC) and 100U/mL Penicillin-Streptomycin (Gibco) at 37 °C in the presence of 5% CO_2.

Immunoblotting. Cells were lysed in M-PER buffer (Thermo Scientific) containing protease and phosphatase inhibitor cocktail (Roche). Lysate concentrations were measured and normalized using a BCA assay (Pierce). Equal amounts of lysates were loaded onto 4-12% Bis-Tris gels (Invitrogen), transferred to nitrocellulose membranes (BioRad), and blocked with Intercept blocking buffer (LI-COR). Membranes were then incubated with primary antibodies against ERK5 (Cell Signaling Technology, #3372S), AURKA (Cell Signaling Technology #14475S), BRD4 (Fortis Life Sciences, # A301-985A-M), and Actin (Cell Signaling Technology, #3700S) overnight at 4 °C, followed by incubation with IRDye®800-labeled goat anti-rabbit IgG and IRDye®680-labeled goat anti-mouse IgG (LI-COR) secondary antibodies for detection on an Odyssey CL_x System.

***In vitro* kinase assays.** Biochemical binding constants (K_d) of compounds to ERK5 was determined through the *Kd*ELECT assays provided by Eurofins Discovery using an 11-point dose response curve.

Biochemical selectivity assay. Biochemical selectivity across 468 kinases was measured through the *scan*MAX kinase assay panel provided through Eurofins Discovery.

Proliferation assays. Cell lines were plated at densities ranging from 500 to 1000 cells per well in 384-well plates. Cells were treated at the indicated concentrations for 72 hours, after which anti-proliferative effects of compounds were assessed using CellTiter-Glo (Promega). EC_{50} values were calculated using the GraphPad Prism nonlinear regression curve fit.

For MM.1S cells stimulated with IL-6, cells were treated in 96 well plates at 10,000 cells per well. Cells were pre-treated with compounds at indicated concentrations for 5 hours before adding recombinant human IL-6 (Biolegend) at 5 nM. After 72 hours, the anti-proliferative effects were assessed using CellTiter-Glo (Promega).

IL-6 and IL-8 ELISA. HUVECs were plated at cell densities ranging from 30,000 to 60,000 cells per well in 96 well plates. The cells were pre-treated with indicated compounds for 5 or 24 hours, after which the cells were stimulated with LPS (Sigma-Aldrich) at 10 µg/mL for 6 hours. IL-6 and IL-8 levels in the supernatant were measured using LEGEND MAX^{TM} Human IL-6 (Biolegend, #430507) and Human IL-8 (Biolegend, #431507) ELISA kits, following the manufacturer's protocols. The data was analyzed with GraphPad Prism.

Generation of ERK5 HiBiT cell lines. Introduction of a HiBiT tag into the endogenous ERK5 locus in Molt4 cells was performed via CRISPR-Cas9 editing. ALT-R CRISPR RNA (crRNA) and trans-activating CRISPR RNA (tracrRNA) (Integrated DNA Technologies, IDT) were resuspended in nuclease-free duplex buffer at a final concentration of 100 µM. Equal volumes of crRNA and tracrRNA were mixed and heated for 5 min at 95 °C. After heating, the complex was gradually cooled to room temperature. The oligo complex was then incubated at room temperature for 20 min with Cas9 Nuclease V3 (IDT) to form the ribonucleoprotein complex. Subsequently, the double-stranded DNA HDR template, which incorporated the HiBiT sequence into the C-terminus of the ERK5 genome, the RNP complex, and an electroporation enhancer (IDT) were co-electroporated into Molt4 cells using the Neon Electroporator (Thermo Fisher). Cells were seeded into media with HDR enhancer (IDT). Subsequently, single cells were isolated via FACS sorting, and HiBiT expression from individual clones was detected using the Nano-Glo® HiBiT Lytic Detection System (Promega). Correct insertion of the HiBiT tag in the genome of the knocked-in cells was confirmed by sequencing.

TMT LC-MS3 mass spectrometry. MOLT4 cells were treated with DMSO (biological triplicate) or INY-06-061 (100 nM), INY-05-091 (250 nM) or INY-05-128-01 (250 nM) degrader for 5 h and cells were harvested by centrifugation. Cell lysis and Tandem Mass Tagged (TMT) tryptic peptides were prepared for LC-MS analysis following procedures published (Donovan *et al.*, 2018). Data were collected using an Orbitrap Fusion Lumos mass spectrometer (Thermo Fisher Scientific, San Jose, CA, USA) coupled with a Proxeon EASY-nLC 1200 LC pump (Thermo Fisher Scientific). Peptides were separated on a 50 cm 75 µm inner diameter EasySpray ES903

microcapillary column (Thermo Fisher Scientific). Peptides were separated using a 190 min gradient of 6 - 27% acetonitrile in 1.0% formic acid with a flow rate of 300 nL/min.

Each analysis used a MS3-based TMT method as described previously (McAlister et al., 2014). The data were acquired using a mass range of m/z 340 – 1350, resolution 120,000, AGC target 5 $\times$ 105, maximum injection time 100 ms, dynamic exclusion of 120 s for the peptide measurements in the Orbitrap. Data dependent MS2 spectra were acquired in the ion trap with a normalized collision energy (NCE) set at 35%, AGC target set to 1.8×104 and a maximum injection time of 120 ms. MS3 scans were acquired in the Orbitrap with HCD collision energy set to 55%, AGC target set to 2×105, maximum injection time of 150 ms, resolution at 50,000 and with a maximum synchronous precursor selection (SPS) precursor set to 10.

Proteome Discoverer 2.4 (Thermo Fisher Scientific) was used for .RAW file processing and controlling peptide and protein level false discovery rates, assembling proteins from peptides, and protein quantification from peptides. MS/MS spectra were searched against a Swissprot human database (February 2020) with both the forward and reverse sequences as well as known contaminants such as human keratins. Database search criteria were as follows: tryptic with two missed cleavages, a precursor mass tolerance of 20 ppm, fragment ion mass tolerance of 0.6 Da, static alkylation of cysteine (57.0215 Da), static TMT labeling of lysine residues and N-termini of peptides (304.2071 Da), and variable oxidation of methionine (15.9949 Da). TMT reporter ion intensities were measured using a 0.003 Da window around the theoretical m/z for each reporter ion in the MS3 scan. The peptide spectral matches with poor quality MS3 spectra were excluded from quantitation (summed signal-to-noise across channels < 100 and precursor isolation specificity < 0.5), and the resulting data was filtered to only include proteins with a minimum of 2 unique peptides quantified. Reporter ion intensities were normalized and scaled using in-house

scripts in the R framework (Team, 2014).Statistical analysis was carried out using the limma

package within the R framework (Ritchie *et al.*, 2015).

Chemistry Synthetic Scheme

Scheme 1

1a: R = cyclopentyl
1b: R = sec-butyl

2a: R = cyclopentyl
2b: R = sec-butyl

DCM:TFA (4:1)
3 h

3a: R = cyclopentyl
3b: R = sec-butyl

HATU, DIEA,
DMF, 1 h

INY-05-091: R = cyclopentyl
INY-05-128: R = sec-butyl

Scheme 2

4

Pd(OAc)$_2$, BINAP,
Cs$_2$CO$_3$, toluene,
100 °C, o/n

5

DCM:TFA (3:1)
1 h

6

HATU, DIEA,
DMF, 1 h

INY-06-086

Scheme 3

4

Pd(OAc)$_2$, BINAP,
Cs$_2$CO$_3$, toluene,
100 °C, o/n

7

DCM:TFA (3:1)
1 h

8

1. HATU, DIEA,
DMF, 1 h
2. Pd/C, H$_2$ (g),
MeOH, 4 h

9

1. K$_2$CO$_3$, MeCN
80 °C, o/n
2. DCM:TFA (3:1)
4 h

10

HATU, DIEA,
DMF, 1 h

INY-06-061

General Chemistry Methods. Reagents and solvents were purchased from commercial vendors and used without further purification otherwise noted. Reactions were monitored using a Waters Acquity UPLC/MS system (Waters PDA eλ Detector, QDa Detector, Sample manager - FL, Binary Solvent Manager) using Acquity UPLC® BEH C18 column (2.1 x 50 mm, 1.7 μm particle size): solvent gradient = 85% A at 0 min, 1% A at 1.7 min; solvent A = 0.1% formic acid in Water; solvent B = 0.1% formic acid in Acetonitrile; flow rate: 0.6 mL/min. Products were purified by CombiFlash®Rf with Teledyne Isco RediSep® normal-phase silica flash columns (4 g, 12 g, 24 g, 40 g) and preparative HPLC using Waters SunFireTM Prep C18 column (19 x 100 mm, 5 μm particle size) using a gradient of 0-100% methanol in water containing 0.05% trifluoroacetic acid (TFA) over 48 minutes at a flow of 40 mL/min. ^{1}H NMR spectra were recorded on 500 MHz Bruker Avance III spectrometer, and chemical shifts are reported in million (ppm, δ) downfield from tetramethylsilane (TMS). Coupling constants (J) are reported in Hz. Spin multiplicities are described as s (singlet), br (broad singlet), d (doublet), t (triplet), q (quartet) and m (multiplet). Purities of assayed compounds were in all cases greater than 95%, as determined by reverse-phase HPLC analysis.

Synthesis of INY-05-091 and INY-05-128

tert-butyl-6-(4-(4-((11-cyclopentyl-5-methyl-6-oxo-6,11-dihydro-5H-benzo[e]pyrimido[5,4-b][1,4]diazepin-2-yl)amino)benzoyl)piperazin-1-yl)hexanoate (2a)

To **1a** (20 mg, 0.033 mmol) dissolved in MeCN (1 mL) was added potassium carbonate (18 mg, 0.132 mmol) and tert-butyl 6-bromohexanoate (12 mg, 0.049 mmol), which was stirred at 80 °C overnight. Next day, the reaction mixture was diluted with ethyl acetate (15 mL) and washed with brine (4 x 5mL). The organic layer was dried over anhydrous sodium sulfate, filtered, and

concentrated *in vacuo*. The crude material was purified by column chromatography on silica gel (0-20% MeOH/DCM) to afford **2a** (18 mg, 82% yield). LC-MS: m/z 668.51 [M+H]$^+$.

6-(4-(4-((11-cyclopentyl-5-methyl-6-oxo-6,11-dihydro-5H-benzo[e]pyrimido[5,4-b][1,4]diazepin-2-yl)amino)benzoyl)piperazin-1-yl)hexanoic acid (3a)

To **2a** (18 mg, 0.027 mmol) was added 800 µL of DCM and 200 µL of TFA. The reaction was stirred for 4 hours at room temperature. The reaction mixture was concentrated *in vacuo* to afford crude **3a** (quantitative yield), which was used directly for the next reaction. LC-MS: m/z 612.49 [M+H]$^+$.

(2S,4R)-1-((S)-2-(6-(4-(4-((11-cyclopentyl-5-methyl-6-oxo-6,11-dihydro-5H-benzo[e]pyrimido[5,4-b][1,4]diazepin-2-yl)amino)benzoyl)piperazin-1-yl)hexanamido)-3,3-dimethylbutanoyl)-4-hydroxy-N-((S)-1-(4-(4-methylthiazol-5-yl)phenyl)ethyl)pyrrolidine-2-carboxamide (INY-05-091)

To a solution of **3a** (17 mg, 0.027 mmol) and (2S,4R)-1-((S)-2-amino-3,3-dimethylbutanoyl)-4-hydroxy-N-((S)-1-(4-(4-methylthiazol-5-yl)phenyl)ethyl)pyrrolidine-2-carboxamide (13 mg, 0.027 mmol) in DMF (1 mL) was added HATU (10 mg, 0.027 mmol) and DIEA (28 µL, 0.16 mmol). The reaction was stirred for 1 hour. The reaction mixture was purified by reverse-phase HPLC (30-90% methanol in water) to obtain **INY-05-091** as a TFA salt (10 mg, 29% yield). LC-MS: m/z 1038.62 [M+H]$^+$. ^{1}H NMR (500 MHz, DMSO) δ 9.95 (s, 1H), 9.83 (s, 1H), 9.00 (s, 1H), 8.49 (s, 1H), 8.36 (d, J = 7.8 Hz, 1H), 7.90 – 7.78 (m, 3H), 7.59 (dd, J = 7.8, 1.7 Hz, 1H), 7.50 – 7.37 (m, 6H), 7.36 – 7.27 (m, 1H), 7.18 (td, J = 7.5, 1.0 Hz, 1H), 4.96 – 4.87 (m, 1H), 4.73 (p, J = 6.4 Hz, 1H), 4.54 (d, J = 9.4 Hz, 1H), 4.42 (t, J = 8.1 Hz, 1H), 4.32 – 4.27 (m, 1H), 3.66 – 3.56 (m,

2H), 3.56 – 3.48 (m, 2H), 3.45 (s, 3H), 3.09 (s, 4H), 2.46 (s, 3H), 2.39 – 2.25 (m, 2H), 2.20 – 2.09 (m, 2H), 2.06 – 1.99 (m, 1H), 1.84 – 1.78 (m, 1H), 1.74 – 1.40 (m, 11H), 1.38 (d, J = 7.0 Hz, 3H), 1.34 – 1.20 (m, 4H), 0.94 (s, 9H).

(2S,4R)-1-((2S)-2-(6-(4-(4-((11-(sec-butyl)-5-methyl-6-oxo-6,11-dihydro-5H-benzo[e]pyrimido[5,4-b][1,4]diazepin-2-yl)amino)benzoyl)piperazin-1-yl)hexanamido)-3,3-dimethylbutanoyl)-4-hydroxy-N-((S)-1-(4-(4-methylthiazol-5-yl)phenyl)ethyl)pyrrolidine-2-carboxamide (INY-05-128)

INY-05-128 was synthesized with similar procedure as **INY-05-091** using intermediate **1b** as the starting material (15 mg, 20% yield). LC-MS: m/z 1026.74 [M+H]$^+$. ^{1}H NMR (500 MHz, DMSO) δ 9.90 (d, J = 35.8 Hz, 1H), 9.77 (s, 1H), 9.00 (s, 1H), 8.50 (d, J = 5.1 Hz, 1H), 8.36 (d, J = 7.8 Hz, 1H), 7.84 – 7.81 (m, 2H), 7.60 (t, J = 7.3 Hz, 1H), 7.49 – 7.47 (m, 1H), 7.45 – 7.43 (m, 3H), 7.40 – 7.37 (m, 2H), 7.33 – 7.27 (m, 1H), 7.19 (q, J = 6.9 Hz, 1H), 4.92 (p, J = 7.2 Hz, 1H), 4.54 (d, J = 9.3 Hz, 1H), 4.42 (t, J = 8.1 Hz, 1H), 4.34 – 4.27 (m, 2H), 4.19 – 4.14 (m, 1H), 3.66 – 3.58 (m, 2H), 3.56 – 3.48 (m, 2H), 3.44 (s, 3H),f 3.10 (s, 5H), 2.46 (s, 3H), 2.33 – 2.26 (m, 1H), 2.20 – 2.13 (m, 1H), 2.05 – 2.00 (m, 1H), 1.87 – 1.77 (m, 3H), 1.70 – 1.60 (m, 3H), 1.60 – 1.45 (m, 5H), 1.39 – 1.35 (m, 4H), 1.32 – 1.24 (m, 3H), 0.94 (s, 9H), 0.84 (t, J = 7.4 Hz, 3H).

Synthesis of INY-06-086

tert-butyl 4-(7-(4-methylpiperazin-1-yl)quinazolin-4-yl)piperidine-1-carboxylate (5)

To a solution of intermediate **4** (100 mg, 0.29 mmol) and 1-methylpiperazine (43 mg, 0.43 mmol) in toluene (3 mL) was added Pd(OAc)$_2$ (7 mg, 0.03 mmol), BINAP (36 mg, 0.06 mmol) and cesium carbonate (284 mg, 0.87 mmol). The reaction mixture was purged with nitrogen, and stirred

overnight at 100 °C. The next day, the reaction mixture was diluted with DCM (20 mL) and filtered through celite. The organic layer was washed with sat. aq sodium bicarbonate (20 mL) and extracted with DCM (2 x 10 mL). The organic layers were combined, dried over anhydrous sodium sulfate, filtered, and concentrated *in vacuo*. The crude material was purified by column chromatography on silica gel (0-30% MeOH/DCM) to obtain intermediate **5** (115 mg, 97% yield). LC-MS: m/z 412.3 [M+H]$^+$.

7-(4-methylpiperazin-1-yl)-4-(piperidin-4-yl)quinazoline (6)

To intermediate **5** (115 mg, 0.28 mmol) was added DCM (1.5 mL) and TFA (0.5 mL). The reaction was stirred at room temperature for 1 hour. The reaction mixture was concentrated *in vacuo* to obtain crude **6** (quantitative yield), which was used directly for the next reaction. LC-MS: m/z 312.25 [M+H]$^+$.

(2-amino-4-(trifluoromethoxy)phenyl)(4-(7-(4-methylpiperazin-1-yl)quinazolin-4-yl)piperidin-1-yl)methanone (INY-06-086)

To a solution of intermediate **6** (87 mg, 0.28 mmol) and 2-amino-4-(trifluoromethoxy)benzoic acid (62 mg, 0.28 mmol) in DMF (2 mL) was added HATU (106 mg, 0.28 mmol) and DIEA (490 µL, 2.8 mmol). The reaction was stirred at room temperature for 1 hour, then purified by reverse-phase HPLC (15-75% methanol in water) to obtain **INY-06-086** (29 mg, 14% yield). LC-MS: m/z 515.27 [M+H]$^+$. ^{1}H NMR (500 MHz, DMSO) δ 9.96 (s, 1H), 9.03 (s, 1H), 8.33 (d, J = 9.5 Hz, 1H), 7.60 (dd, J = 9.5, 2.7 Hz, 1H), 7.28 (d, J = 2.6 Hz, 1H), 7.14 (d, J = 8.3 Hz, 1H), 6.70 – 6.65 (m, 1H), 6.54 – 6.48 (m, 1H), 4.28 (d, J = 13.1 Hz, 2H), 3.98 – 3.88 (m, 1H), 3.57 (d, J = 11.3 Hz, 2H), 3.31 – 3.12 (m, 6H), 2.88 (s, 3H), 1.94 – 1.73 (m, 4H), 1.32 – 1.21 (m, 1H).

Synthesis of INY-06-061

benzyl 4-(4-(1-(tert-butoxycarbonyl)piperidin-4-yl)quinazolin-7-yl)piperazine-1-carboxylate (7)

To a solution of intermediate **4** (389 mg, 1.12 mmol) and benzyl piperazine-1-carboxylate (370 mg, 1.68 mmol) in toluene (12 mL) was added Pd(OAc)$_2$ (25 mg, 0.11 mmol), BINAP (140 mg, 0.22 mmol) and cesium carbonate (1.1 g, 3.36 mmol). The reaction mixture was purged with nitrogen, and stirred overnight at 100 °C. The next day, the reaction mixture was diluted with DCM (30 mL) and filtered through celite. The organic layer was washed with sat. aq sodium bicarbonate (30 mL) and extracted with DCM (2 x 20 mL). The organic layers were combined, dried over anhydrous sodium sulfate, filtered, and concentrated *in vacuo*. The crude material was purified by column chromatography on silica gel (0-100% EA/DCM) to obtain **7** (507 mg, 85% yield). LC-MS: m/z 532.35 [M+H]$^+$.

benzyl 4-(4-(1-(tert-butoxycarbonyl)piperidin-4-yl)quinazolin-7-yl)piperazine-1-carboxylate (8)

To **7** (507 mg, 0.95 mmol) was added DCM (6 mL) and TFA (2 mL). The reaction was stirred at room temperature for 1 hour and concentrated *in vacuo* to obtain crude **8** (quantitative yield). LC-MS: m/z 432.27 [M+H]$^+$.

(2-amino-4-(trifluoromethoxy)phenyl)(4-(7-(piperazin-1-yl)quinazolin-4-yl)piperidin-1-yl)methanone (9)

To a solution of **8** (390 mg, 0.9 mmol) and 2-amino-4-(trifluoromethoxy)benzoic acid (199 mg, 0.9 mmol) in DMF (10 mL) was added HATU (342 mg, 0.9 mmol) and DIEA (1.6 mL, 9 mmol). The reaction was stirred at room temperature for 1 hour. The reaction mixture was diluted with ethyl acetate (50 mL) and washed with brine (5 x 10 mL). The organic layer was dried over

anhydrous sodium sulfate, filtered, and concentrated *in vacuo* to obtain crude benzyl 4-(4-(1-(2-amino-4-(trifluoromethoxy)benzoyl)piperidin-4-yl)quinazolin-7-yl)piperazine-1-carboxylate (quantitative yield). LC-MS: m/z 635.32 $[M+H]^+$. The crude material was dissolved in MeOH (10 mL)and Pd/C (50 mg) was added. H_2 (g) was introduced to the reaction, and the reaction was stirred at room temperature for 4 hours. The reaction mixture was filtered over celite, concentrated *in vacuo* and purified by column chromatography on silica gel (0-30% MeOH with 1.75N NH_3/DMC) to obtain **9** (166 mg, 43% yield over 2 steps). LC-MS: m/z 501.23 $[M+H]^+$.

6-(4-(4-(1-(2-amino-4-(trifluoromethoxy)benzoyl)piperidin-4-yl)quinazolin-7-yl)piperazin-1-yl)hexanoic acid (10)

To **9** (27 mg, 0.054 mmol) in MeCN (1 mL) was added tert-butyl 6-bromohexanoate (27 mg, 0.11 mmol) and potassium carbonate (30 mg, 0.22 mmol). The reaction was stirred at 80 °C overnight. Next day, the reaction mixture was concentrated *in vacuo* and purified by column chromatography on silica gel (0-20% MeOH/DCM) to obtain tert-butyl 6-(4-(4-(1-(2-amino-4-(trifluoromethoxy)benzoyl)piperidin-4-yl)quinazolin-7-yl)piperazin-1-yl)hexanoate (36 mg, 100% yield). LC-MS: m/z 671.45 $[M+H]^+$. The product was then dissolved in DCM (750 µL) and TFA (250 µL) at room temperature for 1 hour and concentrated *in vacuo*. The crude material **10** (quantitative yield) was directly used for the next step without further purification. LC-MC: m/z 615.33 $[M+H]^+$.

(2S,4R)-1-((S)-2-(6-(4-(4-(1-(2-amino-4-(trifluoromethoxy)benzoyl)piperidin-4-yl)quinazolin-7-yl)piperazin-1-yl)hexanamido)-3,3-dimethylbutanoyl)-4-hydroxy-N-((S)-1-(4-(4-methylthiazol-5-yl)phenyl)ethyl)pyrrolidine-2-carboxamide (INY-06-061)

To **10** (33 mg, 0.054 mmol) and (2S,4R)-1-((S)-2-amino-3,3-dimethylbutanoyl)-4-hydroxy-N-((S)-1-(4-(4-methylthiazol-5-yl)phenyl)ethyl)pyrrolidine-2-carboxamide (25 mg, 0.054 mmol) in DMF (1 mL) was added HATU (21 mg, 0.054 mmol) and DIEA (47 µL, 0.27 mmol). The reaction was stirred at room temperature for 1 hour and purified by reverse-phase HPLC (35-95% methanol in water) to obtain **INY-06-061** (18 mg, 26% yield). LC-MS: m/z 1041.69 [M+H]$^+$. ^{1}H NMR (500 MHz, DMSO) δ 9.78 (s, 1H), 9.04 (s, 1H), 9.00 (s, 1H), 8.40 – 8.32 (m, 2H), 7.83 (d, J = 9.3 Hz, 1H), 7.62 (dd, J = 9.5, 2.5 Hz, 1H), 7.48 – 7.43 (m, 2H), 7.41 – 7.37 (m, 2H), 7.30 – 7.27 (m, 1H), 7.14 (d, J = 8.4 Hz, 1H), 6.70 – 6.66 (m, 1H), 6.51 (d, J = 8.4 Hz, 1H), 4.92 (p, J = 7.1 Hz, 1H), 4.54 (d, J = 9.4 Hz, 1H), 4.42 (t, J = 8.1 Hz, 1H), 4.33 – 4.23 (m, 3H), 3.99 – 3.91 (m, 1H), 3.68 – 3.55 (m, 4H), 3.33 – 3.24 (m, 2H), 3.17 (s, 6H), 2.46 (s, 3H), 2.35 – 2.27 (m, 1H), 2.21 – 2.14 (m, 1H), 2.06 – 1.99 (m, 1H), 1.92 – 1.76 (m, 5H), 1.76 – 1.66 (m, 2H), 1.62 – 1.48 (m, 3H), 1.38 (d, J = 7.0 Hz, 3H), 1.36 – 1.23 (m, 3H), 0.94 (s, 9H).

(2R,4S)-1-((S)-2-(6-(4-(4-(1-(2-amino-4-(trifluoromethoxy)benzoyl)piperidin-4-yl)quinazolin-7-yl)piperazin-1-yl)hexanamido)-3,3-dimethylbutanoyl)-4-hydroxy-N-((S)-1-(4-(4-methylthiazol-5-yl)phenyl)ethyl)pyrrolidine-2-carboxamide (INY-06-089)

INY-06-089 was synthesized with similar procedure as **INY-06-061** using intermediate **10** and (2R,4S)-1-((S)-2-amino-3,3-dimethylbutanoyl)-4-hydroxy-N-((S)-1-(4-(4-methylthiazol-5-yl)phenyl)ethyl)pyrrolidine-2-carboxamide as the starting materials (33 mg, 65% yield). LC-MS: m/z 1041.67 [M+H]$^+$. ^{1}H NMR (500 MHz, DMSO) δ 9.71 (s, 1H), 9.04 (s, 1H), 9.00 (s, 1H), 8.34 (d, J = 9.5 Hz, 1H), 8.18 (d, J = 7.9 Hz, 1H), 7.92 (d, J = 8.3 Hz, 1H), 7.61 (dd, J = 9.5, 2.5 Hz, 1H), 7.51 – 7.41 (m, 4H), 7.30 – 7.25 (m, 1H), 7.14 (d, J = 8.4 Hz, 1H), 6.69 – 6.66 (m, 1H), 6.54 – 6.48 (m, 1H), 4.90 (p, J = 6.7 Hz, 1H), 4.47 (d, J = 8.3 Hz, 1H), 4.45 – 4.39 (m, 1H), 4.35 – 4.31

(m, 1H), 4.25 (d, J = 13.2 Hz, 2H), 3.98 – 3.90 (m, 1H), 3.80 – 3.74 (m, 1H), 3.63 – 3.55 (m, 2H), 3.52 (dd, J = 10.5, 3.9 Hz, 1H), 3.25 (t, J = 12.5 Hz, 3H), 3.19 – 3.05 (m, 5H), 2.47 (s, 3H), 2.32 – 2.24 (m, 1H), 2.19 – 2.11 (m, 1H), 2.07 – 1.90 (m, 3H), 1.90 – 1.80 (m, 4H), 1.67 – 1.59 (m, 2H), 1.55 – 1.48 (m, 2H), 1.33 (d, J = 7.0 Hz, 3H), 1.28 – 1.20 (m, 2H), 0.97 (s, 9H).

Chapter 4: Triple degradation of CDK4, CDK6 and Helios

Attributions

The work is this chapter is adapted from a manuscript published in *ACS Chemical Biology* entitled "Redirecting the Neo-Substrate Specificity of Cereblon-Targeting PROTACs to Helios" by Verano and You *et al*.

Contributions

A.L.V. designed and synthesized all compounds. I.N.Y. and E.S.W. performed the immunoblotting, proliferation, flow cytometry, and ELISA experiments. K.A.D. and N.M. conducted the mass spectrometry experiments. H.Y. and R.P.N. conducted the cellular CRBN engagement experiments. A.L.V. and I.N.Y wrote the manuscript. E.S.F., E.S.W., and N.S.G. supervised all aspects of the project. All authors read, revised, and approved the manuscript.

Funding Acknowledgments

Introduction

The impressive clinical advances generated by immunotherapies such as immune checkpoint blockade and chimeric antigen receptor (CAR) T-cell therapies have revolutionized cancer therapy. However, as only a subset of patients benefits from these treatments, developing complementary approaches that modulate the host immune response against tumors is critical.

Small molecules offer a compelling approach (Adams et al., 2015; Huck et al., 2018; van der Zanden et al., 2020), in particular because many of the factors identified via genetic studies as regulators of immune cell function and plasticity (Crawford et al., 2014; Manguso et al., 2017; Mognol et al., 2017; Pan et al., 2018; Singer et al., 2016) are intracellular and not accessible to antibodies. For example, we and others recently discovered that the FDA-approved inhibitors of cyclin-dependent kinases 4 and 6 (CDK4/6), which were developed based on the key roles of CDK4/6 regulating cell cycle progression, also have potent immunomodulatory functions (Deng et al., 2018; Goel et al., 2017; Heckler et al., 2021; Jerby-Arnon et al., 2018; Schaer et al., 2018). Specifically, we found that CDK4/6 inhibition enhanced IL-2 secretion in human and murine CD4+ T cells and synergized with PD-1 blockade to enhance control of tumor growth in syngeneic tumor models (Deng *et al.*, 2018).

Separately, we also reported the first example of small molecule degraders of the transcription factor Helios (IKZF2), which is critical for maintaining the suppressive phenotype of regulatory T cells (Tregs) as *Ikzf2$^{-/-}$* Tregs lose their suppressive activity (Kim et al., 2015; Nakagawa et al., 2016; Wang *et al.*, 2021b; Yates et al., 2018). Specifically, we developed novel 'molecular glue' compounds that bind to the Cullin Ring E3 ubiquitin ligase substrate adaptor cereblon (CRBN) and enable the recruitment, ubiquitination and subsequent proteasomal degradation of Helios but not its closely related family member Ikaros (IKZF1) or Aiolos (IKZF3),

the canonical immunomodulatory imide drug (IMiD) neo-substrates(Kronke *et al.*, 2014; Lu *et al.*, 2014). Treatment of human Tregs with Helios degraders *ex vivo* resulted in increased secretion of the effector cytokines IL-2 and IFNγ, as well as reduced suppressive activity, demonstrating that acute pharmacological loss of Helios destabilizes the hallmark features of Tregs (Wang *et al.*, 2021b).

As either pharmacologically inhibiting CDK4/6 or degrading Helios had potent immunomodulatory effects, we sought a strategy to combine these activities into a single molecule. One approach is to develop bivalent degrader molecules (also known as proteolysis targeting chimeras, or PROTACs) that consist of an E3 ubiquitin ligase-binding moiety and a target-binding moiety connected by an optimizable linker. We and others have demonstrated that these bivalent molecules can be engineered to exploit the activities of the E3 ligase-binding moiety. For example, co-degradation of BTK, IKZF1 and IKZF3 using thalidomide-based PROTACs had enhanced anti-proliferative activity in mantle cell lymphoma cells in comparison to selective BTK degradation (Dobrovolsky *et al.*, 2018). Similarly, nutlin-based PROTACs that induced BRD4 degradation and stabilized p53 levels by inhibiting the E3 ligase MDM2 had superior anti-proliferative activity compared to VHL-based PROTACs with similar BRD4 degradation potencies (Hines *et al.*, 2019).

However, it was unclear whether it would be possible to rationally re-direct the neo-substrate specificity of PROTACs. Here, we demonstrate that conjugation of the selective Helios degrader DKY709 to the CDK4/6 inhibitor palbociclib enabled the generation of bivalent degrader molecules that not only co-targeted CDK4, CDK6 and Helios for degradation, but also exhibited heightened immunostimulatory activity compared to CDK4/6 inhibitors or selective Helios degraders alone.

Development and characterization of ALV-07-082-03, a triple CDK4/CDK6/Helios degrader

To determine whether it was possible to rationally re-direct the neo-substrate specificity of PROTACs, we sought to use CRBN ligands that spared the downregulation of the traditional IMiD neo-substrates Ikaros (IKZF1) and Aiolos (IKZF3) and instead induced Helios (IKZF1) degradation (**Figure 4-1**). While we recently reported the discovery of selective anilinomaleimide-based Helios degraders (Wang *et al.*, 2021b), we reasoned that the larger size and extended conformation of these molecules, as well as a lack of knowledge of appropriate linker attachment sites, made this class of compounds poorly suitable for designing bivalent degraders. Instead, a search of patent literature revealed that Novartis recently developed DKY709 (also known as I-57), a selective Helios degrader that is currently in Phase 1 clinical trials (Solomon et al., 2022).
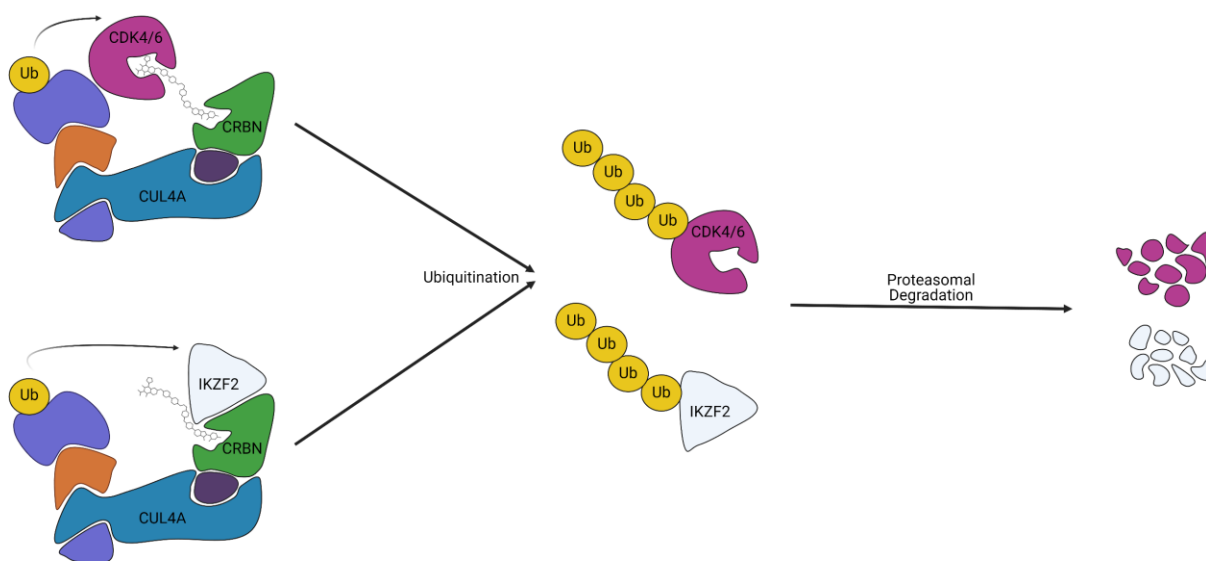
Figure 4-1. Scheme of reprogramming bivalent and molecular glue degrader activity of PROTACs

As we and others recently reported that inhibitors of CDK4 and CDK6 have potent immunomodulatory effects (Deng *et al.*, 2018; Goel *et al.*, 2017; Heckler *et al.*, 2021; Jerby-Arnon *et al.*, 2018; Schaer *et al.*, 2018), we hypothesized that a compound that induced CDK4/6 and Helios degradation would have more potent immunomodulatory effects than CDK4/6 inhibitors

or Helios degraders alone. As such, we developed bifunctional degraders in which we conjugated the FDA-approved CDK4/6 inhibitor palbociclib to DKY709. Based on previous work in which we developed thalidomide-based degraders of CDK4/6 (Brand *et al.*, 2018; Jiang *et al.*, 2019), we chose to alkylate the 4-nitrogen of the piperazine of palbociclib with various polyethylene glycol (PEG) or alkyl linkers. Attachment of the linker was made at the 3- or 4- position of the terminal phenyl ring of DKY709 to generate several heterobifunctional degraders (**Figure 4-2**). Using commercial enzymatic assays, we verified that the heterobifunctional molecules retained their abilities to biochemically inhibit CDK4/6 with half maximal inhibitory concentrations (IC_{50}) ranging from 16 to 122 nM (**Figure 4-2**).
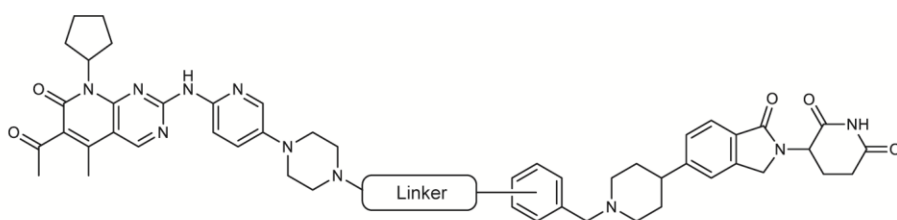
	Meta/Para	Linker	Biochemical IC_{50} (nM)	
			CDK4	CDK6
Palbociclib	N/A	N/A	14	5
ALV-06-149-02	Meta		116	26
ALV-07-036-01	Para		55	26
ALV-07-037-01	Meta		122	42
ALV-07-037-02	Para		106	53
ALV-07-038-01	Meta		56	26
ALV-07-038-02	Para		37	16
ALV-07-070-03	Meta		65	55
ALV-07-082-03	Para		70	33

Figure 4-2. Chemical structures and biochemical IC_{50} values against CDK4 and CDK6 of CDK4-CDK6-Helios targeting degraders

Next, we determined whether these compounds could induce degradation of CDK4, CDK6, and Helios in Jurkat cells. We found that treatment with 1 µM of degraders for 4 hours induced Helios degradation without affecting Ikaros protein levels, suggesting that we were ale to redirect the neo-substrate specificity towards Helios (**Figure 4-3**). We also observed downregulation of CDK4 and CDK6 protein levels to varying degrees based on the length, chemical composition and attachment site of the linker, as observed previously with thalidomide based CDK4/6 degraders (Jiang *et al.*, 2019).
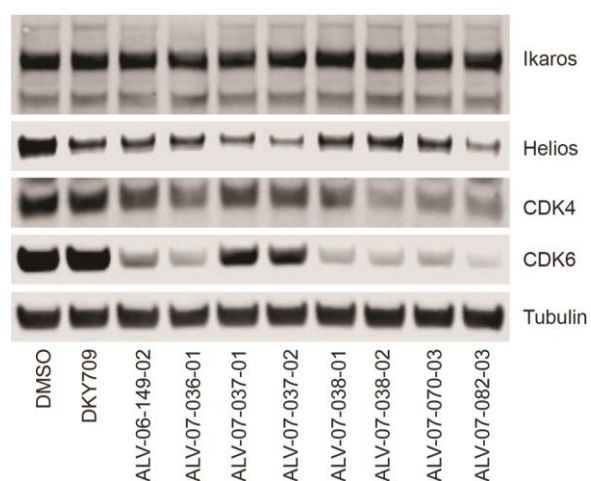
Figure 4-3. Immunoblots of Jurkat cells treated with 1 µM of indicated compounds for 4 hours.

To verify the mechanism of action of the degraders, we tested ALV-07-082-03, the most potent CDK4/CDK6/Helios degrader in biological and chemical rescue experiments. As expected, ALV-07-082-03-induced degradation of CDK4, CDK6 and Helios were dependent on the expression of CRBN (**Figure 4-4A**). Moreover, co-treatment with proteasome inhibitor carfilzomib or the NEDD8-activating enzyme E1 (NAE1) inhibitor MLN4924, which prevents activation of cullin-RING ligases such as CRL4^{CRBN}, ablated the degradation activity of ALV-07-082-03 (**Figure 4-4B**). Finally, ESW-08-032-01 (**Figure 4-4C**), a negative control compound with an N-methylated glutarimide that significantly compromises CRBN binding, had no degradation

activity against CDK4, CDK6 and Helios, validating that ALV-07-082-03 acts in a proteasome- and CRBN- dependent manner (**Figure 4-4D**).
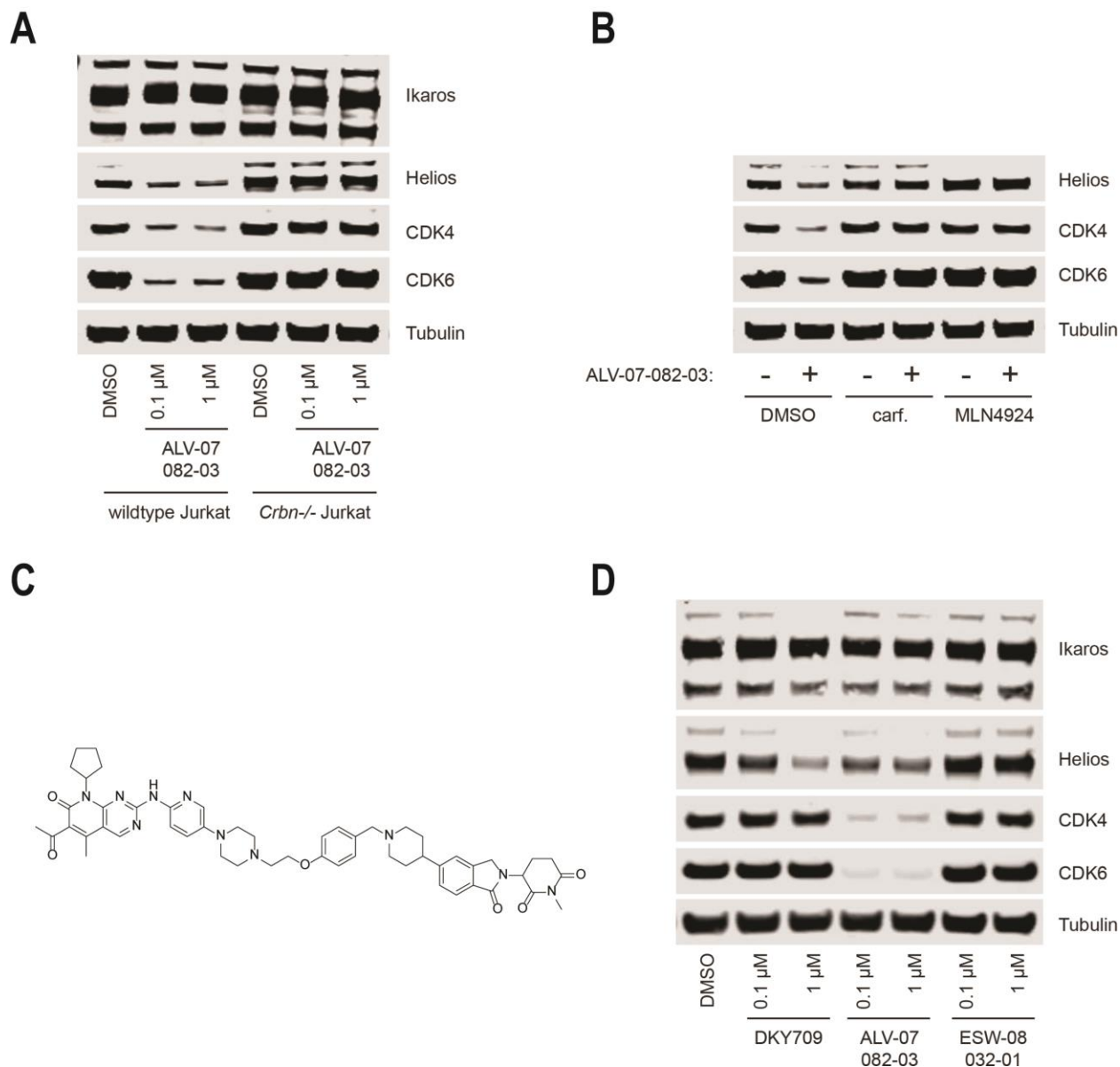
Figure 4-4. Mechanism of action of ALV-07-082-03. (A) Immunoblot of wildtype or CRBN$^{-/-}$ Jurkat cells treated with ALV-07-082-03 for 4 hours. (B) Immunoblot of Jurkat cells co-treated with ALV-07-082-03 and carfilzomib (1 µM) or MLN4924 (1 µM) for 4 hours. (C) Chemical structure of ESW-08-032-01, the N-methyl negative control analog of ALV-07-082-03. (D) Immunoblot of Jurkat cells treated with indicated compounds for 4 hours.

To globally assess the selectivity of ALV-07-082-03, we performed multiplexed mass spectrometry-based proteomics of Molt4 cells following 5-hour treatment (**Figure 4-5**). Across approximately 7,500 quantified proteins, we found that ALV-07-082-03 was highly potent for inducing degradation of CDK4, CDK6 and Helios. In addition to CDK4, CDK6 and Helios, we observed modest downregulation of select targets, including the zinc finger protein FIZ1 (**Figure 4-5**).
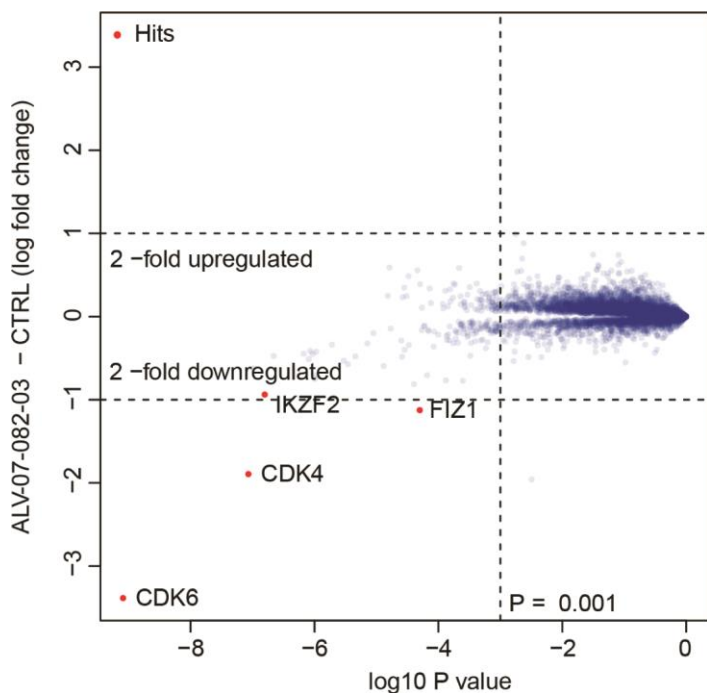
Figure 4-5. Quantitative proteomics profile (7,500 total proteins) of wildtype Molt4 cells treated for 5 hours with 1 μM of ALV-07-082-03. Significant changes were assessed using a moderated t-test as implemented in Bioconductor's Limma package.

Cell cycle and anti-proliferative effects of CDK4, CDK6 and Helios degradation

To assess the effects of ALV-07-082-03 on CDK4/6 signaling, we investigated its effects on phosphorylation of retinoblastoma (Rb), the canonical CDK4/6 substrate. Similar to palbociclib, treatment with ALV-07-082-03 reduced levels of phosphorylated Rb, while the parent Helios degrader DKY709 and the negative control compound ESW-08-032-01 had minimal effects on Rb phosphorylation (**Figure 4-6A**). ALV-07-082-03 had modestly more potent anti-proliferative activity than palbociclib in Jurkat cells, which was slightly rescued with the negative control compound ESW-08-032-01 (**Figure 4-6B**). Moreover, ALV-07-082-03 induced G1 arrest in Jurkat cells to similar extents as the parental inhibitor palbociclib and reported CDK4/6 degrader BSJ-02-162 (Jiang *et al.*, 2019) , and this effect was less evident in cells treated with ESW-08-032-01 (**Figure 4-6C**). The relatively similar anti-proliferative potencies and cell cycle effects of ALV-07-082-03 and ESW-08-032-01 are likely driven by the retention of CDK4 and CDK6 inhibitor activities of the compounds.
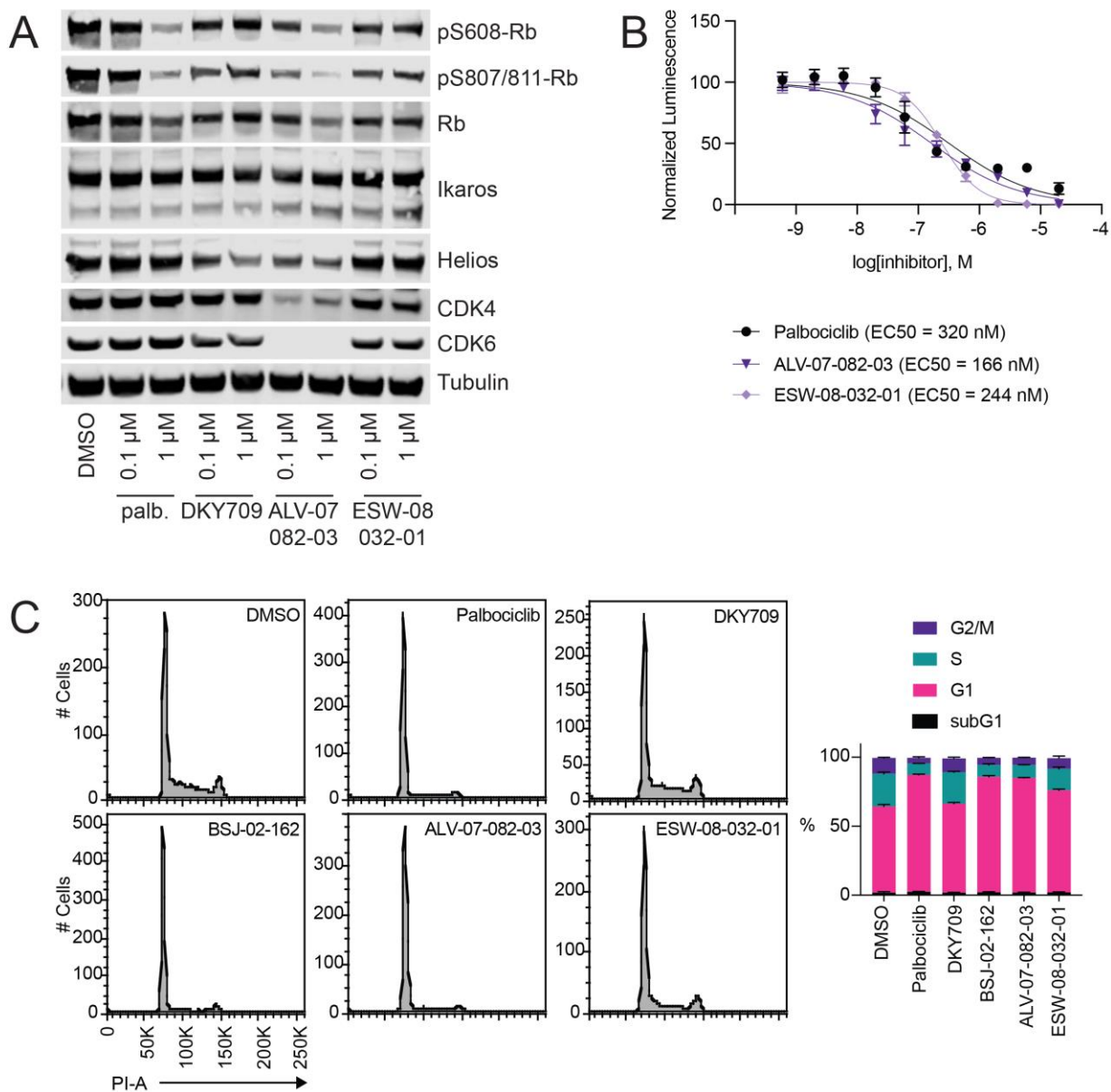
Figure 4-6. CDK4-CDK6-Helios degraders induce cell cycle arrest and inhibit proliferation. (A) Immunoblot of Jurkat cells treated with indicated compounds for 16 hours. (B) Proliferation assays were performed by treating Jurkat cells with the indicated compounds at indicated concentrations for 72 hours. Anti-proliferative effects of compounds were assessed using Cell Titer Glo assay kit (Promega), and EC_{50} values were determined using Graphpad Prism nonlinear regression curve fit. (C) Fluorescence histograms and quantitation of Jurkat cells treated with 100 nM of indicated compounds for 24 hours and stained with PI.

Degradation of CDK4/CDK6/Helios de-represses expression of IL-2

We had previously reported that CDK4 and CDK6 inhibitors could enhance the secretion of IL-2 in cultured T cell lines and primary CD4+ T cells (Deng *et al.*, 2018). In addition, we found that acute Helios degradation promoted IL-2 secretion in Jurkat cells and primary human regulatory T cells (Wang *et al.*, 2021b), consistent with previous reports that Helios negatively regulates *Il2* expression (Baine et al., 2013). Thus, we investigated whether triple degradation of CDK4, CDK6 and Helios could synergistically de-repress IL-2 secretion in Jurkat cells. As expected, pre-treatment of Jurkat cells with palbociclib followed by T-cell receptor (TCR) stimulation with α-CD3/CD28 antibody complexes led to enhanced IL-2 secretion (**Figure 4-7**). Lenalidomide and DKY709 treatment both resulted in elevated IL-2 secretion, although it did not reach statistical significance. While the CDK4/CDK6-selective degrader BSJ-03-204 had similar activity as palbociclib, the CDK4/CDK6/Ikaros/Aiolos degrader BSJ-02-162 (Jiang *et al.*, 2019) induced even greater IL-2 secretion, which was not surprising as Ikaros and Aiolos are known negative regulators of *Il2* (Corral et al., 1999; Gandhi et al., 2014; Haslett *et al.*, 1998). Notably, treatment with the CDK4/CDK6/Helios degrader ALV-07-082-03 induced elevated levels of IL-2 that were comparable to that of BSJ-02-162, while the inactive chemical control compound ESW-08-032-01 had similar activity to that of palbociclib (**Figure 4-7**).
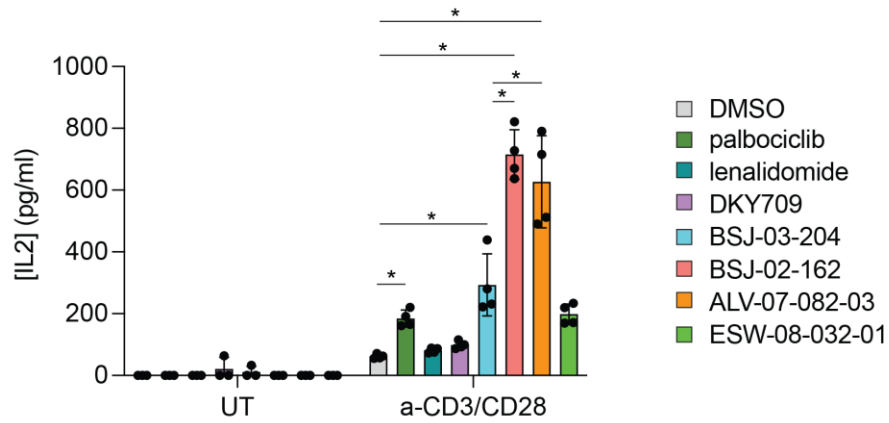
Figure 4-7. CDK4, CDK6 and Helios co-degradation enhances IL-2 secretion. Quantification of IL-2 levels by ELISA from Jurkat cells pre-treated with 1 µM of indicated compounds for 24 hours, then TCR-stimulated for 18 hours. Results shown as mean ± SD. Untreated (UT) is biological replicates of n=3, while TCR-stimulated samples have biological replicates of n=4 (*p<0.05).

Conclusion

In sum, we report here the first CDK4/CDK6/Helios triple degrader ALV-07-082-03 and demonstrate that it potently suppressed downstream CDK4/6 signaling and inhibited proliferation of cancer cells as well as enhanced immunomodulatory activity in comparison to the parental CDK4/6 inhibitor Palbociclib or the selective Helios degrader DKY709. Thus, we demonstrate the possibility of rationally redirecting the neo-substrate specificity of PROTACs by incorporating alternative molecular glue molecules as E3 ligase ligands.

Materials and methods

Cell lines. Wildtype or CRBN-/- Jurkat cells were cultured in RPMI-1640 media supplemented with 10% FBS and 1% penicillin/streptomycin in a 37°C incubator with 5% CO_2.

Western blots and antibodies. Cells were lysed in M-PER buffer (Thermo Scientific) containing protease/phosphatase inhibitor cocktail (Roche). Protein concentration was measured using a BCA assay (Pierce). Equivalent amounts of each sample were loaded on 4-12% Bis-Tris gels (Invitrogen), transferred to nitrocellulose membranes, and immunoblotted with antibodies against IKZF1 (Cell Signaling Technology, #14859S), IKZF2 (Cell Signaling Technology, #42427S), CDK4 (Cell Signaling Technology, #12790S), CDK6 (Cell Signaling Technology, #13331S), Tubulin (Cell Signaling Technology, #3873S), phospho-S608-Rb (Cell Signaling Technology, #8147S), phospho-S807/811-Rb (Cell Signaling Technology, #8516S), and Rb (Cell Signaling Technolgoy, #9309S). IRDye®800-labeled goat anti-rabbit IgG and IRDye®680-labeled goat anti-mouse IgG (LI-COR) secondary antibodies were used and detected on an Odyssey CL_x system.

Proliferation assay. Proliferation assays were performed by treating Jurkat cells with at the concentrations indicated for 72 h. Anti-proliferative effects of compounds were assessed using CellTiter-Glo (Promega). IC_{50}s were calculated with Graphpad Prism nonlinear regression curve fit.

Cell cycle analysis. Cells were treated with the indicated compounds and fixed for at least 24h in 70% EtOH/PBS. Subsequently, fixed cells were stained with 25 µg/ml propidium iodide (Life Technologies) with 200 µg/ml RNaseA (Life Technologies) in 0.1% TritonX-100/PBS for 24h.

DNA content was quantified by flow cytometry on a LSRFortessa flow cytometer (BD Biosciences).

IL2 ELISA. Jurkat cells were pre-treated with 1 µM of the indicated compounds for 24h. Subsequently, cells were washed, and then equivalent numbers of cells from each treatment cohort were stimulated with ImmunoCult Human CD3/CD28 T Cell Activator (StemCell #10971) in the presence of 1 µM of the indicated compounds for 18h. IL-2 levels in the supernatant were analyzed using the LEGEND MAX™ Human IL-2 ELISA Kit (Biolegend #431807) according to the manufacturer's protocol.

Proteomics. MOLT4 cells were treated with 1 µM of ALV-07-082-03 in biological duplicate and DMSO vehicle control in biological triplicate for 5h. Cell lysis and Tandem Mass Tagged (TMT) tryptic peptides were prepared for LC-MS analysis following procedures previously reported (Donovan *et al.*, 2018).

Data were collected using an Orbitrap Fusion Lumos mass spectrometer (Thermo Fisher Scientific, San Jose, CA, USA) coupled with a Proxeon EASY-nLC 1200 LC pump (Thermo Fisher Scientific). Peptides were separated on a 50 cm 75 µm inner diameter EasySpray ES903 microcapillary column (Thermo Fisher Scientific) using a 190 min gradient of 6 - 27% acetonitrile in 1.0% formic acid with a flow rate of 300 nL/min.

Each analysis used a MS3-based TMT method as described previously (McAlister et al., 2014). The data were acquired using a mass range of m/z 340 – 1350, resolution 120,000, AGC target 5 $\times 10^5$, maximum injection time 100 ms, dynamic exclusion of 120 s for the peptide measurements in the Orbitrap. Data dependent MS2 spectra were acquired in the ion trap with a normalized

collision energy (NCE) set at 35%, AGC target set to 1.8×10^4 and a maximum injection time of 120 ms. MS3 scans were acquired in the Orbitrap with HCD collision energy set to 55%, AGC target set to 2×10^5, maximum injection time of 150 ms, resolution at 50,000 and with a maximum synchronous precursor selection (SPS) precursors set to 10.

Proteome Discoverer 2.4 (Thermo Fisher Scientific) was used for .RAW file processing and controlling peptide and protein level false discovery rates, assembling proteins from peptides, and protein quantification from peptides. MS/MS spectra were searched against a Swissprot human database (February 2020) with both the forward and reverse sequences as well as known contaminants such as human keratins. Database search criteria were as follows: tryptic with two missed cleavages, a precursor mass tolerance of 20 ppm, fragment ion mass tolerance of 0.6 Da, static alkylation of cysteine (57.02146 Da), static TMT labeling of lysine residues and N-termini of peptides (229.16293 Da), and variable oxidation of methionine (15.99491 Da). TMT reporter ion intensities were measured using a 0.003 Da window around the theoretical m/z for each reporter ion in the MS3 scan. The peptide spectral matches with poor quality MS3 spectra were excluded from quantitation (summed signal-to-noise across channels < 100 and precursor isolation specificity < 0.5), and the resulting data was filtered to only include proteins with a minimum of 2 unique peptides quantified. Reporter ion intensities were normalized and scaled using in-house scripts in the R framework (Team, 2014). Statistical analysis was carried out using the limma package within the R framework (Ritchie *et al.*, 2015).

Chemistry Synthetic Scheme

Scheme 1 – Synthesis of intermediate 7
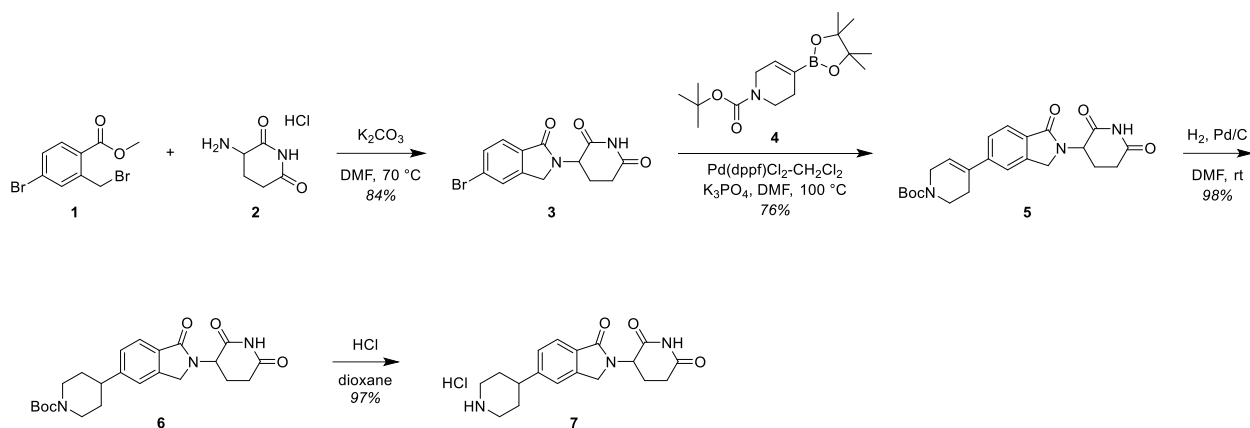
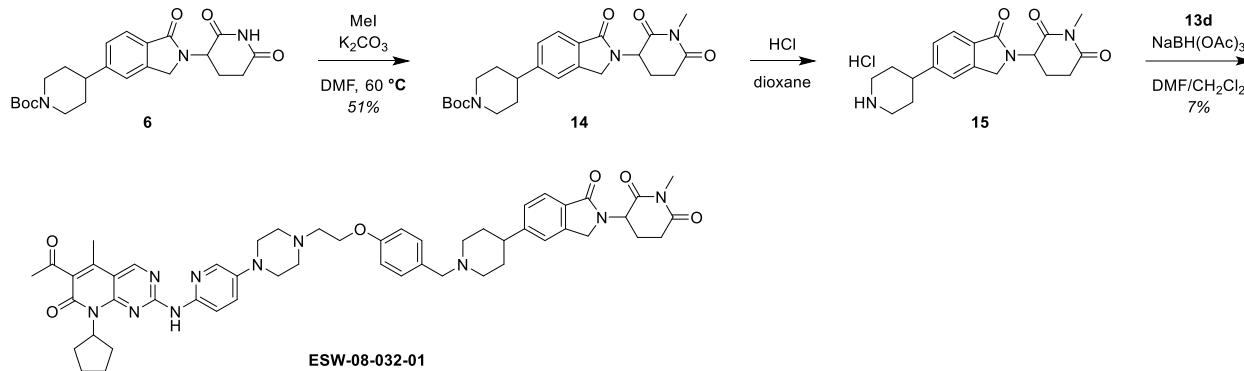## Scheme 2 – General synthetic route towards bifunctional degraders
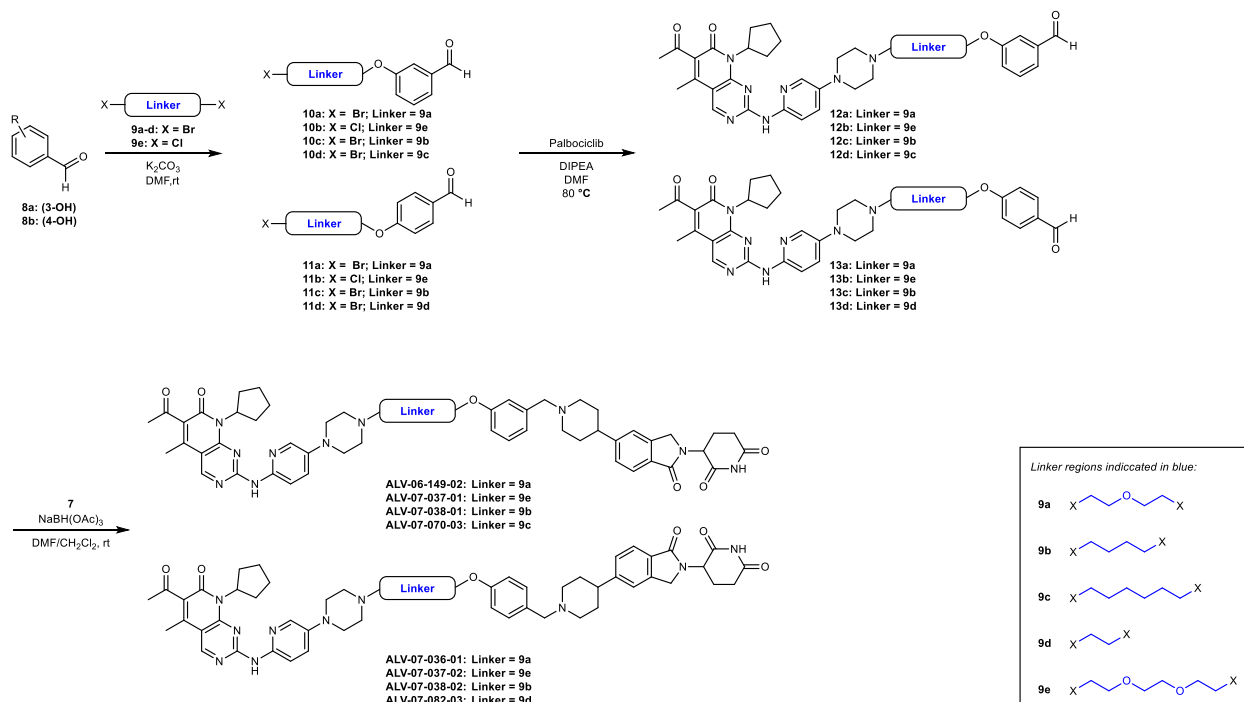
Scheme 3 – Synthetic route of ESW-08-032-01

ESW-08-032-01

General chemistry methods. Unless otherwise noted, reagents and solvents were obtained from commercial suppliers and used without further purification. Reactions were monitored using a Waters Aquity UPLC/MS system (Waters PDA eλ Detector, QDa Detector, Sample manager – FL, Binary Solvent Manager) using Acquity UPLC® BEH C18 column (2.1 x 50 mm, 1.7 µm particle size): solvent gradient = 85% A at 0 min, 1% A at 1.7 min; solvent A = 0.1% formic acid in water; solvent B = 0.1% formic acid in acetonitrile; flow rate: 0.6 mL/min. Products were purified by flash column chromatography using CombiFlash®Rf with Teledyne Isco RediSep® normal-phase silica flash columns and preparative HPLC using Waters SunFire[TM] Prep C18 column (19 x 100 mm, 5 µm particle size) using a gradient of 15-75% methanol in water containing 0.05% trifluoroacetic acid (TFA) over 48 min (60 min run time) at a flow of 40 mL/min. ^{1}H NMR spectra were recorded on a 500 MHz Bruker Avance III spectrometer, and chemical shifts are reported in parts per million (ppm, δ) downfield from tetramethylsilane (TMS). Coupling constants (*J*) are reported in Hz. Spin multiplicities are described as s (singlet), br (broad singlet), d (doublet), t (triplet), q (quartet) and m (multiplet). Purities of assayed compounds were in all cases greater than 95%, as determined by reverse-phase HPLC analysis.

Synthesis of intermediate 7

3-(5-bromo-1-oxoisoindolin-2-yl)piperidine-2,6-dione (3)
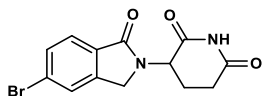
Potassium carbonate (2.29 g, 16.6 mmol) was added to a solution of methyl 4-bromo-2-(bromomethyl)benzoate **1** (1.70 g, 5.52 mmol) and 3-aminopiperidine-2,6-dione hydrochloride **2** (1.0 g, 6.1 mmol) in *N,N*-dimethylformamide (DMF, 18 mL, 0.30 M) and stirred at 70 °C for 17 h. The reaction mixture was concentrated *in vacuo* and water was added to the residue to give a precipitate, which was collected by gravity filtration and dried to yield the title compound as a solid (1.5 g, 84% yield). LC-MS (ESI): *m/z* 322.9 [M+H]$^+$.

tert-butyl   4-(2-(2,6-dioxopiperidin-3-yl)-1-oxoisoindolin-5-yl)-3,6-dihydropyridine-1(2H)-carboxylate (5).
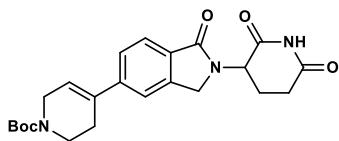
3-(5-Bromo-1-oxoisoindolin-2-yl)piperidine-2,6-dione **3** (1.50 g, 4.64 mmol) and *tert*-butyl 4-(4,4,5,5-tetramethyl-1,3,2-dioxaborolan-2-yl)-3,6-dihydropyridine-1(2H)-carboxylate **4** (1.87 g, 6.03 mmol) were dissolved in DMF (30.0 mL, 0.155 M) under nitrogen atmosphere. Pd(dppf)Cl$_2$-CH$_2$Cl$_2$ (189 mg, 0.232 mmol) and potassium phosphate (K$_3$PO$_4$, 1.18 g, 5.57 mmol) were added, and the reaction mixture was stirred at 100 °C for 15 h. Upon cooling to rt, the reaction mixture was diluted with EtOAc. The organic layer was washed with water 2x, brine, dried over Na$_2$SO$_4$, filtered, and concentrated *in vacuo*. Purification by flash chromatography (SiO$_2$: 0-100% EtOAc

in hexanes) provided the title compound as a light brown solid (1.5 g, 76% yield). LC-MS (ESI): *m/z* 426.2 [M+H]$^+$.

tert-butyl 4-(2-(2,6-dioxopiperidin-3-yl)-1-oxoisoindolin-5-yl)piperidine-1-carboxylate (6)
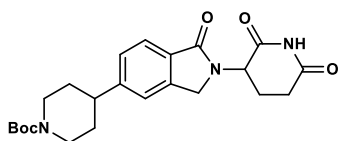
In a 100-mL round bottom flask equipped with a stir bar and under N$_2$ atmosphere, *tert*-butyl 4-(2-(2,6-dioxopiperidin-3-yl)-1-oxoisoindolin-5-yl)-3,6-dihydropyridine-1(2*H*)-carboxylate **5** (1.50 g, 3.53 mmol) was dissolved in DMF (20 mL, 0.18 M). Palladium on carbon (10 wt%, 375 mg, 0.353 mmol) was added, and the flask was equipped with a H$_2$ balloon and flushed with H$_2$. After stirring at room temperature (rt) for 20 h under H$_2$ atmosphere, the reaction mixture was filtered over celite to remove Pd catalyst and rinsed with DMF. The filtrate was concentrated *in vacuo* to give the title compound as an off-white solid (1.51 g, 99% yield), which was carried forward without purification. LC-MS (ESI): *m/z* 372.1 [M+H-*t*Bu]$^+$, *m/z* 328.1 [M+H-Boc]$^+$.

3-(1-oxo-5-(piperidin-4-yl)isoindolin-2-yl)piperidine-2,6-dione hydrochloride (7)
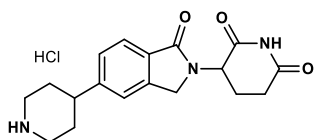
4 M HCl in dioxane (10 mL) was added to a solution of *tert*-butyl 4-(2-(2,6-dioxopiperidin-3-yl)-1-oxoisoindolin-5-yl)piperidine-1-carboxylate **6** (1.51 g, 3.53 mmol) in CH$_2$Cl$_2$ (10 mL, 0.35 M) and stirred at rt for 12 h. The reaction mixture was concentrated *in vacuo* to give the title compound as a solid (1.156 g, 90%), which was carried forward without purification. ^{1}H NMR (500 MHz, DMSO-d6) δ 10.98 (s, 1H), 8.95 (d, *J* = 9.7 Hz, 1H), 8.88 – 8.72 (m, 1H), 7.70 (d, *J* = 7.9 Hz, 1H),

7.46 (s, 1H), 7.41 – 7.34 (m, 1H), 5.11 (dd, J = 13.3, 5.1 Hz, 1H), 4.45 (d, J = 17.3 Hz, 1H), 4.32 (d, J = 17.3 Hz, 1H), 3.44 – 3.36 (m, 2H), 3.04 – 2.88 (m, 4H), 2.63 – 2.57 (m, 1H), 2.39 (ddd, J = 13.3, 4.5 Hz, 1H), 2.03 – 1.85 (m, 5H). LC-MS (ESI): m/z 328.1 [M+H]$^+$.

Synthesis of bifunctional degraders

3-(2-(2-bromoethoxy)ethoxy)benzaldehyde (10a)
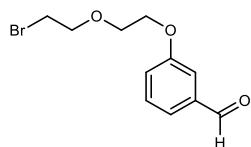
Potassium carbonate (0.410 g, 2.96 mmol) was added to a solution of 3-hydroxybenzaldehyde **8a** (302 mg, 2.47 mmol) in DMF (10 mL, 0.25 M) and stirred at rt for 10 min. 1-Bromo-2-(2-bromoethoxy)ethane **9a** (687 mg, 2.96 mmol) was added via syringe, and the reaction mixture was stirred at rt for 15 h. The reaction mixture was extracted with ethyl acetate (EtOAc), washed with saturated aqueous (satd aq) NH$_4$Cl, water (2x), and brine. The organic layers were collected, dried over Na$_2$SO$_4$, filtered, and concentrated *in vacuo.* Purification by flash chromatography (SiO$_2$: 0-100% EtOAc in hexanes) provided the title compound as a yellow solid (452 mg, 67% yield). LC-MS (ESI): m/z 272.9 [M+H]$^+$.

3-(2-(2-(4-(6-((6-acetyl-8-cyclopentyl-5-methyl-7-oxo-7,8-dihydropyrido[2,3-*d*]pyrimidin-2-yl)amino)pyridin-3-yl)piperazin-1-yl)ethoxy)ethoxy)benzaldehyde (12a)
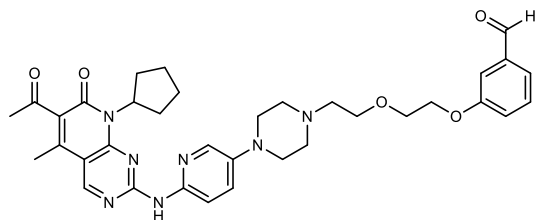
N,*N*-Diisopropylethylamine (DIPEA, 0.440 mL, 2.52 mmol) was added to a solution of 3-(2-(2-bromoethoxy)ethoxy)benzaldehyde **10a** (229 mg, 0.839 mmol) and Palbociclib **11** (0.250 g, 1.09 mmol) in DMF (4.0 mL, 0.21 M) and stirred at 80 °C for 15 h. Upon cooling to rt, the reaction mixture was extracted with EtOAc, washed with water 2x, brine, dried over Na_2SO_4, filtered, and concentrated *in vacuo*. Purification by flash chromatography (SiO_2: 0-80% EtOAc in CH_2Cl_2, then 0-20% MeOH in CH_2Cl_2) provided the title compound as a yellow solid (332 mg, 62% yield). LC-MS (ESI): *m/z* 640.4 $[M+H]^+$.

3-(6-(1-(3-(2-(2-(4-(6-((6-acetyl-8-cyclopentyl-5-methyl-7-oxo-7,8-dihydropyrido[2,3-*d*]pyrimidin-2-yl)amino)pyridin-3-yl)piperazin-1-yl)ethoxy)ethoxy)benzyl)piperidin-4-yl)-1-oxoisoindolin-2-yl)piperidine-2,6-dione (ALV-06-149-02)
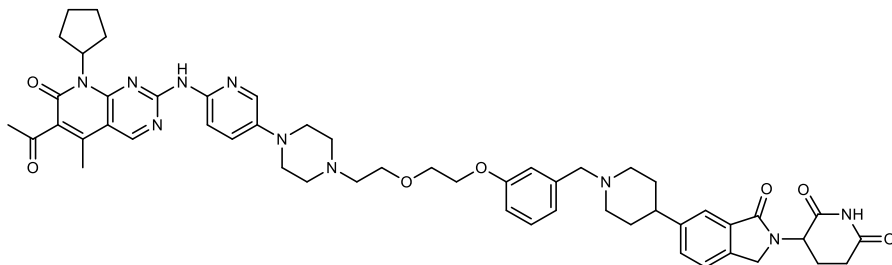
Sodium triacetoxyborohydride ($NaBH(OAc)_3$, 64 mg, 0.30 mmol) was added to a solution of 3-(2-(2-(4-(6-((6-acetyl-8-cyclopentyl-5-methyl-7-oxo-7,8-dihydropyrido[2,3-*d*]pyrimidin-2-yl)amino)pyridin-3-yl)piperazin-1-yl)ethoxy)ethoxy)benzaldehyde **(12a)** (96 mg, 0.15 mmol) and 3-(1-oxo-5-(piperidin-4-yl)isoindolin-2-yl)piperidine-2,6-dione hydrochloride **7** (59 mg, 0.18 mmol) in 4:1 DMF/CH_2Cl_2 (3 mL, 0.05 M). Purification by flash chromatography (SiO_2: 0-80% EtOAc in CH_2Cl_2, then 0-20% MeOH in CH_2Cl_2) provided the title compound **ALV-06-149-02** as a yellow solid (5.1 mg, 3% yield). ^{1}H NMR (500 MHz, DMSO-d6) δ 10.96 (s, 1H), 10.08 (s, 1H), 8.94 (s, 1H), 8.03 (d, *J* = 2.8 Hz, 1H), 7.84 (d, *J* = 9.0 Hz, 1H), 7.61

(d, J = 7.8 Hz, 1H), 7.46 (s, 1H), 7.44 (dd, J = 9.1, 2.8 Hz, 1H), 7.37 (d, J = 7.9 Hz, 1H), 7.23 (t, J = 8.0 Hz, 1H), 6.94 – 6.87 (m, 2H), 6.83 (dd, 1H), 5.81 (p, J = 8.8 Hz, 1H), 5.08 (dd, J = 13.3, 5.0 Hz, 1H), 4.39 (d, J = 17.2 Hz, 1H), 4.26 (d, J = 17.2 Hz, 1H), 4.12 – 4.07 (m, 2H), 3.77 – 3.72 (m, 2H), 3.63 (t, J = 5.6 Hz, 2H), 3.47 (s, 2H), 3.15 – 3.09 (m, 4H), 2.95 – 2.85 (m, 3H), 2.64 – 2.54 (m, 8H), 2.42 (s, 3H), 2.37 (dd, J = 13.2, 4.5 Hz, 1H), 2.30 (s, 3H), 2.27 – 2.19 (m, 2H), 2.09 – 1.94 (m, 3H), 1.90 – 1.83 (m, 2H), 1.81 – 1.64 (m, 6H), 1.62 – 1.53 (m, 2H). LC-MS (ESI): m/z 951.5 [M+H]$^+$.

3-(5-(1-(4-(2-(2-(4-(6-((6-acetyl-8-cyclopentyl-5-methyl-7-oxo-7,8-dihydropyrido[2,3-*d*]pyrimidin-2-yl)amino)pyridin-3-yl)piperazin-1-yl)ethoxy)ethoxy)benzyl)piperidin-4-yl)-1-oxoisoindolin-2-yl)piperidine-2,6-dione (ALV-07-036-01)
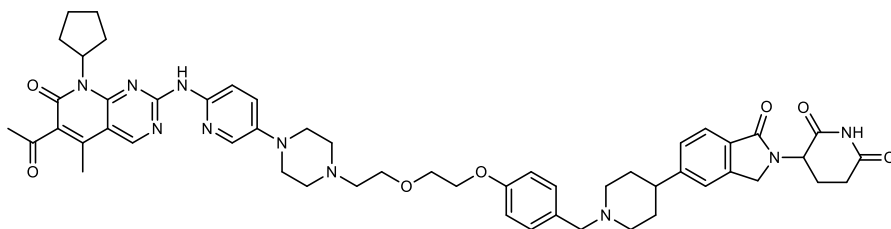
The title compound **ALV-07-036-01** was prepared with similar protocols as **ALV-06-198-02,** using 4-hydroxybenzaldehyde **8b** and linker **9a** from **Scheme 2** as the starting materials. ^{1}H NMR (500 MHz, DMSO-d_6) δ 10.97 (s, 1H), 10.09 (s, 1H), 8.94 (s, 1H), 8.04 (d, J = 2.9 Hz, 1H), 7.84 (d, J = 9.0 Hz, 1H), 7.62 (d, J = 7.9 Hz, 1H), 7.48 – 7.42 (m, 2H), 7.37 (d, J = 7.8 Hz, 1H), 7.33 – 7.20 (m, 2H), 6.93 (d, J = 8.1 Hz, 2H), 5.81 (p, J = 8.8 Hz, 1H), 5.09 (dd, J = 13.3, 5.1 Hz, 1H), 4.40 (d, J = 17.2 Hz, 1H), 4.27 (d, J = 17.2 Hz, 1H), 4.14 – 4.05 (m, 2H), 3.76 – 3.72 (m, 2H), 3.69 – 3.42 (m, 4H), 3.21 – 2.84 (m, 7H), 2.74 – 2.54 (m, 8H), 2.42 (s, 3H), 2.40 – 2.33 (m, 1H), 2.30 (s, 3H), 2.28 – 2.18 (m, 3H), 2.02 – 1.94 (m, **1H**), 1.93 – 1.68 (m, 9H), 1.62 – 1.53 (m, 2H). LC-MS (ESI): m/z 951.6 [M+H]$^+$.

3-(5-(1-(3-(2-(2-(2-(4-(6-((6-acetyl-8-cyclopentyl-5-methyl-7-oxo-7,8-dihydropyrido[2,3-*d*]pyrimidin-2-yl)amino)pyridin-3-yl)piperazin-1-yl)ethoxy)ethoxy)ethoxy)benzyl)piperidin-4-yl)-1-oxoisoindolin-2-yl)piperidine-2,6-dione (ALV-07-037-01)

The title compound **ALV-07-037-01** was prepared with similar protocols as **ALV-06-149-02**, using 3-hydroxybenzaldehyde **8a** and linker **9e** from **Scheme 2** as the starting materials. ^{1}H NMR (500 MHz, DMSO-d_6) δ 10.97 (s, 1H), 10.08 (s, 1H), 8.94 (s, 1H), 8.02 (d, $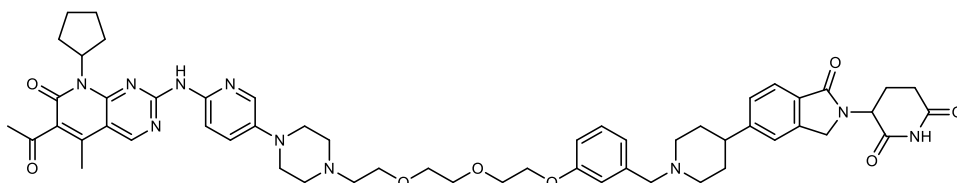J$ = 2.9 Hz, 1H), 7.84 (d, J = 9.0 Hz, 1H), 7.61 (d, J = 7.8 Hz, 1H), 7.46 (s, 1H), 7.42 (dd, J = 9.1, 3.0 Hz, 1H), 7.36 (d, J = 7.9 Hz, 1H), 7.23 (t, J = 8.0 Hz, 1H), 6.91 – 6.88 (m, 2H), 6.83 (dd, J = 8.1, 2.3 Hz, 1H), 5.83 – 5.78 (m, 1H), 5.09 (dd, J = 13.3, 5.1 Hz, 1H), 4.39 (d, J = 17.2 Hz, 1H), 4.27 (d, J = 17.2 Hz, 1H), 4.08 (dd, J = 5.5, 3.7 Hz, 2H), 3.76 (dd, J = 5.5, 3.7 Hz, 2H), 3.62 – 3.59 (m, 3H), 3.58 – 3.54 (m, 6H), 3.13 – 3.10 (m, 4H), 2.92 – 2.89 (m, 2H), 2.59 – 2.53 (m, 8H), 2.42 (s, 3H), 2.30 (s, 3H), 1.90 (s, 3H), 1.78 – 1.67 (m, 8H), 1.59 – 1.54 (m, 3H). LC-MS (ESI): *m/z* 995.6 [M+H]$^+$.

3-(5-(1-(4-(2-(2-(2-(4-(6-((6-acetyl-8-cyclopentyl-5-methyl-7-oxo-7,8-dihydropyrido[2,3-*d*]pyrimidin-2-yl)amino)pyridin-3-yl)piperazin-1-yl)ethoxy)ethoxy)ethoxy)benzyl)piperidin-4-yl)-1-oxoisoindolin-2-yl)piperidine-2,6-dione (ALV-07-037-02)
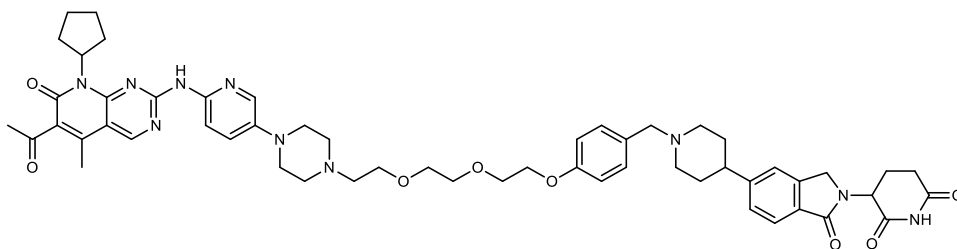

The title compound **ALV-07-037-02** was prepared with similar protocols as **ALV-06-149-02**, using 4-hydroxybenzaldehyde **8b** and linker **9e** from **Scheme 2** as the starting materials. ^{1}H NMR (500 MHz, DMSO-d6) δ 10.97 (s, 1H), 10.16 (s, 1H), 8.95 (s, 1H), 8.02 (s, 1H), 7.88 (d, *J* = 8.5 Hz, 1H), 7.65 (d, *J* = 7.8 Hz, 1H), 7.60 – 7.51 (m, 2H), 7.47 (d, *J* = 7.6 Hz, 1H), 7.41 (s, 1H), 7.33 (d, *J* = 7.6 Hz, 1H), 7.02 (d, *J* = 8.4 Hz, 2H), 5.81 (p, *J* = 8.8 Hz, 1H), 5.08 (dd, *J* = 13.2, 5.0 Hz, 1H), 4.41 (d, *J* = 17.3 Hz, 1H), 4.28 (d, *J* = 17.3 Hz, 1H), 4.16 – 4.10 (m, 2H), 3.80 – 3.74 (m, 3H), 3.65 – 3.57 (m, 6H), 3.23 – 3.08 (m, 5H), 3.04 (q, *J* = 7.2 Hz, 3H), 3.00 – 2.85 (m, 4H), 2.63 – 2.55 (m, 2H), 2.41 (s, 4H), 2.30 (s, 3H), 2.27 – 2.05 (m, 5H), 1.99 – 1.84 (m, 6H), 1.79 – 1.72 (m, 2H), 1.59 – 1.54 (m, 2H). LC-MS (ESI): *m/z* 995.6 [M+H]+.

3-(5-(1-(3-(4-(4-(6-((6-acetyl-8-cyclopentyl-5-methyl-7-oxo-7,8-dihydropyrido[2,3-d]pyrimidin-2-yl)amino)pyridin-3-yl)piperazin-1-yl)butoxy)benzyl)piperidin-4-yl)-1-oxoisoindolin-2-yl)piperidine-2,6-dione (ALV-07-038-01)
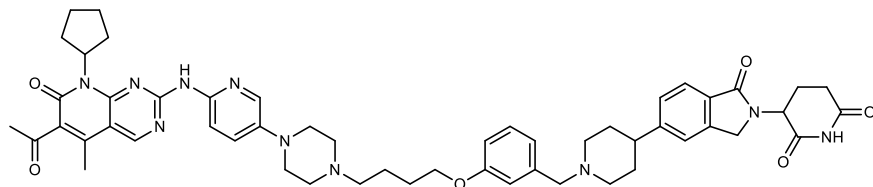

The title compound **ALV-07-038-01** was prepared with similar protocols as **ALV-06-149-02**, using 3-hydroxybenzaldehyde **8a** and linker **9b** from **Scheme 2** as the starting materials. ^{1}H NMR (500 MHz, DMSO-d6) δ 10.97 (s, 1H), 10.08 (s, 1H), 8.94 (s, 1H), 8.04 (d, J = 2.8 Hz, 1H), 7.84 (d, J = 9.0 Hz, 1H), 7.62 (d, J = 7.8 Hz, 1H), 7.48 – 7.43 (m, 2H), 7.38 (d, J = 7.8 Hz, 1H), 7.23 (t, J = 7.8 Hz, 1H), 6.93 – 6.87 (m, 2H), 6.82 (d, J = 7.1 Hz, 1H), 5.81 (p, J = 8.8 Hz, 1H), 5.09 (dd, J = 13.3, 5.1 Hz, 1H), 4.40 (d, J = 17.2 Hz, 1H), 4.27 (d, J = 17.2 Hz, 1H), 4.05 – 3.96 (m, 3H), 3.17 – 3.12 (m, 4H), 2.99 – 2.84 (m, 3H), 2.61 – 2.52 (m, 4H), 2.44 – 2.35 (m, 7H), 2.30 (s, 3H), 2.27 – 2.17 (m, 4H), 1.98 – 1.94 (m, 1H), 1.90 – 1.83 (m, 3H), 1.79 – 1.71 (m, 8H), 1.65 – 1.56 (m, 5H). LC-MS (ESI): *m/z* 935.5 [M+H]$^+$.

3-(5-(1-(4-(4-(4-(6-((6-acetyl-8-cyclopentyl-5-methyl-7-oxo-7,8-dihydropyrido[2,3-*d*]pyrimidin-2-yl)amino)pyridin-3-yl)piperazin-1-yl)butoxy)benzyl)piperidin-4-yl)-1-oxoisoindolin-2-yl)piperidine-2,6-dione (ALV-07-038-02)
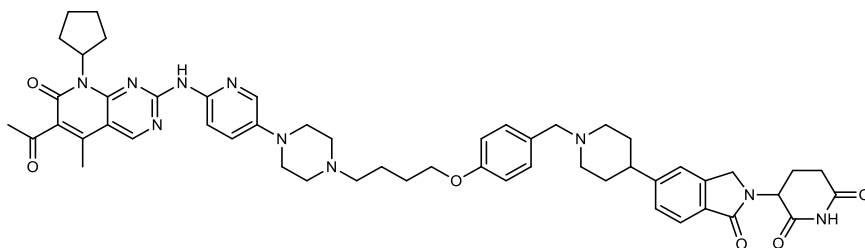

The title compound **ALV-07-038-02** was prepared with similar protocols as **ALV-06-149-02**, using 4-hydroxybenzaldehyde **8b** and linker **9b** from **Scheme 2** as the starting materials. ^{1}H NMR (500 MHz, DMSO-d6) δ 10.97 (s, 1H), 10.09 (s, 1H), 8.94 (s, 1H), 8.05 (d, *J* = 2.8 Hz, 1H), 7.84 (d, *J* = 9.0 Hz, 1H), 7.63 (d, *J* = 7.8 Hz, 1H), 7.50 – 7.43 (m, 2H), 7.38 (d, *J* = 7.8 Hz, 1H), 7.28 (s, 2H), 6.92 (d, *J* = 6.7 Hz, 2H), 5.81 (p, *J* = 8.7 Hz, 1H), 5.09 (dd, *J* = 13.3, 5.1 Hz, 1H), 4.41 (d, *J* = 17.3 Hz, 1H), 4.28 (d, *J* = 17.2 Hz, 1H), 4.05 – 3.94 (m, 3H), 3.16 (s, 4H), 3.04 – 2.85 (m, 3H), 2.62 – 2.53 (m, 4H), 2.46 – 2.35 (m, 7H), 2.34 – 2.19 (m, 7H), 2.01 – 1.96 (m, 1H), 1.87 (s, 3H), 1.82 – 1.53 (m, 13H). LC-MS (ESI): *m/z* 935.5 [M+H]⁺.

3-(5-(1-(3-((6-(4-(6-((6-acetyl-8-cyclopentyl-5-methyl-7-oxo-7,8-dihydropyrido[2,3-*d*]pyrimidin-2-yl)amino)pyridin-3-yl)piperazin-1-yl)hexyl)oxy)benzyl)piperidin-4-yl)-1-oxoisoindolin-2-yl)piperidine-2,6-dione (ALV-07-070-03)

The title compound **ALV-07-070-03** was prepared with similar protocols as **ALV-06-149-02**, using 3-hydroxybenzaldehyde **8a** and linker **9c** from **Scheme 2** as the starting materials. ^{1}H NMR

(500 MHz, DMSO-d6) δ 10.97 (s, 1H), 10.08 (s, 1H), 8.95 (s, 1H), 8.04 (d, J = 2.6 Hz, 1H), 7.84 (d, J = 9.0 Hz, 1H), 7.62 (d, J = 7.8 Hz, 1H), 7.48 – 7.43 (m, 2H), 7.38 (d, J = 7.9 Hz, 1H), 7.21 (d, J = 8.1 Hz, 2H), 6.87 (d, J = 8.3 Hz, 2H), 5.82 (p, J = 8.8 Hz, 1H), 5.09 (dd, J = 13.3, 5.1 Hz, 1H), 4.40 (d, J = 17.2 Hz, 1H), 4.27 (d, J = 17.2 Hz, 1H), 3.94 (t, J = 6.3 Hz, 2H), 3.16 – 3.12 (m, 4H), 2.95 – 2.86 (m, 3H), 2.59 (d, J = 16.9 Hz, 2H), 2.42 (s, 3H), 2.38 (dd, J = 13.4, 4.7 Hz, 1H), 2.35 – 2.28 (m, 6H), 2.28 – 2.20 (m, 3H), 2.05 – 1.95 (m, 3H), 1.92 – 1.85 (m, 3H), 1.78 – 1.67 (m, 8H), 1.60 – 1.55 (m, 2H), 1.51 – 1.41 (m, 5H), 1.39 – 1.34 (m, 2H). LC-MS (ESI): *m/z* 963.6 [M+H]$^+$.

3-(5-(1-(4-(2-(4-(6-((6-acetyl-8-cyclopentyl-5-methyl-7-oxo-7,8-dihydropyrido[2,3-*d*]pyrimidin-2-yl)amino)pyridin-3-yl)piperazin-1-yl)ethoxy)benzyl)piperidin-4-yl)-1-oxoisoindolin-2-yl)piperidine-2,6-dione (ALV-07-082-03)
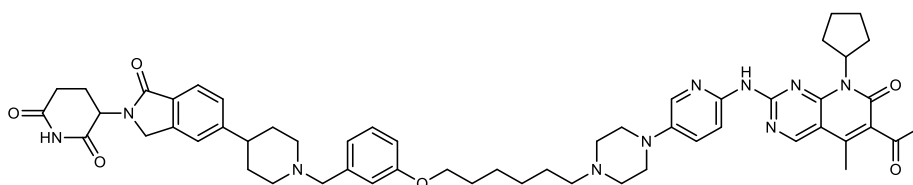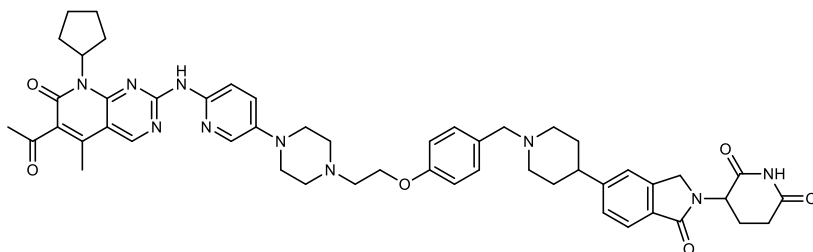

The title compound **ALV-07-082-03** was prepared with similar protocols as **ALV-06-149-02**, using 4-hydroxybenzaldehyde **8b** and linker **9d** from **Scheme 2** as the starting materials. ^{1}H NMR (500 MHz, DMSO-*d*$_6$) δ 10.97 (s, 1H), 10.08 (s, 1H), 8.94 (s, 1H), 8.05 (d, J = 3.0 Hz, 1H), 7.84 (d, J = 9.0 Hz, 1H), 7.63 (d, J = 7.9 Hz, 1H), 7.49 – 7.45 (m, 2H), 7.39 (d, J = 8.0 Hz, 1H), 7.23 (t, J = 8.4 Hz, 2H), 6.92 (d, J = 8.5 Hz, 2H), 5.81 (p, J = 8.5 Hz, 1H), 5.09 (dd, J = 13.3, 5.1 Hz, 1H), 4.41 (d, J = 17.2 Hz, 1H), 4.28 (d, J = 17.4 Hz, 1H), 4.12 (t, J = 5.7 Hz, 2H), 3.18 – 3.16 (m, 3H), 2.95 – 2.86 (m, 4H), 2.77 (t, J = 5.6 Hz, 2H), 2.69 – 2.64 (m, 4H), 2.62 – 2.56 (m, 2H), 2.43 – 2.36 (m, 4H), 2.30 (s, 2H), 2.26 – 2.21 (m, 2H), 2.20 – 2.16 (m, 2H), 2.09 – 2.03 (m, 2H), 2.01

– 1.95 (m, 2H), 1.89 – 1.84 (m, 2H), 1.80 – 1.74 (m, 4H), 1.72 – 1.67 (m, 2H), 1.61 – 1.55 (m, 2H). LC-MS (ESI): *m/z* 907.5 [M+H]$^+$.

Synthesis of ESW-08-032-01

tert-butyl 4-(2-(1-methyl-2,6-dioxopiperidin-3-yl)-1-oxoisoindolin-5-yl)piperidine-1-carboxylate (14)
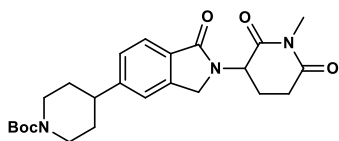
Potassium carbonate (189 mg, 1.4 mmol) was added to a solution of *tert*-butyl 4-(2-(2,6-dioxopiperidin-3-yl)-1-oxoisoindolin-5-yl)piperidine-1-carboxylate **6** (446 mg, 1.04 mmol) in DMF (10 mL) and stirred at rt for 10 min. Methyl iodide (0.970 mL, 1.56 mmol) was added to the solution in dropwise fashion at rt. The resulting mixture was heated to 60 °C for 4 h. The reaction mixture was diluted with EtOAc and washed with water (2x) and brine (2x). The organic layer was dried over Na$_2$SO$_4$, filtered, and concentrated *in vacuo*. Purification by flash chromatography (SiO$_2$: 0–100% EtOAc in hexanes) provided the title compound as a tan solid (233 mg, 51% yield). LC-MS (ESI): *m/z* 386.1 [M+H-tBu]$^+$, *m/z* 342.2 [M+H-Boc]$^+$.

1-methyl-3-(1-oxo-5-(piperidin-4-yl)isoindolin-2-yl)piperidine-2,6-dione hydrochloride (15)
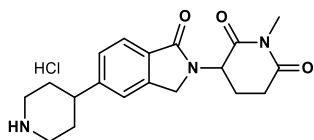
4 M HCl in dioxane (4 mL) was added to a solution of *tert*-butyl 4-(2-(1-methyl-2,6-dioxopiperidin-3-yl)-1-oxoisoindolin-5-yl)piperidine-1-carboxylate **14** (340 mg, 0.77 mmol) in CH$_2$Cl$_2$ (4 mL) and stirred at rt for 12 h. The reaction mixture was concentrated *in vacuo* to give

the title compound as a solid (278 mg, 91%), which was carried forward without purification. ^{1}H NMR (500 MHz, DMSO-d6) δ 9.14 – 9.01 (m, 2H), 7.70 (d, *J* = 7.5 Hz, 1H), 7.46 (s, 1H), 7.37 (s, 1H), 5.17 (dd, *J* = 12.8, 4.2 Hz, 1H), 4.44 (d, *J* = 17.1 Hz, 1H), 4.31 (d, *J* = 17.0 Hz, 1H), 3.36 (d, *J* = 11.2 Hz, 2H), 3.03 – 2.94 (m, 7H), 2.76 (d, *J* = 16.7 Hz, 1H), 2.43 – 2.34 (m, 1H), 2.02 – 1.90 (m, 5H). LC-MS (ESI): *m/z* 342.1 [M+H]+.

3-(5-(1-(4-(2-(4-(6-(((6-acetyl-8-cyclopentyl-5-methyl-7-oxo-7,8-dihydropyrido[2,3-d]pyrimidin-2-yl)amino)pyridin-3-yl)piperazin-1-yl)ethoxy)benzyl)piperidin-4-yl)-1-oxoisoindolin-2-yl)-1-methylpiperidine-2,6-dione (ESW-08-032-01)
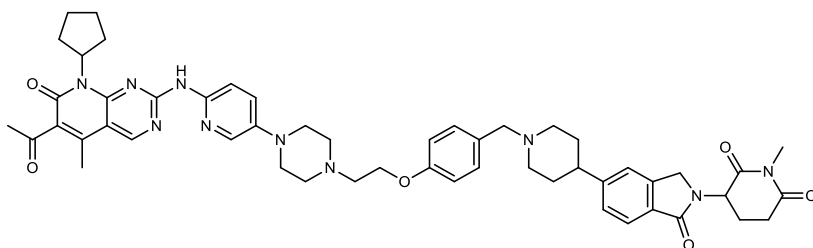

Reductive amination of *tert*-butyl 4-(2-(1-methyl-2,6-dioxopiperidin-3-yl)-1-oxoisoindolin-5-yl)piperidine-1-carboxylate **14** (50 mg, 0.13 mmol) and 4-(2-(4-(6-((6-acetyl-8-cyclopentyl-5-methyl-7-oxo-7,8-dihydropyrido[2,3-*d*]pyrimidin-2-yl)amino)pyridin-3-yl)piperazin-1-yl)ethoxy)benzaldehyde **13d** as described above afforded the title compound **ESW-08-032-01** as a yellow solid (10 mg, 7% yield). ^{1}H NMR (500 MHz, DMSO) δ 10.08 (s, 1H), 8.95 (s, 1H), 8.05 (d, *J* = 3.0 Hz, 1H), 7.84 (d, *J* = 9.0 Hz, 1H), 7.64 (d, *J* = 7.8 Hz, 1H), 7.50 – 7.45 (m, 2H), 7.39 (d, *J* = 7.9 Hz, 1H), 7.24 (d, *J* = 8.1 Hz, 2H), 6.92 (d, *J* = 8.1 Hz, 2H), 5.81 (p, *J* = 8.8 Hz, 1H), 5.16 (dd, *J* = 13.4, 5.1 Hz, 1H), 4.41 (d, *J* = 17.2 Hz, 1H), 4.27 (d, *J* = 17.1 Hz, 1H), 4.12 (t, *J* = 5.7 Hz, 2H), 3.45 (s, 2H), 3.17 (t, *J* = 5.1 Hz, 4H), 3.00 (s, 3H), 2.95 (m, 2H), 2.77 (m, 3H), 2.73 (m, 1H), 2.66 (t, *J* = 5.0 Hz, 4H), 2.42 (s, 3H), 2.40 – 2.35 (m, 1H), 2.30 (s, 3H), 2.24 (t, *J* = 9.7 Hz, 2H), 2.02 – 1.97 (m, 2H), 1.88 (m, 2H), 1.76 (m, 5H), 1.70 (m, 1H), 1.57 (q, *J* = 6.0 Hz, 2H), 1.23 (m, 1H). LC-MS (ESI): *m/z* 921.5 [M+H]+.

Chapter 5: DCAF11-mediated Protein Degradation using Covalent Degraders

Attributions

The work is this chapter is adapted from a manuscript in preparation entitled "Discovery of Covalent DCAF11-based Degraders" by Toenjes and You *et al*.

Contributions

S.T. designed and synthesized all compounds. I.N.Y performed the biological characterization of all compounds. K.A.D. conducted the mass spectrometry experiments. F.W. carried out all structural biology experiments. S.T. and I.N.Y wrote the manuscript. N.S.G. supervised all aspects of the project.

Funding Acknowledgments

Introduction

Traditional small-molecule therapeutics work by directly inhibiting the function of the targeted protein, typically through occupancy-driven pharmacology. Another emerging class of therapeutics impart their pharmacological effects through an event-driven process, in which the compound catalyzes a reaction between two proteins (Paiva and Crews, 2019). This method has been utilized for targeted protein degradation (TPD), in which a compound (molecular glue or heterobifunctional molecule) recruits an E3 ligase to a protein of interest (POI), leading to proximity induced ubiquitination and subsequential proteasomal dependent degradation of the POI (Burslem and Crews, 2020). Several advantages of TPD have been demonstrated, including the potential to abrogate scaffolding functions (Cromm *et al.*, 2018) and target proteins that have previously been classified as 'undruggable' (Burslem and Crews, 2020; Kronke *et al.*, 2014).

TPD approaches have garnered significant interest from both academic and industry labs, resulting in several compounds in clinical trials. However, only a limited number of E3 ligases have been successfully implemented for TPD. Out of the approximately 600 E3 ligases known, the majority of monovalent molecular glue degraders and bivalent PROTACs have used small molecule recruiters of the Cullin Ring E3 ubiquitin ligase substrate adaptor cereblon (CRBN) and von-Hippel-Landau tumor suppressor protein (VHL) (Ishida and Ciulli, 2021).

To expand the number of E3 ligases that can be leveraged for PROTAC development, several screening strategies have been employed, such as activity-based protein profiling (ABPP) and functional cell-based degradation assays. (Backus *et al.*, 2016; Zhang *et al.*, 2021). These efforts have led to the discovery of several electrophilic E3 ligase ligands, including ligands for DCAF11 (Zhang *et al.*, 2021), DCAF16 (Zhang *et al.*, 2019b), RNF114 (Tong et al., 2020), RNF4 (Ward *et al.*, 2019) and FEM1B (Henning *et al.*, 2022). Using similar approaches, we report here

the discovery of ZNL-06-031, an electrophilic ligand that targets the substrate adaptor protein DCAF11.

DCAF11 (also known as WDR23) is a substrate recognition protein for the cullin4-RING E3 ubiquitin ligase (CRL4) complex, which consists of cullin4 (CUL4) as a scaffold protein, DNA damage binding protein 1 (DDB1) as an adaptor protein and Ring-box 1 (RBX1) as the RING-finger protein (Zhou et al., 2020). DCAF11 has been reported to regulate the degradation of several proteins, including KAP1 (Le et al., 2021), CENP-A (Wang et al., 2021c), Stem-loop binding protein (Djakbarova et al., 2016), and p21 (Chen et al., 2017). Notably, DCAF11 has been reported to regulate the expression of NRF2 (Lo et al., 2017), independent of the canonical Kelch-like ECH-associated protein 1 (KEAP1)-CUL3 complex, suggesting that DCAF11 may have redox-sensing cysteines that could be targeted through cysteine-reactive electrophiles. Consistently, DCAF11 has previously been leveraged as an E3 ligase to induce protein degradation via electrophilic PROTACs (Zhang *et al.*, 2021). However, the potential for DCAF11 to be utilized as a general E3 ligase in the field of TPD was not fully explored, as the target scope of proteins degraded by DCAF11 (FKBP12 and androgen receptor) was limited. In addition, the potencies of the DCAF11-based PROTACs were relatively weak (degradation was only observed at µM concentrations), which may have been due to the lack of optimization of the DCAF11 ligand.

Here, we carry out cellular degradation screens to identify ZNL-06-031 as an electrophilic ligand for DCAF11. Through the conjugation of promiscuous kinase binder TL13-87 (Huang et al., 2018) and bromodomain and extra-terminal motif (BET) protein inhibitor JQ-1 to ZNL-06-031, we further explore the target scope of DCAF11-based PROTACs. In addition, we generate a DCAF11-degrader by conjugating of a VHL ligand to ZNL-06-031, which may serve as a useful tool compound to investigate DCAF11 function.

STT-02-040 is a multi-kinase degrader

In order to discover electrophilic ligands that can be utilized for PROTAC development, a set of electrophilic molecules were conjugated to the promiscuous kinase inhibitor TL13-87 (data not shown). We then employed an unbiased quantitative multiplexed proteomics approach to identify compounds that induced degradation of kinases and found that STT-02-040 (**Figure 5-1A**) induced significant downregulation of 32 proteins (out of 7369 identified proteins) by at least 50% (false discovery rate adjusted to p value < 0.05), of which 9 proteins (CDK12, CDK13, ABL2, ITK, PTK2B, CDK9, AURKA, WEE1 and AURKB) were kinases **(Figure 5-1B)**. As the other 22 non-kinase proteins were also downregulated upon treatment with 1 μM of TL12-186, a potent multi-kinase degrader (Huang *et al.*, 2018), downregulation of these proteins were likely secondary effects due to the degradation or inhibition of multiple kinases. Further immunoblot analysis on a subset of kinases confirmed downregulation of multiple kinases (CDK9, CDK12, CDK13, PTK2B, WEE1, AURKA and AURKB) to varying degrees (**Figure 5-1C**), validating STT-02-040 as a multi-kinase degrader.
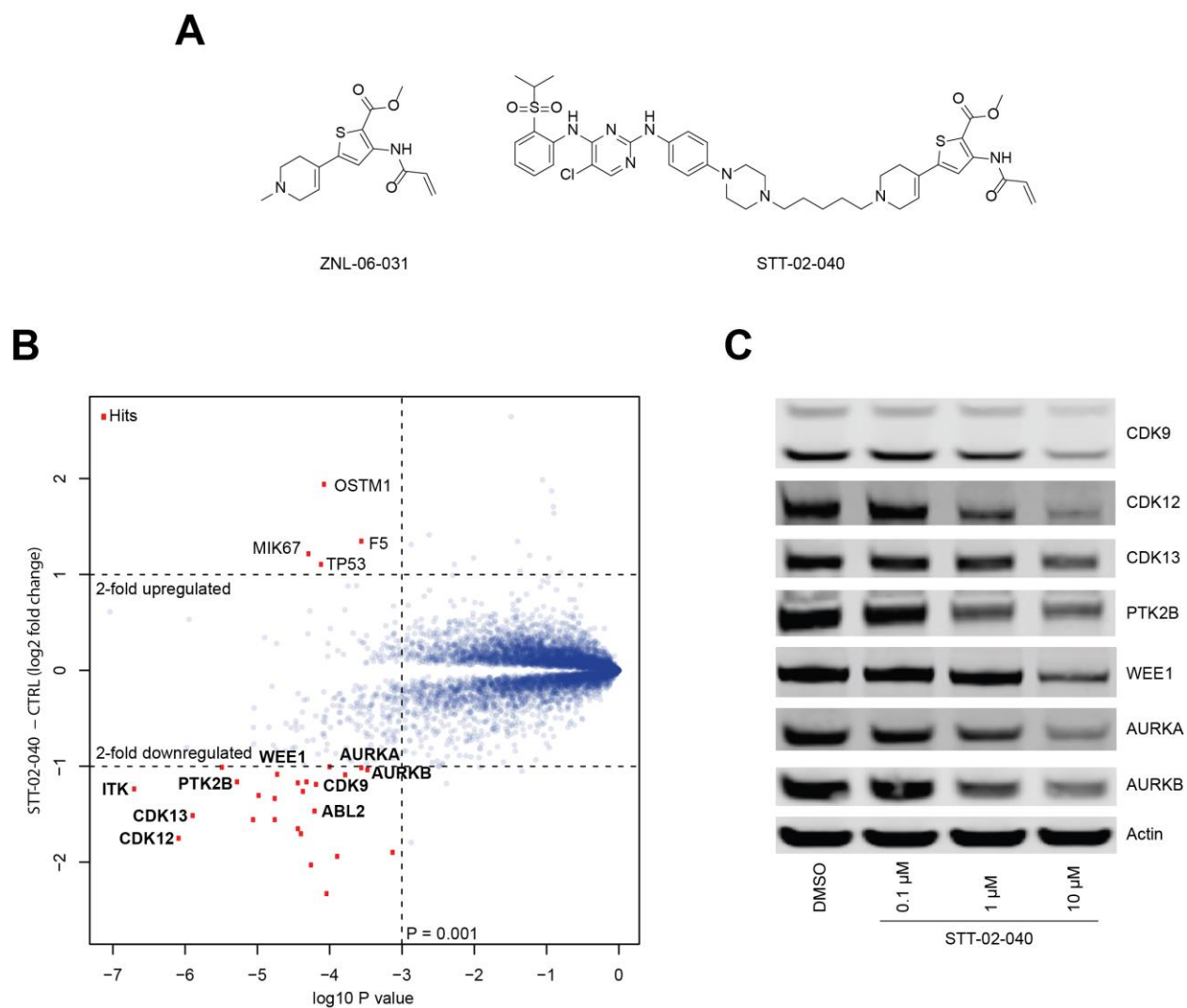
Figure 5-1. STT-02-040 induces degradation of multiple kinases. (A) Chemical structure of ZNL-06-031 and STT-02-040. (B) Quantitative proteomics profile (7,400 total proteins) of MOLT4 cells treated for 6 hours with 1 μM of STT-02-040. Significant changes were assessed using a moderated t-test as implemented in Bioconductor's Limma package. Only significantly downregulated kinases are shown. (C) Immunoblot analysis of CDK9, CDK12, CDK13, PTK2B, WEE1, AURKA, AURKB and Actin in MOLT4 cells treated with indicated concentrations of STT-02-040 for 6 hours.

STT-02-052 is a potent BRD4 degrader

Encouraged by our ability to employ ZNL-06-031 as a putative E3 ligase-recruiting ligand, we next sought to investigate the target scope of ZNL-06-031-mediated degradation beyond kinases. As BRD4 has been shown to be highly degradable with multiple reported PROTACs (Winter et al., 2017; Zengerle et al., 2015), we conjugated the BET bromodomain inhibitor JQ-1 to ZNL-06-031 through a PEG2 linker to generate STT-02-052 (**Figure 5-2A**).

We found that STT-02-052 induced potent BRD4 degradation in a dose-dependent manner after 5-hour treatment in MOLT4 cells, with degradation observed starting at 50 nM (**Figure 5-2B**). At concentrations of 5µM or higher, we observed diminished BRD4 degradation, consistent with the hook effect, in which independent engagement of STT-02-052 to BRD4 and its corresponding E3 ligase prevents productive ternary complex formation (An and Fu, 2018). To broadly assess degrader selectivity, MOLT4 cell lines were treated with 100 nM of STT-02-052 for 5 hours and an unbiased, multiplexed mass spectrometry-based proteomics analysis was performed (Donovan *et al.*, 2018). Of the 6225 proteins identified, BRD3 and BRD4 were revealed to be significantly downregulated, while BRD2 was largely spared (**Figure 5-2C**). As JQ-1 is a pan BET bromodomain inhibitor, further investigation will be needed to confirm the selectivity of STT-02-052 among the BET family of proteins.
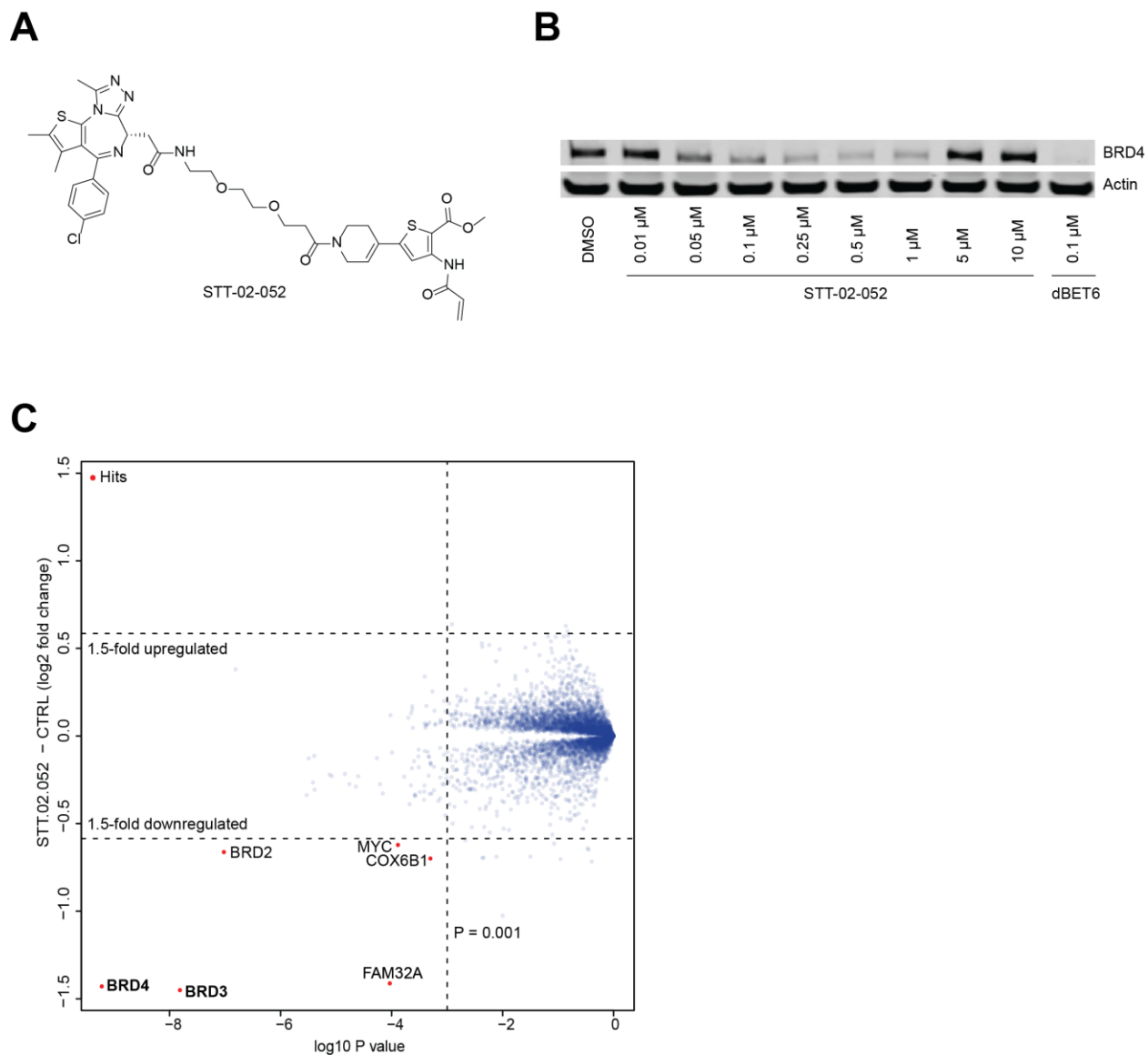
Figure 5-2. Characterization of STT-02-052. (A) Chemical structure of STT-02-052. (B) Immunoblot analysis of BRD4 and Actin in MOLT4 cells after treatment with STT-02-52 or dBET6 at indicated concentrations for 5 hours. (C) Quantitative proteomics profile (6,200 total proteins) of MOLT4 cells treated for 5 hours with 100 nM of STT-02-052. Significant changes were assessed using a moderated t-test as implemented in Bioconductor's Limma package.

To verify the mechanism of action of STT-02-052, we pre-treated cells with either the proteasome inhibitor bortezomib or the NEDD8-activating enzyme E1 (NAE1) inhibitor MLN4924, which prevents activation of cullin-RING ligases (CRL). We found that either pre-treatments prevented BRD4 destabilization (**Figure 5-3A**), demonstrating that STT-02-052-induced BRD4 degradation was dependent not only on the ubiquitin-proteasome system (UPS), but also CRL activation. In addition, pre-treatment with excess quantities of JQ-1 and ZNL-06-031 to compete for binding to BRD4 and the E3 ligase, respectively, prevented BRD4 degradation, demonstrating that engagement to BRD4 and the E3 ligase was required (**Figure 5-3A**). Finally, we synthesized STT-02-71-2, a noncovalent negative control analogue of STT-02-052 that exchanges the electrophilic acrylamide with a propionamide **(Figure 5-3B)**. STT-02-071-2 was unable to induce BRD4 downregulation at concentrations up to 10 µM, indicating that STT-02-052-induced BRD4 degradation was dependent on its electrophile **Figure 5-3C**).

A

STT-02-052 (100 nM)

| | - | + | - | + | - | + | - | + | - | + |

DMSO | Bortezomib 0.4 µM | MLN4924 1 µM | JQ-1 2 µM | ZNL-06-031 5 µM

B

STT-02-071-2

C

DMSO | 0.1 µM | 0.1 µM | 1 µM | 10 µM

STT-02-052 | STT-02-071-2
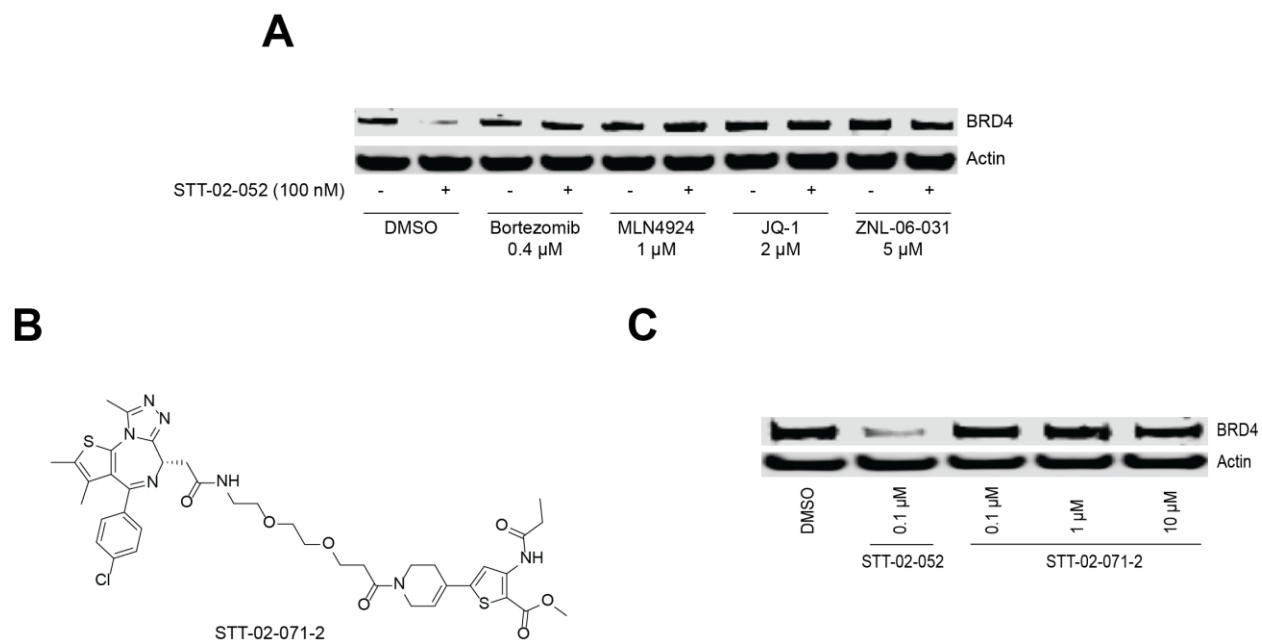
Figure 5-3. Mechanism of action of STT-02-052. (A) Immunoblot analysis of BRD4 and Actin in MOLT4 cells pre-treated with bortezomib, MLN4924, JQ-1 and ZNL-06-031 at indicated concentrations for 1 hour, followed by 5-hour treatment with 100 nM of STT-02-052. (B) Chemical structure of STT-02-071-2. (C) Immunoblot analysis of BRD4 and Actin in MOLT4 cells treated with STT-02-052 or STT-02-071-2 at indicated concentrations for 5 hours.

DCAF11 mediates degradation of ZNL-06-031 conjugated PROTACs

Having verified that ZNL-06-031 could be successfully incorporated into active PROTACs that targeted a diverse set of proteins, we next sought to identify what E3 ligase(s) complexes may be responsible. To do so, we carried out a targeted CRISPR screen of ubiquitin ligase component (Słabicki et al., 2020). While CRISPR/Cas9-mediated deletion of several genes were able to rescue STT-02-052-induced BRD4 degradation, components of the $CRL4^{DCAF11}$ E3 ligase complex (DCAF11, DDB1, CUL4A, CUL4B and RBX1) were enriched/scored highly (**Figure 5-4A**), suggesting that ZNL-06-031 covalently bound to the E3 ligase substrate adaptor DCAF11.

To further validate the CRISPR screen results, we synthesized STT-03-066, a desthiobitoin (DTB)-conjugated analogue of ZNL-06-031 (**Figure 5-4B**). In MOLT4 lysates, we found that STT-03-066 successfully engaged DCAF11, as we achieved robust pulldown at 1 µM after 2-hour incubation (**Figure 5-4C**). To assess the ability of ZNL-06-031 to engage DCAF11 in cells, we next performed live cell competitive pulldown assays in MOLT4 cells. Pre-treatment of live MOLT4 cells with ZNL-06-031 followed by pulldown of treated lysates with STT-03-066 demonstrated that ZNL-06-031 could bind to DCAF11 in cells to prevent pulldown by STT-03-066, with maximal engagement observed between 5 to 10 µM (**Figure 5-4D**). In addition, the reversible control analogue of ZNL-06-031, STT-02-060 (**Figure 5-4E**), displayed no competition with STT-03-066, indicating that the acrylamide of ZNL-06-031 was crucial for DCAF11 engagement (**Figure 5-4D**).
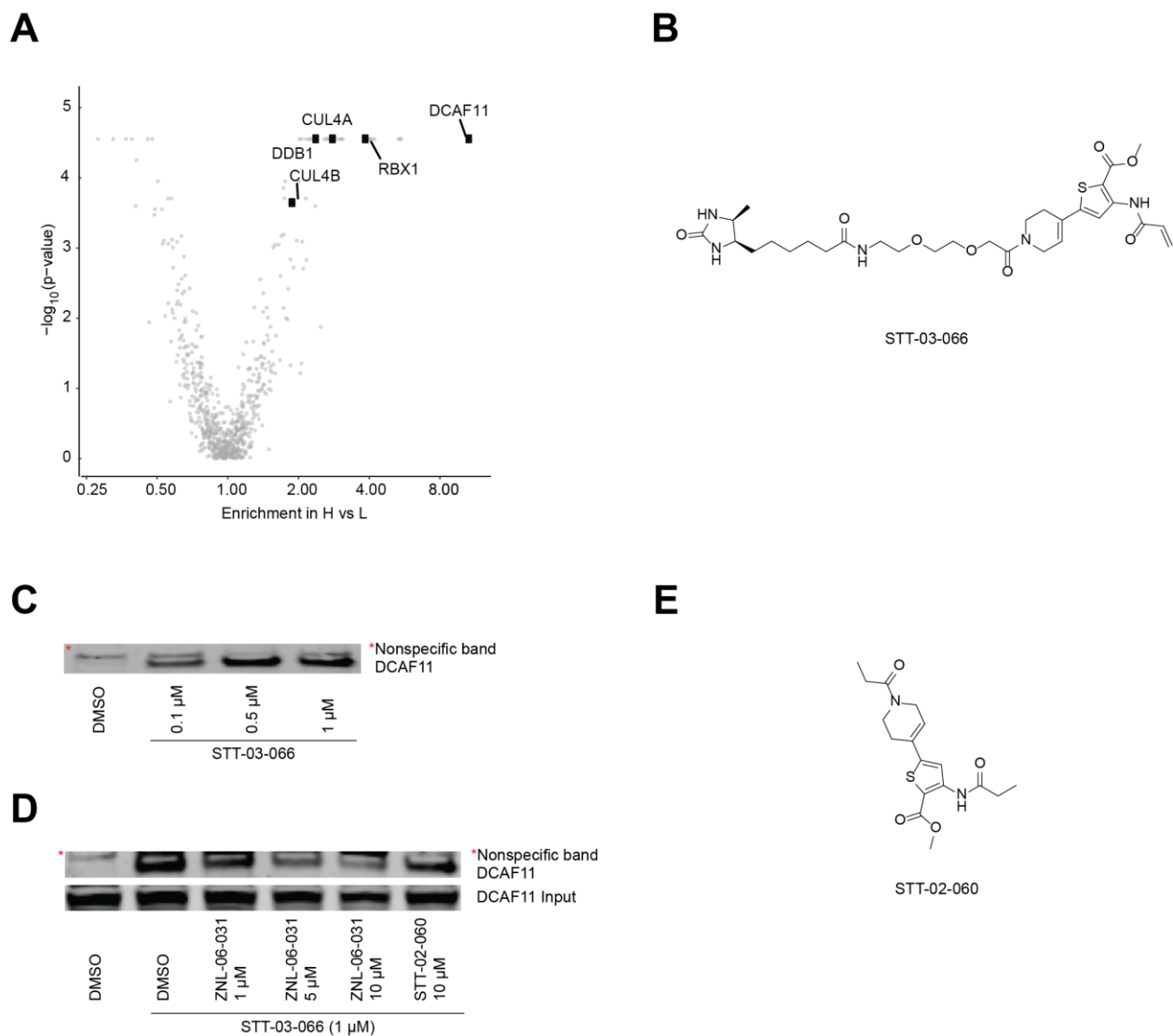
Figure 5-4. ZNL-06-031 covalently engages DCAF11 to mediate degradation. (A). E3 CRISPR screen in K562 cells expressing BD1-pCilantro with 3.3 µM of STT-02-052 for 10 hours. CRL4^{DCAF11} proteins are highlighted in dark black dots. (B) Chemical structure of STT-03-066. (C) MOLT4 lysates were incubated with indicated concentrations of STT-03-066 for 2 hours at 4 °C, followed by streptavidin pulldown and immunoblot analysis of DCAF11. * indicates a nonspecific band observed. (D) MOLT4 cells were treated with ZNL-06-031 or STT-02-060 for 2 hours at indicated concentrations, followed by cell lysis, incubation with STT-03-066 (1 µM) overnight at 4 °C, streptavidin pulldown and immunoblot analysis of DCAF11. * indicates a nonspecific band observed. (E) Chemical structure of STT-02-060.

As it was possible that DCAF11was engaged by ZNL-06-031 but did not mediate degradation of ZNL-06-031 conjugated PROTACs STT-02-040 and STT-02-052, we utilized CRISPR/Cas9 editing to generate DCAF11 knockout (KO) MOLT4 cells. Consistent with the CRISPR screen and DCAF11 engagement data, STT-02-040 and STT-02-052 both did not induce degradation of their respective kinase and bromodomain targets in DCAF11 KO MOLT4 cells (**Figure 5-5A** and **5B**). In addition, the anti-proliferative effects of STT-02-052 were dependent on DCAF11, as STT-02-052 lost 4 fold potency in DCAF11 KO MOLT4 cells relative to wild-type (WT) MOLT4 cells, while the negative control analogue STT-02-071-2 displayed similar potencies in both cell lines (**Figure 5-5C**). Overall, the data indicate that ZNL-06-031 conjugated PROTACs directly recruit DCAF11 to induce degradation of their respective targets.
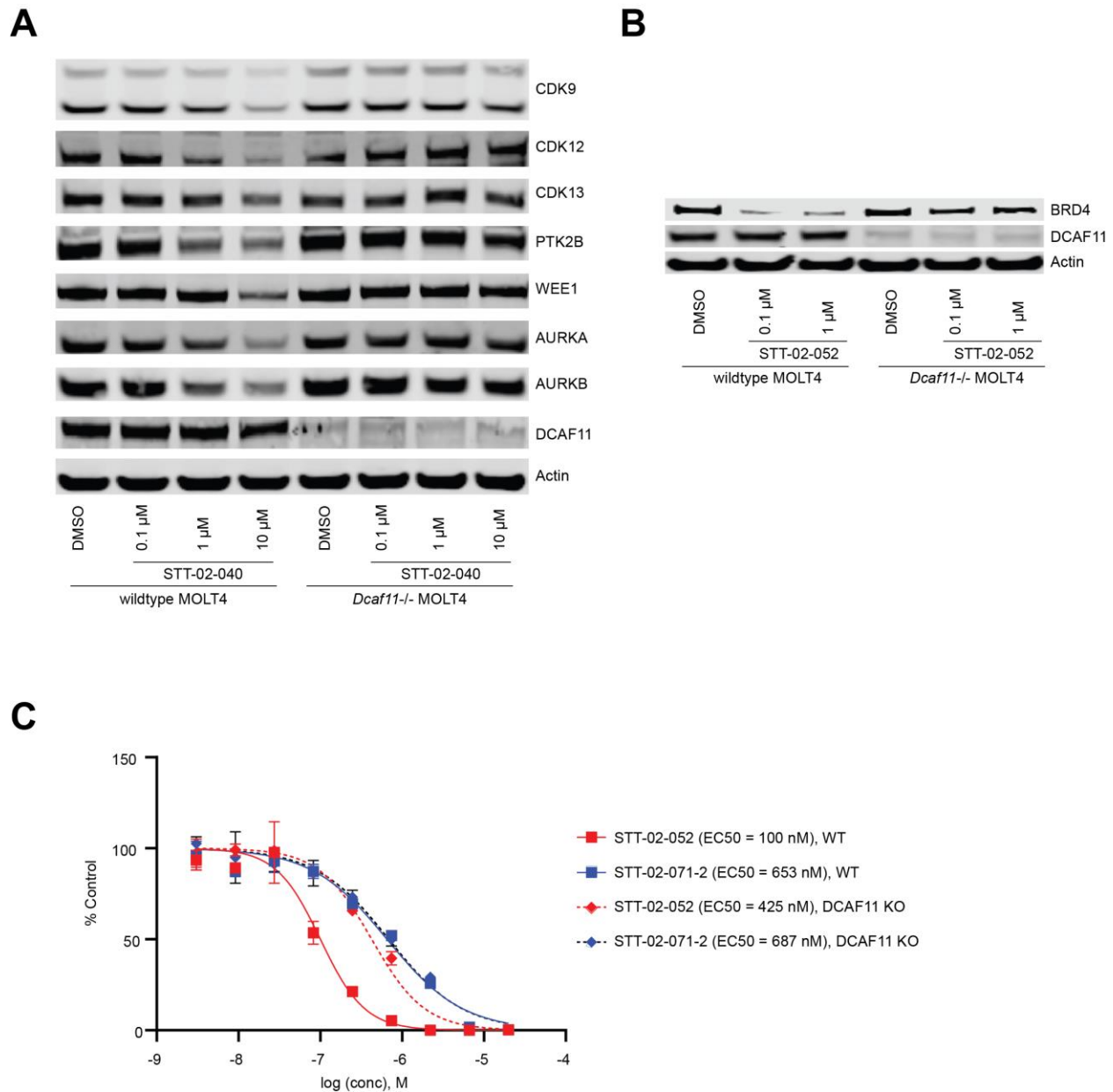
Figure 5-5. STT-02-040 and STT-02-052 display DCAF11-dependent degradation. (A) Immunoblot analysis of CDK9, CDK12, CDK13, PTK2B, WEE1, AURKA, AURKB, DCAF11 and Actin in wildtype or DCAF11$^{-/-}$ MOLT4 cells treated with indicated concentrations of STT-02-040 for 6 hours. (B) Immunoblot analysis of BRD4, DCAF11 and Actin in wildtype or DCAF11$^{-/-}$ MOLT4 cells treated with indicated concentrations of STT-02-052 for 5 hours. (C) Proliferation assays were carried out by treating wildtype or DCAF11$^{-/-}$ MOLT4 cells with indicated concentrations of STT-02-052 or STT-02-071-2 for 72 hours. Anti-proliferative effects of the compounds were assessed using Cell Titer Glo (Promega) and EC$_{50}$ values were calculated using the Graphpad Prism nonlinear regression curve fit.

Development of VHL-based DCAF11 degraders

With the development of a DCAF11 binder, we next sought to assess the consequences of recruiting DCAF11 to other E3 ligases, as had been previously reported for homo- and hetero-PROTACs for CRBN and VHL (Girardini et al., 2019; Maniaci et al., 2017; Powell et al., 2021). Through the conjugation of ZNL-06-031 with the VHL ligand at two different exit vectors, we generated STT-02-049-2 and STT-03-029-3 (**Figure 5-6A**). Both compounds induced potent DCAF11 degradation, but spared VHL protein levels in MOLT4 cells (**Figure 5-6B**). Further mechanistic studies will be necessary in order to validate the mechanism of action of the DCAF11 degraders.

To assess selectivity of the DCAF11 degraders, MOLT4 cells were treated with STT-03-029-3 for 5 and 16 hours and subjected to an unbiased multiplexed mass spectrometry-based proteomics analysis (Donovan *et al.*, 2018). Of ~6300 proteins identified in both analyses, DCAF11 was shown to be the most downregulated target (**Figure 5-6C and 6D**), suggesting STT-3-029-3 to be a potent DCAF11 degrader. Notably, NMRAL1 and MTPN were both significantly downregulated by STT-03-029-3 after 5- and 16-hour treatments, suggesting that these two proteins may be potential off-targets of ZNL-06-031. Collectively, we show that DCAF11 is susceptible to PROTAC mediated degradation and characterize STT-03-029-3 as a chemical tool compound that can be used to explore DCAF11 function.
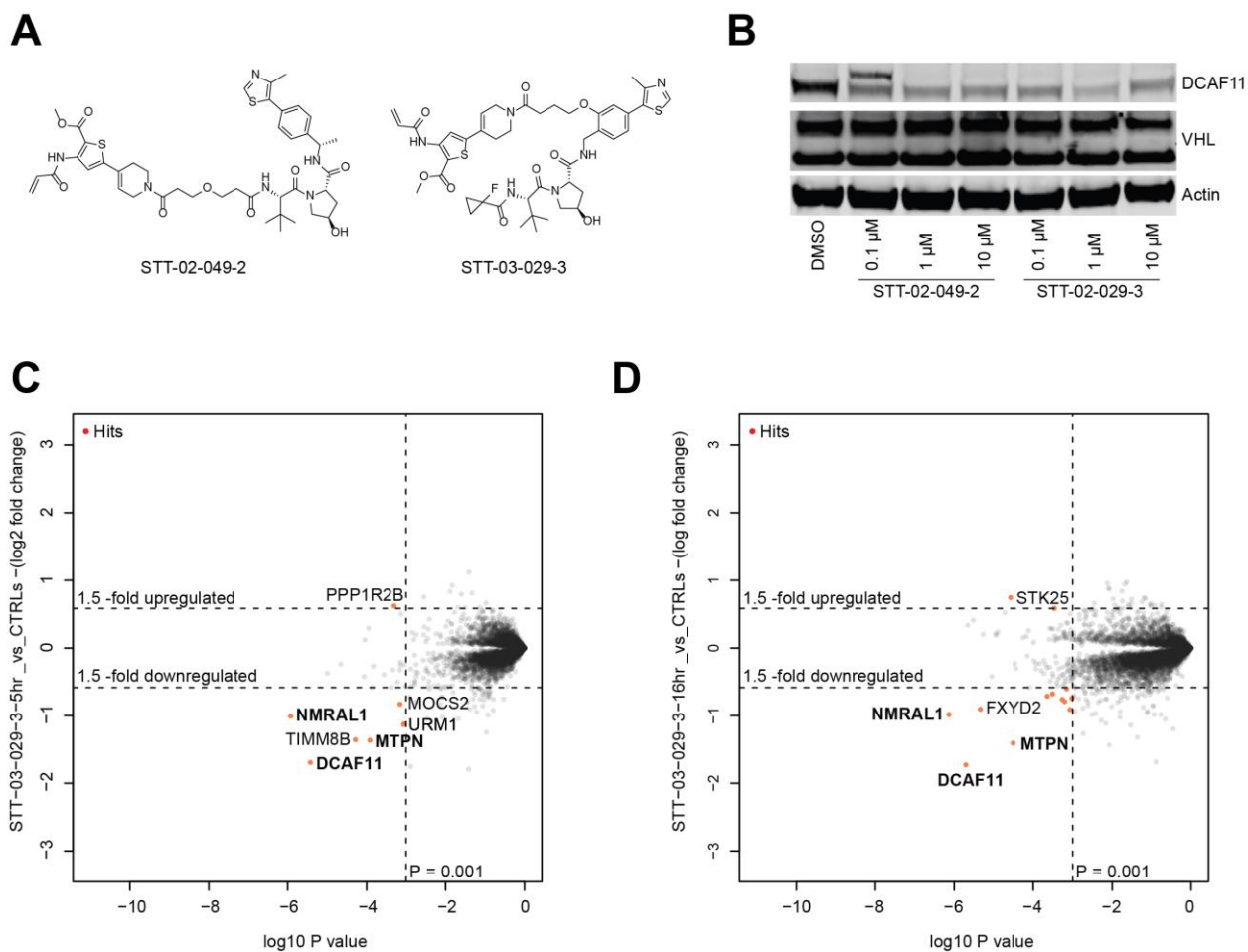
Figure 5-6. Characterization of VHL-DCAF11 PROTACs. (A) Chemical structures of STT-02-049-2 and STT-03-029-3. Immunoblot analysis of DCAF11, VHL and Actin in MOLT4 cells treated with indicated compounds at indicated concentrations for 6 hours. Quantitative proteomics profile (6,300 total proteins) of MOLT4 cells treated with 1 µM of STT-03-029-3 for (C) 5 hours and (D) 16 hours. Significant changes were assessed using a moderated t-test as implemented in Bioconductor's Limma package.

Conclusion

The TPD field has expanded exponentially over the past few years, with several PROTACs currently in clinical trials. Although different E3 ligase ligands have been reported (Henning *et al.*, 2022; Hines *et al.*, 2019; Naito et al., 2019; Tong *et al.*, 2020; Zhang *et al.*, 2019b; Zhang *et al.*, 2021), CRBN- and VHL-recruiting PROTACs continue to dominate the TPD field, highlighting the challenges of identifying new E3 ligases for PROTAC development.

Here, we address this challenge through the characterization of ZNL-06-031 as a covalent DCAF11 ligand. While electrophilic PROTACs acting through DCAF11 have previously been reported, these PROTACs only explored the degradation of FKBP12 and androgen receptor at single digit µM concentrations (Zhang *et al.*, 2021). Therefore, additional studies to characterize the potential of DCAF11-based PROTACs are necessary. Through the development of STT-02-040, we demonstrate that multiple kinases can be downregulated through DCAF11-mediated PROTACs, although the effects were not as robust as observed with CRBN- or VHL-recruiting PROTACs. We further characterize STT-02-052, a BRD4 degrader, to illustrate that potent PROTACs that display degradation at nanomolar concentrations can be generated through the recruitment of DCAF11.

Further mechanistic studies are still necessary in order to understand the binding mode of ZNL-06-031. As the cysteine that ZNL-06-031 covalently labels has yet to be identified, we are currently carrying out chemoproteomics and mutagenesis studies. In addition, structural biology efforts are on-going in attempt to obtain a crystal structure of DCAF11, as well as a co-crystal structure with either ZNL-06-031 and STT-02-052.

In addition to investigating the ability to recruit DCAF11 for PROTAC development, we also generated hetero-PROTACs conjugating DCAF11 ligand ZNL-06-031 with the VHL ligand.

This effort led to potent DCAF11 degraders, which may be used as a chemical probe to further explore pharmacological downregulation of DCAF11 signaling.

Materials and methods

Cell lines. Wildtype or DCAF11-/- MOLT4 cells were cultured in RPMI-1640 media supplemented with 10% FBS and 1% penicillin/streptomycin in a 37°C incubator with 5% CO_2.

Immunoblots and antibodies. Cells were lysed in M-PER buffer (Thermo Scientific) containing protease/phosphatase inhibitor cocktail (Roche). Protein concentration was measured using a BCA assay (Pierce). Equivalent amounts of each sample were loaded on 4-12% Bis-Tris gels (Invitrogen), transferred to nitrocellulose membranes, and immunoblotted with antibodies against CDK9 (Cell Signaling Technology, #2316), CDK12 (Cell Signaling Technology, #11973), CDK13 (ThermoFisher, #PA5-67681), PTK2B (Cell Signaling Technology, #3292), WEE1 (Cell Signaling Technology, #4936), AURKA (Cell Signaling Technology, #14475), AURKB (Cell Signaling Technology, #3094), VHL (Cell Signaling Technology, #68547), Actin (Cell Signaling Technology, #3700), BRD4 (Fortis Life Sciences, #A301-985A-M) and DCAF11 (Novus, NBP2-92244). IRDye®800-labeled goat anti-rabbit IgG and IRDye®680-labeled goat anti-mouse IgG (LI-COR) secondary antibodies were used and detected on an Odyssey CL_x system.

Proliferation assay. Proliferation assays were performed by treating wildtype or DCAF11-/- MOLT4 cells with at the concentrations indicated for 72 h. Anti-proliferative effects of compounds were assessed using CellTiter-Glo (Promega). EC_{50}s were calculated with Graphpad Prism nonlinear regression curve fit.

Lysate pulldown. Indicated cell lysates were lysed with Pierce™ IP Lysis Buffer (ThermoFisher) containing protease/phosphatase inhibitor cocktail (Roche). After clarification (21000 RCF for 15

178

minutes), lysates were incubated with indicated concentrations of STT-03-066 at 4 °C for 2 hours, using 500 µg of lysates per sample. Lysates were then incubated with Dynabeads™ MyOne™ Streptavidin C1 (40 µL, ThermoFisher) for 1.5 hours at 4 °C. Beads were washed with IP lysis buffer four times and boiled at 95 °C for 5 minutes in 50 µL of 2× lithium dodecyl sulfate (LDS) + 5% β-mercaptoethanol. Lysates were probed for specified proteins by immunoblotting.

Cellular target engagement and competition with STT-03-066. 10 x 10^6 MOLT4 cells were plated in 3 mL of media. Cells were treated with DMSO or indicated concentrations of ZNL-06-031 for 2 hours. Cells were then lysed with 230 µL of Pierce™ IP Lysis Buffer (ThermoFisher) containing protease/phosphatase inhibitor cocktail (Roche). After clarification (21000 RCF for 15 minutes), 10 µL of each sample was combined with with 4× LDS + 10% β-mercaptoethanol (ratio 3:1), boiled for 5 min and set aside for input loading control (later to be loaded directly on the gel). Then, 200 µl of each lysate sample was incubated with 1 µM of STT-03-066 overnight at 4 °C and processed as described in the lysate pulldown protocol.

BISON CRISPR – BRD4(BD) stability reporter screen. The BISON CRISPR library targets 713 E1, E2, and E3 ubiquitin ligases, deubiquitinases, and control genes and contains 2,852 guide RNAs. It was cloned into the pXPR003 as previously described by the Broad Institute Genome Perturbation Platform (GPP). The virus for the library was produced in a T-175 flask format, as described above with the following adjustments: 1.8×10^7 HEK293T cells in 25 mL complete DMEM medium, 244 µL of TransIT-LT1, 5 mL of OPTI-MEM, 32 µg of library, 40 µg psPAX2, and 4 µg pVSV-G in 1 mL OPTI-MEM. 10% (v/v) of BISON CRISPR library was infected to 2×10^6 of K562$_{Cas9}$ cells that has previously transduced with BRD4(BD1)$_{eGFP}$ or

BRD4(BD2)$_{eGFP}$ stability reporter. Nine days later cells were treated with 3 µM STT-02-052 or

DMSO for 16 hours and the BRD4(BD) stable population were separated using fluorescence

activated cell sorting. Two populations were collected (top 5% and lowest 5%) based on the

BRD4(BD)$_{eGFP}$ to mCherry mean fluorescent intensity (MFI) ratio on MA900 Cell Sorter (Sony).

Sorted cells were harvested by centrifugation and resuspended in multiple direct lysis buffer

reactions (1 mM CaCl$_2$, 3 mM MgCl$_2$, 1 mM EDTA, 1% Triton X-100, Tris pH 7.5 - with

freshly supplemented 0.2 mg/mL Proteinase) with 1×10^6 cells per 100 µL reaction. The sgRNA

sequence was amplified in a first PCR reaction with eight staggered forward primers. 20 µL of

direct lysed cells was mixed with 0.04U Titanium Taq (Takara Bio 639210), 0.5 x Titanium Taq

buffer, 800 µM dNTP mix, 200 nM SBS3-Stagger-pXPR003 forward primer, 200 nM SBS12-

pXPR003 reverse primer in a 50 µL reaction (cycles: 5 minutes at 94°C, 15 x (30 sec at 94°C, 15

sec at 58°C, 30 sec at 72°C), 2 minutes at 72°C). 2 µL of the first PCR reaction was used as the

template for 15 cycles of the second PCR, where Illumina adapters and barcodes were added

(0.04U Titanium Taq, 1 x Titanium Taq buffer, 800 µM dNTP mix, 200 nM P5-SBS3 forward

primer, 200 nM P7-barcode-SBS12 reverse primer). An equal amount of all samples was pooled

and subjected to preparative agarose electrophoresis followed by gel purification (Qiagen).

Eluted DNA was further purified by NaOAc and isopropanol precipitation. Amplified sgRNAs

were quantified using Illumina NextSeq platform (Genomics Platform, Broad Institute). Read

counts for all guides targeting the same gene were used to generate p-values. The screen was

analyzed by comparing stable populations (top 5% eGFP/mCherry expression) to unstable

populations (lowest 5% eGFP/mCherry expression). Hits enriched in BRD4(BD) stable

population with FDR < 0.05 are labelled on the plot.

Generation of DCAF11 knockout cells. DCAF11 knockouts were generated in MOLT4 cells via CRISPR-Cas9 editing. ALT-R CRISPR RNA (crRNA) and trans-activating CRISPR RNA (tracrRNA) (Integrated DNA Technologies) were resuspended in nuclease-free duplex buffer At final at a final concentration of 100 µM. Equal volumes of crRNA and tracrRNA were mixed and heated for 5 min at 95 °C. After heating, the complex was gradually cooled to room temperature. The oligo complex was then incubated at room temperature for 20 min with Cas9 Nuclease V3 (Integrated DNA Technologies) to form the ribonucleoprotein complex. Subsequently, the RNP complex and an electroporation enhancer (IDT) were co-electroporated into MOLT4 cells using the Neon Electroporator (ThermoFisher). Cells were seeded into media with HDR enhancer (Integrated DNA Technologies). Subsequently, single cells were isolated via FACS sorting and DCAF11 levels were analyzed immunoblot analysis.

Proteomics. MOLT4 cells were treated with STT-02-040 (1 µM, 6 hours), STT-02-052 (100 nM, 5 hours) and STT-03-029-3 (1 µM, 5 and 16 hours). Cell lysis and Tandem Mass Tagged (TMT) tryptic peptides were prepared for LC-MS analysis following procedures previously reported (Donovan *et al.*, 2018).

Data were collected using an Orbitrap Fusion Lumos mass spectrometer (Thermo Fisher Scientific, San Jose, CA, USA) coupled with a Proxeon EASY-nLC 1200 LC pump (Thermo Fisher Scientific). Peptides were separated on a 50 cm 75 µm inner diameter EasySpray ES903 microcapillary column (Thermo Fisher Scientific) using a 190 min gradient of 6 - 27% acetonitrile in 1.0% formic acid with a flow rate of 300 nL/min.

Each analysis used a MS3-based TMT method as described previously (McAlister *et al.*, 2014). The data were acquired using a mass range of m/z 340 – 1350, resolution 120,000, AGC target 5 $\times 10^5$, maximum injection time 100 ms, dynamic exclusion of 120 s for the peptide measurements

in the Orbitrap. Data dependent MS2 spectra were acquired in the ion trap with a normalized collision energy (NCE) set at 35%, AGC target set to 1.8×10^4 and a maximum injection time of 120 ms. MS3 scans were acquired in the Orbitrap with HCD collision energy set to 55%, AGC target set to 2×10^5, maximum injection time of 150 ms, resolution at 50,000 and with a maximum synchronous precursor selection (SPS) precursors set to 10.

Proteome Discoverer 2.4 (Thermo Fisher Scientific) was used for .RAW file processing and controlling peptide and protein level false discovery rates, assembling proteins from peptides, and protein quantification from peptides. MS/MS spectra were searched against a Swissprot human database (February 2020) with both the forward and reverse sequences as well as known contaminants such as human keratins. Database search criteria were as follows: tryptic with two missed cleavages, a precursor mass tolerance of 20 ppm, fragment ion mass tolerance of 0.6 Da, static alkylation of cysteine (57.02146 Da), static TMT labeling of lysine residues and N-termini of peptides (229.16293 Da), and variable oxidation of methionine (15.99491 Da). TMT reporter ion intensities were measured using a 0.003 Da window around the theoretical m/z for each reporter ion in the MS3 scan. The peptide spectral matches with poor quality MS3 spectra were excluded from quantitation (summed signal-to-noise across channels < 100 and precursor isolation specificity < 0.5), and the resulting data was filtered to only include proteins with a minimum of 2 unique peptides quantified. Reporter ion intensities were normalized and scaled using in-house scripts in the R framework (Team, 2014). Statistical analysis was carried out using the limma package within the R framework (Ritchie *et al.*, 2015).

General Chemistry Methods. Analytical grade solvents and commercially available reagents were purchased from commercial sources and used directly without further purification unless otherwise stated. Thin-layer chromatography (TLC) was carried out on Merck 60 F254 precoated, glass silica plates which were visualized by ultraviolet light. Experiments were conducted under ambient conditions unless otherwise stated. ^{1}H-NMR, ^{13}C-NMR, and ^{19}F-NMR spectra were recorded at room temperature using a Bruker 500 (^{1}H-NMR at 500 MHz, ^{13}C-NMR at 125 MHz, and ^{19}F-NMR at 471 MHz). Chemical shifts are reported in ppm with reference to solvent signals [^{1}H-NMR: CDCl$_3$ (7.26 ppm), DMSO-d6 (2.50 ppm); ^{13}C-NMR: CDCl$_3$ (77.16 ppm), DMSO-d6 (39.52 ppm)]. Signal patterns are indicated as s, singlet; br s, broad singlet; d, doublet; t, triplet, q, quartet; p, pentet; and m, multiplet. Mass spectrometry (MS) analysis was obtained on a Waters Acquity UPLC-MS system using electrospray ionization (ESI) in positive ion mode, reporting the molecular ion [M+H]$^+$, [M+Na]$^+$, or a suitable fragment ion. Flash chromatography purification was conducted using an ISCO CombiFlash RF+ with RediSep Rf silica cartridges. Preparative reverse-phase HPLC purification was conducted using a Waters model 2545 pump and 2489 UV/Vis detector using SunFire Prep C18 5 µm columns (18x100 mm, 20 mL/min flow rate; 30x250 mm, 40 mL/min flow rate), and a gradient solvent system of water (0.035% TFA)/methanol (0.035% TFA) or water (0.035% TFA)/acetonitrile (0.035% TFA).

Abbreviations. DCM, dichloromethane; DIPEA, diisopropylethylamine; DMF, N,N-dimethylformamide; DMSO, dimethyl sulfoxide; EtOAc, ethyl acetate; HATU, hexafluorophosphate azabenzotriazole tetramethyl uronium; HPLC, high-performance liquid chromatography; MeCN, acetonitrile; MeOH, methanol; TEA, triethylamine; TFA, trifluoroacetic acid; UPLC-MS, ultra-performance liquid chromatography-mass spectrometry;

Experimental procedures and characterization

Synthesis of ZNL-06-031 and STT-02-060
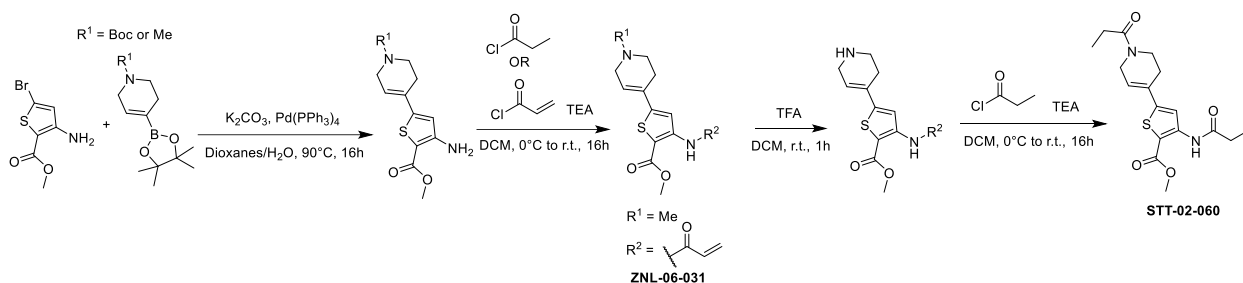
Methyl 3-amino-5-(1-methyl-1,2,3,6-tetrahydropyridin-4-yl)thiophene-2-carboxylate
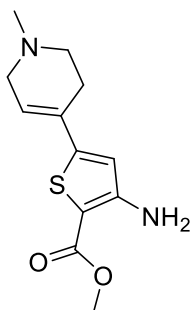
To a solution of methyl 3-amino-5-bromothiophene-2-carboxylate (500 mg, 2.12 mmol, 1 eq) in degassed 1,4-dioxane (10 mL) and water (2.5 mL), 1-methyl-4-(4,4,5,5-tetramethyl-1,3,2-dioxaborolan-2-yl)-1,2,3,6-tetrahydropyridine (520 mg, 2.33 mmol, 1.1 eq), potassium carbonate (673 mg, 4.87 mmol, 2.3 eq) and tetrakis(triphenylphosphine)palladium(0) (122 mg, 0.106 mmol, 0.05 eq) were added under inert atmosphere. The reaction mixture was stirred for 16 hours at 90 °C. The reaction was then cooled and suspended in brine and ethyl acetate. The organic layer was dried over NaSO₄, filtered, and concentrated in vacuo. The crude material was purified via silica gel chromatography (20% to 70% ethyl acetate/hexanes) to afford the title compound as a dark orange oil (310 mg, 58% yield). LCMS (ESI) calculated for [M+H]⁺ 253.09, found 253.11.

Tert-butyl   4-(4-amino-5-(methoxycarbonyl)thiophen-2-yl)-3,6-dihydropyridine-1(2H)-carboxylate
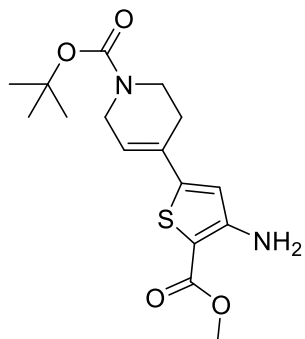
To a solution of methyl 3-amino-5-bromothiophene-2-carboxylate (1.25 g, 5.29 mmol, 1 eq) in degassed 1,4-dioxane (15 mL) and water (3.8 mL), tert-butyl 4-(4,4,5,5-tetramethyl-1,3,2-dioxaborolan-2-yl)-3,6-dihydropyridine-1(2H)-carboxylate (1.8 g, 5.82 mmol, 1.1 eq), potassium carbonate (1.68 g, 12.2 mmol, 2.3 eq) and tetrakis(triphenylphosphine)palladium(0) (306 mg, 0.265 mmol, 0.05 eq) were added under inert atmosphere. The reaction mixture was stirred for 16 hours at 90 °C. The reaction was then cooled and suspended in brine and ethyl acetate. The organic layer was dried over NaSO₄, filtered, and concentrated in vacuo. The crude material was purified via silica gel chromatography (20% to 70% ethyl acetate/hexanes) to afford the title compound as a dark orange oil (871 mg, 49% yield). LCMS (ESI) calculated for [M+H]⁺ 339.13, found 339.10.

Methyl   3-acrylamido-5-(1-methyl-1,2,3,6-tetrahydropyridin-4-yl)thiophene-2-carboxylate (ZNL-06-031)
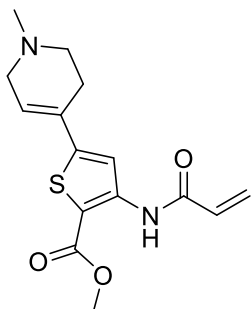
A solution of methyl 3-amino-5-(1-methyl-1,2,3,6-tetrahydropyridin-4-yl)thiophene-2-carboxylate (30 mg, 0.119 mmol, 1 eq) and triethylamine (24.9 µL, 0.178 mmol, 1.5 eq) in dichloromethane (0.5 mL) was cooled to 0 °C. After the dropwise addition of acryloyl chloride (14.5 µL, 0.178 mmol, 1.5 eq), the reaction was stirred overnight and allowed to warm to room temperature. The reaction mixture was then suspended in brine and dichloromethane. The organic layer was dried over NaSO$_4$, filtered, and concentrated in vacuo. The crude oil was then diluted with 1.0 mL of dimethyl sulfoxide and purified by reverse-phase prep HPLC (95 to 15% H$_2$O/MeOH, 40 mL/min, 45 min). Lyophilization from H$_2$O/MeCN provided the title compound as a white powder (16.7 mg, 31% yield TFA salt). LCMS (ESI) calculated for [M+H]$^+$ 307.10, found 307.01.

Tert-butyl 4-(4-acrylamido-5-(methoxycarbonyl)thiophen-2-yl)-3,6-dihydropyridine-1(2H)-carboxylate

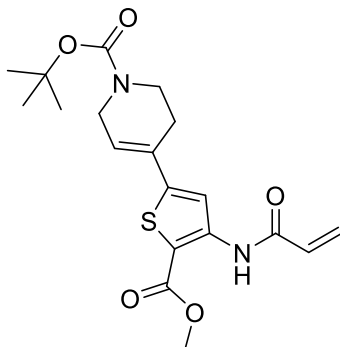A solution of tert-butyl 4-(4-amino-5-(methoxycarbonyl)thiophen-2-yl)-3,6-dihydropyridine-1(2H)-carboxylate (400 mg, 1.18 mmol, 1 eq) and triethylamine (247 µL, 1.77 mmol, 1.5 eq) in dichloromethane (5 mL) was cooled to 0 °C. After the dropwise addition of acryloyl chloride (144 µL, 1.77 mmol, 1.5 eq), the reaction was stirred overnight and allowed to warm to room temperature. The reaction mixture was then suspended in brine and dichloromethane. The organic

layer was dried over NaSO₄, filtered, and concentrated in vacuo. The crude material was purified via silica gel chromatography (20% to 70% ethyl acetate/hexanes) to afford the title compound as a yellow oil (270 mg, 58.2% yield). LCMS (ESI) calculated for [M+H]⁺ 393.14, found 393.09.

Tert-butyl   4-(5-(methoxycarbonyl)-4-propionamidothiophen-2-yl)-3,6-dihydropyridine-1(2H)-carboxylate
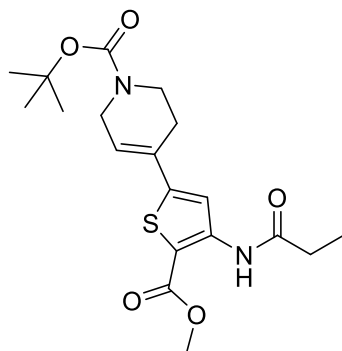
A solution of tert-butyl 4-(4-amino-5-(methoxycarbonyl)thiophen-2-yl)-3,6-dihydropyridine-1(2H)-carboxylate (150 mg, 0.443 mmol, 1 eq) and triethylamine (90 µL, 0.665 mmol, 1.5 eq) in dichloromethane (1.7 mL) was cooled to 0 °C. After the dropwise addition of propionyl chloride (58 µL, 0.665 mmol, 1.5 eq), the reaction was stirred overnight and allowed to warm to room temperature. The reaction mixture was then suspended in brine and dichloromethane. The organic layer was dried over NaSO₄, filtered, and concentrated in vacuo. The crude material was purified via silica gel chromatography (10% to 70% ethyl acetate/hexanes) to afford the title compound as a clear yellow oil (111 mg, 63.6% yield). LCMS (ESI) calculated for [M+H]⁺ 395.16, found 395.12.

Methyl 3-acrylamido-5-(1,2,3,6-tetrahydropyridin-4-yl)thiophene-2-carboxylate
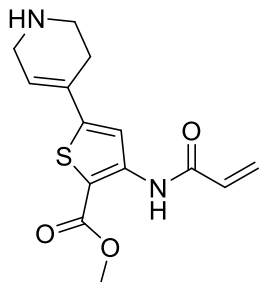
A solution of tert-butyl 4-(4-acrylamido-5-(methoxycarbonyl)thiophen-2-yl)-3,6-dihydropyridine-1(2H)-carboxylate (270 mg, 0.688 mmol, 1 eq) in dichloromethane (2.75 mL) and trifluoracetic acid (0.68 mL) was stirred at room temperature for 1 hour. The reaction mixture was concentrated to provide the titled compound as a dark brown oil (245 mg, 89% yield TFA salt). The product was shown pure via mass spec, LCMS (ESI) calculated for $[M+H]^+$ 293.08, found 293.05.

Methyl 3-propionamido-5-(1,2,3,6-tetrahydropyridin-4-yl)thiophene-2-carboxylate
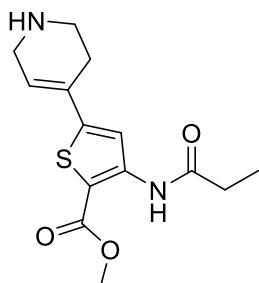
A solution of tert-butyl 4-(5-(methoxycarbonyl)-4-propionamidothiophen-2-yl)-3,6-dihydropyridine-1(2H)-carboxylate (100 mg, 0.253 mmol, 1 eq) in dichloromethane (1.00 mL) and trifluoracetic acid (0.250 mL) was stirred at room temperature for 1 hour. The reaction mixture was concentrated to provide the titled compound as a dark brown oil (95 mg, 92% yield TFA salt). The product was shown pure via mass spec, LCMS (ESI) calculated for $[M+H]^+$ 295.10, found 295.08.

Methyl 3-propionamido-5-(1-propionyl-1,2,3,6-tetrahydropyridin-4-yl)thiophene-2-carboxylate (STT-02-060)
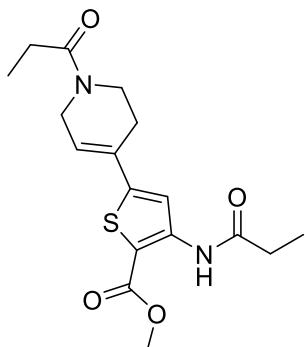
A solution of methyl 3-propionamido-5-(1,2,3,6-tetrahydropyridin-4-yl)thiophene-2-carboxylate (20 mg, 0.067 mmol, 1 eq) and triethylamine (29 µL, 0.201 mmol, 3 eq) in dichloromethane (1.0 mL) was cooled to 0 °C. After the dropwise addition of propionyl chloride (9.2 µL, 0.1 mmol, 1.5 eq), the reaction was stirred overnight and allowed to warm to room temperature. The reaction mixture was then suspended in brine and dichloromethane. The organic layer was dried over NaSO₄, filtered, and concentrated in vacuo. The crude material was diluted in 1 mL of dimethyl sulfoxide and purified by reverse-phase prep HPLC (95 to 15% H_2O/MeOH, 40 mL/min, 45 min). Lyophilization from H_2O/MeCN provided the title compound as a white powder (10.5 mg, 45% yield).

Synthesis of STT-02-040
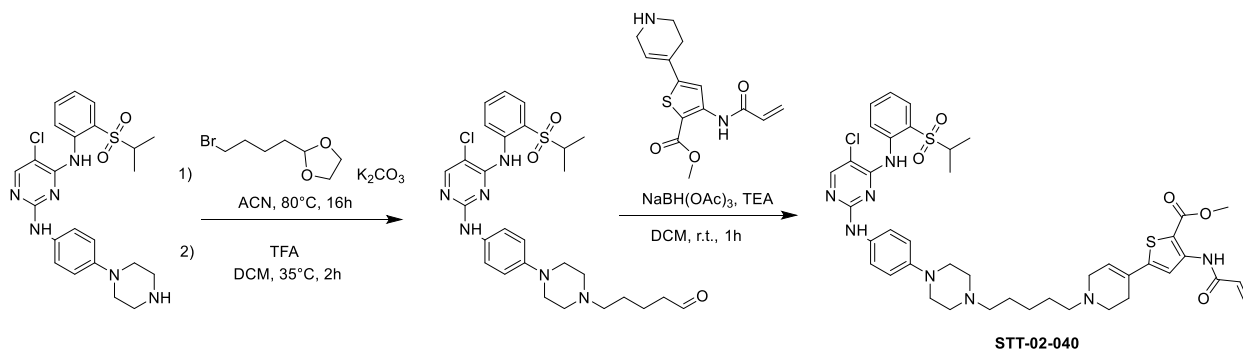
189

5-(4-(4-((5-chloro-4-((2-(isopropylsulfonyl)phenyl)amino)pyrimidin-2-yl)amino)phenyl)piperazin-1-yl)pentanal
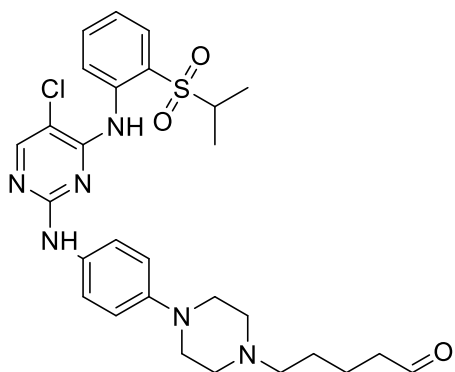
To a solution of 5-chloro-N^4-(2-(isopropylsulfonyl)phenyl)-N^2-(4-(piperazin-1-yl)phenyl)pyrimidine-2,4-diamine (100 mg, 0.166 mmol, 1 eq) in acetonitrile (1.6 mL), potassium carbonate (68.7 mg, 0.598 mmol, 3 eq) and 2-(4-bromobutyl)-1,3-dioxolane (41.6 mg, 0.199 mmol, 1.2 eq) were added. The mixture was then heated to 80 °C and stirred for 16 hours. Upon cooling to room temperature, the reaction was concentrated then diluted with brine and dichloromethane. The organic layer was dried over NaSO₄, filtered, and concentrated to provide a clear yellow oil (90 mg). The SN2 product was shown as the major component via mass spec: LCMS (ESI) calculated for [M+H]⁺ 615.24, found 615.20. The crude product was moved forward without purification.

To a solution of 15 mg of crude residue in dichloromethane (0.2 mL), trifluoracetic acid (0.2 mL) was added. The reaction mixture was heated to 35 °C and stirred for 2 hours. The reaction mixture was concentrated to provide the titled compound as a yellow oil (12.2 mg, 90% yield). The product was shown as the major component via mass spec, LCMS (ESI) calculated for [M+H]⁺ 571.22, found 571.12, and moved on to the next step without purification.

Methyl **3-acrylamido-5-(1-(5-(4-(4-((5-chloro-4-((2-(isopropylsulfonyl)phenyl)amino)pyrimidin-2-yl)amino)phenyl)piperazin-1-yl)pentyl)-1,2,3,6-tetrahydropyridin-4-yl)thiophene-2-carboxylate STT-02-040**
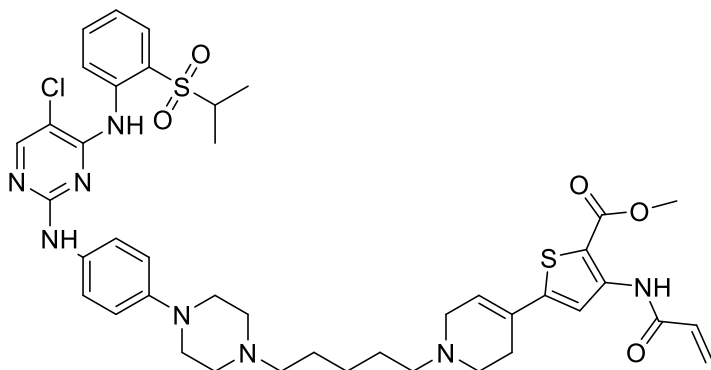
To a solution of solution of 5-(4-(4-((5-chloro-4-((2-(isopropylsulfonyl)phenyl)amino)pyrimidin-2-yl)amino)phenyl)piperazin-1-yl)pentanal (12.0 mg, 0.021 mmol, 1 eq) in dichloromethane (0.5 mL), triethylamine (7.3 µL, 0.058 mmol, 2.5 eq) and methyl 3-acrylamido-5-(1,2,3,6-tetrahydropyridin-4-yl)thiophene-2-carboxylate (6 mg, 0.021 mmol, 1 eq) were added. After stirring the mixture at room temperature for 1 minute, sodium triacetoxyborohydride (6.6 mg, 0.032 mmol, 1.5 eq) was added. After 1 hour of stirring, the reaction mixture was evaporated then diluted with 1.0 mL of dimethyl sulfoxide and purified by reverse-phase prep HPLC (95 to 15% H_2O/MeOH, 40 mL/min, 45 min). Lyophilization from H_2O/MeCN provided the title compound as a yellow powder (3.07 mg, 17% yield TFA salt).

^{1}H NMR (500 MHz, DMSO) δ 10.20 (s, 1H), 10.01 – 9.74 (m, 2H), 9.63 – 9.34 (m, 2H), 8.65 (s, 1H), 8.26 (s, 1H), 8.06 (s, 1H), 7.86 (d, J = 7.9 Hz, 1H), 7.75 (t, J = 8.1 Hz, 1H), 7.50 (d, J = 8.5 Hz, 2H), 7.38 (t, J = 7.7 Hz, 1H), 6.96 (d, J = 9.0 Hz, 2H), 6.61 (dd, J = 16.9, 10.3 Hz, 1H), 6.45 – 6.28 (m, 2H), 5.90 (d, J = 11.7 Hz, 1H), 4.04 (s, 1H), 3.92 – 3.81 (m, 3H), 3.80 – 3.73 (m, 2H), 3.20 – 3.16 (m, 5H), 2.96 (s, 2H), 2.83 (s, 2H), 2.54 (s, 3H), 1.74 (s, 6H), 1.39 (s, 2H), 1.18 (d, J = 6.7 Hz, 6H). LCMS (ESI) calculated for [M+H]$^+$ 847.31, found 847.21.

Synthesis of STT-02-052 and STT-02-071-2
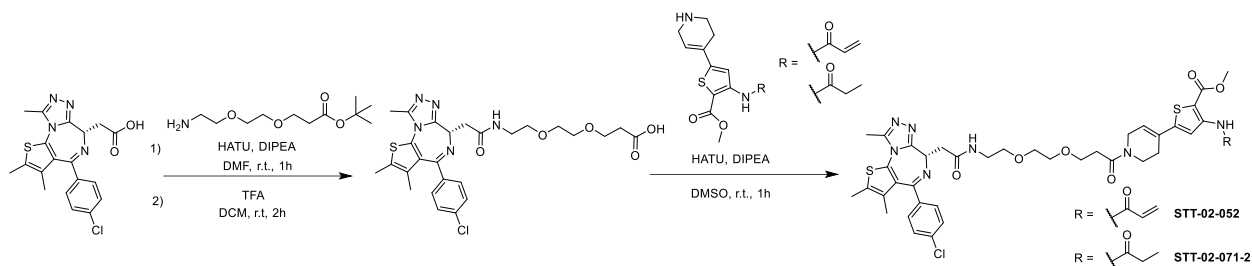
(S)-3-(2-(2-(2-(4-(4-chlorophenyl)-2,3,9-trimethyl-6H-thieno[3,2-f][1,2,4]triazolo[4,3-a][1,4]diazepin-6-yl)acetamido)ethoxy)ethoxy)propanoic acid
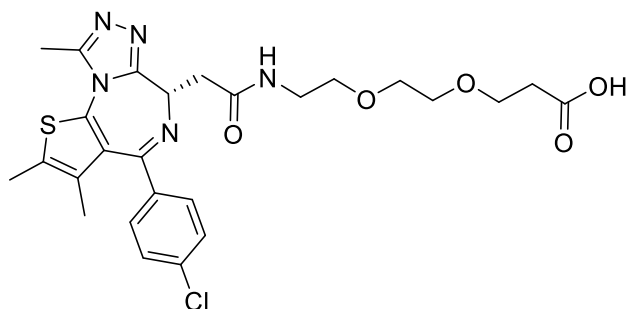
To a solution of commercially available (S)-2-(4-(4-chlorophenyl)-2,3,9-trimethyl-6H-thieno[3,2-f][1,2,4]triazolo[4,3-a][1,4]diazepin-6-yl)acetic acid (50 mg, 0.124 mmol, 1 eq) in N, N-dimethylformamide (1 mL), disopropylamine (77 μL, 0.434 mmol, 3.5 eq) and HATU (56 mg, 0.148 mmol, 1.2 eq) were added. After stirring the mixture at room temperature for 5 minutes, tert-butyl 3-(2-(2-aminoethoxy)ethoxy)propanoate (31 mg, 0.137 mmol, 1.1 eq) was added. After 1 hour of stirring, the reaction mixture was suspended in brine and ethyl acetate. The organic layer was dried over NaSO$_4$, filtered, and concentrated to provide a yellow oil (58 mg). The amide product was shown as the major component via mass spec: LCMS (ESI) calculated for [M+H]$^+$ 616.23, found 616.20. The crude product was moved forward without purification.

To a solution of 58 mg of crude residue in dichloromethane (0.5 mL), trifluoracetic acid (0.125 mL) was added. The reaction mixture was stirred at room temperature for 2 hours. The reaction

mixture was concentrated to provide the titled compound as a dark brown oil (40 mg, 90% yield). The product was shown as the major component via mass spec, LCMS (ESI) calculated for [M+H]$^+$ 560.17, found 560.12, and moved on to the next step without purification.

Methyl (S)-3-acrylamido-5-(1-(3-(2-(2-(2-(4-(4-chlorophenyl)-2,3,9-trimethyl-6H-thieno[3,2-f][1,2,4]triazolo[4,3-a][1,4]diazepin-6-yl)acetamido)ethoxy)ethoxy)propanoyl)-1,2,3,6-tetrahydropyridin-4-yl)thiophene-2-carboxylate (STT-02-052)

To a solution of (S)-3-(2-(2-(2-(4-(4-chlorophenyl)-2,3,9-trimethyl-6H-thieno[3,2-f][1,2,4]triazolo[4,3-a][1,4]diazepin-6-yl)acetamido)ethoxy)ethoxy)propanoic acid (10 mg, 0.018 mmol, 1 eq) in dimethyl sulfoxide (1 mL), disopropylamine (11 µL, 0.063 mmol, 3.5 eq) and HATU (8.2 mg, 0.021 mmol, 1.2 eq) were added. After stirring the mixture at room temperature for 5 minutes, methyl 3-acrylamido-5-(1,2,3,6-tetrahydropyridin-4-yl)thiophene-2-carboxylate (6 mg, 0.020 mmol, 1.1 eq) was added. After 1 hour of stirring, the reaction mixture was purified by reverse-phase prep HPLC (95 to 15% H$_2$O/MeOH, 40 mL/min, 45 min). Lyophilization from H$_2$O/MeCN provided the title compound as a yellow powder (5.12 mg, 34% yield).

^{1}H NMR (500 MHz, DMSO) δ 10.17 (s, 1H), 8.25 (t, J = 5.3 Hz, 1H), 7.96 (d, J = 8.3 Hz, 1H), 7.48 – 7.40 (m, 4H), 6.58 (dd, J = 16.8, 10.3 Hz, 1H), 6.36 (d, J = 11.1 Hz, 1H), 6.30 (dt, J = 17.0,

1.5 Hz, 1H), 5.87 (dd, *J* = 10.2, 1.5 Hz, 1H), 4.51 (dd, *J* = 8.2, 6.0 Hz, 1H), 4.21 – 4.11 (m, 2H),

3.83 (s, 3H), 3.68 – 3.62 (m, 5H), 3.53 (d, *J* = 5.0 Hz, 4H), 3.45 (t, *J* = 5.8 Hz, 2H), 3.32 – 3.17

(m, 5H), 2.70 – 2.61 (m, 2H), 2.59 (s, 3H), 2.40 (s, 3H), 1.64 – 1.59 (m, 3H). LCMS (ESI)

calculated for [M+H]$^+$ 834.24, found 834.14.

Methyl (S)-5-(1-(3-(2-(2-(2-(4-(4-chlorophenyl)-2,3,9-trimethyl-6H-thieno[3,2-f][1,2,4]triazolo[4,3-a][1,4]diazepin-6-yl)acetamido)ethoxy)ethoxy)propanoyl)-1,2,3,6-tetrahydropyridin-4-yl)-3-propionamidothiophene-2-carboxylate (STT-02-071-2)
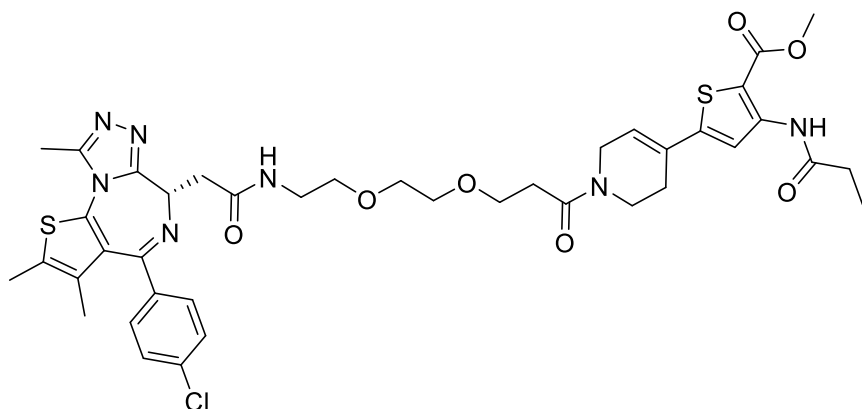
To a solution of (S)-3-(2-(2-(2-(4-(4-chlorophenyl)-2,3,9-trimethyl-6H-thieno[3,2-f][1,2,4]triazolo[4,3-a][1,4]diazepin-6-yl)acetamido)ethoxy)ethoxy)propanoic acid (10 mg, 0.018
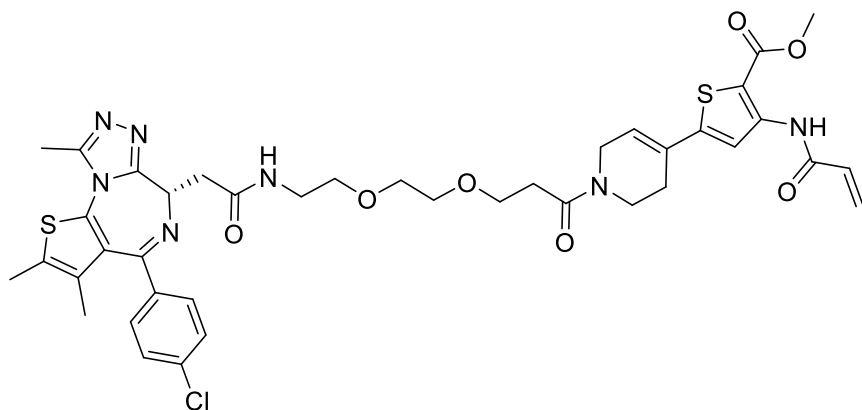
mmol, 1 eq) in dimethyl sulfoxide (1 mL), disopropylamine (11 µL, 0.063 mmol, 3.5 eq) and

HATU (8.2 mg, 0.021 mmol, 1.2 eq) were added. After stirring the mixture at room temperature

for 5 minutes, methyl 3-propionamido-5-(1,2,3,6-tetrahydropyridin-4-yl)thiophene-2-carboxylate

(5.6 mg, 0.020 mmol, 1.1 eq) was added. After 1 hour of stirring, the reaction mixture was purified

by reverse-phase prep HPLC (95 to 15% H$_2$O/MeOH, 40 mL/min, 45 min). Lyophilization from

H$_2$O/MeCN provided the title compound as a yellow powder (4.91 mg, 32% yield). LCMS (ESI)

calculated for [M+H]$^+$ 836.26, found 836.21,

Synthesis of STT-03-029-3
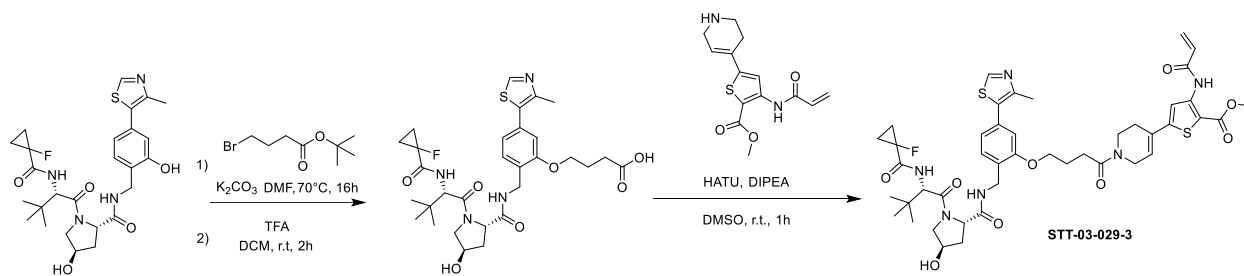
4-(2-(((2S,4R)-1-((S)-2-(1-fluorocyclopropane-1-carboxamido)-3,3-dimethylbutanoyl)-4-hydroxypyrrolidine-2-carboxamido)methyl)-5-(4-methylthiazol-5-yl)phenoxy)butanoic acid
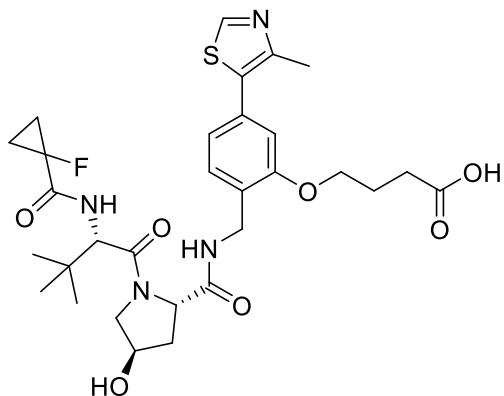
To a solution of commercially available (2S,4R)-1-((S)-2-(1-fluorocyclopropane-1-carboxamido)-3,3-dimethylbutanoyl)-4-hydroxy-N-(2-hydroxy-4-(4-methylthiazol-5-yl)benzyl)pyrrolidine-2-carboxamide (80 mg, 0.150 mmol, 1 eq), in dimethylformamide (1.0 mL), potassium carbonate (51.8 mg, 0.375 mmol, 2.5 eq) and tert-butyl 4-bromobutanoate (40.0 mg, 0.18 mmol, 1.2 eq) were added. The mixture was then heated to 70 °C and stirred for 16 hours. Upon cooling to room temperature, the reaction was concentrated then diluted with brine and dichloromethane. The organic layer was dried over NaSO₄, filtered, and concentrated in vacuo. The crude material was purified via silica gel chromatography (0% to 10% methanol/dichloromethane) to afford the ester

intermediate as a clear oil (80 mg, 79% yield). LCMS (ESI) calculated for [M+H]$^+$ 675.31, found 675.26.

A solution of the ester intermediate (80 mg, .119 mmol, 1 eq) in dichloromethane (0.50 mL) and trifluoracetic acid (0.12 mL) was stirred for 2 hours. The reaction mixture was concentrated to provide the titled compound as a yellow oil (65 mg, 88% yield). LCMS (ESI) calculated for [M+H]$^+$ 619.25, found 619.21.

Methyl 3-acrylamido-5-(1-(4-(2-(((2S,4R)-1-((S)-2-(1-fluorocyclopropane-1-carboxamido)-3,3-dimethylbutanoyl)-4-hydroxypyrrolidine-2-carboxamido)methyl)-5-(4-methylthiazol-5-yl)phenoxy)butanoyl)-1,2,3,6-tetrahydropyridin-4-yl)thiophene-2-carboxylate (STT-03-029-3)
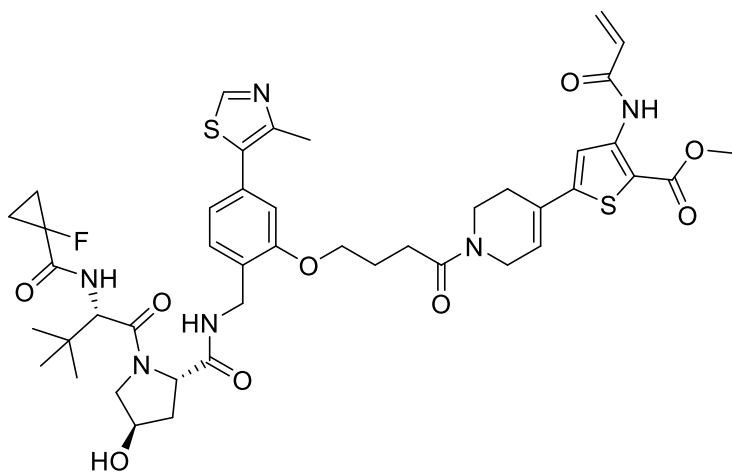
To a solution of 4-(2-(((2S,4R)-1-((S)-2-(1-fluorocyclopropane-1-carboxamido)-3,3-dimethylbutanoyl)-4-hydroxypyrrolidine-2-carboxamido)methyl)-5-(4-methylthiazol-5-yl)phenoxy)butanoic acid (10 mg, 0.016 mmol, 1 eq) in dimethyl sulfoxide (1 mL), disopropylamine (10 µL, 0.056 mmol, 3.5 eq) and HATU (7.3 mg, 0.021 mmol, 1.2 eq) were added. After stirring the mixture at room temperature for 5 minutes, methyl 3-acrylamido-5-(1,2,3,6-tetrahydropyridin-4-yl)thiophene-2-carboxylate (5.1 mg, 0.018 mmol, 1.1 eq) was added. After 1

hour of stirring, the reaction mixture was purified by reverse-phase prep HPLC (95 to 15% H₂O/MeOH, 40 mL/min, 45 min). Lyophilization from H₂O/MeCN provided the title compound as a white powder (3.9 mg, 27% yield). LCMS (ESI) calculated for [M+H]⁺ 893.33, found 893.29.

Synthesis of STT-03-066
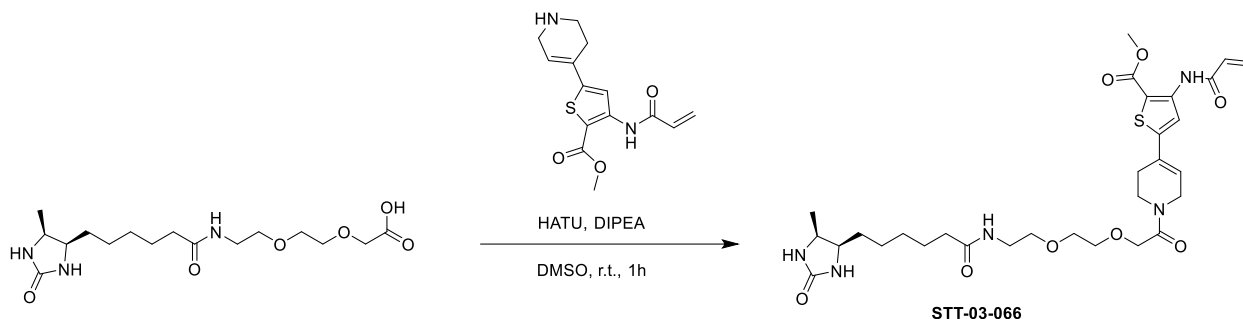
Methyl 3-acrylamido-5-(1-(2-(2-(2-(6-((4R,5S)-5-methyl-2-oxoimidazolidin-4-yl)hexanamido)ethoxy)ethoxy)acetyl)-1,2,3,6-tetrahydropyridin-4-yl)thiophene-2-carboxylate (STT-03-066)
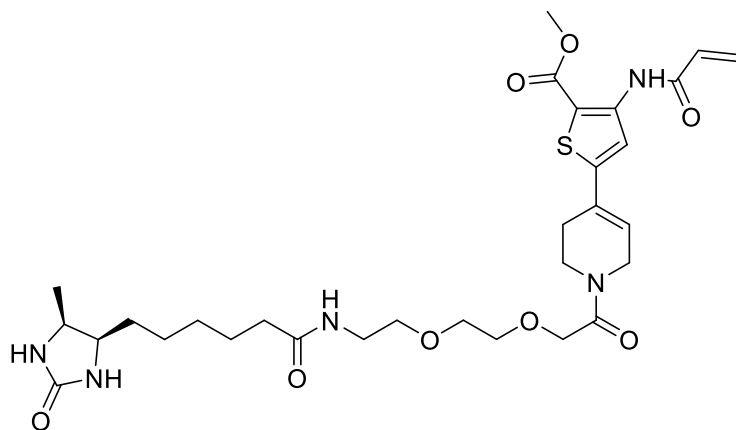
To a solution of 2-(2-(2-(6-((4R,5S)-5-methyl-2-oxoimidazolidin-4-yl)hexanamido)ethoxy)ethoxy)acetic acid (10 mg, 0.028 mmol, 1 eq) in dimethyl sulfoxide (1 mL), disopropylamine (18 µL, 0.097 mmol, 3.5 eq) and HATU (12.8 mg, 0.034 mmol, 1.2 eq) were

added. After stirring the mixture at room temperature for 5 minutes, methyl 3-acrylamido-5-(1,2,3,6-tetrahydropyridin-4-yl)thiophene-2-carboxylate (9 mg, 0.031 mmol, 1.1 eq) was added. After 1 hour of stirring, the reaction mixture was purified by reverse-phase prep HPLC (95 to 15% H_2O/MeOH, 40 mL/min, 45 min). Lyophilization from H_2O/MeCN provided the title compound as a white powder (6.22 mg, 35% yield). LCMS (ESI) calculated for $[M+H]^+$ 633.28, found 633.31

Chapter 6: Conclusions

While the field of targeted protein degradation has grown exponentially over the past few years, with numerous PROTACs being discovered at a rapid pace, the field remains in its infancy. The first PROTAC to reach clinical trials, ARV-110, has demonstrated promising Phase I results (Petrylak et al., 2020), but further investigations are required to solidify PROTACs as a viable therapeutic modality. In addition, PROTAC design and synthesis are largely empirical, as several challenges remain in predicting the compatibility of the target of interest with the recruited E3 ligase for productive ternary complex formation. Even with the discovery of E3 ligase ligands, the E3 ligase might not be suitable for PROTAC development, as demonstrated by DCAF15 (Faust et al., 2020). The main drivers of productive ternary complex formation also seem to vary among different target/E3 ligase pairs, with some relying on the binding affinities of the two recruiting moieties, while others rely on cooperative protein-protein interactions induced by the degraders (Donovan *et al.*, 2020). Finally, the different target scopes of matched pairs of CRBN vs. VHL-recruiting kinase PROTACs suggest that different E3 ligases preferentially degrade different proteins (Donovan *et al.*, 2020), indicating the need to expand the E3 ligase toolbox. Thus, more efforts are needed to address the challenges that come with PROTAC development.

Although several studies querying the degradable kinome have been reported (Donovan *et al.*, 2020; Huang *et al.*, 2018), AKT remained an elusive kinase to degrade. Chapter 2 of this thesis reports the characterization of two pan-AKT degraders, INY-03-041 and INY-05-040. Durable and prolonged inhibition of downstream signaling was observed with both degraders *in vitro*, even after compound washout, exemplifying the potential to uncouple pharmacodynamics from pharmacokinetics through PROTAC technology. Combining multi-omics profiling with computational network modeling, we further characterize INY-05-040 and establish low baseline JNK signaling as a biomarker for breast cancer sensitivity to AKT degradation, but not catalytic

inhibition. While INY-03-041 and INY-05-040 displayed favorable pharmacokinetic properties, they suffered from dose-limiting toxicities in mice, stalling *in vivo* studies. MS21, a pan-AKT degrader based on the AKT inhibitor AZD5363, has recently been reported to be well tolerated in mice, demonstrating *in vivo* AKT degradation (Xu et al., 2021). Therefore, additional medicinal chemistry efforts are likely needed to investigate GDC-0068-based AKT degraders *in vivo*, as well as explore the therapeutic potential of AKT degradation.

In Chapter 3, we investigate potential non-catalytic functions of ERK5 through the development of INY-06-061, a potent and selective ERK5 degrader. The use of nonselective ERK5 inhibitors has muddied ERK5 literature, which is further complicated by the discrepancies observed between ERK5 kinase inhibition and genetic ERK5 ablation. As non-catalytic functions of ERK5 have been suggested to drive proliferative or inflammatory phenotypes associated with ERK5, we employ PROTAC technology to abrogate potential scaffolding functions of ERK5. Consistent with DepMap, which indicate a lack of ERK5 dependency for cell proliferation, pharmacological degradation of ERK5 did not induce potent anti-proliferative effects in a panel of 750 cancer cell lines, at least at basal conditions. Moreover, INY-06-061 did not reduce cytokine secretion of IL-6 and IL-8 in endothelial cells upon inflammatory stimulation. While our study indicates that pharmacological degradation of ERK5 does not inhibit cellular immune response or proliferation, further investigation will be required to probe ERK5 function.

While Chapter 2 and 3 emphasize expanding the degradable target space of CRBN- and VHL-based PROTACs, Chapter 4 shifts focus to the neo-substrate specificity of PROTACs. IMiDs have the potential to retain their abilities to degrade neo-substrates, even when chemically conjugated as PROTACs. As degradation of neo-substrates are often considered off-targets, medicinal chemistry efforts are often carried out to engineer out the activities of IMiDs. However,

we demonstrate that we can exploit the activities of the E3 ligase ligands to synergistically target multiple proteins with one compound. Through the conjugation of palbociclib, an FDA-approved CDK4/6 inhibitor, with DKY709, a novel IMiD-based Helios degrader, we report the development of ALV-07-082-03. Pharmacological co-degradation of CDK4, CDK6 and Helios resulted in potent downstream signaling and proliferation in cancer cells, as well as enhanced derepression of IL-2 secretion. Thus, not only do we demonstrate the possibility of rationally redirecting neo-substrate specificity of PROTACs, but we also take advantage of the neo-substrate specificity of alternative CRBN ligands to explore potential synergistic effects of co-targeting CDK4, CDK6 and Helios.

In Chapter 5, we explore the potential of DCAF11-based PROTACs. While DCAF11 has previously been reported to support targeted protein degradation, it remained unclear if DCAF11 could be utilized as a general E3 ligase for PROTAC development. Through the identification of ZNL-06-031 as a covalent DCAF11 binder, we further investigate the target scope of DCAF11-based PROTACs. Generation of STT-02-040, a promiscuous DCAF11-based kinase degrader, demonstrate that multiple kinases can be degraded through DCAF11 recruitment, although the effects were not as robust as with CRBN- or VHL-based PROTACs. While STT-02-052, a potent BRD4 degrader, suggests that potent PROTACs that induce degradation at nanomolar concentrations can be generated, further optimizations to improve the selectivity and potency of ZNL-06-031 are required. To date, several novel covalent E3 ligase ligands have been identified and incorporated into PROTACs. However, no advantages of electrophilic PROTACs have been reported to date, especially due to the weak binding potencies of reported ligands. Therefore, ZNL-06-031 may provide an opportunity to not only explore the degradable target space of DCAF11-

recruiting PROTACs, but also investigate potential advantages of covalently binding to the E3 ligase.

In summary, there are many factors to consider, such as compatibility of the target and E3 ligase, when developing PROTACs. This thesis not only highlights the different features of PROTACs that can be modified, but also reports the development of various PROTACs to expand the degradable target space and E3 ligase toolbox.

Bibliography

Abe, J., Kusuhara, M., Ulevitch, R.J., Berk, B.C., and Lee, J.D. (1996). Big mitogen-activated protein kinase 1 (BMK1) is a redox-sensitive kinase. J Biol Chem *271*, 16586-16590. 10.1074/jbc.271.28.16586.

Adams, J. (2001). Proteasome inhibition in cancer: development of PS-341. Semin Oncol *28*, 613-619. 10.1016/s0093-7754(01)90034-x.

Adams, J.L., Smothers, J., Srinivasan, R., and Hoos, A. (2015). Big opportunities for small molecules in immuno-oncology. Nat Rev Drug Discov *14*, 603-622. 10.1038/nrd4596.

Adhikari, B., Bozilovic, J., Diebold, M., Schwarz, J.D., Hofstetter, J., Schröder, M., Wanior, M., Narain, A., Vogt, M., Dudvarski Stankovic, N., et al. (2020). PROTAC-mediated degradation reveals a non-catalytic function of AURORA-A kinase. Nat Chem Biol *16*, 1179-1188. 10.1038/s41589-020-00652-y.

Aghajanian, C., Bell-McGuinn, K.M., Burris, H.A., Siu, L.L., Stayner, L.A., Wheler, J.J., Hong, D.S., Kurkjian, C., Pant, S., Santiago-Walker, A., et al. (2018). A phase I, open-label, two-stage study to investigate the safety, tolerability, pharmacokinetics, and pharmacodynamics of the oral AKT inhibitor GSK2141795 in patients with solid tumors. Invest New Drugs *36*, 1016-1025. 10.1007/s10637-018-0591-z.

Ahn, D.H., Li, J., Wei, L., Doyle, A., Marshall, J.L., Schaaf, L.J., Phelps, M.A., Villalona-Calero, M.A., and Bekaii-Saab, T. (2015). Results of an abbreviated phase-II study with the Akt Inhibitor MK-2206 in Patients with Advanced Biliary Cancer. Sci Rep *5*, 12122. 10.1038/srep12122.

Alessi, D.R., Andjelkovic, M., Caudwell, B., Cron, P., Morrice, N., Cohen, P., and Hemmings, B.A. (1996). Mechanism of activation of protein kinase B by insulin and IGF-1. EMBO J *15*, 6541-6551.

Alessi, D.R., James, S.R., Downes, C.P., Holmes, A.B., Gaffney, P.R., Reese, C.B., and Cohen, P. (1997). Characterization of a 3-phosphoinositide-dependent protein kinase which phosphorylates and activates protein kinase Balpha. Curr Biol *7*, 261-269. 10.1016/s0960-9822(06)00122-9.

Altomare, D.A., and Testa, J.R. (2005). Perturbations of the AKT signaling pathway in human cancer. Oncogene *24*, 7455-7464. 10.1038/sj.onc.1209085.

An, J., Ponthier, C.M., Sack, R., Seebacher, J., Stadler, M.B., Donovan, K.A., and Fischer, E.S. (2017). pSILAC mass spectrometry reveals ZFP91 as IMiD-dependent substrate of the CRL4. Nat Commun *8*, 15398. 10.1038/ncomms15398.

An, S., and Fu, L. (2018). Small-molecule PROTACs: An emerging and promising approach for the development of targeted therapy drugs. EBioMedicine *36*, 553-562. 10.1016/j.ebiom.2018.09.005.

André, F., Ciruelos, E., Rubovszky, G., Campone, M., Loibl, S., Rugo, H.S., Iwata, H., Conte, P., Mayer, I.A., Kaufman, B., et al. (2019). Alpelisib for *PIK3CA*-Mutated, Hormone Receptor-Positive Advanced Breast Cancer. N Engl J Med *380*, 1929-1940. 10.1056/NEJMoa1813904.

Backus, K.M., Correia, B.E., Lum, K.M., Forli, S., Horning, B.D., González-Páez, G.E., Chatterjee, S., Lanning, B.R., Teijaro, J.R., Olson, A.J., et al. (2016). Proteome-wide covalent ligand discovery in native biological systems. Nature *534*, 570-574. 10.1038/nature18002.

Bai, L., Zhou, H., Xu, R., Zhao, Y., Chinnaswamy, K., McEachern, D., Chen, J., Yang, C.Y., Liu, Z., Wang, M., et al. (2019). A Potent and Selective Small-Molecule Degrader of STAT3 Achieves Complete Tumor Regression In Vivo. Cancer Cell *36*, 498-511.e417. 10.1016/j.ccell.2019.10.002.

Baine, I., Basu, S., Ames, R., Sellers, R.S., and Macian, F. (2013). Helios induces epigenetic silencing of IL2 gene expression in regulatory T cells. J Immunol *190*, 1008-1016. 10.4049/jimmunol.1200792.

Banik, S.M., Pedram, K., Wisnovsky, S., Ahn, G., Riley, N.M., and Bertozzi, C.R. (2020). Lysosome-targeting chimaeras for degradation of extracellular proteins. Nature *584*, 291-297. 10.1038/s41586-020-2545-9.

Barabási, A.L., Gulbahce, N., and Loscalzo, J. (2011). Network medicine: a network-based approach to human disease. Nat Rev Genet *12*, 56-68. 10.1038/nrg2918.

Basso, A.D., Solit, D.B., Chiosis, G., Giri, B., Tsichlis, P., and Rosen, N. (2002). Akt forms an intracellular complex with heat shock protein 90 (Hsp90) and Cdc37 and is destabilized by inhibitors of Hsp90 function. J Biol Chem *277*, 39858-39866. 10.1074/jbc.M206322200.

Birmingham, A., Anderson, E.M., Reynolds, A., Ilsley-Tyree, D., Leake, D., Fedorov, Y., Baskerville, S., Maksimova, E., Robinson, K., Karpilow, J., et al. (2006). 3' UTR seed matches, but not overall identity, are associated with RNAi off-targets. Nat Methods *3*, 199-204. 10.1038/nmeth854.

Blake, J.F., Xu, R., Bencsik, J.R., Xiao, D., Kallan, N.C., Schlachter, S., Mitchell, I.S., Spencer, K.L., Banka, A.L., Wallace, E.M., et al. (2012). Discovery and preclinical pharmacology of a selective ATP-competitive Akt inhibitor (GDC-0068) for the treatment of human tumors. J Med Chem *55*, 8110-8127. 10.1021/jm301024w.

Bondeson, D.P., Mares, A., Smith, I.E., Ko, E., Campos, S., Miah, A.H., Mulholland, K.E., Routly, N., Buckley, D.L., Gustafson, J.L., et al. (2015). Catalytic in vivo protein knockdown by small-molecule PROTACs. Nat Chem Biol *11*, 611-617. 10.1038/nchembio.1858.

Brand, M., Jiang, B., Bauer, S., Donovan, K.A., Liang, Y., Wang, E.S., Nowak, R.P., Yuan, J.C., Zhang, T., Kwiatkowski, N., et al. (2018). Homolog-Selective Degradation as a Strategy to Probe the Function of CDK6 in AML. Cell Chem Biol. 10.1016/j.chembiol.2018.11.006.

Brown, J.S., and Banerji, U. (2017). Maximising the potential of AKT inhibitors as anti-cancer treatments. Pharmacol Ther *172*, 101-115. 10.1016/j.pharmthera.2016.12.001.

Buckley, D.L., Gustafson, J.L., Van Molle, I., Roth, A.G., Tae, H.S., Gareiss, P.C., Jorgensen, W.L., Ciulli, A., and Crews, C.M. (2012a). Small-molecule inhibitors of the interaction between the E3 ligase VHL and HIF1α. Angew Chem Int Ed Engl *51*, 11463-11467. 10.1002/anie.201206231.

Buckley, D.L., Van Molle, I., Gareiss, P.C., Tae, H.S., Michel, J., Noblin, D.J., Jorgensen, W.L., Ciulli, A., and Crews, C.M. (2012b). Targeting the von Hippel-Lindau E3 ubiquitin ligase using small molecules to disrupt the VHL/HIF-1α interaction. J Am Chem Soc *134*, 4465-4468. 10.1021/ja209924v.

Burslem, G.M., and Crews, C.M. (2020). Proteolysis-Targeting Chimeras as Therapeutics and Tools for Biological Discovery. Cell *181*, 102-114. 10.1016/j.cell.2019.11.031.

Békés, M., Langley, D.R., and Crews, C.M. (2022). PROTAC targeted protein degraders: the past is prologue. Nat Rev Drug Discov *21*, 181-200. 10.1038/s41573-021-00371-6.

Calleja, V., Alcor, D., Laguerre, M., Park, J., Vojnovic, B., Hemmings, B.A., Downward, J., Parker, P.J., and Larijani, B. (2007). Intramolecular and intermolecular interactions of protein kinase B define its activation in vivo. PLoS Biol *5*, e95. 10.1371/journal.pbio.0050095.

Cantley, L.C., and Neel, B.G. (1999). New insights into tumor suppression: PTEN suppresses tumor formation by restraining the phosphoinositide 3-kinase/AKT pathway. Proc Natl Acad Sci U S A *96*, 4240-4245.

Carracedo, A., Ma, L., Teruya-Feldstein, J., Rojo, F., Salmena, L., Alimonti, A., Egia, A., Sasaki, A.T., Thomas, G., Kozma, S.C., et al. (2008). Inhibition of mTORC1 leads to MAPK pathway activation through a PI3K-dependent feedback loop in human cancer. J Clin Invest *118*, 3065-3074. 10.1172/JCI34739.

Carvajal-Vergara, X., Tabera, S., Montero, J.C., Esparís-Ogando, A., López-Pérez, R., Mateo, G., Gutiérrez, N., Parmo-Cabañas, M., Teixidó, J., San Miguel, J.F., and Pandiella, A. (2005). Multifunctional role of Erk5 in multiple myeloma. Blood *105*, 4492-4499. 10.1182/blood-2004-08-2985.

Chen, Z., Wang, K., Hou, C., Jiang, K., Chen, B., Chen, J., Lao, L., Qian, L., Zhong, G., Liu, Z., et al. (2017). CRL4B. Sci Rep *7*, 1175. 10.1038/s41598-017-01344-9.

Cheng, J.Q., Godwin, A.K., Bellacosa, A., Taguchi, T., Franke, T.F., Hamilton, T.C., Tsichlis, P.N., and Testa, J.R. (1992). AKT2, a putative oncogene encoding a member of a subfamily of protein-serine/threonine kinases, is amplified in human ovarian carcinomas. Proc Natl Acad Sci U S A *89*, 9267-9271. 10.1073/pnas.89.19.9267.

Churcher, I. (2018). Protac-Induced Protein Degradation in Drug Discovery: Breaking the Rules or Just Making New Ones? J Med Chem *61*, 444-452. 10.1021/acs.jmedchem.7b01272.

Ciechanover, A., Orian, A., and Schwartz, A.L. (2000). Ubiquitin-mediated proteolysis: biological regulation via destruction. Bioessays *22*, 442-451. 10.1002/(SICI)1521-1878(200005)22:5<442::AID-BIES6>3.0.CO;2-Q.

Coleman, N., Moyers, J.T., Harbery, A., Vivanco, I., and Yap, T.A. (2021). Clinical Development of AKT Inhibitors and Associated Predictive Biomarkers to Guide Patient Treatment in Cancer Medicine. Pharmgenomics Pers Med *14*, 1517-1535. 10.2147/PGPM.S305068.

Conde, J., and Artzi, N. (2015). Are RNAi and miRNA therapeutics truly dead? Trends Biotechnol *33*, 141-144. 10.1016/j.tibtech.2014.12.005.

Corral, L.G., Haslett, P.A., Muller, G.W., Chen, R., Wong, L.M., Ocampo, C.J., Patterson, R.T., Stirling, D.I., and Kaplan, G. (1999). Differential cytokine modulation and T cell activation by two distinct classes of thalidomide analogues that are potent inhibitors of TNF-alpha. J Immunol *163*, 380-386.

Coulthard, L.R., White, D.E., Jones, D.L., McDermott, M.F., and Burchill, S.A. (2009). p38(MAPK): stress responses from molecular mechanisms to therapeutics. Trends Mol Med *15*, 369-379. 10.1016/j.molmed.2009.06.005.

Crawford, A., Angelosanto, J.M., Kao, C., Doering, T.A., Odorizzi, P.M., Barnett, B.E., and Wherry, E.J. (2014). Molecular and transcriptional basis of CD4^{+} T cell dysfunction during chronic infection. Immunity *40*, 289-302. 10.1016/j.immuni.2014.01.005.

Cristea, S., Coles, G.L., Hornburg, D., Gershkovitz, M., Arand, J., Cao, S., Sen, T., Williamson, S.C., Kim, J.W., Drainas, A.P., et al. (2020). The MEK5-ERK5 Kinase Axis Controls Lipid Metabolism in Small-Cell Lung Cancer. Cancer Res *80*, 1293-1303. 10.1158/0008-5472.CAN-19-1027.

Cromm, P.M., Samarasinghe, K.T.G., Hines, J., and Crews, C.M. (2018). Addressing Kinase-Independent Functions of Fak via PROTAC-Mediated Degradation. J Am Chem Soc. 10.1021/jacs.8b08008.

Cross, D.A., Alessi, D.R., Cohen, P., Andjelkovich, M., and Hemmings, B.A. (1995). Inhibition of glycogen synthase kinase-3 by insulin mediated by protein kinase B. Nature *378*, 785-789. 10.1038/378785a0.

Davis, R.J. (1994). MAPKs: new JNK expands the group. Trends Biochem Sci *19*, 470-473. 10.1016/0968-0004(94)90132-5.

Deng, J., Wang, E.S., Jenkins, R.W., Li, S., Dries, R., Yates, K., Chhabra, S., Huang, W., Liu, H., Aref, A.R., et al. (2018). CDK4/6 Inhibition Augments Antitumor Immunity by Enhancing T-cell Activation. Cancer Discov *8*, 216-233. 10.1158/2159-8290.CD-17-0915.

Deshaies, R.J., and Joazeiro, C.A. (2009). RING domain E3 ubiquitin ligases. Annu Rev Biochem *78*, 399-434. 10.1146/annurev.biochem.78.101807.093809.

Djakbarova, U., Marzluff, W.F., and Köseoğlu, M.M. (2016). DDB1 and CUL4 associated factor 11 (DCAF11) mediates degradation of Stem-loop binding protein at the end of S phase. Cell Cycle *15*, 1986-1996. 10.1080/15384101.2016.1191708.

Do, K., Speranza, G., Bishop, R., Khin, S., Rubinstein, L., Kinders, R.J., Datiles, M., Eugeni, M., Lam, M.H., Doyle, L.A., et al. (2015). Biomarker-driven phase 2 study of MK-2206 and selumetinib (AZD6244, ARRY-142886) in patients with colorectal cancer. Invest New Drugs *33*, 720-728. 10.1007/s10637-015-0212-z.

Dobrovolsky, D., Wang, E.S., Morrow, S., Leahy, C., Faust, T., Nowak, R.P., Donovan, K.A., Yang, G., Li, Z., Fischer, E.S., et al. (2018). Bruton's Tyrosine Kinase degradation as a therapeutic strategy for cancer. Blood. 10.1182/blood-2018-07-862953.

Dong, G., Ding, Y., He, S., and Sheng, C. (2021). Molecular Glues for Targeted Protein Degradation: From Serendipity to Rational Discovery. J Med Chem *64*, 10606-10620. 10.1021/acs.jmedchem.1c00895.

Donovan, K.A., An, J., Nowak, R.P., Yuan, J.C., Fink, E.C., Berry, B.C., Ebert, B.L., and Fischer, E.S. (2018). Thalidomide promotes degradation of SALL4, a transcription factor implicated in Duane Radial Ray syndrome. Elife *7*. 10.7554/eLife.38430.

Donovan, K.A., Ferguson, F.M., Bushman, J.W., Eleuteri, N.A., Bhunia, D., Ryu, S., Tan, L., Shi, K., Yue, H., Liu, X., et al. (2020). Mapping the Degradable Kinome Provides a Resource for Expedited Degrader Development. Cell *183*, 1714-1731.e1710. 10.1016/j.cell.2020.10.038.

Du, G., Jiang, J., Henning, N.J., Safaee, N., Koide, E., Nowak, R.P., Donovan, K.A., Yoon, H., You, I., Yue, H., et al. (2022). Exploring the target scope of KEAP1 E3 ligase-based PROTACs. Cell Chem Biol. 10.1016/j.chembiol.2022.08.003.

Dugourd, A., Kuppe, C., Sciacovelli, M., Gjerga, E., Gabor, A., Emdal, K.B., Vieira, V., Bekker-Jensen, D.B., Kranz, J., Bindels, E.M.J., et al. (2021). Causal integration of multi-omics data with prior knowledge to generate mechanistic hypotheses. Mol Syst Biol *17*, e9730. 10.15252/msb.20209730.

Engelhardt, M., Szymaniak-Vits, M., Ajayi, S., Dold, S.M., Müller, S.J., Scheubeck, S., and Wäsch, R. (2018). Carfilzomib. Recent Results Cancer Res *212*, 265-283. 10.1007/978-3-319-91439-8_13.

English, J.M., Pearson, G., Baer, R., and Cobb, M.H. (1998). Identification of substrates and regulators of the mitogen-activated protein kinase ERK5 using chimeric protein kinases. J Biol Chem *273*, 3854-3860. 10.1074/jbc.273.7.3854.

Esparís-Ogando, A., Díaz-Rodríguez, E., Montero, J.C., Yuste, L., Crespo, P., and Pandiella, A. (2002). Erk5 participates in neuregulin signal transduction and is constitutively active in breast cancer cells overexpressing ErbB2. Mol Cell Biol *22*, 270-285. 10.1128/MCB.22.1.270-285.2002.

Faust, T.B., Yoon, H., Nowak, R.P., Donovan, K.A., Li, Z., Cai, Q., Eleuteri, N.A., Zhang, T., Gray, N.S., and Fischer, E.S. (2020). Structural complementarity facilitates E7820-mediated degradation of RBM39 by DCAF15. Nat Chem Biol *16*, 7-14. 10.1038/s41589-019-0378-3.

Finegan, K.G., Perez-Madrigal, D., Hitchin, J.R., Davies, C.C., Jordan, A.M., and Tournier, C. (2015). ERK5 is a critical mediator of inflammation-driven cancer. Cancer Res *75*, 742-753. 10.1158/0008-5472.CAN-13-3043.

Fruman, D.A., Chiu, H., Hopkins, B.D., Bagrodia, S., Cantley, L.C., and Abraham, R.T. (2017). The PI3K Pathway in Human Disease. Cell *170*, 605-635. 10.1016/j.cell.2017.07.029.

Gandhi, A.K., Kang, J., Havens, C.G., Conklin, T., Ning, Y., Wu, L., Ito, T., Ando, H., Waldman, M.F., Thakurta, A., et al. (2014). Immunomodulatory agents lenalidomide and pomalidomide co-stimulate T cells by inducing degradation of T cell repressors Ikaros and Aiolos via modulation of the E3 ubiquitin ligase complex CRL4(CRBN.). Br J Haematol *164*, 811-821. 10.1111/bjh.12708.

Garcia-Alonso, L., Iorio, F., Matchan, A., Fonseca, N., Jaaks, P., Peat, G., Pignatelli, M., Falcone, F., Benes, C.H., Dunham, I., et al. (2018). Transcription Factor Activities Enhance Markers of Drug Sensitivity in Cancer. Cancer Res *78*, 769-780. 10.1158/0008-5472.CAN-17-1679.

Gasic, I., Groendyke, B.J., Nowak, R.P., Yuan, J.C., Kalabathula, J., Fischer, E.S., Gray, N.S., and Mitchison, T.J. (2020). Tubulin Resists Degradation by Cereblon-Recruiting PROTACs. Cells *9*. 10.3390/cells9051083.

Girardini, M., Maniaci, C., Hughes, S.J., Testa, A., and Ciulli, A. (2019). Cereblon versus VHL: Hijacking E3 ligases against each other using PROTACs. Bioorg Med Chem *27*, 2466-2479. 10.1016/j.bmc.2019.02.048.

Giurisato, E., Xu, Q., Lonardi, S., Telfer, B., Russo, I., Pearson, A., Finegan, K.G., Wang, W., Wang, J., Gray, N.S., et al. (2018). Myeloid ERK5 deficiency suppresses tumor growth by blocking protumor macrophage polarization via STAT3 inhibition. Proc Natl Acad Sci U S A *115*, E2801-E2810. 10.1073/pnas.1707929115.

Goedeke, L., Canfrán-Duque, A., Rotllan, N., Chaube, B., Thompson, B.M., Lee, R.G., Cline, G.W., McDonald, J.G., Shulman, G.I., Lasunción, M.A., et al. (2021). MMAB promotes negative feedback control of cholesterol homeostasis. Nat Commun *12*, 6448. 10.1038/s41467-021-26787-7.

Goel, S., DeCristo, M.J., Watt, A.C., BrinJones, H., Sceneay, J., Li, B.B., Khan, N., Ubellacker, J.M., Xie, S., Metzger-Filho, O., et al. (2017). CDK4/6 inhibition triggers anti-tumour immunity. Nature *548*, 471-475. 10.1038/nature23465.

Goldberg, A.L. (2012). Development of proteasome inhibitors as research tools and cancer drugs. J Cell Biol *199*, 583-588. 10.1083/jcb.201210077.

Haas, A.L., and Rose, I.A. (1982). The mechanism of ubiquitin activating enzyme. A kinetic and equilibrium analysis. J Biol Chem *257*, 10329-10337.

Habermann, T.M., Lossos, I.S., Justice, G., Vose, J.M., Wiernik, P.H., McBride, K., Wride, K., Ervin-Haynes, A., Takeshita, K., Pietronigro, D., et al. (2009). Lenalidomide oral monotherapy

produces a high response rate in patients with relapsed or refractory mantle cell lymphoma. Br J Haematol *145*, 344-349. 10.1111/j.1365-2141.2009.07626.x.

Hafner, M., Heiser, L.M., Williams, E.H., Niepel, M., Wang, N.J., Korkola, J.E., Gray, J.W., and Sorger, P.K. (2017). Quantification of sensitivity and resistance of breast cancer cell lines to anti-cancer drugs using GR metrics. Sci Data *4*, 170166. 10.1038/sdata.2017.166.

Hanada, M., Feng, J., and Hemmings, B.A. (2004). Structure, regulation and function of PKB/AKT--a major therapeutic target. Biochim Biophys Acta *1697*, 3-16. 10.1016/j.bbapap.2003.11.009.

Haslett, P.A., Corral, L.G., Albert, M., and Kaplan, G. (1998). Thalidomide costimulates primary human T lymphocytes, preferentially inducing proliferation, cytokine production, and cytotoxic responses in the CD8+ subset. J Exp Med *187*, 1885-1892. 10.1084/jem.187.11.1885.

Heckler, M., Ali, L.R., Clancy-Thompson, E., Qiang, L., Ventre, K.S., Lenehan, P., Roehle, K., Luoma, A., Boelaars, K., Peters, V., et al. (2021). Inhibition of CDK4/6 Promotes CD8 T-cell Memory Formation. Cancer Discov *11*, 2564-2581. 10.1158/2159-8290.CD-20-1540.

Henning, N.J., Manford, A.G., Spradlin, J.N., Brittain, S.M., Zhang, E., McKenna, J.M., Tallarico, J.A., Schirle, M., Rape, M., and Nomura, D.K. (2022). Discovery of a Covalent FEM1B Recruiter for Targeted Protein Degradation Applications. J Am Chem Soc *144*, 701-708. 10.1021/jacs.1c03980.

Hines, J., Lartigue, S., Dong, H., Qian, Y., and Crews, C.M. (2019). MDM2-Recruiting PROTAC Offers Superior, Synergistic Antiproliferative Activity via Simultaneous Degradation of BRD4 and Stabilization of p53. Cancer Res *79*, 251-262. 10.1158/0008-5472.CAN-18-2918.

Hoang, V.T., Matossian, M.D., La, J., Hoang, K., Ucar, D.A., Elliott, S., Burks, H.E., Wright, T.D., Patel, S., Bhatt, A., et al. (2021). Dual inhibition of MEK1/2 and MEK5 suppresses the EMT/migration axis in triple-negative breast cancer through FRA-1 regulation. J Cell Biochem *122*, 835-850. 10.1002/jcb.29916.

Hoang, V.T., Yan, T.J., Cavanaugh, J.E., Flaherty, P.T., Beckman, B.S., and Burow, M.E. (2017). Oncogenic signaling of MEK5-ERK5. Cancer Lett *392*, 51-59. 10.1016/j.canlet.2017.01.034.

Huang, H.T., Dobrovolsky, D., Paulk, J., Yang, G., Weisberg, E.L., Doctor, Z.M., Buckley, D.L., Cho, J.H., Ko, E., Jang, J., et al. (2018). A Chemoproteomic Approach to Query the Degradable Kinome Using a Multi-kinase Degrader. Cell Chem Biol *25*, 88-99.e86. 10.1016/j.chembiol.2017.10.005.

Huck, B.R., Kötzner, L., and Urbahns, K. (2018). Small Molecules Drive Big Improvements in Immuno-Oncology Therapies. Angew Chem Int Ed Engl *57*, 4412-4428. 10.1002/anie.201707816.

Huck, B.R., and Mochalkin, I. (2017). Recent progress towards clinically relevant ATP-competitive Akt inhibitors. Bioorg Med Chem Lett *27*, 2838-2848. 10.1016/j.bmcl.2017.04.090.

Ishida, T., and Ciulli, A. (2021). E3 Ligase Ligands for PROTACs: How They Were Found and How to Discover New Ones. SLAS Discov *26*, 484-502. 10.1177/2472555220965528.

Ito, T., Ando, H., Suzuki, T., Ogura, T., Hotta, K., Imamura, Y., Yamaguchi, Y., and Handa, H. (2010). Identification of a primary target of thalidomide teratogenicity. Science *327*, 1345-1350. 10.1126/science.1177319.

Itoh, Y., Ishikawa, M., Naito, M., and Hashimoto, Y. (2010). Protein knockdown using methyl bestatin-ligand hybrid molecules: design and synthesis of inducers of ubiquitination-mediated degradation of cellular retinoic acid-binding proteins. J Am Chem Soc *132*, 5820-5826. 10.1021/ja100691p.

Jackson, A.L., Burchard, J., Schelter, J., Chau, B.N., Cleary, M., Lim, L., and Linsley, P.S. (2006). Widespread siRNA "off-target" transcript silencing mediated by seed region sequence complementarity. RNA *12*, 1179-1187. 10.1261/rna.25706.

Jansen, V.M., Mayer, I.A., and Arteaga, C.L. (2016). Is There a Future for AKT Inhibitors in the Treatment of Cancer? Clin Cancer Res *22*, 2599-2601. 10.1158/1078-0432.CCR-16-0100.

Jentsch, S. (1992). The ubiquitin-conjugation system. Annu Rev Genet *26*, 179-207. 10.1146/annurev.ge.26.120192.001143.

Jerby-Arnon, L., Shah, P., Cuoco, M.S., Rodman, C., Su, M.J., Melms, J.C., Leeson, R., Kanodia, A., Mei, S., Lin, J.R., et al. (2018). A Cancer Cell Program Promotes T Cell Exclusion and Resistance to Checkpoint Blockade. Cell *175*, 984-997.e924. 10.1016/j.cell.2018.09.006.

Jiang, B., Wang, E.S., Donovan, K.A., Liang, Y., Fischer, E.S., Zhang, T., and Gray, N.S. (2019). Development of Dual and Selective Degraders of Cyclin-Dependent Kinases 4 and 6. Angew Chem Int Ed Engl *58*, 6321-6326. 10.1002/anie.201901336.

Kamakura, S., Moriguchi, T., and Nishida, E. (1999). Activation of the protein kinase ERK5/BMK1 by receptor tyrosine kinases. Identification and characterization of a signaling pathway to the nucleus. J Biol Chem *274*, 26563-26571. 10.1074/jbc.274.37.26563.

Kasler, H.G., Victoria, J., Duramad, O., and Winoto, A. (2000). ERK5 is a novel type of mitogen-activated protein kinase containing a transcriptional activation domain. Mol Cell Biol *20*, 8382-8389. 10.1128/MCB.20.22.8382-8389.2000.

Kato, Y., Kravchenko, V.V., Tapping, R.I., Han, J., Ulevitch, R.J., and Lee, J.D. (1997). BMK1/ERK5 regulates serum-induced early gene expression through transcription factor MEF2C. EMBO J *16*, 7054-7066. 10.1093/emboj/16.23.7054.

Keppler-Noreuil, K.M., Sapp, J.C., Lindhurst, M.J., Darling, T.N., Burton-Akright, J., Bagheri, M., Dombi, E., Gruber, A., Jarosinski, P.F., Martin, S., et al. (2019). Pharmacodynamic Study of Miransertib in Individuals with Proteus Syndrome. Am J Hum Genet *104*, 484-491. 10.1016/j.ajhg.2019.01.015.

Kim, H.J., Barnitz, R.A., Kreslavsky, T., Brown, F.D., Moffett, H., Lemieux, M.E., Kaygusuz, Y., Meissner, T., Holderried, T.A., Chan, S., et al. (2015). Stable inhibitory activity of regulatory T cells requires the transcription factor Helios. Science *350*, 334-339. 10.1126/science.aad0616.

Kleiger, G., and Mayor, T. (2014). Perilous journey: a tour of the ubiquitin-proteasome system. Trends Cell Biol *24*, 352-359. 10.1016/j.tcb.2013.12.003.

Kondoh, K., Terasawa, K., Morimoto, H., and Nishida, E. (2006). Regulation of nuclear translocation of extracellular signal-regulated kinase 5 by active nuclear import and export mechanisms. Mol Cell Biol *26*, 1679-1690. 10.1128/MCB.26.5.1679-1690.2006.

Kramer, L., and Zhang, X. (2022). Expanding the landscape of E3 ligases for targeted protein degradation. Current Research in Chemical Biology *2*. https://doi.org/10.1016/j.crchbi.2022.100020.

Kronke, J., Fink, E.C., Hollenbach, P.W., MacBeth, K.J., Hurst, S.N., Udeshi, N.D., Chamberlain, P.P., Mani, D.R., Man, H.W., Gandhi, A.K., et al. (2015). Lenalidomide induces ubiquitination and degradation of CK1alpha in del(5q) MDS. Nature *523*, 183-188. 10.1038/nature14610.

Kronke, J., Hurst, S.N., and Ebert, B.L. (2014). Lenalidomide induces degradation of IKZF1 and IKZF3. Oncoimmunology *3*, e941742. 10.4161/21624011.2014.941742.

Kyriakis, J.M., and Avruch, J. (2001). Mammalian mitogen-activated protein kinase signal transduction pathways activated by stress and inflammation. Physiol Rev *81*, 807-869. 10.1152/physrev.2001.81.2.807.

Le, R., Huang, Y., Zhang, Y., Wang, H., Lin, J., Dong, Y., Li, Z., Guo, M., Kou, X., Zhao, Y., et al. (2021). Dcaf11 activates Zscan4-mediated alternative telomere lengthening in early embryos and embryonic stem cells. Cell Stem Cell *28*, 732-747.e739. 10.1016/j.stem.2020.11.018.

Li, L., Mi, D., Pei, H., Duan, Q., Wang, X., Zhou, W., Jin, J., Li, D., Liu, M., and Chen, Y. (2020). In vivo target protein degradation induced by PROTACs based on E3 ligase DCAF15. Signal Transduct Target Ther *5*, 129. 10.1038/s41392-020-00245-0.

Liberzon, A., Birger, C., Thorvaldsdóttir, H., Ghandi, M., Mesirov, J.P., and Tamayo, P. (2015). The Molecular Signatures Database (MSigDB) hallmark gene set collection. Cell Syst *1*, 417-425. 10.1016/j.cels.2015.12.004.

Lin, E.C., Amantea, C.M., Nomanbhoy, T.K., Weissig, H., Ishiyama, J., Hu, Y., Sidique, S., Li, B., Kozarich, J.W., and Rosenblum, J.S. (2016). ERK5 kinase activity is dispensable for cellular immune response and proliferation. Proc Natl Acad Sci U S A *113*, 11865-11870. 10.1073/pnas.1609019113.

Lin, J., Sampath, D., Nannini, M.A., Lee, B.B., Degtyarev, M., Oeh, J., Savage, H., Guan, Z., Hong, R., Kassees, R., et al. (2013). Targeting activated Akt with GDC-0068, a novel selective Akt inhibitor that is efficacious in multiple tumor models. Clin Cancer Res *19*, 1760-1772. 10.1158/1078-0432.CCR-12-3072.

List, A., Dewald, G., Bennett, J., Giagounidis, A., Raza, A., Feldman, E., Powell, B., Greenberg, P., Thomas, D., Stone, R., et al. (2006). Lenalidomide in the myelodysplastic syndrome with chromosome 5q deletion. N Engl J Med *355*, 1456-1465. 10.1056/NEJMoa061292.

Liu, A., Trairatphisan, P., Gjerga, E., Didangelos, A., Barratt, J., and Saez-Rodriguez, J. (2019). From expression footprints to causal pathways: contextualizing large signaling networks with CARNIVAL. NPJ Syst Biol Appl *5*, 40. 10.1038/s41540-019-0118-z.

Lo, J.Y., Spatola, B.N., and Curran, S.P. (2017). WDR23 regulates NRF2 independently of KEAP1. PLoS Genet *13*, e1006762. 10.1371/journal.pgen.1006762.

Lochhead, P.A., Tucker, J.A., Tatum, N.J., Wang, J., Oxley, D., Kidger, A.M., Johnson, V.P., Cassidy, M.A., Gray, N.S., Noble, M.E.M., and Cook, S.J. (2020). Paradoxical activation of the protein kinase-transcription factor ERK5 by ERK5 kinase inhibitors. Nat Commun *11*, 1383. 10.1038/s41467-020-15031-3.

Lu, G., Middleton, R.E., Sun, H., Naniong, M., Ott, C.J., Mitsiades, C.S., Wong, K.K., Bradner, J.E., and Kaelin, W.G. (2014). The myeloma drug lenalidomide promotes the cereblon-dependent destruction of Ikaros proteins. Science *343*, 305-309. 10.1126/science.1244917.

Madsen, R.R., and Semple, R.K. (2022). PIK3CA-related overgrowth: silver bullets from the cancer arsenal? Trends Mol Med *28*, 255-257. 10.1016/j.molmed.2022.02.009.

Mahat, D.B., Kwak, H., Booth, G.T., Jonkers, I.H., Danko, C.G., Patel, R.K., Waters, C.T., Munson, K., Core, L.J., and Lis, J.T. (2016). Base-pair-resolution genome-wide mapping of active RNA polymerases using precision nuclear run-on (PRO-seq). Nat Protoc *11*, 1455-1476. 10.1038/nprot.2016.086.

Manguso, R.T., Pope, H.W., Zimmer, M.D., Brown, F.D., Yates, K.B., Miller, B.C., Collins, N.B., Bi, K., LaFleur, M.W., Juneja, V.R., et al. (2017). In vivo CRISPR screening identifies Ptpn2 as a cancer immunotherapy target. Nature *547*, 413-418. 10.1038/nature23270.

Maniaci, C., Hughes, S.J., Testa, A., Chen, W., Lamont, D.J., Rocha, S., Alessi, D.R., Romeo, R., and Ciulli, A. (2017). Homo-PROTACs: bivalent small-molecule dimerizers of the VHL E3 ubiquitin ligase to induce self-degradation. Nat Commun *8*, 830. 10.1038/s41467-017-00954-1.

Manning, B.D., and Cantley, L.C. (2007). AKT/PKB signaling: navigating downstream. Cell *129*, 1261-1274. 10.1016/j.cell.2007.06.009.

Manning, B.D., and Toker, A. (2017). AKT/PKB Signaling: Navigating the Network. Cell *169*, 381-405. 10.1016/j.cell.2017.04.001.

Mares, A., Miah, A.H., Smith, I.E.D., Rackham, M., Thawani, A.R., Cryan, J., Haile, P.A., Votta, B.J., Beal, A.M., Capriotti, C., et al. (2020). Extended pharmacodynamic responses observed upon PROTAC-mediated degradation of RIPK2. Commun Biol *3*, 140. 10.1038/s42003-020-0868-6.

Matyskiela, M.E., Lu, G., Ito, T., Pagarigan, B., Lu, C.C., Miller, K., Fang, W., Wang, N.Y., Nguyen, D., Houston, J., et al. (2016). A novel cereblon modulator recruits GSPT1 to the CRL4(CRBN) ubiquitin ligase. Nature *535*, 252-257. 10.1038/nature18611.

McAlister, G.C., Nusinow, D.P., Jedrychowski, M.P., Wühr, M., Huttlin, E.L., Erickson, B.K., Rad, R., Haas, W., and Gygi, S.P. (2014). MultiNotch MS3 enables accurate, sensitive, and multiplexed detection of differential expression across cancer cell line proteomes. Anal Chem *86*, 7150-7158. 10.1021/ac502040v.

Mebratu, Y., and Tesfaigzi, Y. (2009). How ERK1/2 activation controls cell proliferation and cell death: Is subcellular localization the answer? Cell Cycle *8*, 1168-1175. 10.4161/cc.8.8.8147.

Mehta, P.B., Jenkins, B.L., McCarthy, L., Thilak, L., Robson, C.N., Neal, D.E., and Leung, H.Y. (2003). MEK5 overexpression is associated with metastatic prostate cancer, and stimulates proliferation, MMP-9 expression and invasion. Oncogene *22*, 1381-1389. 10.1038/sj.onc.1206154.

Meyers, R.M., Bryan, J.G., McFarland, J.M., Weir, B.A., Sizemore, A.E., Xu, H., Dharia, N.V., Montgomery, P.G., Cowley, G.S., Pantel, S., et al. (2017). Computational correction of copy number effect improves specificity of CRISPR-Cas9 essentiality screens in cancer cells. Nat Genet *49*, 1779-1784. 10.1038/ng.3984.

Miller, M.T., and Strömland, K. (1999). Teratogen update: thalidomide: a review, with a focus on ocular findings and new potential uses. Teratology *60*, 306-321. 10.1002/(SICI)1096-9926(199911)60:5<306::AID-TERA11>3.0.CO;2-Y.

Modell, A.E., Lim, D., Nguyen, T.M., Sreekanth, V., and Choudhary, A. (2022). CRISPR-based therapeutics: current challenges and future applications. Trends Pharmacol Sci *43*, 151-161. 10.1016/j.tips.2021.10.012.

Mody, N., Campbell, D.G., Morrice, N., Peggie, M., and Cohen, P. (2003). An analysis of the phosphorylation and activation of extracellular-signal-regulated protein kinase 5 (ERK5) by mitogen-activated protein kinase kinase 5 (MKK5) in vitro. Biochem J *372*, 567-575. 10.1042/BJ20030193.

Mognol, G.P., Spreafico, R., Wong, V., Scott-Browne, J.P., Togher, S., Hoffmann, A., Hogan, P.G., Rao, A., and Trifari, S. (2017). Exhaustion-associated regulatory regions in CD8. Proc Natl Acad Sci U S A *114*, E2776-E2785. 10.1073/pnas.1620498114.

Morimoto, H., Kondoh, K., Nishimoto, S., Terasawa, K., and Nishida, E. (2007). Activation of a C-terminal transcriptional activation domain of ERK5 by autophosphorylation. J Biol Chem *282*, 35449-35456. 10.1074/jbc.M704079200.

Mullard, A. (2021). Targeted protein degraders crowd into the clinic. Nat Rev Drug Discov *20*, 247-250. 10.1038/d41573-021-00052-4.

Naito, M., Ohoka, N., and Shibata, N. (2019). SNIPERs-Hijacking IAP activity to induce protein degradation. Drug Discov Today Technol *31*, 35-42. 10.1016/j.ddtec.2018.12.002.

Nakagawa, H., Sido, J.M., Reyes, E.E., Kiers, V., Cantor, H., and Kim, H.J. (2016). Instability of Helios-deficient Tregs is associated with conversion to a T-effector phenotype and enhanced antitumor immunity. Proc Natl Acad Sci U S A *113*, 6248-6253. 10.1073/pnas.1604765113.

Nalawansha, D.A., and Crews, C.M. (2020). PROTACs: An Emerging Therapeutic Modality in Precision Medicine. Cell Chem Biol *27*, 998-1014. 10.1016/j.chembiol.2020.07.020.

Nguyen, D., Lemos, C., Wortmann, L., Eis, K., Holton, S.J., Boemer, U., Moosmayer, D., Eberspaecher, U., Weiske, J., Lechner, C., et al. (2019). Discovery and Characterization of the Potent and Highly Selective (Piperidin-4-yl)pyrido[3,2- d]pyrimidine Based in Vitro Probe BAY-885 for the Kinase ERK5. J Med Chem *62*, 928-940. 10.1021/acs.jmedchem.8b01606.

Nishimoto, S., and Nishida, E. (2006). MAPK signalling: ERK5 versus ERK1/2. EMBO Rep *7*, 782-786. 10.1038/sj.embor.7400755.

Ohoka, N., Tsuji, G., Shoda, T., Fujisato, T., Kurihara, M., Demizu, Y., and Naito, M. (2019). Development of Small Molecule Chimeras That Recruit AhR E3 Ligase to Target Proteins. ACS Chem Biol *14*, 2822-2832. 10.1021/acschembio.9b00704.

Oliveira, M., Saura, C., Nuciforo, P., Calvo, I., Andersen, J., Passos-Coelho, J.L., Gil Gil, M., Bermejo, B., Patt, D.A., Ciruelos, E., et al. (2019). FAIRLANE, a double-blind placebo-controlled randomized phase II trial of neoadjuvant ipatasertib plus paclitaxel for early triple-negative breast cancer. Ann Oncol. 10.1093/annonc/mdz177.

Olson, C.M., Jiang, B., Erb, M.A., Liang, Y., Doctor, Z.M., Zhang, Z., Zhang, T., Kwiatkowski, N., Boukhali, M., Green, J.L., et al. (2018). Pharmacological perturbation of CDK9 using selective CDK9 inhibition or degradation. Nat Chem Biol *14*, 163-170. 10.1038/nchembio.2538.

Paiva, S.L., and Crews, C.M. (2019). Targeted protein degradation: elements of PROTAC design. Curr Opin Chem Biol *50*, 111-119. 10.1016/j.cbpa.2019.02.022.

Palumbo, A., Hajek, R., Delforge, M., Kropff, M., Petrucci, M.T., Catalano, J., Gisslinger, H., Wiktor-Jędrzejczak, W., Zodelava, M., Weisel, K., et al. (2012). Continuous lenalidomide treatment for newly diagnosed multiple myeloma. N Engl J Med *366*, 1759-1769. 10.1056/NEJMoa1112704.

Pan, D., Kobayashi, A., Jiang, P., Ferrari de Andrade, L., Tay, R.E., Luoma, A.M., Tsoucas, D., Qiu, X., Lim, K., Rao, P., et al. (2018). A major chromatin regulator determines resistance of tumor cells to T cell-mediated killing. Science *359*, 770-775. 10.1126/science.aao1710.

Petrylak, D., Gao, X., Vogelzang, N., Garfield, M., Taylor, I., Moore, M., Peck, R., and Burris III, H. (2020). First-in-human phase I study of ARV-110, an androgen receptor (AR) PROTAC degrader in patients (pts) with metastatic castrate-resistant prostate cancer (mCRPC) following enzalutamide (ENZ) and/or abiraterone (ABI). Journal of Clinical Oncology *38* (*3500*). 10.1200/JCO.2020.38.15_suppl.3500.

Petzold, G., Fischer, E.S., and Thomä, N.H. (2016). Structural basis of lenalidomide-induced CK1α degradation by the CRL4(CRBN) ubiquitin ligase. Nature *532*, 127-130. 10.1038/nature16979.

Pfaff, P., Samarasinghe, K.T.G., Crews, C.M., and Carreira, E.M. (2019). Reversible Spatiotemporal Control of Induced Protein Degradation by Bistable PhotoPROTACs. ACS Cent Sci *5*, 1682-1690. 10.1021/acscentsci.9b00713.

Phong, M.S., Van Horn, R.D., Li, S., Tucker-Kellogg, G., Surana, U., and Ye, X.S. (2010). p38 mitogen-activated protein kinase promotes cell survival in response to DNA damage but is not required for the G(2) DNA damage checkpoint in human cancer cells. Mol Cell Biol *30*, 3816-3826. 10.1128/MCB.00949-09.

Pi, X., Garin, G., Xie, L., Zheng, Q., Wei, H., Abe, J., Yan, C., and Berk, B.C. (2005). BMK1/ERK5 is a novel regulator of angiogenesis by destabilizing hypoxia inducible factor 1alpha. Circ Res *96*, 1145-1151. 10.1161/01.RES.0000168802.43528.e1.

Plotnikov, A., Zehorai, E., Procaccia, S., and Seger, R. (2011). The MAPK cascades: signaling components, nuclear roles and mechanisms of nuclear translocation. Biochim Biophys Acta *1813*, 1619-1633. 10.1016/j.bbamcr.2010.12.012.

Powell, C.E., Du, G., Bushman, J.W., He, Z., Zhang, T., Fischer, E.S., and Gray, N.S. (2021). Selective degradation-inducing probes for studying cereblon (CRBN) biology. RSC Med Chem *12*, 1381-1390. 10.1039/d0md00382d.

Raina, K., Lu, J., Qian, Y., Altieri, M., Gordon, D., Rossi, A.M., Wang, J., Chen, X., Dong, H., Siu, K., et al. (2016). PROTAC-induced BET protein degradation as a therapy for castration-resistant prostate cancer. Proc Natl Acad Sci U S A *113*, 7124-7129. 10.1073/pnas.1521738113.

Ramsay, A.K., McCracken, S.R., Soofi, M., Fleming, J., Yu, A.X., Ahmad, I., Morland, R., Machesky, L., Nixon, C., Edwards, D.R., et al. (2011). ERK5 signalling in prostate cancer promotes an invasive phenotype. Br J Cancer *104*, 664-672. 10.1038/sj.bjc.6606062.

Regan, C.P., Li, W., Boucher, D.M., Spatz, S., Su, M.S., and Kuida, K. (2002). Erk5 null mice display multiple extraembryonic vascular and embryonic cardiovascular defects. Proc Natl Acad Sci U S A *99*, 9248-9253. 10.1073/pnas.142293999.

Remillard, D., Buckley, D.L., Paulk, J., Brien, G.L., Sonnett, M., Seo, H.S., Dastjerdi, S., Wühr, M., Dhe-Paganon, S., Armstrong, S.A., and Bradner, J.E. (2017). Degradation of the BAF Complex Factor BRD9 by Heterobifunctional Ligands. Angew Chem Int Ed Engl *56*, 5738-5743. 10.1002/anie.201611281.

Risso, G., Blaustein, M., Pozzi, B., Mammi, P., and Srebrow, A. (2015). Akt/PKB: one kinase, many modifications. Biochem J *468*, 203-214. 10.1042/BJ20150041.

Ritchie, M.E., Phipson, B., Wu, D., Hu, Y., Law, C.W., Shi, W., and Smyth, G.K. (2015). limma powers differential expression analyses for RNA-sequencing and microarray studies. Nucleic Acids Res *43*, e47. 10.1093/nar/gkv007.

Roberts, O.L., Holmes, K., Müller, J., Cross, D.A., and Cross, M.J. (2009). ERK5 and the regulation of endothelial cell function. Biochem Soc Trans *37*, 1254-1259. 10.1042/BST0371254.

Sakamoto, K.M., Kim, K.B., Kumagai, A., Mercurio, F., Crews, C.M., and Deshaies, R.J. (2001). Protacs: chimeric molecules that target proteins to the Skp1-Cullin-F box complex for ubiquitination and degradation. Proc Natl Acad Sci U S A *98*, 8554-8559. 10.1073/pnas.141230798.

Sampaio, E.P., Sarno, E.N., Galilly, R., Cohn, Z.A., and Kaplan, G. (1991). Thalidomide selectively inhibits tumor necrosis factor alpha production by stimulated human monocytes. J Exp Med *173*, 699-703. 10.1084/jem.173.3.699.

Sarbassov, D.D., Guertin, D.A., Ali, S.M., and Sabatini, D.M. (2005). Phosphorylation and regulation of Akt/PKB by the rictor-mTOR complex. Science *307*, 1098-1101. 10.1126/science.1106148.

Saura, C., Roda, D., Roselló, S., Oliveira, M., Macarulla, T., Pérez-Fidalgo, J.A., Morales-Barrera, R., Sanchis-García, J.M., Musib, L., Budha, N., et al. (2017). A First-in-Human Phase I Study of the ATP-Competitive AKT Inhibitor Ipatasertib Demonstrates Robust and Safe Targeting of AKT in Patients with Solid Tumors. Cancer Discov *7*, 102-113. 10.1158/2159-8290.CD-16-0512.

Schaer, D.A., Beckmann, R.P., Dempsey, J.A., Huber, L., Forest, A., Amaladas, N., Li, Y., Wang, Y.C., Rasmussen, E.R., Chin, D., et al. (2018). The CDK4/6 Inhibitor Abemaciclib Induces a T Cell Inflamed Tumor Microenvironment and Enhances the Efficacy of PD-L1 Checkpoint Blockade. Cell Rep *22*, 2978-2994. 10.1016/j.celrep.2018.02.053.

Schneekloth, A.R., Pucheault, M., Tae, H.S., and Crews, C.M. (2008). Targeted intracellular protein degradation induced by a small molecule: En route to chemical proteomics. Bioorg Med Chem Lett *18*, 5904-5908. 10.1016/j.bmcl.2008.07.114.

Schneekloth, J.S., Fonseca, F.N., Koldobskiy, M., Mandal, A., Deshaies, R., Sakamoto, K., and Crews, C.M. (2004). Chemical genetic control of protein levels: selective in vivo targeted degradation. J Am Chem Soc *126*, 3748-3754. 10.1021/ja039025z.

Shayesteh, L., Lu, Y., Kuo, W.L., Baldocchi, R., Godfrey, T., Collins, C., Pinkel, D., Powell, B., Mills, G.B., and Gray, J.W. (1999). PIK3CA is implicated as an oncogene in ovarian cancer. Nat Genet *21*, 99-102. 10.1038/5042.

Shimano, H., and Sato, R. (2017). SREBP-regulated lipid metabolism: convergent physiology - divergent pathophysiology. Nat Rev Endocrinol *13*, 710-730. 10.1038/nrendo.2017.91.

Simões, A.E., Rodrigues, C.M., and Borralho, P.M. (2016). The MEK5/ERK5 signalling pathway in cancer: a promising novel therapeutic target. Drug Discov Today *21*, 1654-1663. 10.1016/j.drudis.2016.06.010.

Singer, M., Wang, C., Cong, L., Marjanovic, N.D., Kowalczyk, M.S., Zhang, H., Nyman, J., Sakuishi, K., Kurtulus, S., Gennert, D., et al. (2016). A Distinct Gene Module for Dysfunction Uncoupled from Activation in Tumor-Infiltrating T Cells. Cell *166*, 1500-1511.e1509. 10.1016/j.cell.2016.08.052.

Singh, J., Petter, R.C., Baillie, T.A., and Whitty, A. (2011). The resurgence of covalent drugs. Nat Rev Drug Discov *10*, 307-317. 10.1038/nrd3410.

Sohn, S.J., Li, D., Lee, L.K., and Winoto, A. (2005). Transcriptional regulation of tissue-specific genes by the ERK5 mitogen-activated protein kinase. Mol Cell Biol *25*, 8553-8566. 10.1128/MCB.25.19.8553-8566.2005.

Solomon, J., Bonazzi, S., d'Hennezel, E., Beckwith, R., Xu, L., Fazal, A., Magracheva, A., Ramesh, R., Cernijenko, A., Antonakos, B., et al. (2022). Targeted degradation of IKZF2 for cancer immunotherapy. Research Square (Preprint). 10.21203/rs.3.rs-1531006/v1.

Song, C., Wang, L., Xu, Q., Wang, K., Xie, D., Yu, Z., Jiang, K., Liao, L., Yates, J.R., Lee, J.D., and Yang, Q. (2017). Targeting BMK1 Impairs the Drug Resistance to Combined Inhibition of BRAF and MEK1/2 in Melanoma. Sci Rep *7*, 46244. 10.1038/srep46244.

Song, K.W., Edgar, K.A., Hanan, E.J., Hafner, M., Oeh, J., Merchant, M., Sampath, D., Nannini, M.A., Hong, R., Phu, L., et al. (2022). RTK-Dependent Inducible Degradation of Mutant PI3Kα Drives GDC-0077 (Inavolisib) Efficacy. Cancer Discov *12*, 204-219. 10.1158/2159-8290.CD-21-0072.

Soucy, T.A., Smith, P.G., and Rolfe, M. (2009). Targeting NEDD8-activated cullin-RING ligases for the treatment of cancer. Clin Cancer Res *15*, 3912-3916. 10.1158/1078-0432.CCR-09-0343.

Spradlin, J.N., Hu, X., Ward, C.C., Brittain, S.M., Jones, M.D., Ou, L., To, M., Proudfoot, A., Ornelas, E., Woldegiorgis, M., et al. (2019). Harnessing the anti-cancer natural product nimbolide for targeted protein degradation. Nat Chem Biol *15*, 747-755. 10.1038/s41589-019-0304-8.

Sun, X., Gao, H., Yang, Y., He, M., Wu, Y., Song, Y., Tong, Y., and Rao, Y. (2019). PROTACs: great opportunities for academia and industry. Signal Transduct Target Ther *4*, 64. 10.1038/s41392-019-0101-6.

Sun, Y., Liu, W.Z., Liu, T., Feng, X., Yang, N., and Zhou, H.F. (2015). Signaling pathway of MAPK/ERK in cell proliferation, differentiation, migration, senescence and apoptosis. J Recept Signal Transduct Res *35*, 600-604. 10.3109/10799893.2015.1030412.

Słabicki, M., Kozicka, Z., Petzold, G., Li, Y.D., Manojkumar, M., Bunker, R.D., Donovan, K.A., Sievers, Q.L., Koeppel, J., Suchyta, D., et al. (2020). The CDK inhibitor CR8 acts as a molecular glue degrader that depletes cyclin K. Nature *585*, 293-297. 10.1038/s41586-020-2374-x.

Takahashi, D., Moriyama, J., Nakamura, T., Miki, E., Takahashi, E., Sato, A., Akaike, T., Itto-Nakama, K., and Arimoto, H. (2019). AUTACs: Cargo-Specific Degraders Using Selective Autophagy. Mol Cell *76*, 797-810.e710. 10.1016/j.molcel.2019.09.009.

Team, R. (2014). R: A language and environment for statistical computing.

Thibaudeau, T.A., and Smith, D.M. (2019). A Practical Review of Proteasome Pharmacology. Pharmacol Rev *71*, 170-197. 10.1124/pr.117.015370.

Toker, A. (2012). Achieving specificity in Akt signaling in cancer. Adv Biol Regul *52*, 78-87. 10.1016/j.advenzreg.2011.09.020.

Tong, B., Spradlin, J.N., Novaes, L.F.T., Zhang, E., Hu, X., Moeller, M., Brittain, S.M., McGregor, L.M., McKenna, J.M., Tallarico, J.A., et al. (2020). A Nimbolide-Based Kinase Degrader Preferentially Degrades Oncogenic BCR-ABL. ACS Chem Biol *15*, 1788-1794. 10.1021/acschembio.0c00348.

Tsherniak, A., Vazquez, F., Montgomery, P.G., Weir, B.A., Kryukov, G., Cowley, G.S., Gill, S., Harrington, W.F., Pantel, S., Krill-Burger, J.M., et al. (2017). Defining a Cancer Dependency Map. Cell *170*, 564-576.e516. 10.1016/j.cell.2017.06.010.

Tubita, A., Lombardi, Z., Tusa, I., Lazzeretti, A., Sgrignani, G., Papini, D., Menconi, A., Gagliardi, S., Lulli, M., Dello Sbarba, P., et al. (2022). Inhibition of ERK5 Elicits Cellular Senescence in Melanoma via the Cyclin-Dependent Kinase Inhibitor p21. Cancer Res *82*, 447-457. 10.1158/0008-5472.CAN-21-0993.

Turner, N.C., Alarcon, E., Armstrong, A.C., Philco, M., Lopez Chuken, Y.A., Sablin, M.P., Tamura, K., Gomez Villanueva, A., Perez-Fidalgo, J.A., Cheung, S.Y.A., et al. (2019). BEECH: a dose-finding run-in followed by a randomised phase II study assessing the efficacy of AKT inhibitor capivasertib (AZD5363) combined with paclitaxel in patients with estrogen receptor-positive advanced or metastatic breast cancer, and in a PIK3CA mutant sub-population. Ann Oncol *30*, 774-780. 10.1093/annonc/mdz086.

Uhlenbrock, N., Smith, S., Weisner, J., Landel, I., Lindemann, M., Le, T.A., Hardick, J., Gontla, R., Scheinpflug, R., Czodrowski, P., et al. (2019). Structural and chemical insights into the covalent-allosteric inhibition of the protein kinase Akt. Chem Sci *10*, 3573-3585. 10.1039/c8sc05212c.

van der Zanden, S.Y., Luimstra, J.J., Neefjes, J., Borst, J., and Ovaa, H. (2020). Opportunities for Small Molecules in Cancer Immunotherapy. Trends Immunol *41*, 493-511. 10.1016/j.it.2020.04.004.

Vanhaesebroeck, B., Guillermet-Guibert, J., Graupera, M., and Bilanges, B. (2010). The emerging mechanisms of isoform-specific PI3K signalling. Nat Rev Mol Cell Biol *11*, 329-341. 10.1038/nrm2882.

Vaseva, A.V., Blake, D.R., Gilbert, T.S.K., Ng, S., Hostetter, G., Azam, S.H., Ozkan-Dagliyan, I., Gautam, P., Bryant, K.L., Pearce, K.H., et al. (2018). KRAS Suppression-Induced

Degradation of MYC Is Antagonized by a MEK5-ERK5 Compensatory Mechanism. Cancer Cell *34*, 807-822.e807. 10.1016/j.ccell.2018.10.001.

Vivanco, I., Chen, Z.C., Tanos, B., Oldrini, B., Hsieh, W.Y., Yannuzzi, N., Campos, C., and Mellinghoff, I.K. (2014). A kinase-independent function of AKT promotes cancer cell survival. Elife *3*. 10.7554/eLife.03751.

Wang, C., Zhang, Y., Wu, Y., and Xing, D. (2021a). Developments of CRBN-based PROTACs as potential therapeutic agents. Eur J Med Chem *225*, 113749. 10.1016/j.ejmech.2021.113749.

Wang, E.S., Verano, A.L., Nowak, R.P., Yuan, J.C., Donovan, K.A., Eleuteri, N.A., Yue, H., Ngo, K.H., Lizotte, P.H., Gokhale, P.C., et al. (2021b). Acute pharmacological degradation of Helios destabilizes regulatory T cells. Nat Chem Biol *17*, 711-717. 10.1038/s41589-021-00802-w.

Wang, H., Zhang, Q., Wen, Q., Zheng, Y., Lazarovici, P., Jiang, H., Lin, J., and Zheng, W. (2012). Proline-rich Akt substrate of 40kDa (PRAS40): a novel downstream target of PI3k/Akt signaling pathway. Cell Signal *24*, 17-24. 10.1016/j.cellsig.2011.08.010.

Wang, J., Erazo, T., Ferguson, F.M., Buckley, D.L., Gomez, N., Muñoz-Guardiola, P., Diéguez-Martínez, N., Deng, X., Hao, M., Massefski, W., et al. (2018). Structural and Atropisomeric Factors Governing the Selectivity of Pyrimido-benzodiazipinones as Inhibitors of Kinases and Bromodomains. ACS Chem Biol *13*, 2438-2448. 10.1021/acschembio.7b00638.

Wang, K., Liu, Y., Yu, Z., Gu, B., Hu, J., Huang, L., Ge, X., Xu, L., Zhang, M., Zhao, J., et al. (2021c). Phosphorylation at Ser68 facilitates DCAF11-mediated ubiquitination and degradation of CENP-A during the cell cycle. Cell Rep *37*, 109987. 10.1016/j.celrep.2021.109987.

Wang, Q., Chen, X., and Hay, N. (2017). Akt as a target for cancer therapy: more is not always better (lessons from studies in mice). Br J Cancer *117*, 159-163. 10.1038/bjc.2017.153.

Wang, X., and Tournier, C. (2006). Regulation of cellular functions by the ERK5 signalling pathway. Cell Signal *18*, 753-760. 10.1016/j.cellsig.2005.11.003.

Ward, C.C., Kleinman, J.I., Brittain, S.M., Lee, P.S., Chung, C.Y.S., Kim, K., Petri, Y., Thomas, J.R., Tallarico, J.A., McKenna, J.M., et al. (2019). Covalent Ligand Screening Uncovers a RNF4 E3 Ligase Recruiter for Targeted Protein Degradation Applications. ACS Chem Biol *14*, 2430-2440. 10.1021/acschembio.8b01083.

Warner, J.R. (1977). In the absence of ribosomal RNA synthesis, the ribosomal proteins of HeLa cells are synthesized normally and degraded rapidly. J Mol Biol *115*, 315-333. 10.1016/0022-2836(77)90157-7.

Wei, J., Meng, F., Park, K.S., Yim, H., Velez, J., Kumar, P., Wang, L., Xie, L., Chen, H., Shen, Y., et al. (2021). Harnessing the E3 Ligase KEAP1 for Targeted Protein Degradation. J Am Chem Soc *143*, 15073-15083. 10.1021/jacs.1c04841.

Weng, G., Shen, C., Cao, D., Gao, J., Dong, X., He, Q., Yang, B., Li, D., Wu, J., and Hou, T. (2021). PROTAC-DB: an online database of PROTACs. Nucleic Acids Res *49*, D1381-D1387. 10.1093/nar/gkaa807.

Wilhelmsen, K., Mesa, K.R., Lucero, J., Xu, F., and Hellman, J. (2012). ERK5 protein promotes, whereas MEK1 protein differentially regulates, the Toll-like receptor 2 protein-dependent activation of human endothelial cells and monocytes. J Biol Chem *287*, 26478-26494. 10.1074/jbc.M112.359489.

Wilhelmsen, K., Xu, F., Farrar, K., Tran, A., Khakpour, S., Sundar, S., Prakash, A., Wang, J., Gray, N.S., and Hellman, J. (2015). Extracellular signal-regulated kinase 5 promotes acute cellular and systemic inflammation. Sci Signal *8*, ra86. 10.1126/scisignal.aaa3206.

Winter, G.E., Buckley, D.L., Paulk, J., Roberts, J.M., Souza, A., Dhe-Paganon, S., and Bradner, J.E. (2015). DRUG DEVELOPMENT. Phthalimide conjugation as a strategy for in vivo target protein degradation. Science *348*, 1376-1381. 10.1126/science.aab1433.

Winter, G.E., Mayer, A., Buckley, D.L., Erb, M.A., Roderick, J.E., Vittori, S., Reyes, J.M., di Iulio, J., Souza, A., Ott, C.J., et al. (2017). BET Bromodomain Proteins Function as Master Transcription Elongation Factors Independent of CDK9 Recruitment. Mol Cell *67*, 5-18.e19. 10.1016/j.molcel.2017.06.004.

Wortzel, I., and Seger, R. (2011). The ERK Cascade: Distinct Functions within Various Subcellular Organelles. Genes Cancer *2*, 195-209. 10.1177/1947601911407328.

Wu, W.I., Voegtli, W.C., Sturgis, H.L., Dizon, F.P., Vigers, G.P., and Brandhuber, B.J. (2010). Crystal structure of human AKT1 with an allosteric inhibitor reveals a new mode of kinase inhibition. PLoS One *5*, e12913. 10.1371/journal.pone.0012913.

Xu, J., Yu, X., Martin, T.C., Bansal, A., Cheung, K., Lubin, A., Stratikopoulos, E., Cahuzac, K.M., Wang, L., Xie, L., et al. (2021). AKT Degradation Selectively Inhibits the Growth of PI3K/PTEN Pathway-Mutant Cancers with Wild-Type KRAS and BRAF by Destabilizing Aurora Kinase B. Cancer Discov *11*, 3064-3089. 10.1158/2159-8290.CD-20-0815.

Yan, C., Luo, H., Lee, J.D., Abe , J., and Berk, B.C. (2001). Molecular cloning of mouse ERK5/BMK1 splice variants and characterization of ERK5 functional domains. J Biol Chem *276*, 10870-10878. 10.1074/jbc.M009286200.

Yang, C.C., Ornatsky, O.I., McDermott, J.C., Cruz, T.F., and Prody, C.A. (1998). Interaction of myocyte enhancer factor 2 (MEF2) with a mitogen-activated protein kinase, ERK5/BMK1. Nucleic Acids Res *26*, 4771-4777. 10.1093/nar/26.20.4771.

Yang, J., Cron, P., Thompson, V., Good, V.M., Hess, D., Hemmings, B.A., and Barford, D. (2002). Molecular mechanism for the regulation of protein kinase B/Akt by hydrophobic motif phosphorylation. Mol Cell *9*, 1227-1240. 10.1016/s1097-2765(02)00550-6.

Yang, Q., Deng, X., Lu, B., Cameron, M., Fearns, C., Patricelli, M.P., Yates, J.R., Gray, N.S., and Lee, J.D. (2010). Pharmacological inhibition of BMK1 suppresses tumor growth through promyelocytic leukemia protein. Cancer Cell *18*, 258-267. 10.1016/j.ccr.2010.08.008.

Yang, Z., Sun, Y., Ni, Z., Yang, C., Tong, Y., Liu, Y., Li, H., and Rao, Y. (2021). Merging PROTAC and molecular glue for degrading BTK and GSPT1 proteins concurrently. Cell Res *31*, 1315-1318. 10.1038/s41422-021-00533-6.

Yap, T.A., Yan, L., Patnaik, A., Fearen, I., Olmos, D., Papadopoulos, K., Baird, R.D., Delgado, L., Taylor, A., Lupinacci, L., et al. (2011). First-in-man clinical trial of the oral pan-AKT inhibitor MK-2206 in patients with advanced solid tumors. J Clin Oncol *29*, 4688-4695. 10.1200/JCO.2011.35.5263.

Yates, K., Bi, K., Haining, W.N., Cantor, H., and Kim, H.J. (2018). Comparative transcriptome analysis reveals distinct genetic modules associated with Helios expression in intratumoral regulatory T cells. Proc Natl Acad Sci U S A *115*, 2162-2167. 10.1073/pnas.1720447115.

Yoon, S., and Seger, R. (2006). The extracellular signal-regulated kinase: multiple substrates regulate diverse cellular functions. Growth Factors *24*, 21-44. 10.1080/02699050500284218.

Yu, Y., Savage, R.E., Eathiraj, S., Meade, J., Wick, M.J., Hall, T., Abbadessa, G., and Schwartz, B. (2015). Targeting AKT1-E17K and the PI3K/AKT Pathway with an Allosteric AKT Inhibitor, ARQ 092. PLoS One *10*, e0140479. 10.1371/journal.pone.0140479.

Zen, K., Yasui, K., Nakajima, T., Zen, Y., Gen, Y., Mitsuyoshi, H., Minami, M., Mitsufuji, S., Tanaka, S., Itoh, Y., et al. (2009). ERK5 is a target for gene amplification at 17p11 and promotes cell growth in hepatocellular carcinoma by regulating mitotic entry. Genes Chromosomes Cancer *48*, 109-120. 10.1002/gcc.20624.

Zeng, M., Xiong, Y., Safaee, N., Nowak, R.P., Donovan, K.A., Yuan, C.J., Nabet, B., Gero, T.W., Feru, F., Li, L., et al. (2020). Exploring Targeted Degradation Strategy for Oncogenic KRAS. Cell Chem Biol *27*, 19-31.e16. 10.1016/j.chembiol.2019.12.006.

Zengerle, M., Chan, K.H., and Ciulli, A. (2015). Selective Small Molecule Induced Degradation of the BET Bromodomain Protein BRD4. ACS Chem Biol *10*, 1770-1777. 10.1021/acschembio.5b00216.

Zhang, L., Riley-Gillis, B., Vijay, P., and Shen, Y. (2019a). Acquired Resistance to BET-PROTACs (Proteolysis-Targeting Chimeras) Caused by Genomic Alterations in Core Components of E3 Ligase Complexes. Mol Cancer Ther *18*, 1302-1311. 10.1158/1535-7163.MCT-18-1129.

Zhang, X., Crowley, V.M., Wucherpfennig, T.G., Dix, M.M., and Cravatt, B.F. (2019b). Electrophilic PROTACs that degrade nuclear proteins by engaging DCAF16. Nat Chem Biol *15*, 737-746. 10.1038/s41589-019-0279-5.

Zhang, X., Luukkonen, L.M., Eissler, C.L., Crowley, V.M., Yamashita, Y., Schafroth, M.A., Kikuchi, S., Weinstein, D.S., Symons, K.T., Nordin, B.E., et al. (2021). DCAF11 Supports

Targeted Protein Degradation by Electrophilic Proteolysis-Targeting Chimeras. J Am Chem Soc *143*, 5141-5149. 10.1021/jacs.1c00990.

Zhou, G., Bao, Z.Q., and Dixon, J.E. (1995). Components of a new human protein kinase signal transduction pathway. J Biol Chem *270*, 12665-12669. 10.1074/jbc.270.21.12665.

Zhou, X., Liao, W.J., Liao, J.M., Liao, P., and Lu, H. (2015). Ribosomal proteins: functions beyond the ribosome. J Mol Cell Biol *7*, 92-104. 10.1093/jmcb/mjv014.

Zhou, Z., Song, X., Wavelet, C.M., and Wan, Y. (2020). Cullin 4-DCAF Proteins in Tumorigenesis. Adv Exp Med Biol *1217*, 241-259. 10.1007/978-981-15-1025-0_15.

Zhu, Y.X., Braggio, E., Shi, C.X., Bruins, L.A., Schmidt, J.E., Van Wier, S., Chang, X.B., Bjorklund, C.C., Fonseca, R., Bergsagel, P.L., et al. (2011). Cereblon expression is required for the antimyeloma activity of lenalidomide and pomalidomide. Blood *118*, 4771-4779. 10.1182/blood-2011-05-356063.